

**Field and Laboratory Investigation of Frazil Floc and Surface Ice Properties**

by

Chuankang Pei

A thesis submitted in partial fulfillment of the requirements for the degree of

Doctor of Philosophy

in

Water Resources Engineering

Department of Civil and Environmental Engineering  
University of Alberta

© Chuankang Pei, 2024

# Abstract

Frazil ice particles and flocs can adhere to underwater structures causing blockage to water intakes and large accumulation of frazil ice in the channel may cause flooding and property damage. After frazil floc rises to the water surface the resulting surface ice profoundly impacts river hydraulics and bank stability. Significant progress has been made in investigating the properties and evolution of frazil ice particles. However, the physical process in which frazil particles flocculate into flocs and rise to the surface forming ice pans remains largely unknown due to limited data available on the properties of frazil floc and surface ice. The motivation of this study was to determine the properties of frazil floc and surface ice as well as their evolution under changing environmental conditions to better model and predict their physical behavior throughout the river freeze-up.

The use of oblique images of river surfaces captured at long focus distances for long-term monitoring of surface ice conditions and ice pan properties was explored. Image data from a public camera mounted on a building rooftop captured during five freeze-up seasons was used. A deep learning based hybrid image processing algorithm was developed and evaluated to compute surface ice concentrations as well as ice pan sizes and shapes. The ice pans detected were generally elliptical shaped and their diameters ranged from 0.55 to 15.03 m. A lognormal distribution was a good fit for the ice pan size distributions for all years. Time series analysis showed that the appearance of ice pans coincided with supercooling and daily mean ice pan diameter varied from 1 to 3 m. These results demonstrate the viability of this method, which may open opportunities to identify and use public camera images for surface ice quantification.

Properties of frazil flocs were measured for the first time in field by deploying a submersible camera system a total of eleven times during supercooling in the North Saskatchewan, Peace, and Kananaskis Rivers. A lognormal distribution was found to be a good fit for the floc size distribution. The mean floc size ranged from 1.19 to 5.64 mm and decreased linearly as the local Reynolds number increased. The average floc number concentration ranged from  $1.80 \times 10^{-4}$  to  $1.15 \times 10^{-1} \text{ cm}^{-3}$ . The average floc volumetric concentration ranged from  $2.05 \times 10^{-7}$  to  $4.56 \times 10^{-3}$  and was found to correlate strongly with the fractional height above the bed through a power law relationship. No significant correlations were found between the air-water heat flux and floc properties. Floc number concentration and mean size increased significantly just before peak supercooling and reached a maximum near the end of principal supercooling.

To explore how the supercooling curve and frazil ice particle and floc properties vary under different air-water heat flux scenarios, a series of laboratory experiments were conducted in which frazil particles and flocs were generated and imaged when the cold room air temperature was increased or decreased threefold at different times during supercooling events. It was found that increasing the heat flux raised the mean particle number concentration by 25 - 33 % but did not significantly affect the mean floc number concentration. Decreasing the heat flux only produced significant effects when the change occurred before peak supercooling, reducing mean particle and floc number concentration by 10 and 22 %, respectively. Time series analysis showed that varying heat flux during different supercooling phases led to significantly different responses in the supercooling curve and particle and floc evolution.

Additional laboratory frazil tank experiments were performed to investigate the correlation between the time series of frazil particle and floc properties under different air temperatures and turbulent dissipation rates. A strong linear relationship between particle and floc number concentrations was found with the floc-to-particle number concentration ratio ranging from 0.29 - 0.35. The ratio was reduced by 12 - 17 % when the

turbulent dissipation rate was lower. A moderate to strong nonlinear correlation was found between mean particle and floc sizes described by an exponential relationship when particle mean sizes increased or decreased significantly. When particle mean size reaches an approximate equilibrium, a weak to moderate linear correlation was found between mean particle and floc size and the negative slope suggests they are inversely correlated.

# Preface

This paper-based thesis is an original work by Chuankang Pei under the supervision of Dr. Yuntong She and Dr. Mark Loewen.

- Chapter 2 of this thesis has been published as Pei, C., Y. She, and M. Loewen. 2023. "Deep Learning Based River Surface Ice Quantification Using a Distant and Oblique-Viewed Public Camera". *Cold Regions Science and Technology* 206 (February):103736. I was responsible for methodology, investigation, software, formal analysis, validation, data curation, visualization, and writing - original draft. Dr. She and Dr. Loewen were both involved with conceptualization, methodology, resources, supervision, writing - review & editing, project administration, and funding acquisition.
- Chapter 3 of this thesis has been published as Pei, C., J. Yang, Y. She, and M. Loewen. 2024. "Measurements of Frazil Ice Floes in Rivers". *The Cryosphere* 18, no. 9 (September): 4177-4196. I was responsible for methodology, investigation, software, formal analysis, validation, data curation, visualization, and writing - original draft. I worked collaboratively with Yang on the planning and coordination of field work trips, and he was involved with investigation, writing - review & editing. Dr. She and Dr. Loewen were both involved with conceptualization, methodology, resources, supervision, writing - review & editing, project administration, and funding acquisition.
- Chapter 4 and Chapter 5 of this thesis are currently being prepared as journal manuscripts. I was responsible for conceptualization, methodology, investigation,

software, formal analysis, validation, data curation, visualization, and writing - original draft. Dr. She and Dr. Loewen were both involved with conceptualization, methodology, resources, supervision, writing - review & editing, project administration, and funding acquisition.

# Acknowledgements

First and foremost, I would like to extend my deepest gratitude to my supervisors Dr. Yuntong She and Dr. Mark Loewen. They introduced me to this fascinating field of river ice engineering and provided immense resources, guidance, and support throughout my PhD journey, making this work possible. Their rich knowledge and experience, patience and open-mindedness in mentoring, and meticulous approach to research have taught me a great deal. I would like to thank my supervisory committee member Dr. Tadros Ghobrial for your guidance and suggestions. Sincere thanks to Dr. Shawn Clark, Dr. Nicholas Beier, Dr. Sina Ghaemi, Dr. Hongli Liu, and Dr. Wenming Zhang for your valuable time and effort in serving on my candidacy and final examinations.

My heartfelt appreciation goes to everyone who has assisted me during my studies. I would like to thank Perry Fedun for your invaluable technical support throughout my research, Sean Boyd who showed me all the basics of fieldwork when I just started, Igor Jakab for providing the archived EAS camera images, and Jonathan Gelinias for providing access to the EL Smith Water Treatment Plant of EPCOR Utilities Inc. Special thanks to Martin Jasek for providing simulation data to help plan the Peace River deployments, Kerry Paslawski for assisting with the Peace River deployments, and Dr. Vincent McFarlane for assisting with the Kananaskis River deployments and sharing valuable experiences in assembling and operating the FrazilCam system. I must thank my colleagues and friends from the River Ice Research group, Jiaqi Yang, Heyu Fang, and Xun Hong, for their generous assistance especially in the field. Hauling a 90-pound camera system into the river and keeping an eye on it for six hours in Alberta's brutal winters day after day isn't exactly the world's most pleasant work, but you all showed

up every time I needed help.

This research was funded by the Natural Sciences and Engineering Research Council of Canada (NSERC), Part of the research computing was enabled by support provided by WestGrid ([www.westgrid.ca](http://www.westgrid.ca)) and Compute Canada ([www.computecanada.ca](http://www.computecanada.ca)). The maps shown in this thesis were produced with QGIS software (<https://qgis.org/en/site/>) using the data provided by © OpenStreetMap contributors (<https://www.openstreetmap.org/copyright>) and OpenMapTiles (<http://openmaptiles.org/>). I would like to gratefully acknowledge China Scholarship Council (CSC), University of Alberta, R (Larry) Gerard Memorial Graduate Scholarship in Ice Engineering, as well as various travel grants and assistantships for providing financial support during my studies.

Finally, I express my profound appreciation to my friends and family, whose unwavering love and support have always been my anchor through life's turbulent waters. None of this would have been possible without you.

# Table of Contents

|  |             |
|--|-------------|
| <b>Abstract</b>  | <b>ii</b>   |
| <b>Preface</b>   | <b>v</b>    |
| <b>Acknowledgements</b>  | <b>vii</b>  |
| <b>List of Tables</b>  | <b>xiii</b> |
| <b>List of Figures</b>   | <b>xv</b>   |
| <b>1 Introduction</b>  | <b>1</b>    |
| 1.1 Background . . . . .   | 1           |
| 1.2 Literature Review . . . . .  | 4           |
| 1.2.1 Supercooling Process . . . . .   | 4           |
| 1.2.2 Frazil Ice Particles and Flocs . . . . .   | 6           |
| 1.2.3 Surface Ice Characteristics . . . . .  | 8           |
| 1.3 Knowledge Gaps . . . . .   | 9           |
| 1.4 Research Objectives . . . . .  | 10          |
| <b>2 Deep Learning Based River Surface Ice Quantification Using a Distant and Oblique-Viewed Public Camera</b> | <b>12</b>   |
| 2.1 Introduction . . . . .   | 12          |
| 2.2 Study Site . . . . .   | 17          |
| 2.3 Image Source and Instrumentation . . . . .   | 18          |
| 2.4 Image Processing . . . . .   | 19          |

|          |   |           |
|----------|---|-----------|
| 2.4.1    | Image Classification . . . . .  | 20        |
| 2.4.2    | Image Rectification . . . . .   | 22        |
| 2.4.3    | Image Segmentation . . . . .  | 24        |
| 2.4.4    | Ice Pan Properties Extraction . . . . .   | 30        |
| 2.4.5    | Overall Qualitative Performance . . . . .   | 32        |
| 2.5      | Results and Discussion . . . . .  | 33        |
| 2.5.1    | Comparison of Ice Concentrations Estimated From EAS and Bridge-<br>Cam Images . . . . .           | 33        |
| 2.5.2    | Time Series of Surface Ice Concentration . . . . .  | 36        |
| 2.5.3    | Ice Pan Properties . . . . .  | 39        |
| 2.5.4    | Time Series of Ice Pan Properties . . . . .   | 43        |
| 2.6      | Conclusions . . . . .   | 46        |
| <b>3</b> | <b>Measurements of Frazil Ice Floccs in Rivers</b>  | <b>49</b> |
| 3.1      | Introduction . . . . .  | 49        |
| 3.2      | Study Reaches . . . . .   | 52        |
| 3.3      | Instrumentation, Methodology and Deployments . . . . .  | 53        |
| 3.4      | Data Processing . . . . .   | 61        |
| 3.4.1    | Image Processing . . . . .  | 61        |
| 3.4.2    | Heat Flux Analysis at the Water Surface . . . . .   | 66        |
| 3.5      | Results . . . . .   | 68        |
| 3.5.1    | Floc Shape, Size and Concentration . . . . .  | 68        |
| 3.5.2    | Floc Size Distribution . . . . .  | 72        |
| 3.5.3    | Time Series . . . . .   | 72        |
| 3.6      | Discussion . . . . .  | 76        |
| 3.7      | Conclusions . . . . .   | 86        |
| <b>4</b> | <b>Laboratory Study of Supercooling and Frazil Evolution Under Varied Heat<br/>Flux Scenarios</b> | <b>89</b> |

|          |  |            |
|----------|--|------------|
| 4.1      | Introduction . . . . .   | 89         |
| 4.2      | Methodology . . . . .  | 93         |
| 4.2.1    | Experimental Setup . . . . .   | 93         |
| 4.2.2    | Experimental Conditions and Procedures . . . . .   | 94         |
| 4.2.3    | Experiment Repeatability . . . . .   | 97         |
| 4.2.4    | Data Processing and Analysis . . . . .   | 99         |
| 4.3      | Results . . . . .  | 106        |
| 4.3.1    | Time Series . . . . .  | 106        |
| 4.3.2    | Production and Decay Rates . . . . .   | 114        |
| 4.3.3    | Mean Number Concentrations . . . . .   | 116        |
| 4.3.4    | Size Distributions and Properties . . . . .  | 118        |
| 4.4      | Discussion . . . . .   | 120        |
| 4.4.1    | Supercooling Under Varied Heat Flux Scenarios . . . . .                                    | 120        |
| 4.4.2    | Particle and Floc Number Concentrations . . . . .  | 123        |
| 4.4.3    | Particle and Floc Sizes . . . . .  | 125        |
| 4.5      | Conclusions . . . . .  | 125        |
| <b>5</b> | <b>Laboratory Study of the Correlation Between Frazil Ice Particle and Floc Properties</b> | <b>128</b> |
| 5.1      | Introduction . . . . .   | 128        |
| 5.2      | Experimental Setup and Methods . . . . .   | 130        |
| 5.3      | Experiment Repeatability . . . . .   | 132        |
| 5.4      | Data Processing . . . . .  | 134        |
| 5.5      | Results and Discussion . . . . .   | 135        |
| 5.5.1    | Time Series . . . . .  | 135        |
| 5.5.2    | Correlation Between Particle and Floc Number Concentrations . . . . .                      | 140        |
| 5.5.3    | Correlation Between Particle and Floc Mean Sizes . . . . .                                 | 142        |
| 5.6      | Conclusions . . . . .  | 145        |

|          |  |            |
|----------|--|------------|
| <b>6</b> | <b>Conclusions</b>   | <b>146</b> |
| 6.1      | Summary and Conclusions . . . . .  | 146        |
| 6.2      | Recommendations for Future Research . . . . .  | 151        |
|          | <b>Bibliography</b>  | <b>153</b> |
|          | <b>Appendix A: Time Series Plots for the Remaining Eight Field FrazilCam Deployments</b> | <b>164</b> |

# List of Tables

|     |   |    |
|-----|---|----|
| 2.1 | The number of labelled images in each image category. . . . .   | 22 |
| 2.2 | Details of the images and corresponding labels in each condition used for UNet training/testing. . . . .  | 29 |
| 2.3 | UNet segmentation performance for ice pan images. . . . .   | 30 |
| 2.4 | Comparison of UNet segmentation performance between this study and Singh et al. (2020). . . . .   | 30 |
| 2.5 | Examples of ice pans of different shapes and its corresponding $d_p/d$ and $AR$ . Light blue lines denote overlaid ice pan boundary. Note that $d_p/d$ and $AR$ was calculated for the largest pan that appeared in each image. . . . .                                 | 33 |
| 2.6 | Synopsis of freeze-up in each year. . . . .   | 37 |
| 2.7 | Ice pan size properties during the freeze-up period. $N_T$ is the total ice pan count, $N_I$ is the number of ice pans per image, $d_m$ , $\sigma$ , $d_{max}$ is the mean, standard deviation and maximum ice pan size. . . . .  | 41 |
| 3.1 | Summary of the study reach characteristics. . . . .   | 54 |
| 3.2 | The distances between weather stations and deployment sites. . . . .  | 58 |
| 3.3 | Summary of the FrazilCam deployments and site conditions including the number (#) of images captured, mean air temperature $\overline{T_a}$ , mean water depth $\overline{d}$ , depth averaged water velocity $\overline{U}$ , and local Reynolds number $Re$ . . . . . | 60 |

|     |   |     |
|-----|---|-----|
| 3.4 | Supercooling phase, minimum water temperature $T_p$ , mean net surface heat flux $\overline{Q_n}$ , number of flocs $N_T$ , mean floc size $\overline{\mu_f}$ , standard deviation $\sigma_f$ , 95 <sup>th</sup> percentile of floc size $S_{f95}$ , maximum floc size $S_{fmax}$ , average floc number concentration $\overline{C_{fn}}$ , and average volumetric concentration $\overline{C_{fv}}$ for each deployment. . . . . | 71  |
| 4.1 | Summary of experimental conditions. Note that bolded series title denotes baseline series, $t_{c1}$ (31 minutes) and $t_{c6}$ (14 minutes) are the average cooling duration for baseline series S1 and S6, respectively. . . . .  | 95  |
| 4.2 | Summary of experimental statistics including the average root mean square difference for air and water temperature time series $RMSD_a$ and $RMSD_w$ , respectively, as well as the series averaged water cooling rate $R_c$ and the peak supercooling temperature $T_p$ . . . . .  | 100 |
| 4.3 | Ensemble particle and floc mean sizes $\mu_p$ and $\mu_f$ , and corresponding standard deviations $\sigma_p$ and $\sigma_f$ in each series. The bolded number indicates the significantly different values (p-value < 0.05) comparing the means of the baseline series (S1 or S6) and the indicated experiment series using a two-sample t-test. . . . .  | 120 |
| 5.1 | Summary of propeller speed and statistics including the mean ( $\mu$ ) and the coefficient of variation (COV) for the actual mean air temperature $T_{a\mu}$ , water cooling rate $R_c$ , cooling period $t_c$ , and the peak supercooling temperature $T_p$ for each experimental group. . . . .   | 133 |

# List of Figures

|     |  |    |
|-----|--|----|
| 1.1 | Example images of river ice: (a) Frazil ice particle and floc imaged in a laboratory tank using two cross polarization filters, (b) surface ice pans passing downtown Edmonton from left to right with border ice formation visible on both banks, North Saskatchewan River, (c) anchor ice formation on the Fortress field site, Kananaskis River, (d) skim ice formation on the left bank of the Quesnell Bridge field site, North Saskatchewan River, and (e) ice cover on the near field and open leads on far field near Dawson Park in Edmonton, North Saskatchewan River. . . . . | 2  |
| 1.2 | Schematics of a typical classic supercooling curve showing the cooling rate, cooling period, and peak and residual supercooling temperatures. Shaded blue and yellow areas denote principal and residual supercooling phases, respectively. . . . .  | 5  |
| 1.3 | Field measurements of water temperatures showing (a) classic supercooling curve; (b) erratic supercooling curve; and (c) parabolic supercooling curve. (Kalke et al. 2019) . . . . .   | 6  |
| 2.1 | Maps of the North Saskatchewan River showing (a) a large area including 11 km upstream of the field site, (b) study reach including the area of interest (AOI) along with the EAS camera, water temperature logger and LRT bridge locations and (c) zoomed-in view of the AOI. . . . .   | 18 |

|      |   |    |
|------|---|----|
| 2.2  | Examples of raw EAS camera images: (a) slushy ice pan image with zoomed in river surface, (b) crusty ice pan images (lower ice concentration), (c) crusty ice pan images (higher ice concentration) with zoomed in river surface and (d) ice cover image. . . . .   | 20 |
| 2.3  | Framework of the hybrid image processing algorithm. . . . .   | 21 |
| 2.4  | Examples of four image categories (a) night image, (b) blurry image, (c) ice pan image and (d) ice cover image. . . . .   | 23 |
| 2.5  | Confusion matrix for each image category showing % accuracy. . . . .  | 23 |
| 2.6  | (a) Locations of the GCPs $\times$ in a raw image and (b) a geo-rectified image with superimposed GCPs $\times$ , ICPS $\circ$ , and EAS camera location $\times$ . . . . .   | 25 |
| 2.7  | Example of UNet marked watershed transformation to separate wrongly connected ice pans highlighted in a red circle, (a) rectified images, (b) UNet segmented binary images, (c) watershed transformed markers and (d) overlaid marker boundary in light blue. . . . .   | 31 |
| 2.8  | Examples of 2016 freeze-up image processing results on unlabelled images: left to right: original EAS images, rectified images, predicted binary labels, watershed transformed markers, overlaid marker boundary in light blue. Various surface ice conditions shown: (a) no ice, (b-c) slushy pans, (d-f) crusty pans and (g) ice cover. . . . . | 34 |
| 2.9  | Comparison of the time series of surface ice concentrations from the EAS Camera images and BridgeCam images during the 2016 freeze-up between Nov. 24 and Dec. 8 as well as image comparison for three selected times. Only the black information banner has been cropped from the BridgeCam images. . . . .                                      | 36 |
| 2.10 | Time series of surface ice concentration ( $C_{ice}$ ) and air temperature ( $T_a$ ) in the AOI during freeze-up of (a) 2015, (b) 2016, (c) 2017, (d) 2019 and (e) 2020. . . . .  | 38 |

|      |  |    |
|------|--|----|
| 2.11 | Normalized size distributions of ice pans for (a) 2015 freeze-up, (b) 2017 freeze-up, (c) 2020 freeze-up and (d) Five-year combined. Blue line denotes fitted log-normal distribution, $N$ is the number of ice pans in each bin and $N_T$ is the total number of ice pans. . . . .  | 40 |
| 2.12 | Scatter density plot illustrating (a) the relationship between $d$ and $d_p$ , and (b) the relationship between the major and minor axis length of the fitted ellipse for all detected ice pans combined. . . . .  | 42 |
| 2.13 | Time series of (a) surface ice concentration ( $C_{ice}$ ) and air temperature ( $T_a$ ), (b) upstream water temperature ( $T_w$ ) at Emily Murphy Park (red shading denotes supercooling events), (c) daily $d_{mean}$ and $(d_p/d)_{mean}$ and (d) daily $d_{max}$ and $(d_p/d)_{max}$ during 2016 freeze-up between Nov. 20 to Dec. 8, grey shaded area corresponds to slushy pan condition. . . . .  | 44 |
| 2.14 | Time series of (a) surface ice concentration ( $C_{ice}$ ) and air temperature ( $T_a$ ), (b) upstream water temperature ( $T_w$ ) at Emily Murphy Park (red shading denotes supercooling events), (c) daily $d_{mean}$ and $(d_p/d)_{mean}$ and (d) daily $d_{max}$ and $(d_p/d)_{max}$ during 2020 freeze-up between Oct. 24 to Nov. 24, grey shaded area corresponds to slushy pan condition. . . . . | 45 |
| 3.1  | Maps showing (a) the locations of the deployment sites in Alberta, enlarged views of the locations on (b) the North Saskatchewan, (c) Kananaskis, and (d) Peace rivers. . . . .  | 54 |
| 3.2  | An image showing the configuration of the FrazilCam system. . . . .  | 55 |
| 3.3  | An image showing the ice accumulation on the FrazilCam system. . . . .   | 56 |
| 3.4  | Image of the FrazilCam deployed during (a) NSR-L6, and (b) KR-E1. The arrow indicates the flow direction. . . . .  | 59 |
| 3.5  | An example of (a) a raw FrazilCam image captured on Dec 3, 2021, and (b) the corresponding processed binary image. . . . .   | 62 |
| 3.6  | A flow chart showing the image processing procedure. . . . .   | 63 |

|      |   |    |
|------|---|----|
| 3.7  | Images of frazil flocs of different sizes and shapes from the following deployments: (a) NSR-L1, (b) NSR-L6, (c) PR-F1, (d) KR-E1, (e) KR-F1, and (f) KR-F2. The white scale bar in each image represents a length of 3 mm. Note that in some images the surrounding ice particles were masked out to highlight the floc at the centre of the image. . . . .    | 70 |
| 3.8  | Distributions of floc size $S_f$ for deployments (a) NSR-L1, (b) NSR-L6, (c) KR-F1, and (d) PR-F1. The red line denotes a fitted lognormal distribution, $N$ is the number of flocs in each bin, and $N_T$ is the total number of flocs. . . . .  | 73 |
| 3.9  | Time series of (a) water and air temperatures $T_w$ and $T_a$ , (b) heat flux $Q$ , (c) floc mean size $\mu_f$ , (d) floc number concentration $C_{fn}$ and (e) floc volumetric concentration $C_{fv}$ for deployment NSR-L4 on December 12, 2021. The vertical dashed grey line indicates the time when the peak supercooling temperature is achieved. . . . . | 74 |
| 3.10 | Time series of (a) water and air temperatures $T_w$ and $T_a$ , (b) heat flux $Q$ , (c) floc mean size $\mu_f$ , (d) floc number concentration $C_{fn}$ and (e) floc volumetric concentration $C_{fv}$ for deployment KR-F1 on January 30, 2023. . . . .  | 76 |
| 3.11 | Time series of (a) water and air temperatures $T_w$ and $T_a$ , (b) heat flux $Q$ , (c) floc mean size $\mu_f$ , (d) floc number concentration $C_{fn}$ and (e) floc volumetric concentration $C_{fv}$ for deployment PR-F2 on December 13, 2022. . . . .   | 77 |
| 3.12 | Relationship between local Reynolds number $Re$ and mean floc size $\overline{\mu_f}$ in mm. . . . .  | 85 |
| 3.13 | Relationship between the fractional height $d_m/\bar{d}$ and the average floc volumetric concentration $\overline{C_{fv}}$ . . . . .  | 86 |
| 4.1  | (a) Rectified plan view image of the frazil tank and (b) front view of the frazil tank showing the locations of instruments and equipment. . . . .  | 95 |

|     |   |     |
|-----|---|-----|
| 4.2 | Time series of (a-b) air temperature $T_a$ and (c-d) corresponding water temperature $T_w$ time series from six series of experiments. Time $t$ is normalized using the average cooling duration used for the G1 and G2 experiments $t_{c1}$ and $t_{c6}$ , respectively. Note each color represents one series of experiments with three repeated runs plotted and zero time is the start of supercooling. . . . . | 99  |
| 4.3 | An example of (a) an annotated raw image captured during a laboratory experiment, and (b) the corresponding processed binary image. . . . .   | 102 |
| 4.4 | Typical time series of normalized particle number concentration $N_p/N_{pm}$ . Note the data used for plotting is from a S2 experiment, the shaded areas represent the interval used to calculate the production (red) and decay (grey) rates. . . . .  | 106 |
| 4.5 | Time series of (a) air temperature $T_a$ , (b) water temperature $T_w$ , (c) particle number concentration $N_p$ , (d) floc number concentration $N_f$ , (e) particle mean size $\mu_p$ , (f) floc mean size $\mu_f$ , and (g) total ice concentration $C_i$ for all S4 experiments in G1. . . . .  | 108 |
| 4.6 | Ensemble-averaged time series of (a) air temperature $T_a$ , (b) water temperature $T_w$ , (c) particle number concentration $N_p$ , (d) floc number concentration $N_f$ , (e) particle mean size $\mu_p$ , and (f) floc mean size $\mu_f$ for all G1 experiments. Note the time $t$ is nondimensionalized by $t_{c1}$ , the averaged cooling duration obtained from the baseline experiment series S1. . . . .     | 111 |
| 4.7 | Ensemble-averaged time series of (a) air temperature $T_a$ , (b) water temperature $T_w$ , (c) particle number concentration $N_p$ , (d) floc number concentration $N_f$ , (e) particle mean size $\mu_p$ , and (f) floc mean size $\mu_f$ for all G2 experiments. Note the time $t$ is nondimensionalized by $t_{c6}$ , the averaged cooling duration obtained from the baseline experiment series S6. . . . .     | 112 |

|      |   |     |
|------|---|-----|
| 4.8  | Ensemble-averaged time series of measured and theoretically calculated total ice concentration $C_i$ for (a) S1, (b) S2, (c) S6, and (d) S7 experiments plotted with nondimensionalized time. The shaded area corresponds to the period after $N_p$ started to decrease. . . . .  | 114 |
| 4.9  | Bar plots of (a) particle production rate $n_{pp}$ and particle decay rate $n_{pd}$ , and (b) floc production rate $n_{fp}$ and floc decay rate $n_{fd}$ during G1 experiments, and (c-d) are for the G2 experiments. The error bar represents the standard error, and the number above the error bar indicates the significant p-value ( $< 0.05$ ) from a two-sample t-test comparing the means between the baseline series (S1 or S6) and the plotted experiment series. | 116 |
| 4.10 | Bar plots of $\bar{N}_p$ and $\bar{N}_f$ , the mean particle and floc number concentration, respectively, for the entire experiment duration of (a) G1 and (b) G2 experiments. The error bar represents the standard error, and the number above the error bar indicates the significant p-value ( $< 0.05$ ) from a two-sample t-test comparing the means of the baseline series (S1 or S6) and the indicated experiment series. . . . .                                   | 117 |
| 4.11 | Frequency distributions of (a) particle size $S_p$ and (b) floc size $S_f$ in S2. The red line is a fitted log-normal distribution, $N$ is the number of particles/flocs in each bin and $N_T$ is the total number of particles/flocs. . . .  | 118 |
| 4.12 | Empirical cumulative frequency distributions of (a) particle size $S_p$ and (b) floc size $S_f$ for series S1 - S5 in group G1. The y-axis limits for all inserts are from 0.4 to 0.6. . . . .  | 119 |
| 5.1  | Plan view of the frazil tank showing the locations of instrumentation and equipment. . . . .  | 131 |
| 5.2  | Superimposed (a) air temperature $T_a$ and (b) water temperature $T_w$ time series from Group #1 experiments. Note each color represents one repeat experiment. . . . .   | 133 |

|     |  |     |
|-----|--|-----|
| 5.3 | Schematics of water temperature time series during a supercooling event showing the cooling rate $R_c$ , the cooling period $t_c$ , and peak supercooling temperature $T_p$ . . . . .  | 134 |
| 5.4 | Ensemble-averaged time series of (a) water temperature $T_w$ , (b) number concentration $N$ of particle and floc, and (c) mean size $\mu$ of particle and floc for G1 experiments. The time period between $t_s$ and $t_e$ is shaded in yellow. . . . .                | 137 |
| 5.5 | Ensemble-averaged time series of (a) water temperature $T_w$ , (b) number concentration $N$ of particle and floc, and (c) mean size $\mu$ of particle and floc for G2 experiments. The time period between $t_s$ and $t_e$ is shaded in yellow. . . . .                | 138 |
| 5.6 | Ensemble-averaged time series of (a) water temperature $T_w$ , (b) number concentration $N$ of particle and floc, and (c) mean size $\mu$ of particle and floc for G3 experiments. The time period between $t_s$ and $t_e$ is shaded in yellow. . . . .                | 139 |
| 5.7 | Correlation between particle number concentration $N_p$ and floc number concentration $N_f$ during (a) the <i>increasing period</i> from $t_s$ to $t_N$ and (b) the <i>decreasing period</i> from $t_N$ to $t_e$ . . . . .   | 141 |
| 5.8 | A comparison between observed and calculated floc number concentration time series for the three groups of experiments. . . . .  | 142 |
| 5.9 | Correlation between particle mean size $\mu_p$ and floc mean size $\mu_f$ during (a) the period from $t_s$ to $t_{\mu 1}$ , (b) the period from $t_{\mu 1}$ to $t_{\mu 2}$ , and (c) the period from $t_{\mu 2}$ to $t_e$ for the three groups of experiments. . . . . | 144 |
| A.1 | Time series of (a) water and air temperatures $T_w$ and $T_a$ , (b) heat flux $Q$ , (c) floc mean size $\mu_f$ , (d) floc number concentration $C_{fn}$ and (e) floc volumetric concentration $C_{fv}$ for deployment NSR-L1 on December 3, 2021. . . . .              | 164 |

A.2 Time series of (a) water and air temperatures  $T_w$  and  $T_a$ , (b) heat flux  $Q$ , (c) floc mean size  $\mu_f$ , (d) floc number concentration  $C_{fn}$  and (e) floc volumetric concentration  $C_{fv}$  for deployment NSR-L2 on December 3, 2021. . . . . 165

A.3 Time series of (a) water and air temperatures  $T_w$  and  $T_a$ , (b) heat flux  $Q$ , (c) floc mean size  $\mu_f$ , (d) floc number concentration  $C_{fn}$  and (e) floc volumetric concentration  $C_{fv}$  for deployment NSR-L3 on December 9, 2021. . . . . 166

A.4 Time series of (a) water and air temperatures  $T_w$  and  $T_a$ , (b) heat flux  $Q$ , (c) floc mean size  $\mu_f$ , (d) floc number concentration  $C_{fn}$  and (e) floc volumetric concentration  $C_{fv}$  for deployment NSR-L5 on December 12, 2021. . . . . 167

A.5 Time series of (a) water and air temperatures  $T_w$  and  $T_a$ , (b) heat flux  $Q$ , (c) floc mean size  $\mu_f$ , (d) floc number concentration  $C_{fn}$  and (e) floc volumetric concentration  $C_{fv}$  for deployment NSR-L6 on November 7, 2022. . . . . 168

A.6 Time series of (a) water and air temperatures  $T_w$  and  $T_a$ , (b) heat flux  $Q$ , (c) floc mean size  $\mu_f$ , (d) floc number concentration  $C_{fn}$  and (e) floc volumetric concentration  $C_{fv}$  for deployment PR-F1 on December 12, 2022. . . . . 169

A.7 Time series of (a) water and air temperatures  $T_w$  and  $T_a$ , (b) heat flux  $Q$ , (c) floc mean size  $\mu_f$ , (d) floc number concentration  $C_{fn}$  and (e) floc volumetric concentration  $C_{fv}$  for deployment KR-E1 on January 29, 2023. 170

A.8 Time series of (a) water and air temperatures  $T_w$  and  $T_a$ , (b) heat flux  $Q$ , (c) floc mean size  $\mu_f$ , (d) floc number concentration  $C_{fn}$  and (e) floc volumetric concentration  $C_{fv}$  for deployment KR-F2 on January 31, 2023. 171

# Chapter 1

## Introduction

### 1.1 Background

Freeze-up in northern rivers typically begins when the turbulent water becomes supercooled below its freezing point due to heat loss to the atmosphere and suspended frazil ice particles (Figure 1.1a) form in the water column. These individual frazil ice particles are predominantly disk-shaped (Andres 1982; McFarlane et al. 2015). They are inherently adhesive in the supercooled water and may collide with each other and freeze together into clusters as they are transported by the turbulent flow. The clusters are commonly referred to as frazil flocs as shown in Figure 1.1a and the process creating the flocs is called flocculation (Clark and Doering 2009). Frazil flocs gain mass either by the thermal growth of the crystals and/or by further aggregation of individual frazil ice particles or flocs. Once frazil flocs become buoyant enough to overcome the turbulence of the flow, they rise to the surface of the river and continue to combine together into larger slush balls and if the exposed portion freezes they form frazil ice pans (Hicks 2016) as shown in Figure 1.1b. Frazil pans tend to collide with each other creating upturned white edges as they move with the flow. The collisions may also cause frazil pans to freeze together to form large multi-pan rafts.

During freeze-up, anchor ice may form on the river bed by the deposition of suspended frazil ice particles and/or flocs or by in-situ nucleation of ice crystals (Tsang 1982). An example image of anchor ice is shown in Figure 1.1c. Anchor ice accumula-

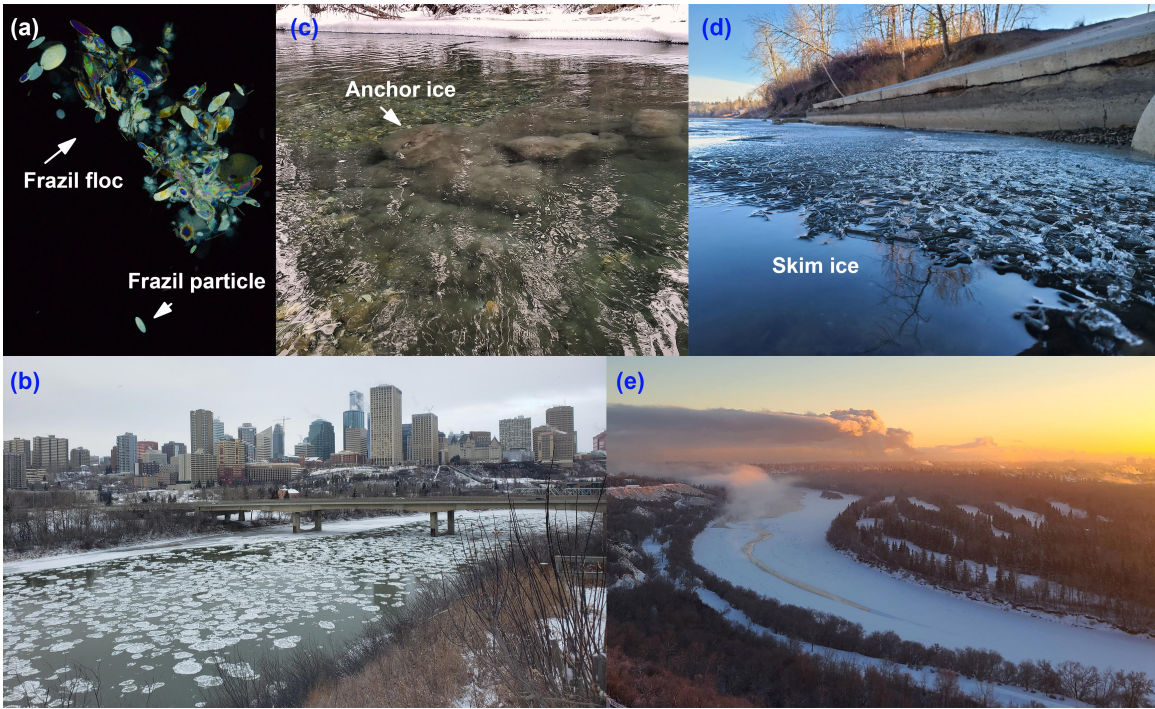


Figure 1.1: Example images of river ice: (a) Frazil ice particle and floc imaged in a laboratory tank using two cross polarization filters, (b) surface ice pans passing downtown Edmonton from left to right with border ice formation visible on both banks, North Saskatchewan River, (c) anchor ice formation on the Fortress field site, Kananaskis River, (d) skim ice formation on the left bank of the Quesnell Bridge field site, North Saskatchewan River, and (e) ice cover on the near field and open leads on far field near Dawson Park in Edmonton, North Saskatchewan River.

tions grow in size either by the deposition of frazil ice particles/flocs or by in-situ growth of ice crystals on the bed material (Kempema and Ettema 2011; Ghobrial and Loewen 2021). Anchor ice can release from the bed due to either mechanical or thermal forcing and rise to the surface (Kempema et al. 2001). The resulting anchor ice pans often appear darker than frazil ice pans due to embedded sediments and this “rafting” process can contribute significantly to sediment transport in rivers (Kempema and Ettema 2011).

During freeze-up border ice (Figure 1.1b) and skim ice (Figure 1.1d) can form on the water along river banks where the water is shallow and moves slowly (Hicks 2016). As freeze-up progresses it may grow out from the banks narrowing river widths. As border ice grows and more and more surface ice pans form, congestion of incoming

ice pans often occurs and pans can bridge at certain locations such as constrictions or sharp bends and become immobile (Beltaos 2013). From there, a solid ice cover will form and propagate upstream. The formation of a continuous solid ice cover typically insulates the flowing water from further heat loss to the atmosphere, thus preventing the occurrence of supercooling and the production of frazil ice until the ice cover thaws or breaks up (Beltaos 2013). However, in some river reaches, open water areas called open leads (Figure 1.1e) can be found when parts of the ice cover are melted locally by high water temperatures or washed away by increased flow velocities (Vuyovich et al. 2009). Without an ice cover to insulate the water, supercooling events and frazil generation may occur throughout the winter in these river reaches when the air temperature is sufficiently cold.

The flocculation of frazil ice particles plays a key role in river freeze-up processes as frazil flocs are important to surface and anchor ice production. The generation of frazil ice pans and the subsequent ice cover formation during river freeze-up have profound impacts on river hydraulics (Ashton 1978), river morphology (Ettema and Zabilansky 2004), bank stability (Chassiot et al. 2020), and sediment transport (Kempema and Ettema 2011). In addition to rising to the water surface, frazil particles and flocs can attach to underwater structures causing full or partial blockage of water intakes for both water supply and hydroelectric facilities (Ettema and Zabilansky 2004; Barrette 2021). Conditions like significant anchor ice formation on the river bed or hanging dam formation by frazil accumulation underneath the ice cover may cause flooding and damage property and infrastructure (Beltaos 2013). Therefore, it is of great importance to obtain a better understanding of the frazil floc and surface ice properties as well as their evolution under the changing environmental conditions in order to model and predict their physical behavior throughout the freeze-up processes.

## 1.2 Literature Review

### 1.2.1 Supercooling Process

Frazil ice production in rivers requires supercooling of the water column. The water supercooling temperature is predominantly a function of the air-water heat flux and the latent heat released by growing ice crystals in the water (Daly 2008). Laboratory studies often perform supercooling experiments by exposing the turbulent water body to a constant sub-zero air temperature or constant upward heat flux, creating a “classic” supercooling curve. Figure 1.2 shows an example of a classic supercooling curve with illustrations of the principal and residual supercooling phases. The principal supercooling phase denotes the period when the water temperature varies transiently and the residual supercooling phase is the period when an approximately constant water temperature (residual supercooling temperature) is reached (Michel 1972). Various characteristics of the classic supercooling curve have been defined and investigated in laboratory experiments (Carstens 1966; Ye et al. 2004; Clark and Doering 2006). The cooling rate is defined as the slope of the water temperature time series prior to when frazil ice crystals start to form. The cooling period is defined as the time period from the start of supercooling to when the peak supercooling temperature is achieved. The peak supercooling temperature is the lowest supercooling temperature. Laboratory experiments have shown that higher cooling rates resulted in greater peak supercooling temperature magnitudes (Carstens 1966) and shorter cooling periods (Ye et al. 2004). In addition, it has been observed that the water depth affects supercooling with deeper flows resulting in longer principal supercooling phase duration, smaller cooling rates and larger peak supercooling magnitudes (Ye et al. 2004). The only study that performed laboratory supercooling experiments when the heat flux was varied was reported in Carstens (1966). He explored the effect of increasing the upward heat flux after a residual temperature had been reached to the supercooling curve. He observed that the water temperature dropped off again and reached smaller second peak supercooling and residual supercooling temperature magnitudes than the first.

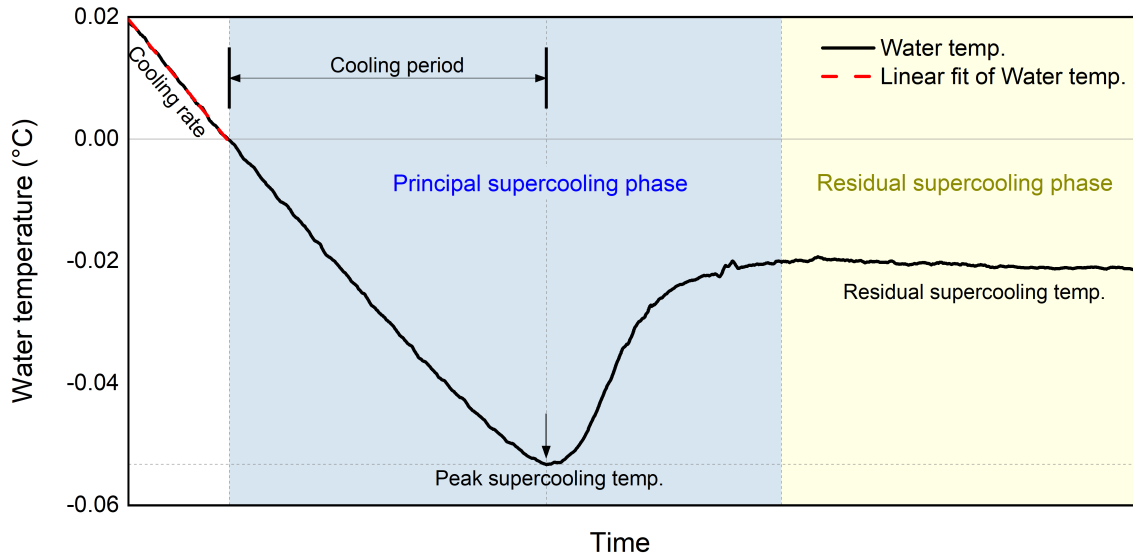


Figure 1.2: Schematics of a typical classic supercooling curve showing the cooling rate, cooling period, and peak and residual supercooling temperatures. Shaded blue and yellow areas denote principal and residual supercooling phases, respectively.

Several previous field studies have reported supercooling measurements in rivers. Richard and Morse (2008) measured peak supercooling temperature in the St. Lawrence River ranging from  $-0.01\text{ }^{\circ}\text{C}$  to  $-0.06\text{ }^{\circ}\text{C}$ . Nafziger et al. (2013) investigated supercooling on small streams in New Brunswick and Newfoundland, Canada and found the measured peak supercooling degree to be  $0.07\text{ }^{\circ}\text{C}$  and supercooling events can last for up to 42.7 hours. Boyd et al. (2022) studied the characteristics of the supercooling events in three Alberta rivers and reported that a typical supercooling event lasting less than 24 hours with a peak supercooling between  $-0.01\text{ }^{\circ}\text{C}$  and  $-0.02\text{ }^{\circ}\text{C}$ . Pei et al. (2021) compared supercooling events measured in deep and shallow water and it was found that supercooling events that occurred in deep water were significantly longer in duration and had larger peak supercooling magnitudes. McFarlane and Clark (2021) analyzed the energy budget throughout six supercooling events and found that the most significant heat source and heat loss were net shortwave radiation and net longwave radiation, respectively. Kalke et al. (2019) classified 93 supercooling events observed in the North Saskatchewan River into three types and concluded that about one-third of the observed events followed the classic supercooling curve shape which may be produced

due to approximately constant upward air-water heat flux (Figure 1.3a). The rest were classified as either erratic (Figure 1.3b) or parabolic (Figure 1.3c) in shape and which were probably produced due to varying air-water heat flux.

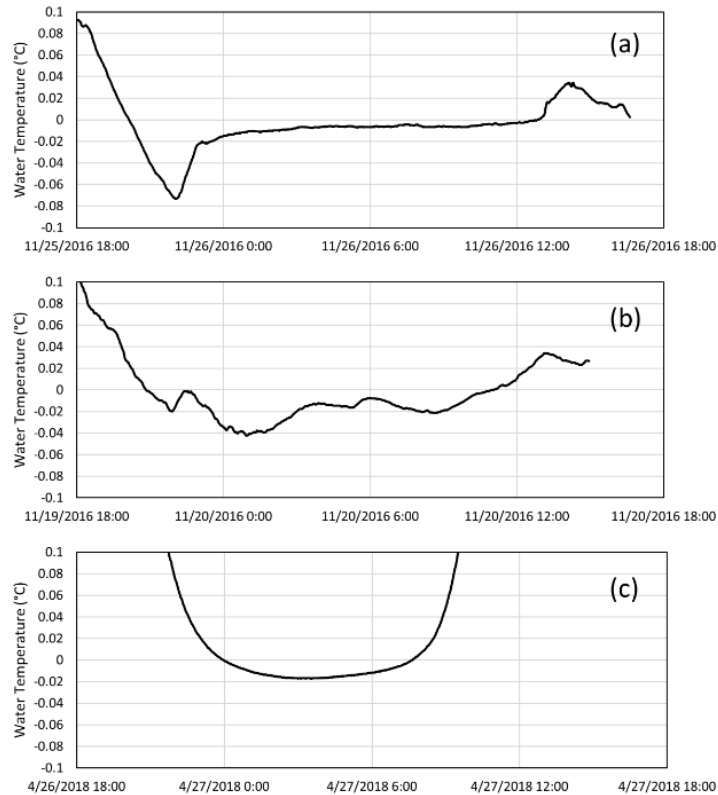


Figure 1.3: Field measurements of water temperatures showing (a) classic supercooling curve; (b) erratic supercooling curve; and (c) parabolic supercooling curve. (Kalke et al. 2019)

## 1.2.2 Frazil Ice Particles and Floccs

The properties of individual frazil ice particles have been investigated both in laboratory studies and field. Their size ranged from 0.022 to 6 mm (McFarlane et al. 2017) and the size distribution can be described by a lognormal distribution (Clark and Doering 2006; Daly and Colbeck 1986; McFarlane et al. 2015; Ye et al. 2004). Laboratory studies showed that during the principal supercooling phase, the mean particle diameter first increased before reaching an approximately constant value (Clark and Doering 2006; McFarlane et al. 2015). The number concentration of frazil particles first in-

creased slowly and then rapidly at a fairly constant rate, peaking just after the peak supercooling had been reached (Clark and Doering 2006; McFarlane et al. 2015). The rapid multiplication of frazil ice particles was most commonly considered a result of secondary nucleation, which refers to the nucleation of new crystals due to the presence of a stable parent crystal (Evans et al. 1974). The rate of secondary nucleation was assumed to be governed by collisions of crystals and fluid shear which break crystals up to create new crystals (Clark and Doering 2009; Daly 1984). After peaking the particle number concentration decreased as particles were removed via flocculation. Some recent field measurements reported in-situ measurements of frazil particle size evolution using underwater photography (McFarlane et al. 2017; McFarlane et al. 2019b). It was found that in most cases the mean frazil particle size remained approximately constant during the residual supercooling phase while in some cases changing environmental conditions caused changes in the mean particle size. However, no definitive conclusions were reached with regard to the evolution of the frazil ice characteristics during the principal supercooling phase due to limited data.

A small number of laboratory studies have investigated frazil floc properties and the flocculation process (Clark and Doering 2009; Kempema et al. 1993; Park and Gerard 1984; Schneck et al. 2019; Reimnitz et al. 1993) and no field measurements have been reported to the best of the author's knowledge. The most comprehensive laboratory measurements of frazil flocs were made by Schneck et al. (2019) using a frazil ice tank. Schneck et al. (2019) reported that the mean floc size was 2.57 mm in freshwater and 1.47 mm in saline water and a lognormal distribution was found to fit the floc size distribution closely. The floc porosity was estimated to vary between 0.75 and 0.86 under different salinities by equating the estimated volume concentration of floc and the theoretical volume concentration computed from well-mixed heat balance equations. Reimnitz et al. (1993) investigated the rise velocity of frazil in seawater using a vertical tank and found that floc rise velocities were functions of their size and ranged from 1 to 5 *cm/s*. Clark and Doering (2009) investigated frazil flocculation in a counter-rotating

flume and measured the vertical number variations of frazil flocs under different turbulence intensities considering a frazil floc to be any particle with an equivalent diameter greater than 17 mm. Results showed that the number of observed flocs near the water surface exceeds the number of flocs near the bed, and the number of flocs overall decreases with increasing turbulence intensity. A few studies have considered frazil flocculation processes when modelling frazil ice dynamics (Rees Jones and Wells 2018; Svensson and Omstedt 1998). However, due to the poor understanding of the underlying physical mechanisms and limited data available for verification, a universally accepted formulation for frazil flocculation remains elusive.

### **1.2.3 Surface Ice Characteristics**

The temporal and spatial variations of surface ice properties (*i.e.* ice concentration, ice pan size and shape) are of great interest for ice-related hazard monitoring (Ettema and Zabilansky 2004). Time series estimation of surface ice concentration can provide calibration and validation data, as well as boundary conditions for comprehensive river ice models used to predict freeze-up processes (Blackburn and She 2019; Shen 2005). Measurements of ice pan size and shapes can be used to improve river ice models based on the discrete element method (Zhai et al. 2022). A number of previous studies have investigated methods to monitor surface ice concentration (Emond et al. 2011; Ghobrial et al. 2013; Kalke and Loewen 2018; Singh et al. 2020), ice cover extent (Ansari et al. 2017), and border ice growth (Simoës and Clark 2020). Ghobrial et al. (2013) investigated ice pan and raft lengths on the NSR computed from sonar data during one freeze-up season and found they varied from less than 1 m to 20 m. Jasek (2016) estimated ice pan lengths on the Peace River using one week of sonar measurements and found the 5<sup>th</sup> and 95<sup>th</sup> percentile lengths were 2.3 and 41 m, respectively. There are currently rather limited data on multi-year surface ice characteristics especially ice pan properties which is in part due to the challenges of making measurements during the harsh winter environments.

Current methods of monitoring surface ice conditions can be categorised into sonar-based methods and camera-based methods. Upward looking sonars record reflected acoustic signals as ice passes over the location of the vertical acoustic beam which can then be translated into measurements of ice concentration, ice pan drafts and lengths (Ghobrial et al. 2013; Jasek 2016; Morse et al. 2003). Camera-based methods utilize images/videos of river surface ice conditions to monitor surface ice conditions and use image processing methods to obtain quantitative measurements of surface ice characteristics (Ansari et al. 2017; Kalke and Loewen 2018; Vuyovich et al. 2009). Standard image processing techniques like thresholding, contour-based edge detection and georectification have been applied alone or in combination to extract river ice conditions (Ansari et al. 2017). Recent studies that applied machine learning and deep learning methods found them to be more robust than traditional methods and perform well in accurately segmenting surface ice (Ansari et al. 2021; Kalke and Loewen 2018; Singh et al. 2020; Zhang et al. 2021). Singh et al. (2020) compared four state-of-the-art deep learning models (UNet, SegNet, DeepLab and DenseNet) to Support Vector Machine (SVM) and found that the deep learning models were significantly more accurate than SVM.

### **1.3 Knowledge Gaps**

The above literature review shows that despite significant progress being made on the formation and evolution of individual frazil ice particles, our understanding of the physical process in which individual frazil ice particles combine into flocs and rise to the surface forming ice pans remains limited, which is largely due to a scarcity of data available in the literature. First, measurements of frazil floc properties are very rare which has limited our understanding of the flocculation process. Secondly, the evolution of both frazil ice particles and flocs under varying heat flux when the supercooling curve may not follow a classic shape is largely unknown. Such knowledge is crucial to enhancing our understanding of how heat flux variations during supercooling affect frazil ice and

floc production in field conditions where the heat flux is rarely constant. Lastly, long-term monitoring data of surface ice properties reported in the literature is very limited, especially ice pan sizes and shapes. Surface ice pans are the direct product of suspended frazil ice production, and a robust monitoring method for the surface ice characteristics can provide the necessary data as a foundation to establish connections between frazil production and surface ice evolution. Therefore, collecting and analyzing data on frazil floc and surface ice properties are crucial for improving our understanding of the river freeze-up process.

## **1.4 Research Objectives**

This study aims to advance our understanding of the properties of frazil floc and surface ice as well as their evolution under changing environmental conditions to better model and predict their physical behavior throughout the river freeze-up. The study included a series of field measurements of time-series of frazil floc and surface ice properties and concentrations. It also included laboratory experiments to determine how different heat flux scenarios affect the production and evolution of frazil ice particle and floc properties in a controlled setting, as well as how frazil ice particle and floc sizes and concentrations correlate with each other. The study addressed four objectives, each described below along with a brief summary of the corresponding chapters.

Objective 1 was to investigate freeze-up surface ice concentrations and ice pan properties using multi-year public camera images and a deep learning approach. Chapter 2 describes the development, validation, and application of a deep learning based hybrid image processing algorithm in order to quantify surface ice concentration and ice pan properties on the North Saskatchewan River from oblique and distant public camera images. Images captured during five freeze-up seasons were processed and the results were analyzed to demonstrate that the method provides valuable information on both the long- and short-term temporal variations on river ice conditions as well as on the statistical properties of ice pans.

Objective 2 was to investigate the key factors that govern the properties and evolution of frazil flocs in rivers. In Chapter 3 field measurements of frazil ice flocs using a submersible high-resolution camera system to capture time-series images of frazil flocs for 2021-2023 freeze-up seasons in three Alberta rivers are presented. Images were analyzed to accurately determine floc sizes and concentrations. Key hydraulic and meteorological measurements were collected and air-water heat fluxes were estimated to investigate their influence on floc properties. Time series of floc size, number concentration and volumetric concentrations as well as size distributions measured in rivers during the principal and residual supercooling phase are presented for the first time.

Objective 3 was to determine how frazil ice particle/floc properties vary under different air-water heat flux scenarios. Chapter 4 describes a series of laboratory frazil ice tank experiments in which the upward heat flux was increased or decreased at different times during a supercooling event by changing the cold room temperature. Images of frazil ice particles and flocs passing between two cross-polarizing filters were captured using a high-resolution camera system. Precision temperature recorders were used to monitor water and air temperatures. The sizes and concentrations of frazil particles and flocs measured during supercooling are presented. The effect of varying the heat flux at different times of supercooling on the supercooling curve and the properties of frazil ice particles and floc are discussed.

Objective 4 was to explore how frazil ice particle and floc properties correlate with each other under different cooling rates and turbulent intensities. In Chapter 5 a laboratory study was conducted using experimental setups similar to the ones described in the previous paragraph to investigate the correlation between frazil ice particles and floc number concentrations and sizes at different air temperatures and turbulent dissipation rates. The correlations between frazil ice particle and floc sizes and concentrations during different stages of supercooling are presented. Effects of different turbulent dissipation rates and air temperatures on the correlation between frazil ice and floc properties are discussed.

## Chapter 2

# Deep Learning Based River Surface Ice Quantification Using a Distant and Oblique-Viewed Public Camera

### 2.1 Introduction

The freeze-up processes that lead to the formation of an ice cover on rivers are complex and dynamic. Freeze-up typically begins when the turbulent water becomes supercooled by exposure to cold air and suspended frazil ice particles form in the water column. Adhesive frazil particles can collide with each other and sinter together into groups, forming frazil flocs. Once frazil flocs become buoyant enough to overcome the turbulence of the flow, they rise to the water surface and combine into larger clumps of frazil slush. The frazil slush is initially flexible and quite transparent, but as freeze-up progresses, the portions exposed to the atmosphere freeze producing rigid frazil ice pans (Hicks 2016). Frazil pans tend to collide with each other creating upturned white edges as they move with the flow. The collisions may also cause frazil pans to freeze together to form large multi-pan rafts. During freeze-up anchor ice can also form either by deposition of adhesive suspended frazil ice particles onto the river bed or by in-situ nucleation of ice crystals on the bed material. Anchor ice can release from the bed due to either mechanical or thermal forcing and rise to the surface (Kempema et al. 2001). The resulting anchor ice pans often appear much darker than frazil ice pans due to embedded river bed sediments and this mechanism can transport significant amounts

of sediment downstream particularly coarser materials (Kempema and Ettema 2011; Kalke and Loewen 2018). Once a high concentration of surface ice pans is reached, congestion of incoming ice pans will occur and the pans will bridge at certain locations (e.g. a constriction or sharp bend) becoming immobile and an ice cover will form and propagate upstream (Beltaos 2013). During the ice cover period, open water areas called open leads can form when parts of the ice cover are melted locally by high water temperatures or washed away by increased flow velocities (Vuyovich et al. 2009).

Monitoring the characteristics of surface ice (*i.e.* ice concentration, ice pan size and shape properties) and their variation both temporally and spatially is of considerable importance to establish a better understanding of freeze-up processes. The evolution of surface ice pans and the formation of ice covers during river freeze-up have profound impacts on river hydraulics (Ashton 1978), river morphology (Ettema and Zabilansky 2004), bank stability (Chassiot et al. 2020; Vandermause et al. 2021), and sediment transport (Kempema and Ettema 2011). In addition, timely data of surface ice characteristics can be valuable for effective water resources management and hazard assessments related to ice jam induced flooding or bank erosion (Ettema and Zabilansky 2004). Accurate estimation of surface ice concentrations can provide calibration and validation data, as well as boundary conditions for river ice process models such as CRISSP1D/2D (Shen 2005) and River1D (Blackburn and She 2019). Detailed measurements of ice pan properties may aid in the discrete element modelling of surface ice processes (Zhai et al. 2022). A number of previous studies have investigated methods to quantify surface ice concentration (Emond et al. 2011; Ghobrial et al. 2013; Kalke and Loewen 2018; Singh et al. 2020; Sola and Scott 2022), ice cover extent (Ansari et al. 2017), and border ice growth (Simoes and Clark 2020). Some studies reported estimations of ice pan properties during freeze-up. Ghobrial et al. (2013) computed time-series of ice pan drafts and lengths by analyzing Shallow Water Ice Profiling Sonar (SWIPS) signals from a single freeze-up season. Jasek (2016) reported ice pan drafts and lengths during frazil and anchor ice runs based on one week of SWIPS measure-

ments. There is currently rather limited data on ice pan properties available in the literature due to the challenging winter environments. The size distributions and inter-annual variations of surface ice pans during freeze-up as well as time-series variation of ice pan properties still remain largely unknown and require further investigation. Therefore, it is of considerable interest to conduct long-term monitoring of surface ice conditions especially detailed ice pan properties. Note that in this study the term ice pan is used to represent both individual ice pans and multi-pan rafts.

There are two primary methods of monitoring surface ice conditions namely sonar-based methods and camera-based method. Sonar-based methods can provide continuous measurements of surface ice concentration, ice pan drafts, and lengths (Morse et al. 2003; Ghobrial et al. 2013; Jasek 2016). Camera-based methods utilize images/videos of river surface ice conditions from different sources to monitor surface ice conditions. The captured images are analyzed using image processing methods to obtain quantitative measurements of surface ice characteristics that are visible in the images. A variety of image sources have been used in past studies, including aerial photography (Daly et al. 1986), unmanned aerial vehicle or UAV (Kalke and Loewen 2018; Zhang et al. 2020; Zhang et al. 2021), near-shore or bridge-mounted cameras (Kalke and Loewen 2018; Ansari et al. 2017), web-based cameras (Vuyovich et al. 2009) and infrared thermography (Emond et al. 2011).

The major advantage of the sonar-based method is its capability to measure ice pan drafts and to conduct continuous measurements of surface ice characteristics. However, sonars only provide point measurements, parameters such as the threshold and persistence levels are site-specific and need to be determined for each site and a series of assumptions need to be made in order to derive ice pan properties (Ghobrial et al. 2013). The biggest disadvantage of sonars is that they need to be deployed underwater on the riverbed and as a result, deployment and retrieval require a properly equipped boat. Compared to the sonar-based method, most camera-based methods lack the ability to conduct 24-hour continuous monitoring since there is insufficient light at

night. Harsh winter weather conditions like fog or heavy snow may also compromise the image quality. However, setting up, operating, and maintaining camera-based systems are significantly easier and less expensive than sonar systems. Another significant advantage is that analysis of the captured images enables surface ice properties to be monitored over a wide area. These advantages make camera-based methods the logical choice for long-term multi-year measurements of surface ice characteristics.

A variety of methods have been developed to extract reliable surface ice information from camera images. Early studies used manual inspection of the images to estimate surface ice conditions (Osterkamp and Gosink 1983), which is time-consuming and the accuracy of the resulting data is uncertain. Standard image processing techniques like thresholding, contour-based edge detection and geo-rectification have been applied alone or in combination to extract information of river ice conditions. For example, Ansari et al. (2017) developed an automated algorithm based on standard image processing techniques to monitor the ice cover characteristics from oblique shore-based cameras consisting of image pre-processing, registration, rectification, target detection and calculation of ice characteristics. The algorithm was evaluated with two sites on the St. Lawrence River and quantified ice cover properties with acceptable accuracy. Images captured during night time are typically not processed but Emond et al. (2011) investigated the use of infrared thermography to measure river ice properties which enables images captured at night to be analyzed. These previous studies that utilized standard image processing techniques are heavily dependent on image quality and as a result do not perform well when conditions such as the ambient light are changing.

Image processing algorithms that use machine learning methods have been found to be more robust and perform better than traditional methods at extracting river ice properties from images (Singh et al. 2020). First introduced in the late 1950s, machine learning algorithms have evolved rapidly and have demonstrated superior performance in many imaging applications such as medical image classification and disease diagnosis (Li et al. 2014), nucleus segmentation (Xing et al. 2016), face recognition (Lawrence

et al. 1997) and remote sensing (Maggiori et al. 2017). Recently, several studies have applied machine learning algorithms to extract river ice properties from images. Kalke and Loewen (2018) trained four SVMs (Support Vector Machine) to perform frazil/anchor ice pan segmentation using images captured from bridge-mounted trail cameras and UAVs. Their results showed a significant increase in accuracy compared to thresholding methods. Ansari et al. (2019) coupled fast superpixel segmentation with iterative edge refinement technique to train an SVM and used it for the classification of water, sky, bank, border ice, ice cover and pan ice. Singh et al. (2020) compared four state-of-the-art deep learning models (UNet, SegNet, DeepLab and DenseNet) to SVM and found that the deep learning models were significantly more accurate when segmenting images and videos of river surfaces into water, frazil pans and anchor ice pans. Zhang et al. (2020) and Zhang et al. (2021) proposed a semantic segmentation deep network called ICENET to segment UAV images of the Yellow River into water, ice and land. Ansari et al. (2021) used a modified Mask R-CNN to perform segmentation of open water, broken ice, frazil pan, frazil slush, border ice and ice cover in oblique UAV photos and obtained good accuracy. Sola and Scott (2022) proposed a novel convolutional block to construct a shallow UNet style architecture for river ice segmentation and achieved comparable performance to UNet with higher efficiency.

The objective of this study is to investigate the use of oblique images of river surfaces captured at long focus distances for long-term monitoring of surface ice conditions. Images from a public camera mounted on a building roof top captured during five freeze-up seasons was used in this study. A deep learning based hybrid image processing algorithm consisting of image classification, rectification, segmentation and extraction of river ice properties was developed to compute surface ice concentrations as well as ice pan size and shape properties. Time series of multi-year surface ice concentrations as well as size distributions and shape properties of ice pans during freeze-up in the North Saskatchewan River are presented.

## 2.2 Study Site

Figure 2.1 shows three maps of the North Saskatchewan River (NSR) in the City of Edmonton with varying scales. The NSR is a glacier-fed, regulated river that originates from the Canadian Rockies. The discharge is affected by the Brazeau and Bighorn Dams which are approximately 240 km and 430 km upstream of the Dudley B. Menzies LRT bridge in the study reach, respectively. A daily water level fluctuation of  $\sim 0.3$  m to  $\sim 0.4$  m can be observed on the NSR at Edmonton due to hydropeaking effects of the upstream dams (McFarlane et al. 2017). The river is irregularly meandering with point bars and side channel bars. The average daily winter discharge at Edmonton is  $126 \text{ m}^3/\text{s}$  (Hicks 1997), and the average depth and width in the study reach are approximately 1.4 m and 180 m, respectively (Kellerhals et al. 1972). Freeze-up on the study reach can start as early as late-October and a complete stable ice cover can form as late as the end of December. During a typical freeze-up season frazil slush, frazil ice pans, border ice and released anchor ice pans are observed in this reach. The only ice-induced flooding and bank erosion that has been observed in this reach was caused by a freeze-up ice jam that occurred in early December 2019. This was an unusual event that was likely triggered by the construction of temporary cofferdams during bridge construction downstream that constricted the channel by  $\sim 50$  %. The jam only caused some minor flooding but significant bank erosion was observed. Under normal conditions flow regulation at the two upstream dams virtually eliminates any risk of ice-induced or open water flooding in this reach. In addition, multiple water intakes are located along the study reach which can be blocked by the frazil ice formed during freeze-up. Warm water discharges from the University of Alberta's cooling water plant often lead to the formation of a narrow open lead in the study reach.

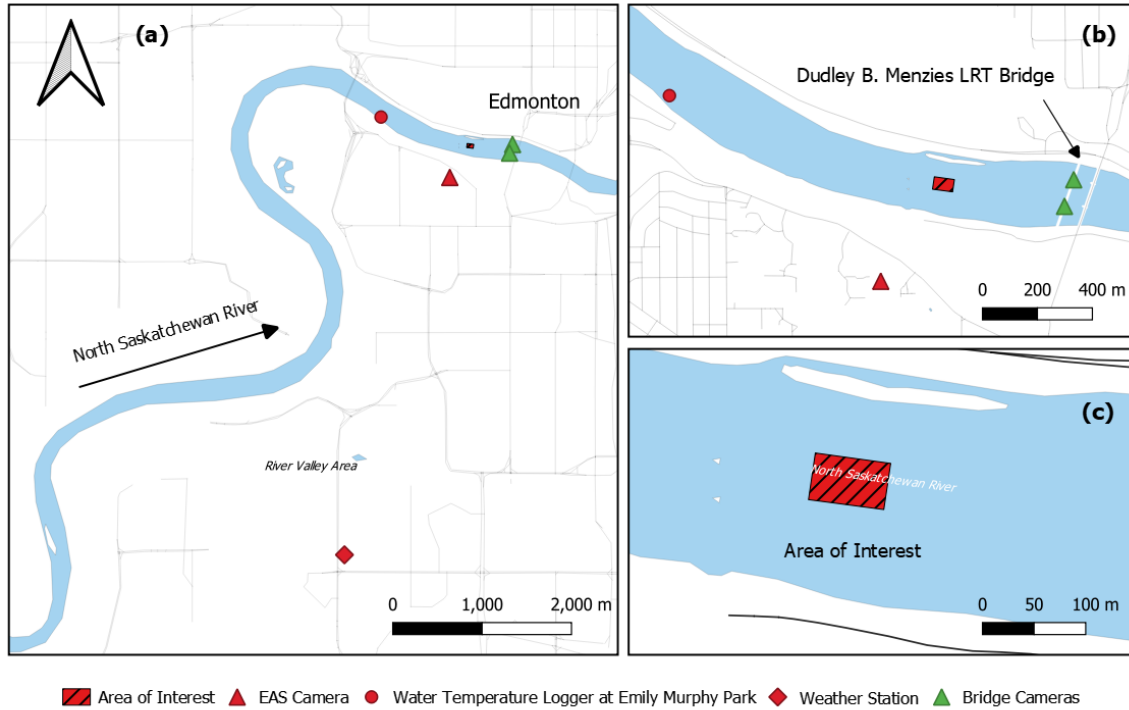


Figure 2.1: Maps of the North Saskatchewan River showing (a) a large area including 11 km upstream of the field site, (b) study reach including the area of interest (AOI) along with the EAS camera, water temperature logger and LRT bridge locations and (c) zoomed-in view of the AOI.

## 2.3 Image Source and Instrumentation

Images of surface ice conditions were obtained from the University of Alberta (UA) Department of Earth and Atmospheric Sciences (EAS) Weather Station Cameras. Four AXIS P1355 network cameras are mounted on the roof of the UA Tory Building at an elevation of  $\sim 122$  m above the NSR water surface. The cameras continuously sample 2.1-megapixel ( $1920 \times 1080$ ) RGB images at 15-minute intervals. Images from these cameras are publicly available at the EAS website (University of Alberta 2021). The network cameras were installed as a part of the EAS weather observation system and were not intentionally set up for river ice research. However, the four cameras provide very good views of the NSR near the UA campus and therefore provide an opportunity for studying the river ice processes. The cameras are enclosed in weather proof housings

to prevent any undesired camera movement or damage. The location of the EAS cameras is shown in Figure 2.1b and examples of raw images are presented in Figure 2.2. Images captured during five freeze-up seasons (2015 - 2017 and 2019 - 2020) by the camera with a horizontal FOV (field-of-view) of  $41.5^\circ$  looking  $\sim 0.4$  km upstream of the LRT bridge were obtained and processed. Note that images from the 2018 freeze-up were not processed due to poor image quality that year (*i.e.* adverse weather conditions). The AOI (area-of-interest) shown in Figure 2.1b-c is the water surface area that corresponds to the sub-region in the images where it was possible to extract accurate estimates of river ice properties. The AOI is located near the centreline of the NSR and covers approximately 27 % of the river width. The line of sight distance to the centre of the AOI is  $\sim 460$  m.

## 2.4 Image Processing

The appearance of the water surface and the different types of river ice in the EAS images can vary significantly under different conditions. Figure 2.2 presents four examples of high-quality images when the water surface and several different types of ice including slushy ice pans, crusty ice pans and ice cover were clearly visible. Slushy ice pans (Figure 2.2a) are defined as newly formed “younger” ice pans which appear relatively transparent in the image and their edges can be quite blurry. Crusty ice pans (Figure 2.2b-c) are “older” ice pans that appear with whiter edges than the slushy pans due to collisions with other ice pans. The ice cover imaged in Figure 2.2d is defined as a static ice sheet that appears white and covers the majority of the water surface.

The visibility of the water surface and ice was reduced significantly by insufficient light during the night and/or blurriness caused by inclement weather, which tended to lower image quality and make extracting quantitative information on river ice properties more difficult or impossible. A deep learning based hybrid image processing algorithm was developed to address the aforementioned challenges. The framework of the algorithm is shown schematically in Figure 2.3 and includes four major steps:

image classification, image rectification, image segmentation and ice pan properties extraction. The algorithm was executed on a personal computer (Intel Core i7-8700 CPU @3.20GHz; 16 GB RAM) and it took approximately 25 s to analyze a single image.

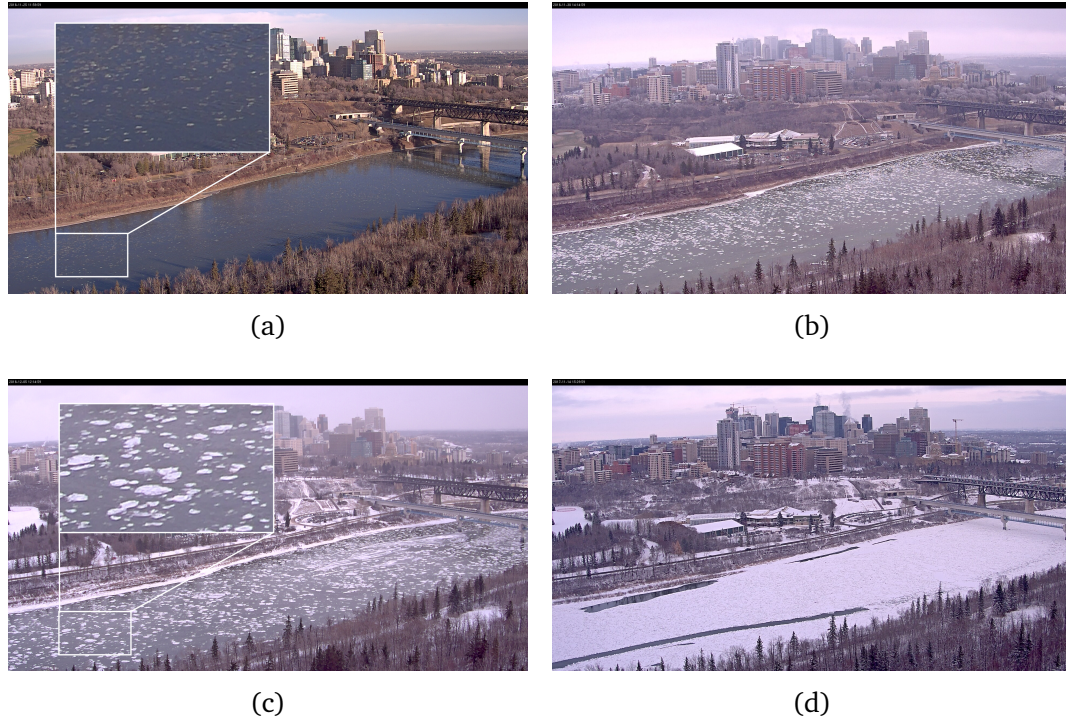


Figure 2.2: Examples of raw EAS camera images: (a) slushy ice pan image with zoomed in river surface, (b) crusty ice pan images (lower ice concentration), (c) crusty ice pan images (higher ice concentration) with zoomed in river surface and (d) ice cover image.

### 2.4.1 Image Classification

The goal of the image classification is to remove unusable night and blurry images from the dataset as shown in Figure 2.3. Therefore, in this study, the EAS camera images were first classified into four categories: night, blurry, ice pan and ice cover and examples of each are shown in Figure 2.4. The four image categories are defined as follows: night images (Figure 2.4a) were captured when there was insufficient light to illuminate the AOI; blurry images (Figure 2.4b) are any image in which the AOI is blurred or obscured for any other reason (*e.g.* clouding of the housing lens and inclement weather); ice pan images (Figure 2.4c) are images captured prior to ice cover formation which contain

water surface and/or discrete ice pan elements; and ice cover images (Figure 2.4d) are images that contain a static continuous ice cover.

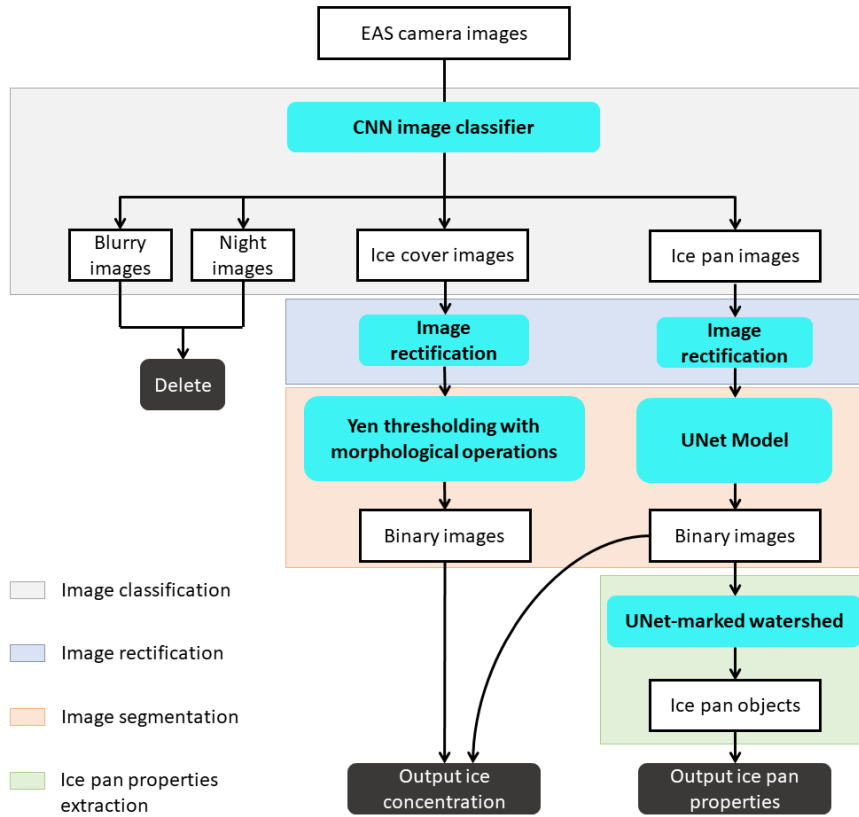


Figure 2.3: Framework of the hybrid image processing algorithm.

A simple CNN architecture containing two convolutional layers (Pillai 2018) was trained to automatically classify the EAS camera images into the four categories. A total of 1893 full resolution camera images captured from the 2017 - 2019 freeze-up periods were manually selected and labelled into the aforementioned four categories to construct the training and testing datasets for image classification. Table 2.1 lists the details of the labelled images in each category. A total of 1445 images were used for training, and 448 images were used for testing. The inputs to the network are  $256 \times 256$  RGB image patches resized and normalized from the original full-HD ( $1920 \times 1080$ ) images, each patch was subjected to random shear, zoom and horizontal flip to generate more augmented data. The commonly-adopted categorical cross-entropy loss function was used since there are four output categories and implementation was done

using the Keras framework (Chollet 2015). The model was trained for 300 epochs. The trained model used for evaluation was the one with either the maximum validation accuracy or the minimum validation loss depending on how well the training accuracy and validation accuracy match in the two cases. Batch sizes of 16, 32 and dropout rates of 0.25, 0.5 were tested which resulted in 4 combinations to train the model. Each combination was evaluated and it was found a batch size of 32 and a 0.25 dropout rate achieved optimum performance. Figure 2.5 shows the normalized confusion matrix of each category. Results show that the model is quite accurate, identifying night, ice cover, ice pan and blurry images with an accuracy of 100 %, 98.28 %, 98.69 % and 94.74 %, respectively. Overall, the model performed well with a frequency weighted average accuracy of 98.66 % in all categories. As a final step the image sequences were manually examined to identify and correct the small number of misclassified images to ensure the accuracy of the following steps.

Table 2.1: The number of labelled images in each image category.

| Class           | Train | Test |
|-----------------|-------|------|
| Blurry image    | 127   | 38   |
| Ice cover image | 414   | 116  |
| Night image     | 469   | 141  |
| Ice pan image   | 435   | 153  |
| Total           | 1445  | 448  |

### 2.4.2 Image Rectification

The EAS camera is mounted on a tower on the rooftop of the UA Tory Building looking down at an oblique angle towards the NSR. The view angle from the north, dip and tilt angles of the camera could not be directly measured due to its hazardous high installation position. However, estimates were made by calculating the geometric properties of objects in the image, which gave a view angle of  $47.2^\circ$  from the north (*i.e.* NE di-



Figure 2.4: Examples of four image categories (a) night image, (b) blurry image, (c) ice pan image and (d) ice cover image.

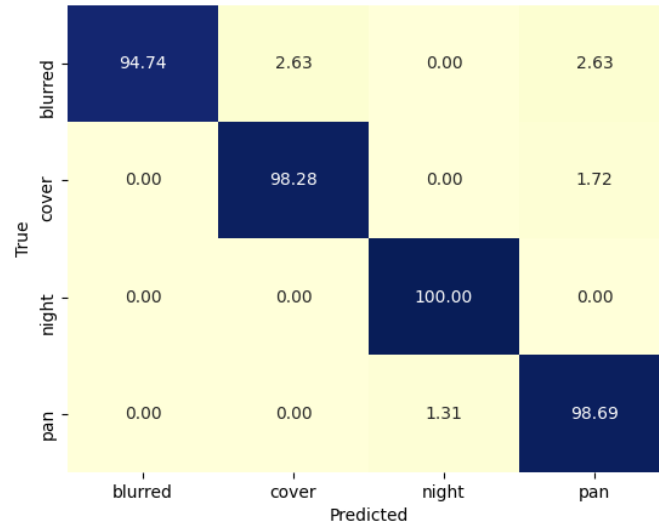


Figure 2.5: Confusion matrix for each image category showing % accuracy.

rection), a dip angle of  $7.8^\circ$  and a tilt angle of  $-1.8^\circ$ . Since the camera was installed at an oblique angle, the ice cover and ice pan images needed to be geo-rectified to obtain quantitative data. In this study, an open-source MATLAB program “g\_rect” (Bourgault

2008) was used to geo-rectify the ice pan and ice cover images. This algorithm takes camera view and positional parameters, ground control points (GCPs) and their associated image control points (ICPs) as inputs. It allows users to perform geo-rectification with undetermined camera parameters and uses an iterative algorithm to minimize the root mean square distance between the GCPs and associated ICPs, which is especially suitable for conditions where camera parameters cannot be easily and accurately determined.

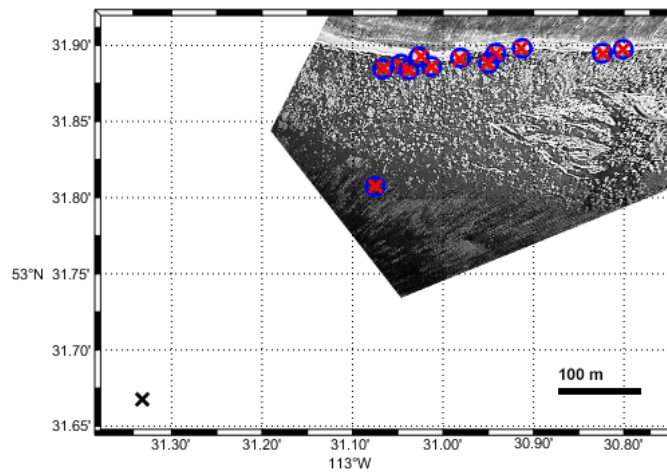
The coordinates and elevation of 12 GCPs were surveyed using a Trimble R8 RTK GPS system by wading into the river and capturing images in which the top of the rover was visible. The EAS camera sampling frequency was changed briefly during the survey to capture an image every 30 seconds. The GCPs were surveyed at locations in the reach that were visible in the images that could be reached safely by wading and where RTK GPS signals were reliable enough to ensure survey accuracy. At each GCP the rover was held in place for two minutes, and four images were captured. The resulting average horizontal and vertical precision of the GCPs recorded by the RTK GPS was 0.008 m and 0.014 m, respectively. Figure 2.6a shows the 12 GCPs used in the rectification algorithm in a raw image and in Figure 2.6b superimposed GCPs and ICPs are shown plotted on the geo-rectified image. The close alignment of the GCPs and ICPs in the geo-rectified image indicates that there was a good fit between the calculated coordinates and the original coordinates. The estimated root mean square error (RMSE) of the distance between the GCPs and the rectified ICPs is 0.867 m, which is considered acceptable given the scale of the domain included in the image.

### **2.4.3 Image Segmentation**

The rectified images encompass a relatively large river surface area as shown in Figure 2.6b. However, the rectified images needed to be cropped to minimize the effect of reflected sunlight and increase the effective pixel resolution. This resulted in smaller images with pixel dimensions of  $820 \times 500$  representing a smaller AOI near the cen-



(a)



(b)

Figure 2.6: (a) Locations of the GCPs  $\times$  in a raw image and (b) a geo-rectified image with superimposed GCPs  $\times$ , ICPs  $\circ$ , and EAS camera location  $\times$ .

treline of the river which did not cover the entire river width. The cropped image has a pixel length of 0.092 m and covers approximately  $3470 \text{ m}^2$  of water surface area, which is shown in Figure 2.1c. The growth of border ice in the study reach was observed to be restricted to regions very close to the banks which were not imaged in the selected AOI. Therefore, this study focused exclusively on detecting surface ice pans and the ice cover, and the surface ice concentration is defined as the percentage of water surface in the AOI covered by surface ice pans and/or ice cover.

Freeze-up generally begins with free-flowing surface ice pans and ends when a complete ice cover forms on the water surface. The accuracy of various thresholding methods was first tested on both ice cover and ice pan images. The tests showed that for ice cover images, using a thresholding method for ice segmentation produced accurate results. However, during the free-flowing surface ice phase, distinguishing ice pans from water using thresholding was found to be inaccurate due to variations in the texture and transparency of ice pans formed under different weather and light conditions. This is especially the case when ice pans were newly formed on the water surface at the beginning of freeze-up and appeared slushy and this required a more robust method for accurate segmentation of surface ice pans from water. Therefore, in this study, the cropped ice cover images were segmented using a thresholding method and the cropped ice pan images were segmented using a deep-learning model as shown in Figure 2.3.

Five ice cover testing images were selected from the 2019 and 2020 freeze-up seasons that showed a complete ice cover including some with open leads under different light conditions and ice texture variations. The images were manually labelled to generate ground truth labels. The testing images were thresholded using 16 automatic thresholding methods with morphological operations. The segmentation results were evaluated using four metrics: pixel accuracy, mean accuracy, mean intersection over union (IoU) and frequency weighted IoU (Singh et al. 2020) defined as follows:

$$\text{Pixel accuracy} = \frac{\sum_i n_{ii}}{\sum_i t_i} \quad (2.1)$$

$$\text{Mean accuracy} = \frac{1}{n} \sum_i \frac{n_{ii}}{t_i} \quad (2.2)$$

$$\text{Mean IoU} = \frac{1}{n} \sum_i \frac{n_{ii}}{t_i + \sum_j (n_{ji} - n_{ii})} \quad (2.3)$$

$$\text{Frequency weighted IoU} = \sum_k (t_k)^{-1} \sum_i \frac{t_i n_{ii}}{t_i + \sum_j (n_{ji} - n_{ii})} \quad (2.4)$$

where  $n$  is the number of classes,  $n_{ji}$  is the number of pixels of class  $j$  predicted to belong to class  $i$ , and  $t_i$  is the total number of pixels of class  $i$  in the ground truth testing image labels. The pixel accuracy can also be considered as a frequency weighted

accuracy. In addition, the mean absolute difference of surface ice concentration  $MAD C_{ice}$  between testing image labels and predicted image labels was calculated to estimate the accuracy of ice concentration estimates. The Yen thresholding method (Yen et al. 1995) with morphological operations was found to be the most accurate among all tested thresholding methods, achieving 96.84 %, 95.81 %, 86.34 %, 94.48 % and 2.44 %, respectively for pixel accuracy, mean accuracy, mean IoU, frequency weighted IoU and  $MAD C_{ice}$ . Therefore, the Yen thresholding method was selected to segment ice cover images.

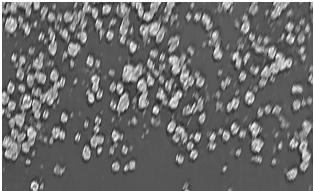
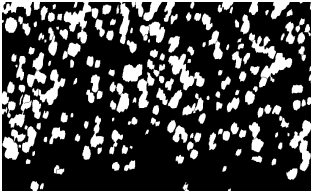
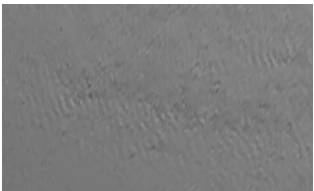
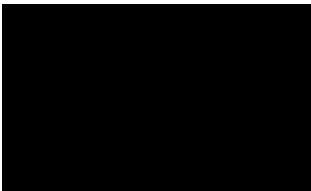
UNet is a fully convolutional neural network initially designed for biomedical image segmentation (Ronneberger et al. 2015). The network consists of a contracting path to extract context features and an expansive path for accurate localization, forming a symmetric “U” shaped encoder-decoder architecture. Since its introduction in 2015, the UNet architecture has been shown to achieve promising performance with relative fewer annotated training samples and heavy use of data augmentation, which makes it quite suitable for ice pan segmentation. Singh et al. (2020) investigated the application of four state-of-the-art deep learning methods including UNet for segmenting river ice images. They concluded that UNet was probably the best method based on the fact that it provided a good balance between generalization and overfitting. Therefore, the ice pan images in this study were segmented using UNet.

A total of 50 rectified and cropped ice pan images from the 2019 - 2020 freeze-up seasons were manually selected and labelled to train and test the UNet model for binary ice and water segmentation. The images were selected to represent three different ice conditions including no ice, slushy pans and crusty pans. The 50 labelled images were divided into 80 % for training and 20 % for testing, images in the testing dataset were randomly selected in each of the three ice conditions to ensure that each condition is represented and evaluated in the testing dataset. The details of the labelled images for each surface ice condition are listed in Table 2.2. To generate a large set of sub-images from each training/testing image, each of the  $820 \times 500$  images was first converted

to grayscale, then resized and cropped into six  $256 \times 256$  patches. Then each patch was used to generate three more images by randomly rotating ( $0 - 45^\circ$ ), width/height shifting ( $0 - 20\%$ ), shearing ( $0 - 0.2^\circ$ ) and flipping. The blank areas generated during these operations were filled by reflecting the pixel values along the image boundary. The model was trained for 1000 epochs, a batch size of 8 and a dropout rate of 0.2 were used. The binary focal loss function (Lin et al. 2017) was used to address the class imbalances of ice and water since it was found that the ice only covers 20 - 30 % of the water surface in the majority of the images. Implementation was done using the Keras framework (Chollet 2015). Model training was conducted on the Compute Canada Cedar platform using one GPU node with 6 CPU and 32000 MB memory. The trained model used for evaluation was the one with either the maximum validation accuracy or the minimum validation loss depending on how well the training accuracy and validation accuracy match in the two cases.

Each of the 10 ice pan testing images was first cropped into 6 sub-patches for UNet segmentation, then the segmented sub-patches were stitched back together to get the final predicted results for evaluation. The segmentation results were evaluated using the metrics in Equation (2.1) - Equation (2.4) and  $MAD C_{ice}$ . Table 2.3 presents the UNet segmentation performance for ice pan images. As shown in Table 2.3, UNet achieved 100 % in all accuracy/IoU metrics and 0 % in  $MAD C_{ice}$  for images with no ice, demonstrating that the model is accurate at detecting the water surface without mislabeling shadows/ripples as ice. For slushy pan images, the frequency weighted accuracy and IoU were 92.93 % and 91.37 %, respectively. The mean accuracy and IoU were 70.98 % and 68.64 %, respectively which were significantly lower than the frequency weighted values. The low mean accuracy and IoU may be due to the imbalanced water/ice ratio in the low-concentration slushy ice pan images which may lead to biased evaluation results since the number of pixels is not evenly distributed between ice and water class. The low variance of pixel intensity between open water and slushy ice pans may also influence the segmentation accuracy for slushy pan images. A  $MAD C_{ice}$  of 1.80 % was

Table 2.2: Details of the images and corresponding labels in each condition used for UNet training/testing.

| Water surface condition | Example training images  | Example training labels   | Total training images | Total testing images |
|-------------------------|--|---|-----------------------|----------------------|
| Slushy pan              |   |   | 18                    | 4                    |
| Crusty pan              |   |   | 21                    | 5                    |
| No ice                  |  |  | 1                     | 1                    |
| Total                   | -  | -   | 40                    | 10                   |

achieved. For crusty pan images, the model performed more uniformly with all four accuracy/IoU metrics exceeding 70 %, and a MAD  $C_{ice}$  of 2.68 % was achieved. This is not unexpected since the ice concentration in crusty pan images is significantly higher than in slushy pan images. Overall, the model achieved 85 - 87 % in frequency weighted metrics, 74 - 77 % in terms of mean metrics, and about 2 % of MAD  $C_{ice}$ .

In Table 2.4 the accuracy/IoU metrics achieved with UNet trained using EAS images is compared with the UNet results of Singh et al. (2020) which were trained using images obtained from UAV and game cameras. The results obtained in this study using UNet are comparable with the UNet results presented by Singh et al. (2020) except for the mean accuracy. The EAS images were rectified from oblique camera images collected from a much greater distance and as a result the image quality and resolution

Table 2.3: UNet segmentation performance for ice pan images.

| Evaluation metrics         | Slushy pan images | Crusty pan images | No ice image | Overall (Frequency weighted) |
|----------------------------|-------------------|-------------------|--------------|------------------------------|
| Pixel accuracy (%)         | 92.93             | 79.59             | 100.00       | 86.97                        |
| Mean accuracy (%)          | 70.98             | 76.34             | 100.00       | 76.56                        |
| Mean IoU (%)               | 68.64             | 72.37             | 100.00       | 73.64                        |
| Frequency weighted IoU (%) | 91.37             | 76.78             | 100.00       | 84.93                        |
| MAD $C_{ice}$ (%)          | 1.80              | 2.68              | 0.00         | 2.06                         |

are considerably lower than the images used by Singh et al. (2020). Therefore, because the UNet model developed in this study achieved comparable accuracy to Singh et al. (2020), this was taken as confirmation that it was segmenting the ice pans with sufficient accuracy in the EAS images.

Table 2.4: Comparison of UNet segmentation performance between this study and Singh et al. (2020).

| Evaluation metrics         | This study               | Singh et al. (2020)           |
|----------------------------|--------------------------|-------------------------------|
|                            | Image source: EAS Camera | Image source: UAV/Game Camera |
| Pixel accuracy (%)         | 86.97                    | 88.69                         |
| Mean accuracy (%)          | 76.56                    | 85.13                         |
| Mean IoU (%)               | 73.64                    | 73.19                         |
| Frequency weighted IoU (%) | 84.93                    | 81.73                         |

#### 2.4.4 Ice Pan Properties Extraction

It was found that computing ice pan properties directly from the UNet segmented ice pan images using simple connected component analysis (CCA) based separation sometimes led to overestimation of ice pan sizes when two or more individual ice pans were

incorrectly identified as a single pan due to noisy boundaries. An example of this is shown in Figure 2.7a-b where two separate pans in the raw image are shown connected in the UNet segmented image and were subsequently identified as a single pan using CCA based separation. Therefore, a marker-based watershed transformation was used to extract ice pan properties and overcome this drawback. The watershed transformation is a widely used mathematical morphological method for image segmentation and instance separation of definite object classes (Ibrahim et al. 2019). It treats input grayscale images as a topographic surface and separates different components by flooding this surface from its minima until a peak (edge) has been reached. Marker-controlled watershed transformation (Roerdink and Meijster 2000) utilizes the exact region of object instance markers to guide the flooding process. The region of objects is often obtained by performing thresholding on the original images. Studies show that binary labels generated by deep learning based segmentation can further improve the accuracy of watershed transformation since deep learning based segmentation has been shown to generate higher-accuracy results compared to thresholding (Eschweiler et al. 2019; Ibrahim et al. 2019). In this study, the UNet segmented labels of ice pan images were used to perform the marker-controlled watershed transformation. After applying the watershed transformation the two separate pans in Figure 2.7a were correctly identified as separate pans as shown in Figure 2.7c-d.

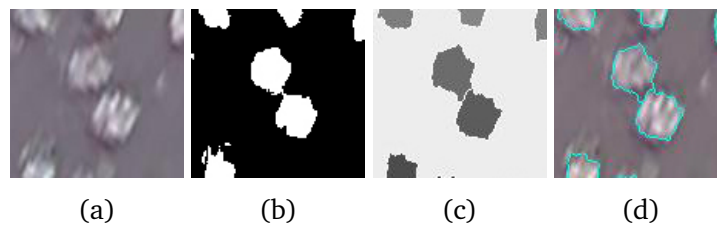


Figure 2.7: Example of UNet marked watershed transformation to separate wrongly connected ice pans highlighted in a red circle, (a) rectified images, (b) UNet segmented binary images, (c) watershed transformed markers and (d) overlaid marker boundary in light blue.

The ice pan objects identified by the watershed transformation were analysed to extract the following pan properties: area ( $A$ ), perimeter ( $p$ ) and the lengths of the major

and minor axis of the ellipse that has the same normalized second central moments as the ice pan. The size of the ice pans was calculated as follows:

$$d = \sqrt{\frac{4A}{\pi}} \quad (2.5)$$

where  $d$  is the equivalent diameter of the ice pan. The ratio  $d_p/d$  was used to quantify the degree of distortion of an ice pan from a circle and is given by:

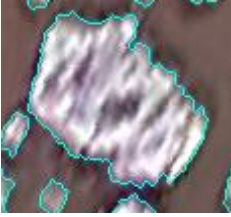
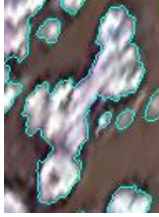
$$d_p/d = \frac{p}{\pi d} \quad (2.6)$$

where  $d_p$  is the diameter derived from the perimeter of an ice pan assuming it to be a circle. This ratio was initially introduced by sea ice researchers to evaluate the shape of sea ice pans (Toyota et al. 2006). To illustrate how this ratio varies with shape four cropped images of ice pans and rafts with shapes varying from approximately circular to very irregular are shown in Table 2.5. The ratio is seen to vary from 1.14 to 3.38 as the shape becomes more irregular and it is evident that higher  $d_p/d$  values might indicate the formation of rafts. The aspect ratio ( $AR$ ) defined as the ratio of the major to minor axis length was also provided to help characterize the shape of ice pans, as can be seen in Table 2.5,  $AR$  increased from 1.35 to 2.84 for the first three pans as they became more irregular but slight decreased to 2.79 for the most irregular pan. All detected ice pans that intersected the image boundaries were excluded from the analysis. By manually checking  $\sim 300$  individual ice pan objects and comparing them to the rectified image, a cut-off  $d$  of 0.55 m was introduced to eliminate inaccurate results since it was found that ice pans with an area less than 28 pixels ( $d = 0.55m$ ) were either false positives or produced by snowflakes in the air between the camera and water surface.

#### 2.4.5 Overall Qualitative Performance

The qualitative performance of the proposed algorithm was assessed by applying the algorithm to segment EAS images from the 2016 freeze-up season. Figure 2.8 presents examples of raw images and the resulting processed images. The images show the progression of the 2016 freeze-up season from top to bottom representing various surface

Table 2.5: Examples of ice pans of different shapes and its corresponding  $d_p/d$  and  $AR$ . Light blue lines denote overlaid ice pan boundary. Note that  $d_p/d$  and  $AR$  was calculated for the largest pan that appeared in each image.

|               |   |   |   |   |
|---------------|---|---|---|---|
| Ice pan image |  |  |  |  |
| $d_p/d$       | 1.14  | 1.36  | 2.01  | 3.38  |
| $AR$          | 1.35  | 1.50  | 2.84  | 2.79  |

ice conditions. The algorithm accurately identified no ice conditions in 98 % of unlabelled no ice images such as the one shown in Figure 2.8a. Figure 2.8b-c demonstrate that the algorithm can capture the initiation of surface ice pan generation by accurately segmenting relatively larger slushy pans but tends to miss smaller pans that were too transparent or blurry. As shown in Figure 2.8d-f, the algorithm performs well when ice pans were crusty since most crusty ice pans were accurately identified and segmented. Figure 2.8g shows that Yen thresholding can successfully segment ice cover images without mislabelling shadows on the ice cover as water. Overall, the examples presented in Figure 2.8 demonstrate qualitatively that the algorithm can accurately segment EAS images captured over the full range of conditions.

## 2.5 Results and Discussion

### 2.5.1 Comparison of Ice Concentrations Estimated From EAS and BridgeCam Images

In order to quantitatively assess the capability of the EAS images in estimating surface ice concentrations, higher-quality images obtained during the 2016 freeze-up from the two BridgeCams (Figure 2.1b) were segmented since they were installed close to the AOI and have  $\sim 20$  times smaller pixel length compared to the rectified EAS images. The resulting BridgeCam ice concentrations were compared with concentrations estimated

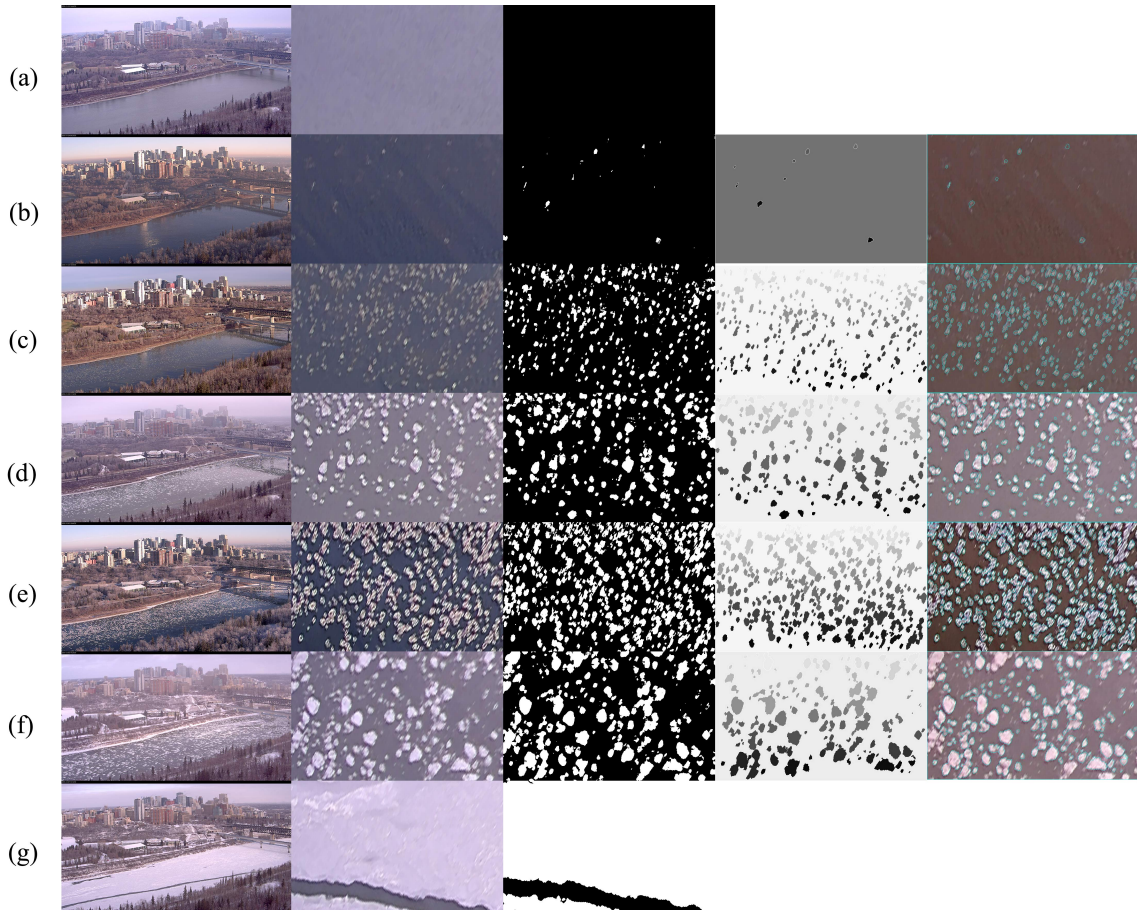


Figure 2.8: Examples of 2016 freeze-up image processing results on unlabelled images: left to right: original EAS images, rectified images, predicted binary labels, watershed transformed markers, overlaid marker boundary in light blue. Various surface ice conditions shown: (a) no ice, (b-c) slushy pans, (d-f) crusty pans and (g) ice cover.

from the EAS images. A binary ice/water UNet model was trained and tested using 50 images and corresponding labels from the Alberta River Ice Segmentation Dataset (Singh et al. 2019) to segment BridgeCam images. The training and testing processes of BridgeCam UNet were kept the same as for the EAS camera images described in Section 2.4.3. The resulting pixel accuracy, mean accuracy, mean IoU, frequency weighted IoU and MAD  $C_{ice}$  are 86.72 %, 82.68 %, 75.51 %, 80.17 %, and 2.97 %, respectively which are comparable to the EAS UNet performance.

In Figure 2.9 time series of surface ice concentrations estimated from EAS and BridgeCams images during the 2016 freeze-up are compared and examples of images from the different cameras are also presented. As can be seen the surface ice concentrations are

varying significantly each day in all three time series but the daily mean concentrations all follow the same general trend. The daily mean concentrations estimated from the EAS and right BridgeCam images agree closely most of the time prior to Dec. 5 with a mean absolute difference of 2.9 % over this period. However, the daily mean concentration estimated from the left BridgeCam images are on average 17 % higher than values estimated from the EAS camera images prior to Dec. 5. The significantly higher values close to the left bank are likely due to the fact that this is the location of the thalweg and the centrifugal force imposed by the river meander upstream of the AOI. The EAS mean daily concentration remained relatively low at 24 % until Dec. 6 and then it abruptly rose to 90 % on Dec. 7 indicating the formation of an ice cover in the central region of the channel. The two BridgeCam concentrations reached 54 % and 50 % on Dec. 5 which is significantly higher than the EAS camera concentration. An ice cover formed earlier in the regions closer to the banks on Dec. 6 and the two BridgeCam concentrations reached 77 % and 84 % on that day.

As can be seen in Figure 2.9 the slushy ice pans are clearly visible in the BridgeCam images from Nov. 26. Compared to the BridgeCams images from Nov. 26 it is evident that the slushy pans also appeared to be visible but blurrier in the EAS images because of the lower image quality. However, the blurriness of the slushy pans in the EAS images did not appear to affect the ice concentration results much since the EAS concentrations agreed closely with the right BridgeCam concentrations as shown in the time series. Both BridgeCam images from Dec. 2 show that the ice pans were mainly crusty and that because of their distinct white edges these crusty pans are also clearly visible in the corresponding EAS image. Interestingly, on Dec. 5 when EAS ice concentrations are drastically different than the two BridgeCam concentrations, the pans appeared much whiter in the EAS image while in the BridgeCam images there were a lot of transparent slush balls visible in addition to the crusty white pans. This comparison indicates that the lower resolution EAS camera is capable of capturing both visible slushy pans and crusty pans but may not capture the transparent slush balls which were

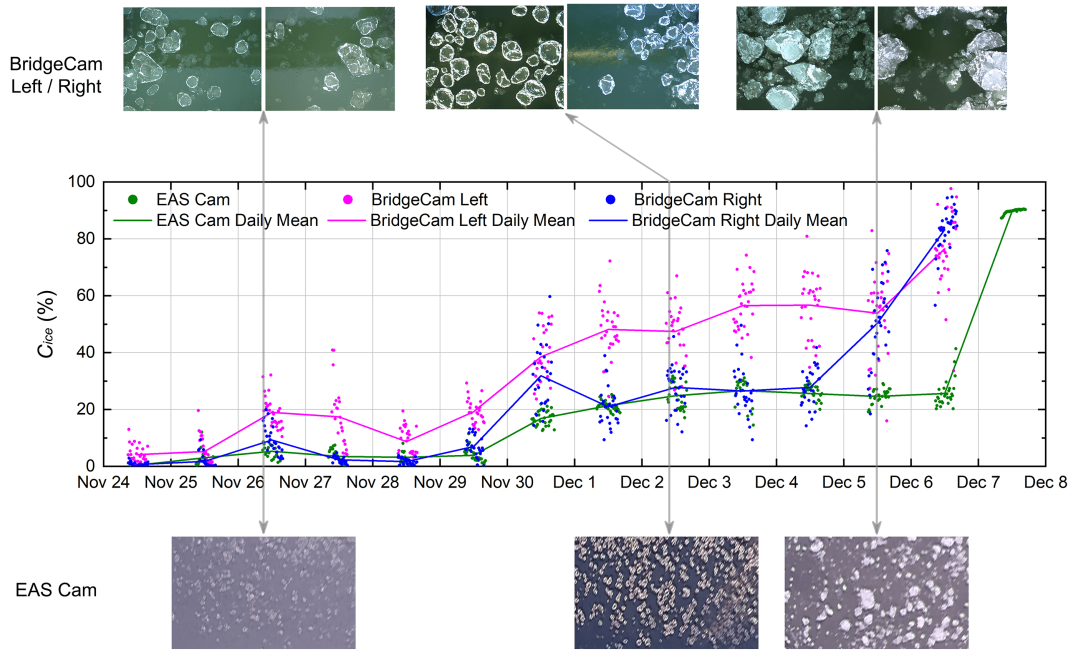


Figure 2.9: Comparison of the time series of surface ice concentrations from the EAS Camera images and BridgeCam images during the 2016 freeze-up between Nov. 24 and Dec. 8 as well as image comparison for three selected times. Only the black information banner has been cropped from the BridgeCam images.

captured by the BridgeCams. This is not surprising since the BridgeCams were mounted much closer to the water surface pointing straight down which resulted in much higher image quality compared to the EAS images. Overall the results from the lower-quality EAS camera images are comparable to the right BridgeCam results, demonstrating that images collected by the EAS camera can be used to accurately monitor surface ice processes.

## 2.5.2 Time Series of Surface Ice Concentration

The algorithm was used to process five years of EAS camera images captured during the freeze-up period. In each year, the start of the freeze-up period was defined as the first day ice appeared and the end as when a stable continuous ice cover had formed. Figure 2.10 presents the time series of surface ice concentrations and air temperatures

during freeze-up for each year. A synopsis of freeze-up in each year is provided in Table 2.6 including the start date, duration, mean air temperature and percentage of time when air temperature was below zero. In each year, three surface ice conditions with different ranges of concentration can be observed. When the daily mean ice concentration was less than 15 %, the ice pans identified in the images were mostly slushy. At times when the daily mean ice concentration increased and was between 15 % and 35 % the ice pans visible in the images were mostly crusty. A continuous ice cover usually formed quickly with daily mean ice concentration rising quickly from ~25 % to 100 %. During freeze-up in 2017, 2019 and 2020 temporary bridging of the ice cover occurred, and the ice concentration increased temporarily to between 80 % and 100 % before decreasing to much lower values.

Table 2.6: Synopsis of freeze-up in each year.

| Year | Start date | Duration (days) | Mean $T_a$ (°C) | % of time $T_a$ below zero |
|------|------------|-----------------|-----------------|----------------------------|
| 2015 | Nov. 18    | 9               | -5.7            | 87 %                       |
| 2016 | Nov. 20    | 17              | -5.3            | 90 %                       |
| 2017 | Nov. 3     | 9               | -9.9            | 100 %                      |
| 2019 | Oct. 29    | 46              | -4.3            | 66 %                       |
| 2020 | Oct. 24    | 29              | -2.8            | 63 %                       |

It is evident in Figure 2.10 that the duration of freeze-up and the nature of the ice concentration time series varied significantly from year-to-year. For the first three years, freeze-up progressed relatively quickly with durations of 9 days in 2015/2017 and 17 days in 2016. As shown in Table 2.6, air temperatures were below zero for more than 85 % of the time during freeze-up in 2015, 2016 and 2017 and mean air temperatures were all below -5 °C. These conditions promoted continuous surface ice generation and resulted in shorter freeze-up durations. The concentration time series in 2015 and 2017 are nearly identical, which is not surprising since the mean air temperature and

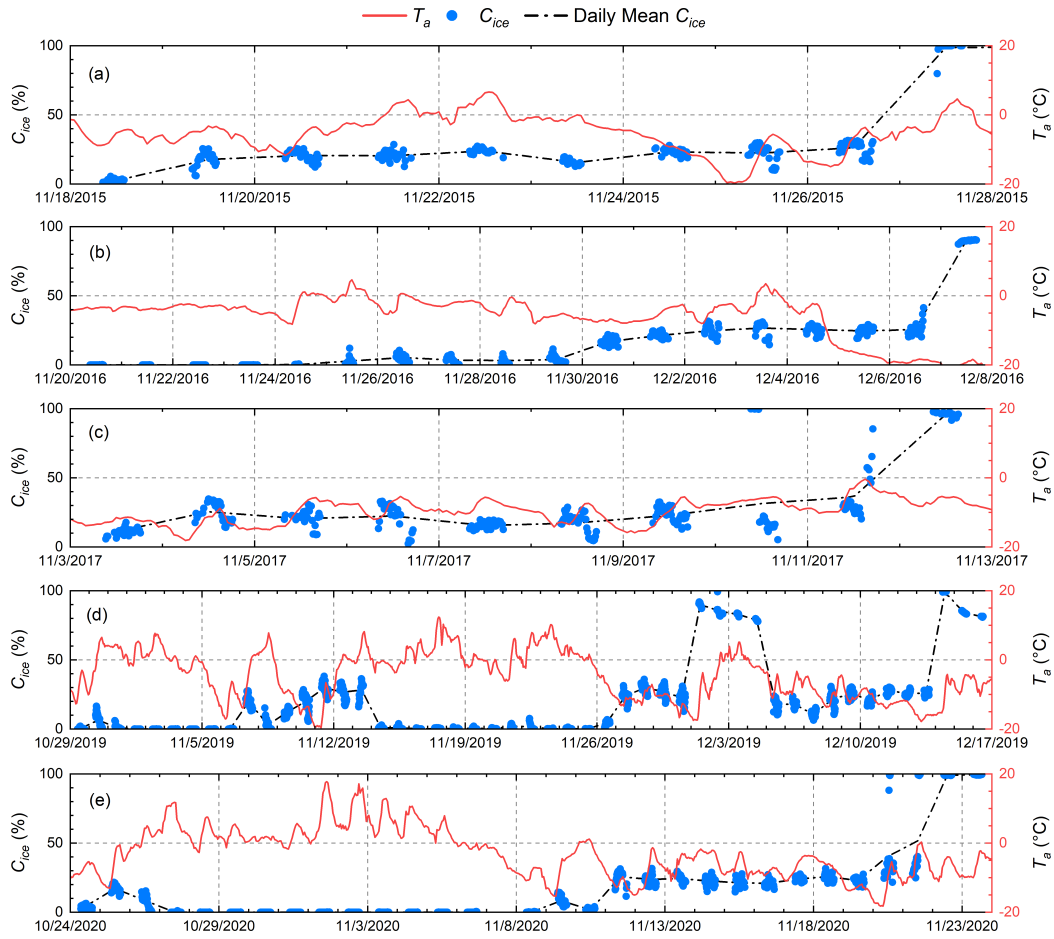


Figure 2.10: Time series of surface ice concentration ( $C_{ice}$ ) and air temperature ( $T_a$ ) in the AOI during freeze-up of (a) 2015, (b) 2016, (c) 2017, (d) 2019 and (e) 2020.

percentage of time the air temperature was below zero during these two years are very similar. In 2016 concentration was  $<1\%$  for the first five days of freeze-up, then from Nov. 25 - 30 increased to  $\sim 4\%$  possibly due to the relatively warm air temperatures up to  $4.6\text{ }^\circ\text{C}$ . On Dec. 1 the concentration increased and for seven days ranged from  $15\%$  to  $25\%$  until reaching  $\sim 90\%$  on Dec. 7 indicating an ice cover had formed. The freeze-up duration in 2016 is almost two times longer than the other two years.

In 2019 and 2020 freeze-up progressed relatively slowly with durations of 46 and 29 days, respectively. The concentration time series in Figure 2.10d-e show that the freeze-up was effectively interrupted twice in 2019 and once in 2020 for extended pe-

riods of time prolonging freeze-up. As shown in Table 2.6, the percentage of time when air temperature below zero is significantly lower than the first three years and mean air temperatures were all above  $-5\text{ }^{\circ}\text{C}$ . Freeze-up in 2020 started with three days of significant daily mean concentration followed by 13 days of interruption with concentrations less than 1 %. This interruption was due to a period of warm air temperatures. After the interruption freeze-up progressed similarly to 2015/2017 over a period of 14 days. Freeze-up in 2019 was much more dynamic since it was interrupted twice due to the above-zero air temperature periods, and a temporary ice cover was formed and remained in place during the freeze-up for four days. Overall, the appearance of surface ice pans and increased ice concentration most of the time correlates with the sub-zero air temperature, while above-zero air temperature may halt the surface ice production resulting in a near-zero ice concentration, or weakening the newly formed ice cover which leads to the breakup of the ice cover.

### 2.5.3 Ice Pan Properties

Surface ice pan size distributions on the NSR from 2015, 2017, 2020 and 5-year combined are plotted in Figure 2.11. Size distributions from 2016 and 2019 are not presented since they were very similar to the ones from 2015 and 2020. A theoretical lognormal distribution can be seen to be a reasonable fit to all of the size distributions in Figure 2.11 but it fits particular well to the 2015 and 5-year size distributions. The peak in the size distributions computed for all years was slightly shifted to the left compared to the theoretical lognormal distribution, which might be caused by the cut-off diameter since only ice pans with a diameter larger than 0.55 m could be accurately identified.

A summary of ice pan properties and statistics is presented in Table 2.7. A total of 314,606 ice pans were detected in the five years and the overall mean ( $d_m$ ), standard deviation ( $\sigma$ ) and maximum diameter ( $d_{max}$ ) of the pans were 1.82 m, 1.08 m and 15.03 m, respectively. The yearly values of  $d_m$  ranged from 1.75 - 2.09 m and  $\sigma$  ranged from

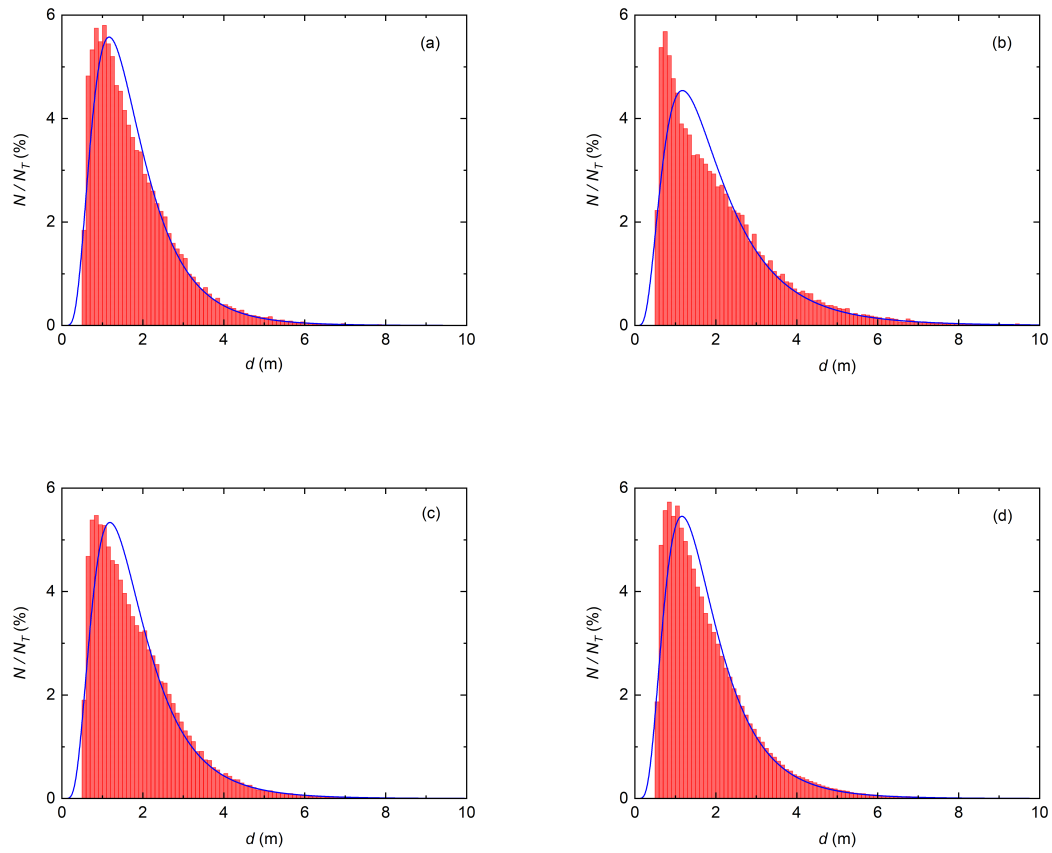


Figure 2.11: Normalized size distributions of ice pans for (a) 2015 freeze-up, (b) 2017 freeze-up, (c) 2020 freeze-up and (d) Five-year combined. Blue line denotes fitted log-normal distribution,  $N$  is the number of ice pans in each bin and  $N_T$  is the total number of ice pans.

1.02 - 1.38 m. The values of  $d_m$  and  $\sigma$  in each year were generally comparable except for in 2017 when both were maximums at 2.09 m and 1.38 m, respectively. In 2019  $d_m$  and  $\sigma$  were both the smallest of the five years at 1.75 m and 1.02 m, respectively and interestingly both the total ice pan count ( $N_T$ ) and the freeze-up duration were maximums this year. This is possibly due to the more dynamic freeze-up process that year hence more small pans were generated during the initiation of each ice pan event. In all years the  $d_{max}$  exceeded 10 m and the biggest ice pan, which was likely a raft, was detected in 2020 with a diameter of 15.03 m.

Several previous studies have reported ice pan sizes during freeze-up. Ghobrial et

Table 2.7: Ice pan size properties during the freeze-up period.  $N_T$  is the total ice pan count,  $N_I$  is the number of ice pans per image,  $d_m$ ,  $\sigma$ ,  $d_{max}$  is the mean, standard deviation and maximum ice pan size.

| Year     | $N_T$   | $N_I$ | $d_m$ (m) | $\sigma$ (m) | $d_{max}$ (m) |
|----------|---------|-------|-----------|--------------|---------------|
| 2015     | 45,844  | 162.6 | 1.79      | 1.04         | 13.02         |
| 2016     | 46,561  | 113.8 | 1.79      | 1.06         | 11.26         |
| 2017     | 29,146  | 93.7  | 2.09      | 1.38         | 14.03         |
| 2019     | 119,335 | 93.5  | 1.75      | 1.02         | 11.66         |
| 2020     | 73,720  | 86.2  | 1.85      | 1.07         | 15.03         |
| Combined | 314,606 | 100.4 | 1.82      | 1.08         | 15.03         |

al. (2013) investigated ice pan lengths on the NSR computed from sonar data and found they varied from less than 1 m to 20 m. They also found that during most of the time when frazil pans were continuously detected, the pan length was quite stable and varied between 1 - 3 m. These measurements were largely comparable to our findings, and the 33 % larger maximum ice pan size may be due to different definitions of ice pan sizes. Sonars measure a chord length as an ice pan passes over the location of the acoustic beam which is quite different than the equivalent diameter used in this study. Jasek (2016) measured the ice pan parameters on the Peace River using a sonar and found the 5<sup>th</sup> to 95<sup>th</sup> percentiles of freeze-up ice pan length ranged from 2.3 - 41 m. These pans were significantly larger than those on the NSR, which is likely because the Peace River is a significantly larger river.

In Figure 2.12a the equivalent diameter  $d$  is plotted versus the perimeter derived diameter  $d_p$  and in Figure 2.12b the major axis length is plotted versus the minor axis length for all 314,606 ice pans identified in the five years. The data in Figure 2.12a show that as  $d$  becomes larger the corresponding range of  $d_p$  also becomes larger which means that larger ice pans can be more irregular. On average the ratio  $d_p/d$  is 1.25 with a standard deviation of 0.21, and the aspect ratio  $AR$  (*i.e.* major axis length/minor axis length) is 1.71 with a standard deviation of 0.50. The ice pan shape for each individual

year was generally similar with the average  $d_p/d$  ranging from 1.24 to 1.28 and the average  $AR$  ranging from 1.70 to 1.76. It was also found that 90 % of the detected ice pans have a  $d_p/d$  less than 1.5 and an  $AR$  less than 2.3 which indicates that the majority of ice pan are approximately elliptically shaped based on the examples given in Table 2.5. The tendency for larger ice pans to be more irregularly shaped is consistent with the images and field observations that large ice pans are usually irregularly shaped rafts formed by small ice pans colliding and freezing together.

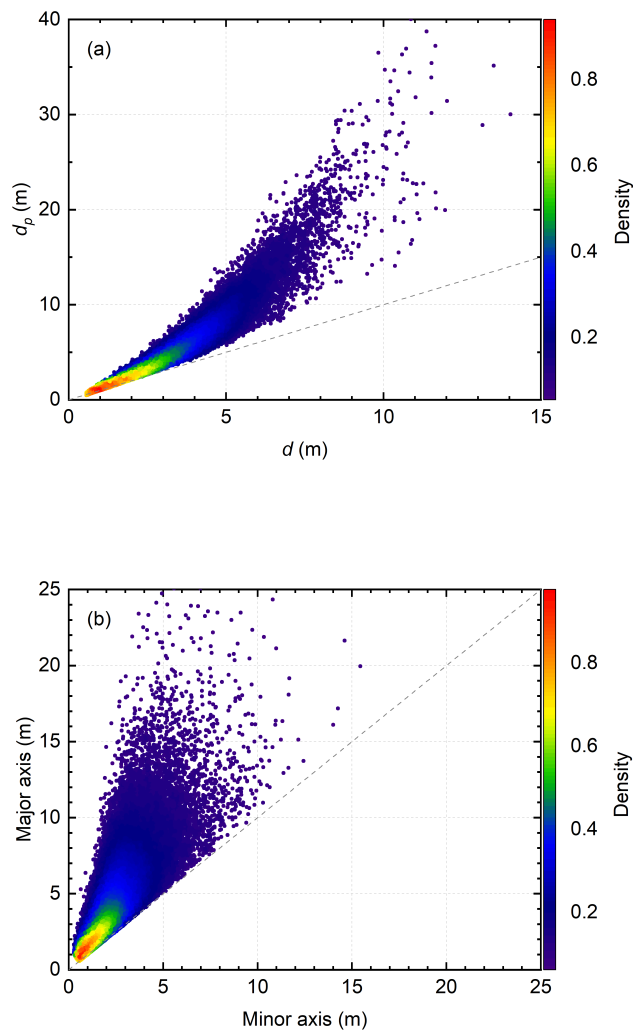


Figure 2.12: Scatter density plot illustrating (a) the relationship between  $d$  and  $d_p$ , and (b) the relationship between the major and minor axis length of the fitted ellipse for all detected ice pans combined.

## 2.5.4 Time Series of Ice Pan Properties

Time series of air temperature ( $T_a$ ), surface ice concentration ( $C_{ice}$ ), water temperature ( $T_w$ ), diameter ( $d$ ) and  $d_p/d$  were evaluated for all five years to investigate the evolution of ice pan properties. Figure 2.13 and Figure 2.14 present the time series during the 2016 and 2020 freeze-up periods, respectively to represent both continuous and interrupted surface ice processes. In these plots slushy pan periods or time periods when slushy pans were determined by visual examination to be dominant are shaded in grey. Time periods when negligible numbers of ice pan were detected (*i.e.* less than 100 per day) were excluded from the analysis of ice pan properties since including these would skew the daily ice pan statistics.

As shown in Figure 2.13a,  $C_{ice}$  was very small and the ice pans were mostly slushy prior to Nov. 30 in 2016 and after this it increased and the ice pans became mostly crusty. Figure 2.13b shows that there was a total of seven significant supercooling events during this freeze-up period. The first supercooling event was observed from midnight Nov. 19 to early Nov. 22 with a peak supercooling of  $-0.027$  °C, but fewer than 100 pans per day were observed during this event. The slushy pan period began on Nov. 24 and lasted for six days until Nov. 29. During this time period daily mean  $C_{ice}$  was less than 6 % and the average  $T_a$  was  $-2.68$  °C. Early on Nov. 29  $T_a$  decreased from close to zero to approximately  $-8$  °C and remained approximately constant for several days and as a result the crusty pan period started on Nov. 30 and lasted to the end of freeze-up on Dec. 6 - 7. A supercooling event began in the morning on Nov. 29 the day before the start of the crusty pan period and persisted for  $\sim 5$  days which might have contributed to the initiation of the crusty pan period. The water was supercooled for 85 % of the time when significant numbers of ice pans appeared on the water surface from Nov. 24 to Dec. 6. Figure 2.13c shows that both  $d_{mean}$  and  $(d_p/d)_{mean}$  were larger in the crusty pan period (1.65 m and 1.26) compared to the slushy pan period (1.23 m and 1.16). In Figure 2.13d, the daily  $d_{max}$  in the slushy pan period was  $\sim 4$  m but increased to 8 - 12 m when the ice pans became crusty. The daily  $(d_p/d)_{max}$  followed

a similar trend increasing from  $\sim 2$  in the slushy pan period to  $\sim 3$  in the crusty pan period. An increasing trend of both daily  $d_{max}$  and  $(d_p/d)_{max}$  prior to the stable ice cover formation was found and visual examination of the images confirmed that this was due to the formation of large rafts.

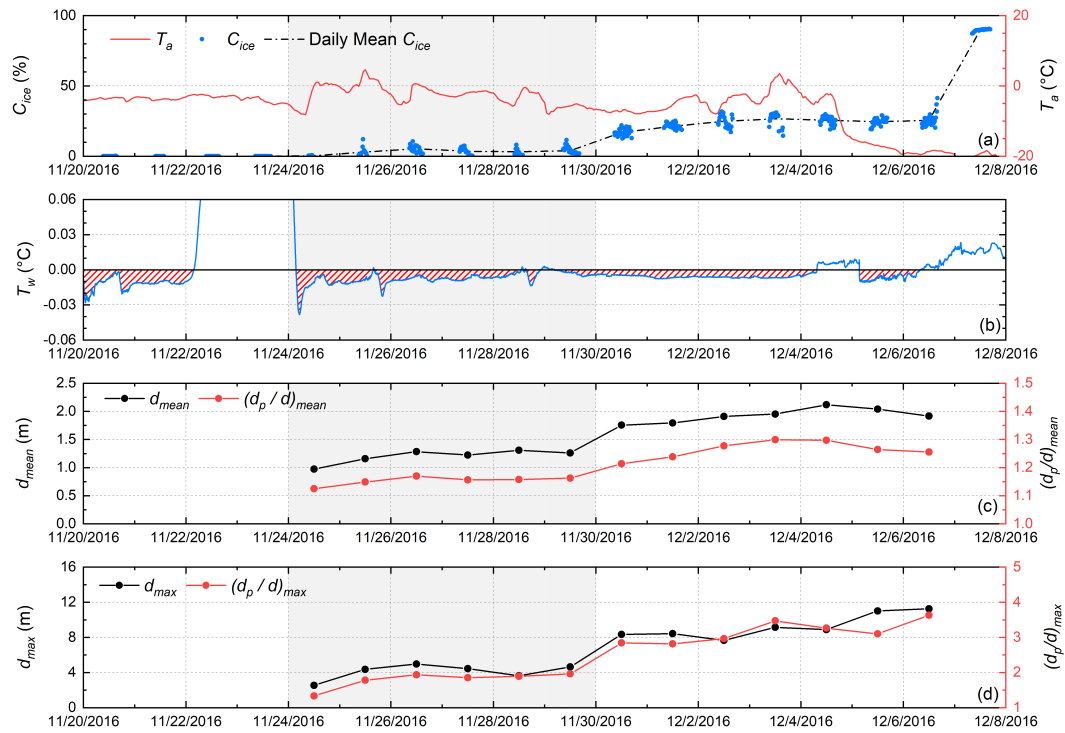


Figure 2.13: Time series of (a) surface ice concentration ( $C_{ice}$ ) and air temperature ( $T_a$ ), (b) upstream water temperature ( $T_w$ ) at Emily Murphy Park (red shading denotes supercooling events), (c) daily  $d_{mean}$  and  $(d_p/d)_{mean}$  and (d) daily  $d_{max}$  and  $(d_p/d)_{max}$  during 2016 freeze-up between Nov. 20 to Dec. 8, grey shaded area corresponds to slushy pan condition.

During the 2020 freeze-up, plotted in Figure 2.14, ice pans first appeared between Oct. 24 - 26 which is quite uncommon on the NSR in Edmonton since freeze-up typically begins several weeks later. During the first continuous ice pan event  $T_a$  was initially -10 °C and then ranged from 5 °C to -13 °C (Figure 2.14a) and three typical supercooling events with large peak supercooling up to -0.057 °C were observed (Figure 2.14b). From Oct. 27 to Nov. 7,  $T_a$  remained mostly above zero and supercooling stopped,

which interrupted freeze-up. On Nov. 7  $T_a$  decreased to  $-8\text{ }^\circ\text{C}$ , freeze-up resumed and then progressed similarly to 2016 during and seven significant supercooling events were observed. Ice pans were initially crusty on Nov. 9 then became slushy on Nov. 10 likely because  $T_w$  rose above zero for  $\sim 8$  hrs on that day (Figure 2.14b). Supercooling occurred for 86 % of the time when non-negligible numbers of ice pans appeared on the water surface in 2020. Figure 2.14c shows that both  $d_{mean}$  and  $(d_p/d)_{mean}$  were larger during crusty versus slushy pan periods, with the averaged  $d_{mean}$  for slushy pans and crusty pans of 1.39 m and 1.91 m, respectively. Figure 2.14d shows that both daily max pan properties increased prior to the stable ice cover formation, which is also similar to 2016.

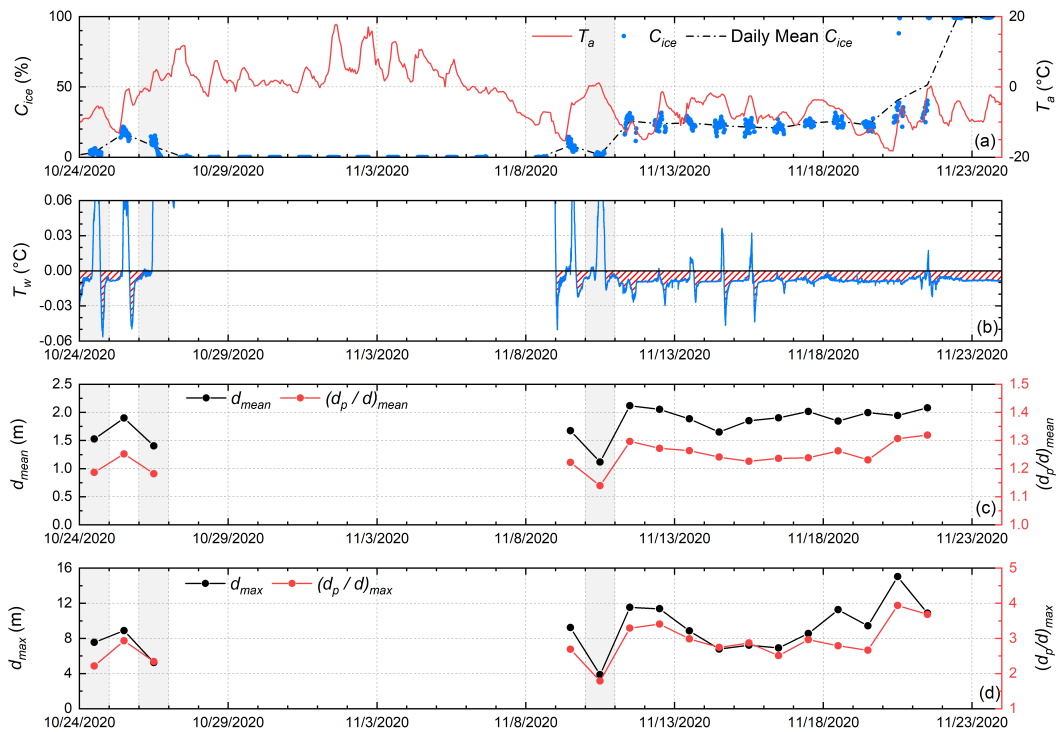


Figure 2.14: Time series of (a) surface ice concentration ( $C_{ice}$ ) and air temperature ( $T_a$ ), (b) upstream water temperature ( $T_w$ ) at Emily Murphy Park (red shading denotes Murphy supercooling events), (c) daily  $d_{mean}$  and  $(d_p/d)_{mean}$  and (d) daily  $d_{max}$  and  $(d_p/d)_{max}$  during 2020 freeze-up between Oct. 24 to Nov. 24, grey shaded area corresponds to slushy pan condition.

In general, the five-year time series results indicate that variations in  $C_{ice}$  were often correlated with fluctuations in  $T_a$  but typically lagged by a day or two. The daily mean ice pan diameter  $d_{mean}$  varied from 1 - 3 m and  $(d_p/d)_{mean}$  varied from 1.1 - 1.3. Both  $d_{mean}$  and  $(d_p/d)_{mean}$  were generally larger in the crusty pan period (1.85 m and 1.26) compared to the slushy pan period (1.40 m and 1.17). An increasing trend in both daily  $d_{max}$  and  $(d_p/d)_{max}$  prior to stable ice cover formation was observed which may indicate the formation of large rafts.

## 2.6 Conclusions

A deep learning based hybrid image processing algorithm consisting of image classification, rectification, segmentation and ice pan properties extraction was developed to quantify surface ice concentration and ice pan properties from oblique low resolution images. The accuracy of this method was first assessed by comparing to ground truth estimates of surface ice concentrations. The accuracy was determined to be 2.44 % and 2.06 % when the method was applied to ice cover and ice pan images, respectively. The accuracy of this method was further assessed by comparing surface ice concentrations estimated from much higher resolution and higher-quality BridgeCam images and the low-resolution EAS camera images. This comparison showed that estimates made from the high- and low-quality images on average had a mean absolute difference of 2.9 %. Therefore, it was concluded that an accuracy of 2 - 3 % was sufficiently accurate and that this method could be used for monitoring surface ice processes.

Images captured during five freeze-up seasons on the North Saskatchewan River were processed to illustrate the usefulness of this method for long-term monitoring of surface ice concentrations and ice pan properties during freeze-up under changing winter environments. Results clearly demonstrate that the method provides valuable information of both the long- and short-term temporal variations on river ice conditions as well as on the statistical properties of ice pans. A lognormal distribution was found to fit ice pan size distributions from all five years. The size and shape of ice pans

were observed to be relatively stable from year to year on the NSR. The diameter of ice pans ranged from 0.55 - 15.03 m with a mean size of 1.82 m. The ice pans are generally elliptical in shape with an average  $d_p/d$  of 1.25 and an average  $AR$  of 1.71. However, bigger ice pans can be more distorted and irregular in shape compared to smaller ice pans. Time series of water temperature and ice pan properties indicated, not surprisingly, that supercooling events and the appearance of ice pans typically coincided. Analysis showed that on the NSR the daily mean ice pan diameter  $d_{mean}$  varied from  $\sim 1$  m to  $\sim 3$  m and  $(d_p/d)_{mean}$  varied from 1.1 - 1.3, and that slushy ice pans were generally smaller than crusty pans (1.40 m versus 1.85 m) and slightly less irregular in shape. These types of detailed measurements of ice pan properties can be used to further our understanding of freeze-up processes in rivers and can be particularly valuable for discrete element modelling of surface ice processes (Zhai et al. 2022). It is noteworthy that the production and evolution of ice pans are not only dependent on the local meteorological variables, since older ice pans advecting through the AOI would be affected by geo-morphological, hydrological and meteorological conditions upstream. Therefore, further study that combines comprehensive spatial and temporal measurements of ice concentration, pan properties and key hydro-meteorological variables including detailed heat flux components is needed to better understand the ice pan evolution during the freeze-up process.

In conclusion, this study has demonstrated that surface ice characteristics can be accurately monitored using images captured by a distant oblique-viewed camera that is not intentionally set up for ice research. This finding may lead to intentional deployments of similar cameras for the purpose of river ice monitoring or the identification of existing cameras that have unintentionally been capturing suitable images of cold-region rivers that can then be analyzed. It should be possible to improve this method for example by training a state-of-the-art deep learning multi-class segmentation model to distinguish between crusty and slushy pans. Due to rapid advancement in the machine learning field it is important to review and evaluate the latest machine learning

methods routinely when attempting to increase the classification and segmentation accuracy. The proposed algorithm framework could also be applied to images captured using inexpensive game cameras provided the cameras are installed with care. They should be mounted sufficiently high and close enough to the riverbank so the water surface fills the field of view and they should be pointed directly north to minimize the effect of sunlight reflecting off the water surface. Further experiments assessing the impacts of installation heights on ice visibility in images may be helpful for planning field monitoring of surface ice conditions.

# Chapter 3

## Measurements of Frazil Ice Floccs in Rivers

### 3.1 Introduction

In northern rivers, individual frazil ice particles form when the water is turbulent and supercooled below its freezing point due to heat loss to the atmosphere. These suspended particles are ice crystals that are inherently adhesive in the supercooled water. As they are transported by the turbulent flow, they may collide with each other due to spatially varying particle velocities resulting from differential rising or due to spatially varying flow velocities created by turbulent eddies and boundary shear (Mercier 1985). Colliding particles may freeze together forming clusters of particles known as frazil floccs in a process called flocculation (Clark and Doering 2009). Frazil floccs increase in size either by the thermal growth of the crystals and/or by further aggregation of individual frazil ice particles or floccs. Once frazil floccs gain sufficient buoyancy they rise to the water surface forming surface ice pans or are deposited under existing surface ice contributing to their mass increase (Hicks 2016). In addition, turbulent flow may transport floccs to the river bed where they may adhere to the bed forming anchor ice (Kempema et al. 1993). Once the surface ice pan concentration is high enough, congestion of incoming ice pans will occur at certain locations where there is a flow constriction and a solid ice cover will form and propagate upstream (Beltaos 2013). The formation of a continuous solid ice cover insulates the flowing water from further heat loss to the at-

mosphere, thus preventing the occurrence of supercooling and the production of frazil ice until the ice cover thaws or breaks up (Beltaos 2013). Frazil flocs may cause serious problems at hydroelectric facilities and water treatment plants by adhering to water intake, trash racks and partially or fully blocking the flow (Ettema and Zabilansky 2004; Barrette 2021; Ghobrial et al. 2023). Therefore, it is important to obtain a better understanding of the properties of frazil flocs as well as their evolution to better model and predict their behavior.

As the constructing unit of frazil flocs, individual frazil ice particles have been investigated both in laboratory settings and field. These particles exhibit various forms including dendritic, needle, and irregular but are predominately disc-shaped with diameters ranging from 0.022 to 6 mm (McFarlane et al. 2017) and diameter-to-thickness ratios of 11 to 71 (McFarlane et al. 2014). A lognormal distribution can be used to describe the particle size distribution (Daly and Colbeck 1986; Clark and Doering 2006; McFarlane et al. 2015). During the principal supercooling period when the water temperature varies transiently, the time from the start of supercooling to when a steady residual supercooling water temperature is reached, the mean diameter of particles was found to first increase before reaching an approximately constant value (Clark and Doering 2006; McFarlane et al. 2015). At the same time the number concentration of suspended particles first increased slowly then more rapidly, peaking just after peak supercooling occurred (*i.e.* the minimum water temperature) (Ye 2002; McFarlane et al. 2015; Clark and Doering 2006). The rapid increase in particle concentration was attributed to secondary nucleation which refers to the formation of new crystals due to the presence of stable parent crystals (Evans et al. 1974). After peaking the particle concentration decreased as particles were removed via flocculation.

There have been a small number of laboratory studies that investigated the properties of frazil flocs as well as the flocculation process. Park and Gerard (1984) used artificial flocs fabricated from plastic discs to investigate the hydraulic characteristics of frazil flocs. They found that the sharp-edged floc surface resulted in a significantly higher

drag coefficient compared to a solid smooth sphere of the same size and density. Kempema et al. (1993) conducted racetrack flume experiments to investigate interactions of frazil and anchor ice with sediments. They observed that in freshwater frazil easily agglomerated into roughly spherical flocs up to 8 cm in diameter. Flocs that struck the bed tended to entrain sediments into their voids and become heavy and settle to the bottom in the shelter of ripples forming anchor ice. Reimnitz et al. (1993) observed the characteristics and behaviour of rising frazil in seawater using a stirred vertical tube or tank. They found that individual frazil crystals combine rapidly into flocs with diameters as large as 5 cm. The rise velocities of flocs ranged from 1 to 5 *cm/s* and rapidly rising large flocs induced small-scale turbulence. The porosities of the resulting surface slush accumulations ranged from 0.68 to 0.85, with an average of 0.77. Clark and Doring (2009) investigated frazil flocculation under different turbulence intensities using a counter-rotating flume. Results showed that higher levels of turbulence increased the rate of secondary nucleation, inhibited the formation of large flocs, and produced more dense flocs.

Schneck et al. (2019) measured the size and number concentration of frazil ice particles and flocs in water of varying salinity using a stirred frazil ice tank. Results showed that the mean floc size was 2.57 mm in freshwater and 1.47 mm in saline water and a lognormal distribution fit the floc size distributions closely. The floc porosity was estimated to vary from 0.75 to 0.86. Time series measurements of floc properties indicated that, in freshwater, the floc number concentration and mean size started to increase significantly just prior to peak supercooling, reached a maximum shortly afterwards. After that floc number concentration decreased slowly while the mean floc size continually increased very slowly during the principal supercooling period.

The above studies were all conducted in laboratory facilities that do not replicate the complex natural environment. Measurements of frazil flocs in supercooled rivers are needed to verify the laboratory results and improve numerical river ice process models. However, no detailed quantitative field measurements of the properties or

evolution of frazil flocs have been reported in the literature. The objective of this study was to determine the statistical characteristics and temporal evolution of floc sizes and concentrations, as well as to investigate the key factors affecting the properties of frazil flocs in rivers. A submersible high-resolution camera system was used to capture time-series images of frazil flocs. Images were analyzed to accurately determine floc sizes and concentrations. Key hydraulic and meteorological measurements were collected and air-water heat fluxes were estimated to investigate their influence on floc properties. Time series of floc size, number concentration and volumetric concentrations as well as size distributions measured in rivers during the principal and residual supercooling phase are presented for the first time.

## 3.2 Study Reaches

Measurements were conducted in three regulated Alberta rivers, the North Saskatchewan River (NSR) at Edmonton, the Peace River (PR) near Fairview, and the Kananaskis River (KR). Figure 3.1 shows the geographical locations of the study reaches, deployment sites and weather stations. The characteristics of the study reaches are summarized in Table 3.1. The turbulent dissipation rate in Table 3.1 was estimated using the listed slope as well as the average depth and width following Clark and Doering (2008). The three rivers are significantly different in terms of their size and hydraulic characteristics. The flow of the NSR is regulated by the Brazeau and Bighorn Dams which are  $\sim 233$  km and  $\sim 423$  km upstream of the Laurier Park site, respectively. A daily water level fluctuation of 0.3 to 0.4 m occurred in the study reach due to hydropeaking (McFarlane et al. 2017). The estimated turbulent dissipation rate is  $0.0058 \text{ m}^2/\text{s}^3$ . Freeze-up typically starts in early November and ends in early to late December with the formation of a static ice cover. However, the 2022 winter freeze-up progressed in a surprisingly rapid manner, starting on Nov 5, 2022, and ending just three days later on Nov 8, 2022.

PR has the largest average discharge, depth, and width of the three rivers (Table 3.1).

The estimated turbulent dissipation rate is  $0.0051 \text{ m}^2/\text{s}^3$  which is slightly smaller than NSR. The flow of PR is regulated by the W.A.C Bennett Dam and the Peace Canyon Dam which are  $\sim 309 \text{ km}$  and  $\sim 288 \text{ km}$  upstream of the Fairview water intake deployment site, respectively. These outflows at the dams are relatively warm water ( $\sim 6 \text{ }^\circ\text{C}$ ) during the winter, affecting the river thermal regime for up to  $550 \text{ km}$  downstream of the dams (Jasek and Pryse-Phillips 2015) which is  $\sim 250 \text{ km}$  downstream of the deployment site. Therefore, supercooling and frazil ice generation only occurs at the deployment site when the zero-degree isotherm is located upstream and ceases when it retreats downstream. This unique condition allows freeze-up to persist until the ice front reaches the Fairview intake site typically in mid-January.

KR is the smallest of the three rivers in terms of average discharge, depth, and width (Table 3.1). It has the largest turbulent dissipation rate with a value of  $0.2066 \text{ m}^2/\text{s}^3$ , which is not unexpected since KR is a small-steep river in the mountains. The flow is regulated by the Pocaterra Dam which is  $12$  and  $31 \text{ km}$  upstream of the Fortress and Evan Thomas deployment sites, respectively. In winter, a dramatic discharge fluctuation from  $\sim 1 \text{ m}^3/\text{s}$  to  $21 \text{ m}^3/\text{s}$  occurred daily in the study reach due to hydropeaking (Government of Alberta 2023). Low flows promote border ice formation reducing channel width, while high flows cause overtopping of existing ice and/or banks and prevent the formation of a complete ice cover. Without an ice cover to insulate the water, supercooling events and frazil generation occur when the air temperature is sufficiently cold.

### **3.3 Instrumentation, Methodology and Deployments**

A submersible camera system initially designed for imaging suspended frazil ice particles named “FrazilCam” (McFarlane et al. 2017) was modified in this study to image frazil flocs in the water column. Figure 3.2 shows the modified configuration of the FrazilCam system. A 36-megapixel Nikon D800 DSLR camera equipped with a Micro-Nikkor 60 mm f/2.8D lens was used to image underwater frazil ice particles and flocs.

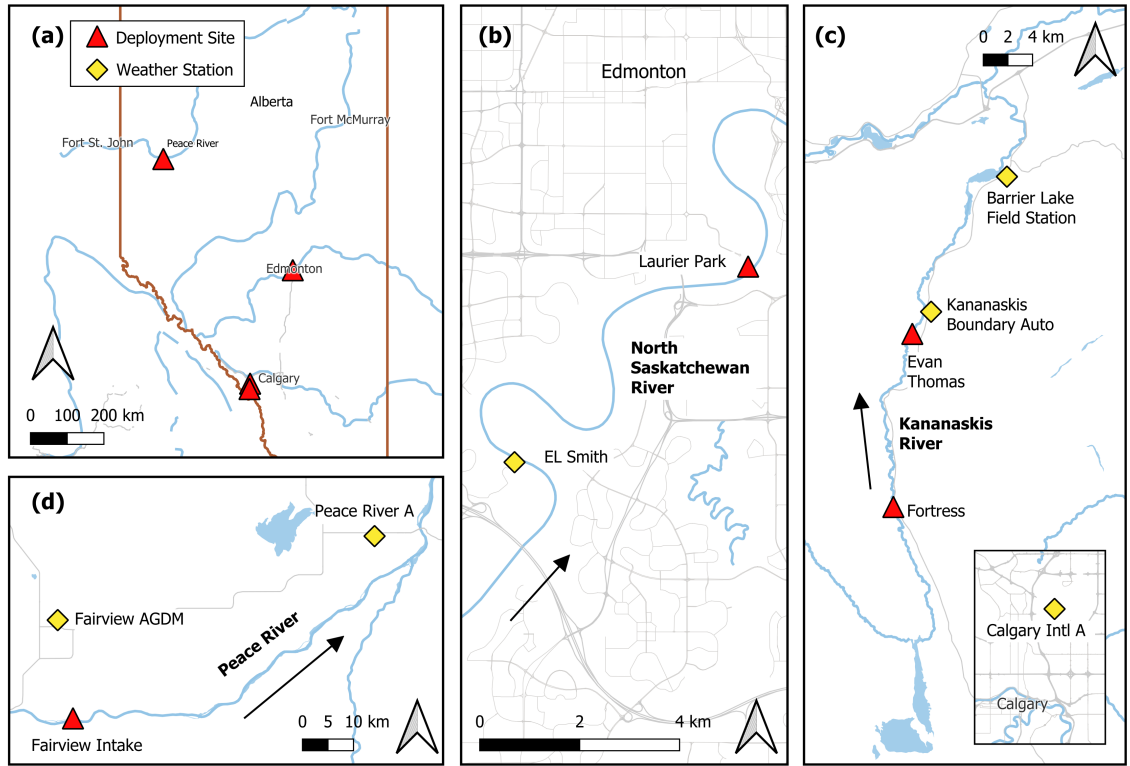


Figure 3.1: Maps showing (a) the locations of the deployment sites in Alberta, enlarged views of the locations on (b) the North Saskatchewan, (c) Kananaskis, and (d) Peace rivers.

Table 3.1: Summary of the study reach characteristics.

| River | Slope   | Average discharge ( $m^3/s$ ) | Average depth (m) | Average width (m) | Average $D_{100}$ of suspended sediment (mm) | Estimated turbulent dissipation rate ( $m^2/s^3$ ) |
|-------|---------|-------------------------------|-------------------|-------------------|--|--|
| NSR   | 0.00035 | 220                           | 1.40              | 136               | 0.50   | 0.0058   |
| PR    | 0.00025 | 1586                          | 2.56              | 227               | 0.68   | 0.0051   |
| KR    | 0.005   | 15                            | 0.61              | 32                | N/A  | 0.2066   |

*Note:* Slope, average discharge, average depth, and average width were obtained from Kellerhals et al. (1972); Average  $D_{100}$  of suspended sediments were computed from Water Survey of Canada historic size distribution data measured at North Saskatchewan River at Edmonton (05DF001) and Peace River at Dunvegan Bridge (07FD003) (Water Survey of Canada 2023).

The camera was enclosed in an Ikelite waterproof housing. Two 16 cm × 16 cm Cavi-sion linear glass cross-polarizing filters were mounted 3.6 cm apart, which is 1.6 times larger than the original configuration. A PVC enclosure with a brass fitting on the top was installed in between the camera lens and polarizing filters to prevent ice or debris from flowing through this region blocking the camera field-of-view (FOV). The brass fitting was used for hot water injection to melt any ice that was initially trapped inside the enclosure. A Nikon SB-910 Speedlight flash in a Subal SN-910 waterproof housing was used as the light source, and a 5 mm thick white acrylic board was placed in between the polarizers and flash to diffuse the light. The camera settings were determined by submerging the system in a laboratory tank filled with tap water and capturing images of a transparent plastic ruler placed inside the camera FOV. This yielded an ISO of 6400, aperture  $f/25$ , and a shutter speed of  $1/320$ . The configuration resulted in an image scale of  $25.6 \mu\text{m}$  per pixel and an average FOV of 11.6 cm by 15.6 cm which is 6 times larger than the original configuration. The reason for enlarging the FOV and increasing the gap between the polarizers was to enable larger flocs to pass through and fit within the FOV.

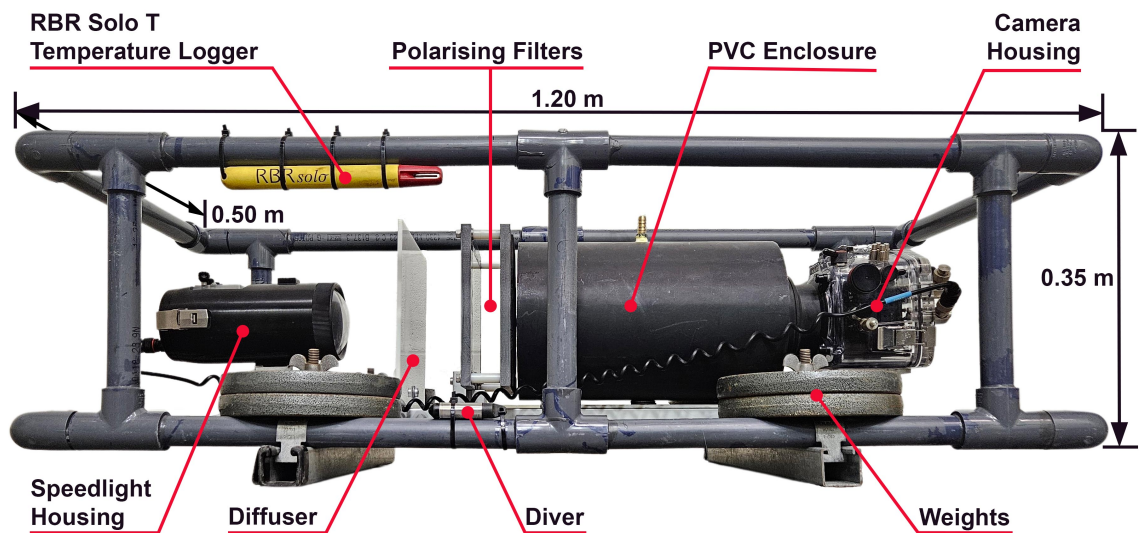


Figure 3.2: An image showing the configuration of the FrazilCam system.

At the start of each deployment, the camera was programmed to acquire 5 images

at 1 Hz every 9 s, 15 s, or 18 s depending on the field conditions until the battery was depleted. A longer sampling interval (*e.g.* 18 s) was chosen for some deployments to prolong the deployment duration with the goal of capturing a complete supercooling event. Just prior to deployment of the FrazilCam in the river, the polarizers were rinsed with hot saline water to prevent ice crystals from forming on them once submerged. The system was then quickly deployed in the river and the PVC enclosure was filled with hot fresh water from an elevated container. During deployments, anchor ice often formed on system components as shown in Figure 3.3 and ice that formed on the polarizers could obstruct the FOV of the camera. To prevent or mitigate this problem, the polarizers were inspected every 30 to 60 minutes and hot saline water was injected onto the polarizers to melt any ice crystals.



Figure 3.3: An image showing the ice accumulation on the FrazilCam system.

During each deployment, an RBR Solo T (accuracy  $\pm 0.002$  °C) temperature logger sampling every second was attached to the top of the frame to measure water temperature, and a Van Essen Diver (accuracy  $\pm 1$  cmH<sub>2</sub>O) water level logger sampling every 10 minutes was attached to the bottom of the frame to measure the water depth (Figure 3.2). The water depth during the PR deployments was measured using a wading rod since the Diver stopped working at that time. For all deployments the depth-averaged

water velocity was estimated using velocities measured adjacent to FrazilCam at 60 % of the water depth. During the 2021 winter, the water velocity was measured using a 2-MHz Nortek AquaDopp High Resolution Acoustic Doppler Current Profiler sampling every second with a blanking distance of 0.1 m and averaging every two minutes. For the rest of the deployments, the water velocity was measured using a SonTek Flow Tracker Handheld Acoustic Doppler Velocimeter (ADV) sampling every second for a total duration of 50 seconds.

Meteorological conditions for the NSR reach were measured by a weather station installed at the E.L. Smith water treatment plant, which is located ~90 m from the river bank and ~6 km upstream of Laurier Park site (Figure 3.1b). The weather station measures the air temperature, solar radiation, relative humidity, atmospheric pressure, wind speed and direction every minute and logs data every 10 minutes. An Apogee SN-500-SS net radiometer was deployed on the river bank at this location, measuring incoming and outgoing shortwave/longwave radiation every minute and logging data every 10 minutes. For the PR, 1-hour interval meteorological data were obtained from ECCC station Fairview AGDM (ID: 3072525) and 3-hour interval cloud coverage data was obtained from the closest ECCC station Peace River A (ID: 3075041) as shown in Figure 3.1d. For the KR, the Kananaskis Boundary Auto weather station operated by Alberta Forestry, Parks and Tourism (ACIS 2021) was used to obtain 1-hour interval air temperature, humidity, wind speed, and wind direction data. In addition, 1-hour solar radiation data was obtained from the University of Calgary Barrier Lake Field Station weather station (University of Calgary 2023), and 3-hour cloud coverage data was obtained from the closest ECCC station Calgary Intl A (ID: 3031092) as shown in Figure 3.1c. Table 3.2 summarizes the distance between weather stations and deployment sites. All weather stations are located within 30 km of their nearby deployment sites, except for those providing cloud coverage data for PR and KR.

The FrazilCam system was deployed a total of eleven times during the 2021 and 2022 freeze-up periods, images of the FrazilCam during two of the deployments are shown

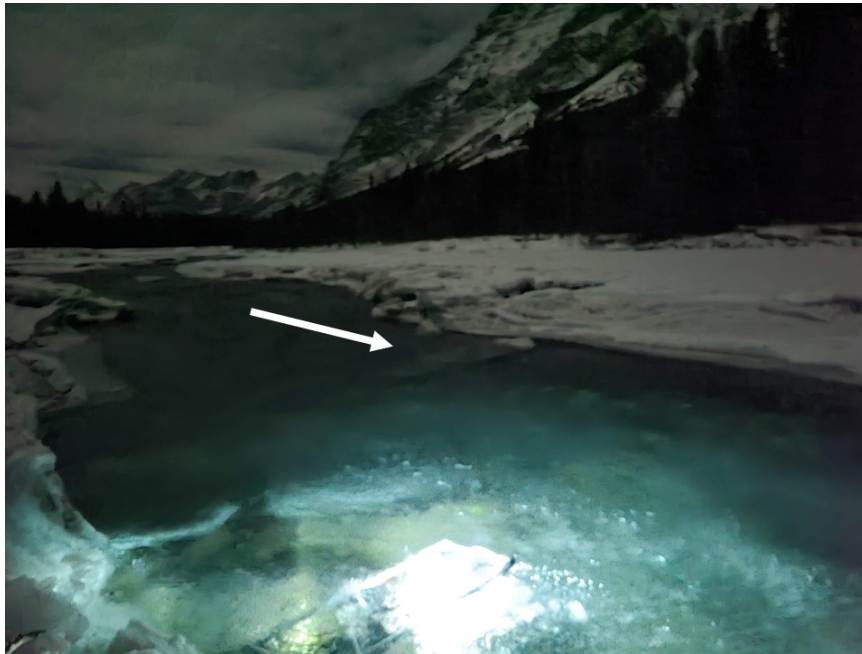
Table 3.2: The distances between weather stations and deployment sites.

| River | Deployment site | Distance - weather station   |
|-------|-----------------|--|
| NSR   | Laurier Park    | 6 km - E.L. Smith  |
| PR    | Fairview Intake | 18 km - Fairview AGDM; 68 km - Peace River A   |
| KR    | Evan Thomas     | 2 km - Kananaskis Boundary Auto; 15 km - Barrier Lake Field Station; 82 km - Calgary Intl A  |
|       | Fortress        | 16 km - Kananaskis Boundary Auto; 28 km - Barrier Lake Field Station; 88 km - Calgary Intl A |

in Figure 3.4. The image sampling protocols were 5 images at 1 Hz every 9 s for all NSR and KR-E1 deployments, for KR-F1 and KR-F2 5 images at 1 Hz every 15 s, and for all PR deployments 5 images at 1 Hz every 18 s. Table 3.3 lists the detailed location, date, time, number of images processed, and deployment number for each deployment. The mean air temperature  $\overline{T}_a$ , mean water depth  $\overline{d}$ , depth-averaged flow velocity  $\overline{U}$ , and the local Reynolds number  $Re$  computed from  $\overline{d}$  and  $\overline{U}$  are also presented in Table 3.3. Eight of eleven deployments started in the afternoon around 2 PM ~ 7 PM when the effect of solar radiation reduced decreasing heat gain of the water body, the time duration of deployments ranged from 1:48 to 3:21. As can be seen from Table 3.3, during these deployments  $\overline{T}_a$  ranged from -3.5 °C to -20.6 °C,  $\overline{d}$  ranged from 0.41 m to 1.24 m,  $\overline{U}$  ranged from 0.12 m/s to 0.36 m/s, and  $Re$  ranged from 44,866 to 160,714, respectively, indicating that frazil floc properties and concentrations were measured and analyzed over a wide range of meteorological and hydraulic conditions. The eleven deployments captured various phases of supercooling but NSR-L4 was the only deployment that captured a complete principal supercooling phase (*i.e.* from when the water temperature first dropped below zero to when an approximately stable residual temperature was reached).



(a)



(b)

Figure 3.4: Image of the FrazilCam deployed during (a) NSR-L6, and (b) KR-E1. The arrow indicates the flow direction.

Table 3.3: Summary of the FrazilCam deployments and site conditions including the number (#) of images captured, mean air temperature  $\bar{T}_a$ , mean water depth  $\bar{d}$ , depth averaged water velocity  $\bar{U}$ , and local Reynolds number  $Re$ .

| River | Date<br>(yyyy.mm.dd) | Time period<br>(hh:mm~hh:mm) | # of<br>processed<br>images | Site            | Deployment<br>No. | $\bar{T}_a$<br>(°C) | $\bar{d}$<br>(m) | $\bar{U}$<br>(m/s) | $Re$    |
|-------|----------------------|------------------------------|-----------------------------|-----------------|-------------------|---------------------|------------------|--------------------|---------|
| NSR   | 2021.12.3            | 16:41~18:49                  | 4,099                       | Laurier Park    | NSR-L1            | -7.2                | 0.89             | 0.21               | 104,297 |
|       |                      | 19:05~21:34                  | 4,797                       | Laurier Park    | NSR-L2            | -10.5               | 0.84             | 0.17               | 79,688  |
|       | 2021.12.9            | 14:46~17:09                  | 4,688                       | Laurier Park    | NSR-L3            | -3.5                | 1.24             | 0.19               | 131,473 |
|       | 2021.12.12           | 15:02~16:50                  | 3,495                       | Laurier Park    | NSR-L4            | -4.6                | 0.87             | 0.22               | 106,808 |
|       |                      | 17:08~19:31                  | 4,091                       | Laurier Park    | NSR-L5            | -9.2                | 0.86             | 0.20               | 95,982  |
|       | 2022.11.7            | 14:31~16:22                  | 3,596                       | Laurier Park    | NSR-L6            | -12.1               | 0.80             | 0.36               | 160,714 |
| PR    | 2022.12.12           | 10:40~13:57                  | 3,155                       | Fairview Intake | PR-F1             | -20.6               | 0.82             | 0.30               | 137,277 |
|       | 2022.12.13           | 9:41~13:02                   | 3,208                       | Fairview Intake | PR-F2             | -6.0                | 0.74             | 0.23               | 94,978  |
| KR    | 2023.1.29            | 18:00~20:02                  | 3,728                       | Evan Thomas     | KR-E1             | -15.8               | 0.41             | 0.22               | 50,335  |
|       | 2023.1.30            | 14:46~17:59                  | 3,379                       | Fortress        | KR-F1             | -11.1               | 0.55             | 0.30               | 92,076  |
|       | 2023.1.31            | 7:28~10:39                   | 3,610                       | Fortress        | KR-F2             | -13.3               | 0.67             | 0.12               | 44,866  |

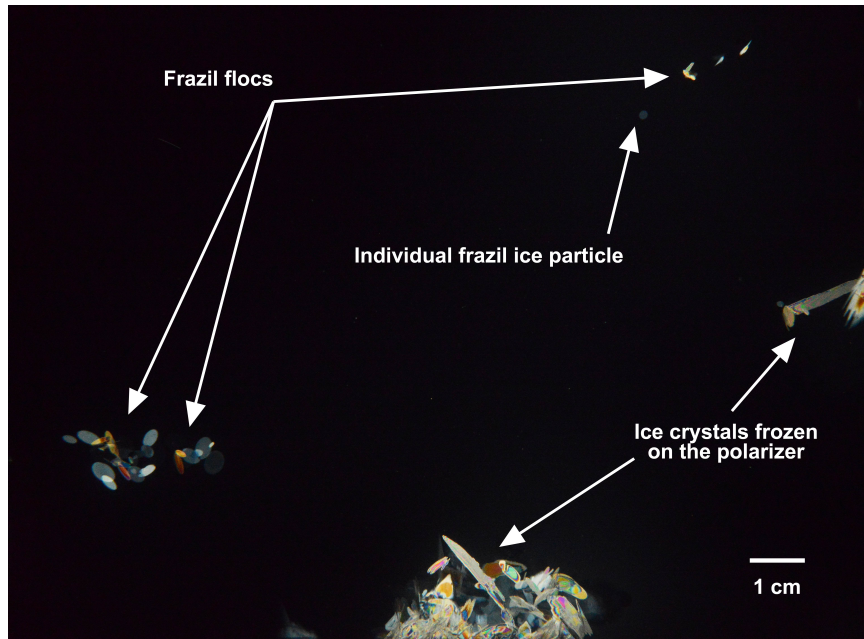
## 3.4 Data Processing

### 3.4.1 Image Processing

Figure 3.5a shows an example of a raw FrazilCam image with individual frazil ice particles, flocs, and ice crystals frozen on the polarizer. Frazil ice particles are predominantly disk-shaped (McFarlane et al. 2017) and therefore depending on their orientation appear in the images as shapes that vary from a line to a circle with the majority being ellipses. Flocs form through the aggregation of frazil ice particles, resulting in varying shapes depending on the number, shape, and size of attached particles. Ice crystals sometimes attached and froze to the surface of the polarizers despite the periodic hot saline water rinsing. These crystals may appear anywhere in the image, blocking certain regions of the FOV.

Figure 3.6 shows a flow chart of the image processing procedure used for extracting frazil floc properties. For each deployment, images were first manually inspected to exclude those taken when the polarizers were being rinsed, which constitutes 2 - 14 % of the total images captured. Each image was then processed using an iterative thresholding algorithm developed by McFarlane et al. (2014) to determine the location and extent of each object. Objects intersecting with the image boundary were eliminated, which also removed the ice crystals that were frozen near polarizer edges. For frozen ice crystals that did not intersect with the image boundary, the affected image area was removed either by cropping or masking, or a combination of both (Figure 3.6). The corresponding processed binary image is shown in Figure 3.5b.

The processed binary images were analyzed to compute each object's basic geometric characteristics such as area, perimeter, centroid, as well as the major and minor axis length of its fitted ellipse. The size  $S$  of both frazil particles and flocs was defined as the major axis length of its fitted ellipse (Clark and Doering 2009). The objects in the processed images may include small-suspended sediments that were thin enough to refract light, which may significantly distort the size distribution of frazil ice particles and flocs (McFarlane et al. 2017; Pei et al. 2022). McFarlane et al. (2019a) used a



(a)



(b)

Figure 3.5: An example of (a) a raw FrazilCam image captured on Dec 3, 2021, and (b) the corresponding processed binary image.

support vector machine (SVM) to distinguish between ice particles and sediments and compute accurate particle size distributions. However, this method requires ice-free sediment images at each site for site-specific SVM training, which is not possible for

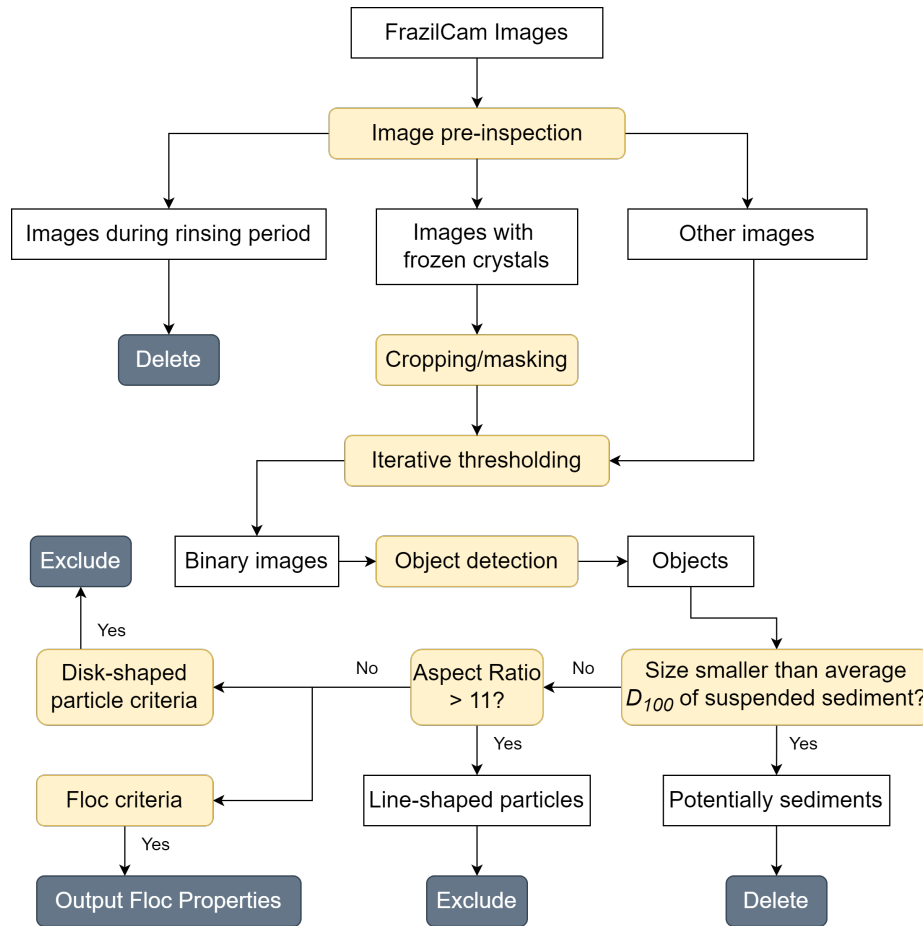


Figure 3.6: A flow chart showing the image processing procedure.

this study due to the lack of ice-free images at the PR and KR sites. Since this study focuses on flocs, which are considerably larger than particles, a simple cut-off criterion was used to minimize the effect of sediment particles in the images. Objects smaller than the average  $D_{100}$  of suspended sediment (see Table 3.1) in a given study reach were removed from the dataset (Figure 3.6). For the KR, since no suspended sediment size distribution measurements were available in the literature, the cut-off size was determined to be 0.27 mm, which is twice the average of seven mean sediment size measurements estimated from FrazilCam images by McFarlane et al. (2019b).

For each object, the following geometric parameters were used to classify the objects into either flocs or particles: the ratio of the object area to that of the fitted ellipse  $a/a_e$ , the absolute percentage difference between the object perimeter and its fitted ellipse

perimeter  $P_{\text{diff}\%}$ , the ratio of an object's fitted ellipse area to its ellipse perimeter divided by the ratio of the object's actual area to its perimeter  $(a_e/P_e)/(a/P)$  (McFarlane et al. 2014; Schneck 2018). Preliminary experiments found that flocs formed by a very small particle attaching to a significantly larger particle remain approximately elliptical since the boundary does not change significantly. As a result, comparing changes in overall area/perimeter with the fitted ellipse did not help with classification. Therefore, the form index was introduced to assess minor changes in object shape (Masad et al. 2001; Al-Rousan et al. 2007). The form index is calculated using the following equation:

$$\text{FI} = \sum_{\theta=0}^{\theta=360-\Delta\theta} \frac{|R_{\theta+\Delta\theta} - R_{\theta}|}{R_{\theta}} \quad (3.1)$$

where  $\theta$  is the directional angle and  $R$  is the radial length between the centroid of the particle and the boundary of the particle. The incremental change in angle  $\Delta\theta$  is set to  $2.81^\circ$ , dividing the particle boundary into 128 segments to factor in minor boundary changes. A perfectly circular object has an FI of 0, and FI will increase as an object's boundary becomes more irregular.

A total of 568 objects were manually labelled as either flocs (109) or disk-shaped frazil particles (459) to construct a test dataset to determine the optimal classification criteria of the aforementioned parameters. Results showed that  $\{a/a_e \geq 0.9 \text{ and } P_{\text{diff}\%} \leq 0.1 \text{ and } S \leq 6\}$  for disk-shaped particles, and  $\{(a/a_e < 0.9 \text{ or } P_{\text{diff}\%} > 0.15) \text{ and } ((a_e/P_e)/(a/P) > 1.1) \text{ and } \text{FI} \geq 6\}$  for flocs provided the optimum classification accuracy of 97.0 % and 92.7 % for particles and flocs, respectively. In NSR-L4 the camera lens was slightly out of focus due to an accidental jarring of the camera during deployment. However, because this was the only deployment that captured a complete principal supercooling event, additional processing was performed on these images to allow for their inclusion in the dataset. Visual examination and analysis of these images indicated that the blurriness predominantly affected the boundary clarity of dim objects with a mean pixel intensity less than 24 and did not significantly affect brighter objects. Therefore, an additional criterion was introduced

for NSR-L4 eliminating flocs with a mean pixel intensity less than 24. The rate of floc detection in the blurry images from deployment NSR-L4 was 4.1 flocs per minute and it was 4.4 flocs per minute in NSR-L5 which occurred immediately afterwards. Therefore, the additional criterion, applied to the blurry images, only slightly reduced the number of flocs detected.

In order to prevent line-shaped frazil ice particles from being misidentified as flocs, frazil particles in the shape of a line were first identified if the aspect ratio of the object (*i.e.* the ratio between the major and minor axis length) was greater than 11 based on minimum frazil ice particle aspect ratio measurements made by McFarlane et al. (2014) as shown in Figure 3.6. Then the classification criteria mentioned above were applied to the remaining objects to identify disk-shaped particles and flocs (Figure 3.6). After classification, the number of flocs  $N_T$ , mean floc size  $\overline{\mu_f}$ , standard deviation  $\sigma_f$ , 95<sup>th</sup> percentile of floc size  $S_{f95}$ , maximum floc size  $S_{fmax}$ , average floc number concentration  $\overline{C_{fn}}$ , and average volumetric concentration  $\overline{C_{fv}}$  for each deployment were computed. It is worth noting that the properties of frazil ice particles were not included in this study since the cut-off size likely eliminated up to 50 % of the particle population which would significantly skew the data. In addition, the mean floc size  $\mu_f$ , floc number concentration  $C_{fn}$ , floc volumetric concentration  $C_{fv}$  were computed for each image throughout a deployment, and a moving average over a period of 35 images was applied to the resulting time series to smooth the data. Note that the 35-image moving average was computed only if two or more non-zero values occurred in the window, if there were less than two non-zero values no average value was recorded. This created gaps in the moving average time series and the rationale for this is that two or more samples are required to compute a valid average value. The measuring volume used for the concentration calculations was the image FOV times the gap distance between the two polarizers. The volume of a frazil floc was assumed to be the volume of an ellipsoid with semi-axis lengths  $a$ ,  $b$ , and  $c$  where  $a$  and  $b$  were equal to the semi-major and semi-minor axis lengths of the floc's fitted ellipse, and  $c$  was equal to the average of  $a$

and  $b$  but no larger than the gap between the two polarizing filters. The volume of ice in a frazil floc  $V_f$  was estimated as:

$$V_f = \frac{4}{3}\pi abc(1 - \eta) \quad (3.2)$$

where  $\eta$  is the porosity of floc taken to be 0.8 (Schneck et al. 2019).

### 3.4.2 Heat Flux Analysis at the Water Surface

The net heat flux  $Q_n$  at the river surface is given by:

$$Q_n = Q_{sw} + Q_{lw} + Q_E + Q_H \quad (3.3)$$

where  $Q_{sw}$  is the net shortwave radiation;  $Q_{lw}$  is the net longwave radiation;  $Q_E$  is the latent heat flux;  $Q_H$  is the sensible heat flux. A positive sign denotes heat loss from the surface.  $Q_{sw}$  was calculated as:

$$Q_{sw} = -(1 - \alpha_{ws})Q_s \quad (3.4)$$

where  $Q_s$  is the measured incoming solar radiation;  $\alpha_{ws}$  is the albedo of water surface to solar radiation, taken to be 0.15 for this study following Howley (2021). The net longwave radiation  $Q_{lw}$  was calculated as:

$$Q_{lw} = Q_{lw}^{out} - (1 - \alpha_{wl})Q_{lw}^{in} \quad (3.5)$$

$$Q_{lw}^{out} = \varepsilon_w \sigma_{sb} T_{wk}^4 \quad (3.6)$$

where  $Q_{lw}^{out}$  is the outgoing longwave radiation emitted from the water;  $\alpha_{wl}$  is the albedo of water surface to longwave radiation, taken as 0.03 (Raphael 1962);  $\varepsilon_w$  is the emissivity of water taken as 0.97 (Ashton 2013);  $\sigma_{sb}$  is the Stefan-Blotzmann constant ( $5.67 \times 10^{-8} \text{ W}/(\text{m}^2\text{K}^4)$ );  $T_{wk}$  is the water surface temperature in  $K$ . Note that it was assumed that the water column was completely mixed and therefore the water temperatures that were measured at the top of the FrazilCam frame (*i.e.* not at the water surface) were used in Equation (3.6).  $Q_{lw}^{in}$  is the incoming longwave radiation which was measured

by a net radiometer for the NSR. For KR and PR,  $Q_{lw}^{in}$  is estimated using the following equations:

$$Q_{lw\_c}^{in} = \varepsilon_{ac} \sigma_{sb} T_{ak}^4 \quad (3.7)$$

$$\varepsilon_{ac} = 1.08 \left[ 1 - \exp(-e_a^{T_{ak}/2016}) \right] \quad (3.8)$$

$$e_s = 6.11 \exp\left(\frac{17.62T_a}{243.12 + T_a}\right) \quad (3.9)$$

$$e_a = RH \times e_s \quad (3.10)$$

$$Q_{lw}^{in} = Q_{lw\_c}^{in} (1 - N^4) + 0.952N^4 \sigma_{sb} T_{ak}^4 \quad (3.11)$$

where  $Q_{lw\_c}^{in}$  is the incoming longwave radiation under the clear sky;  $\varepsilon_{ac}$  is the clear sky atmospheric emissivity calculated using Equation (3.8) by Satterlund (1979);  $T_{ak}$  is the air temperature in  $K$ ;  $e_s$  and  $e_a$  are the saturated and actual vapour pressure of water, respectively;  $RH$  is the relative humidity;  $T_a$  is the air temperature in degree Celsius;  $N$  is the fractional cloud cover. Note that Equation (3.11) was developed by Konzelmann et al. (1994).

$Q_E$  was calculated using the equation suggested by Ryan et al. (1974) following Yang et al. (2023):

$$Q_E = \left[ 2.70 \left( \frac{T_{wk}}{1 - 0.378(e_s/P)} - \frac{T_{ak}}{1 - 0.378(e_a/P)} \right)^{\frac{1}{3}} + 3.2V \right] (e_s - e_a) \quad (3.12)$$

where  $P$  is the atmospheric pressure;  $V$  is the wind speed.  $Q_H$  was calculated from  $Q_E$  using Bowen's ratio  $B$  as follows:

$$B = \frac{C_a P}{0.622 l_v} \times \frac{T_s - T_a}{e_s - e_a} \quad (3.13)$$

$$Q_H = B Q_E \quad (3.14)$$

where  $C_a$  is the specific heat of air;  $l_v$  is the latent heat of vaporization;  $T_s$  is the surface water temperature. In a previous study, Yang et al. (2023) investigated various formulas

used to calculate incoming longwave radiation and the latent and sensible heat fluxes during freeze-up on the North Saskatchewan River in Alberta, and the combination of formulas (Equation (3.7) - Equation (3.14)) used in this study were the ones that provided the most accurate results in Yang et al. (2023). It is also worth noting that only hourly meteorological data were available for the KR and PR regions as described in Section 3.3. As a result, the heat fluxes were calculated on a 1-hour time interval for the KR and PR deployments, and for all the NSR deployments the heat fluxes were calculated on a 10-min time interval.

## 3.5 Results

### 3.5.1 Floc Shape, Size and Concentration

In Figure 3.7 images of typical shapes of frazil flocs observed during the different field deployments are presented. Flocs from NSR deployments (Figure 3.7a-b) were comprised predominantly of disc-shaped frazil ice particles of varying sizes frozen together. The floc shown in Figure 3.7b is representative of flocs observed during deployments NSR-L3 and NSR-L6. As can be seen, it was comprised of much smaller individual particles than the flocs observed during the rest of the NSR deployments (Figure 3.7a). Flocs from deployment PR-F1 (Figure 3.7c) were comprised of disc-shaped particles, irregular particles, and some needle-shaped particles. Flocs from deployment KR-E1 (Figure 3.7d) were formed primarily by densely aggregated irregular particles and some small disc-shaped particles. Flocs from deployments PR-F2, KR-F1 (Figure 3.7e), and KR-F2 (Figure 3.7f) were mostly comprised of disc-shaped and irregular particles, images of flocs from PR-F2 were not shown since they are similar to those shown in Figure 3.7e-f.

Table 3.4 presents the number of flocs  $N_T$ , mean size  $\overline{\mu}_f$ , standard deviation  $\sigma_f$ , 95<sup>th</sup> percentile and maximum of the floc size  $S_f$ , average floc number concentration  $\overline{C_{fn}}$ , and average volumetric concentration  $\overline{C_{fv}}$  for each deployment. The supercooling phase, the minimum water temperature  $T_p$ , and average net surface heat flux  $\overline{Q_n}$

are also presented. Deployments NSR-L1, NSR-L3, and NSR-L4 captured the principal supercooling phase (Principal), while the rest captured only the residual supercooling phase (Residual).  $T_p$  ranged from  $-0.021$  °C to  $-0.031$  °C for Principal deployments, and from  $-0.007$  °C to  $-0.017$  °C for Residual deployments. In all deployments  $\overline{Q_n}$  was positive indicating an overall heat loss.  $N_T$  varied significantly ranging from 442 to 187,288 with the largest  $N_T$  of 187,288 occurring during deployment KR-E1. The mean floc size  $\overline{\mu_f}$  ranged from 1.19 to 5.64 mm with an overall average of 3.8 mm and  $\sigma_f$  ranged from 0.88 to 5.03 mm.  $S_{f95}$  was greater than  $\sim 8$  mm except for deployments NSR-L3 and NSR-L6 with values of 4.44 mm and 2.47 mm, respectively. The largest value of  $S_{fmax}$ , 99.69 mm, was observed during KR-E1 which also had the largest number of flocs. The average floc number concentration  $\overline{C_{fn}}$  varied by three orders of magnitude from  $1.80 \times 10^{-4}$  to  $1.15 \times 10^{-1}$  cm<sup>-3</sup>, and the average floc volumetric concentration  $\overline{C_{fv}}$  over four orders of magnitude from  $2.05 \times 10^{-7}$  to  $4.56 \times 10^{-3}$ .

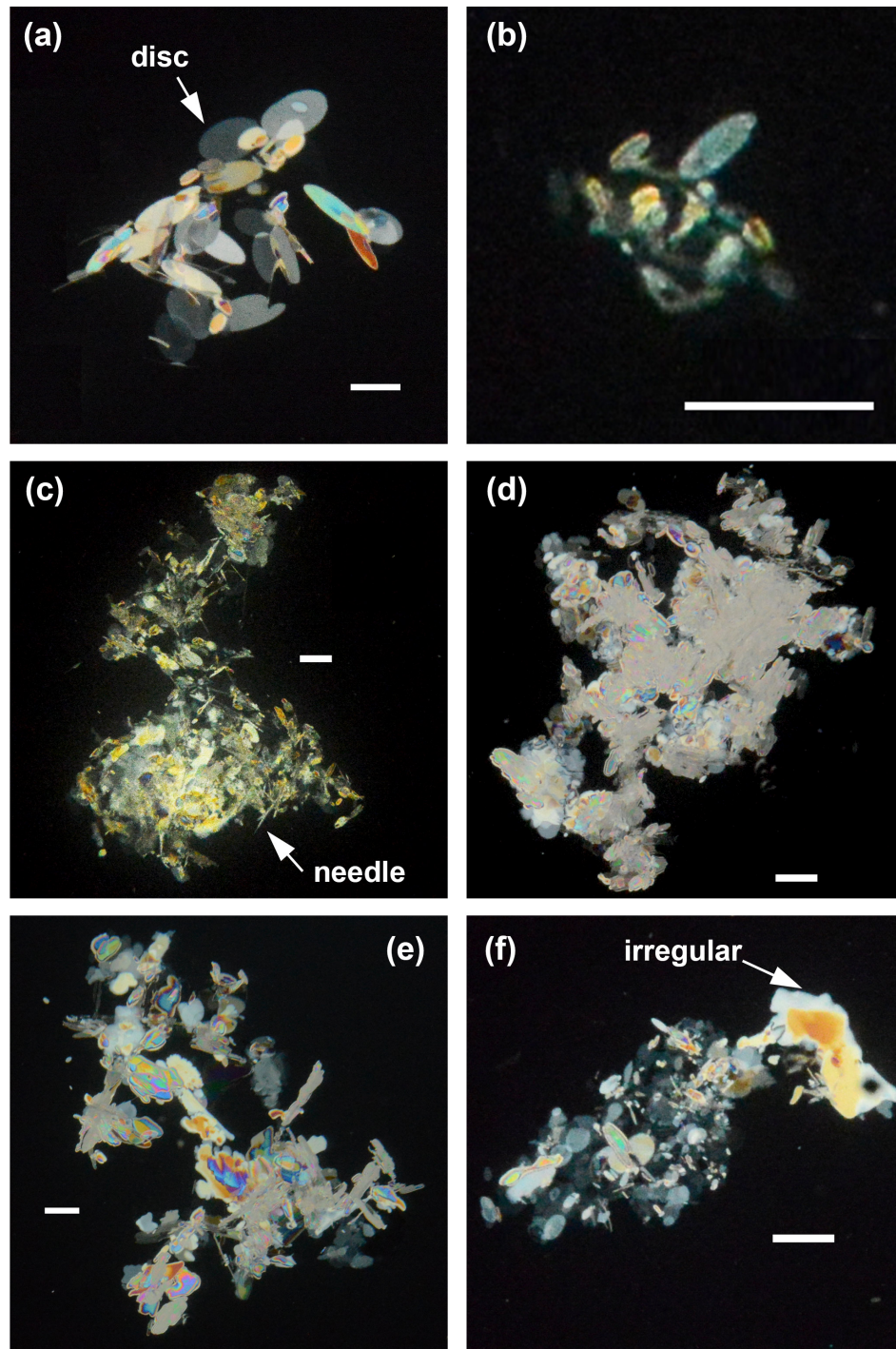


Figure 3.7: Images of frazil floccs of different sizes and shapes from the following deployments: (a) NSR-L1, (b) NSR-L6, (c) PR-F1, (d) KR-E1, (e) KR-F1, and (f) KR-F2. The white scale bar in each image represents a length of 3 mm. Note that in some images the surrounding ice particles were masked out to highlight the flocc at the centre of the image.

Table 3.4: Supercooling phase, minimum water temperature  $T_p$ , mean net surface heat flux  $\overline{Q_n}$ , number of flocs  $N_T$ , mean floc size  $\overline{\mu_f}$ , standard deviation  $\sigma_f$ , 95<sup>th</sup> percentile of floc size  $S_{f95}$ , maximum floc size  $S_{fmax}$ , average floc number concentration  $\overline{C_{fn}}$ , and average volumetric concentration  $\overline{C_{fv}}$  for each deployment.

| Deployment No. | Supercooling phase | $T_p$ (°C) | $\overline{Q_n}$ ( $W/m^2$ ) | $N_T$   | $\overline{\mu_f}$ (mm) | $\sigma_f$ (mm) | $S_{f95}$ (mm) | $S_{fmax}$ (mm) | $\overline{C_{fn}}$ ( $cm^{-3}$ ) | $\overline{C_{fv}}$ ( $cm^3/cm^3$ ) |
|----------------|--------------------|------------|------------------------------|---------|-------------------------|-----------------|----------------|-----------------|-----------------------------------|-------------------------------------|
| NSR-L1         | Principal          | -0.021     | 183.3                        | 2,428   | 4.33                    | 3.08            | 8.73           | 89.58           | $9.65 \times 10^{-4}$             | $1.39 \times 10^{-5}$               |
| NSR-L2         | Residual           | -0.009     | 199.5                        | 879     | 3.70                    | 2.31            | 7.54           | 24.05           | $2.72 \times 10^{-4}$             | $1.39 \times 10^{-6}$               |
| NSR-L3         | Principal          | -0.023     | 95.4                         | 839     | 1.87                    | 1.31            | 4.44           | 9.02            | $3.06 \times 10^{-4}$             | $2.05 \times 10^{-7}$               |
| NSR-L4         | Principal          | -0.031     | 110.3                        | 442     | 4.50                    | 2.45            | 8.37           | 18.53           | $1.80 \times 10^{-4}$             | $1.21 \times 10^{-6}$               |
| NSR-L5         | Residual           | -0.016     | 121.8                        | 631     | 3.50                    | 2.57            | 8.40           | 14.31           | $2.60 \times 10^{-4}$             | $1.19 \times 10^{-6}$               |
| NSR-L6         | Residual           | -0.017     | 157.5                        | 143,097 | 1.19                    | 0.88            | 2.47           | 47.16           | $6.75 \times 10^{-2}$             | $2.99 \times 10^{-5}$               |
| PR-F1          | Residual           | -0.009     | 318.8                        | 2,250   | 3.43                    | 3.72            | 9.16           | 53.35           | $1.11 \times 10^{-3}$             | $1.84 \times 10^{-5}$               |
| PR-F2          | Residual           | -0.007     | 107.4                        | 1,247   | 4.25                    | 5.03            | 13.60          | 53.81           | $5.63 \times 10^{-4}$             | $1.68 \times 10^{-5}$               |
| KR-E1          | Residual           | -0.008     | 243.3                        | 187,288 | 5.64                    | 4.79            | 14.28          | 99.69           | $1.15 \times 10^{-1}$             | $4.56 \times 10^{-3}$               |
| KR-F1          | Residual           | -0.010     | 122.4                        | 23,670  | 4.43                    | 3.86            | 10.69          | 81.38           | $1.05 \times 10^{-2}$             | $2.32 \times 10^{-4}$               |
| KR-F2          | Residual           | -0.011     | 275.2                        | 15,151  | 4.69                    | 4.08            | 11.89          | 68.37           | $6.62 \times 10^{-3}$             | $1.59 \times 10^{-4}$               |

### 3.5.2 Floc Size Distribution

In Figure 3.8, plots of the frazil floc size distribution as well as fitted lognormal distribution curves for four deployments are presented. All of the size distributions obtained from NSR deployments closely resemble deployment NSR-L1 shown in Figure 3.8a, except for deployment NSR-L6 shown in Figure 3.8b. Size distributions from the KR and PR are well represented by deployments KR-F1 and PR-F1 which are shown in Figure 3.8c and Figure 3.8d, respectively. It can be seen from Figure 3.8 that a theoretical lognormal distribution is a reasonable fit to all of the size distributions but a particularly good fit for deployment KR-F1. This may be attributed to the order-of-magnitude larger sample size for KR-F1 (23,670) compared to NSR-L1 (2,428) and PR-F1 (2,250). The size distribution for NSR-L6 shown in Figure 3.8b has the most flocs of the four deployments plotted with a sample size of 143, 097 but it does not fit a lognormal distribution as closely as the others. This is because the distribution was cut off at 0.5 mm to eliminate sediment particles. A similar condition can also be observed for PR-F1 shown in Figure 3.8d where the cut-off was 0.68 mm. Note that the cut-offs were applied to all size distributions but only impacted the distribution significantly if there were a significant number of smaller flocs detected.

### 3.5.3 Time Series

Time series plots of water and air temperatures  $T_w$  and  $T_a$ , heat flux  $Q$ , floc mean size  $\mu_f$ , floc number concentration  $C_{fn}$ , and floc volumetric concentration  $C_{fv}$  for deployments NSR-L4, KR-F1, and PR-F2 are presented in Figure 3.9, Figure 3.10 and Figure 3.11, respectively (Note that similar time series plots for the other eight deployments are presented as Figure A.1 - Figure A.8 in Appendix A). Deployment NSR-L4 occurred during the principal supercooling phase and is the only deployment that captured the entire principal supercooling phase, while KR-F1 and PR-F2 captured the middle and end of the residual supercooling phase, respectively.

During NSR-L4 (Figure 3.9a) supercooling started at 15:25 and after that  $T_w$  de-

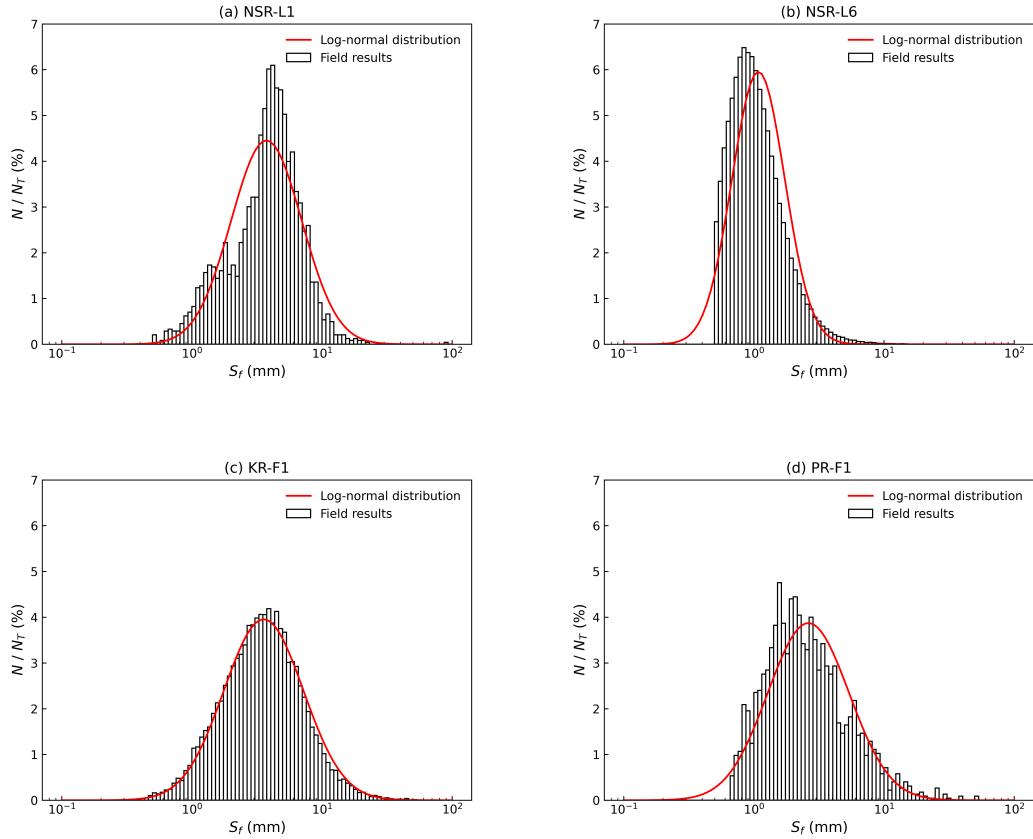


Figure 3.8: Distributions of floc size  $S_f$  for deployments (a) NSR-L1, (b) NSR-L6, (c) KR-F1, and (d) PR-F1. The red line denotes a fitted lognormal distribution,  $N$  is the number of flocs in each bin, and  $N_T$  is the total number of flocs.

creased almost linearly at a cooling rate of  $-0.0009\text{ }^\circ\text{C}/\text{min}$ , reached a  $T_p$  of  $-0.031\text{ }^\circ\text{C}$  (*i.e.* peak supercooling) at 16:02 and then started to increase and reached a stable residual temperature of  $-0.010\text{ }^\circ\text{C}$  at 16:37.  $T_a$  decreased from  $-1.7$  to  $-7.2\text{ }^\circ\text{C}$  with an average of  $-4.6\text{ }^\circ\text{C}$ . Figure 3.9b shows that the net heat flux  $Q_n$  increased from  $26\text{ W}/\text{m}^2$  to  $150\text{ W}/\text{m}^2$  primarily due to the decrease in the magnitude of shortwave radiation  $Q_{sw}$ . The rest of the heat flux components remained positive (heat loss) and relatively stable throughout the deployment, with  $Q_{lw}$  being the dominant component. In Figure 3.9c  $\mu_f$  began increasing significantly  $\sim 7$  minutes before the peak supercooling temperature was reached, reaching a maximum of  $7.8\text{ mm}$   $\sim 37$  minutes after peak supercooling, then it decreased to  $\sim 6\text{ mm}$  and remained approximately constant af-

terwards. Figure 3.9d shows that significant numbers of frazil particles were detected  $\sim 15$  minutes before peak supercooling with  $C_{fn}$  values below  $2 \times 10^{-4} \text{ cm}^{-3}$ . At  $\sim 2$  minutes before peak supercooling  $C_{fn}$  increased rapidly and peaked  $\sim 30$  minutes after peak supercooling at a value of  $9.3 \times 10^{-4} \text{ cm}^{-3}$  and then decreased to  $2 \times 10^{-4} \text{ cm}^{-3}$  at the end of the deployment. Figure 3.9e shows that  $C_{fv}$  only increased notably after peak supercooling and reached a value of  $8.8 \times 10^{-6}$   $\sim 30$  minutes after the peak supercooling. After that it decreased before spiking to  $1.6 \times 10^{-5}$   $\sim 38$  minutes after the peak supercooling and then decreased to  $1.7 \times 10^{-6}$  at the end. An examination of the images showed that the spike was caused by several large flocs up to 18.5 mm in size.

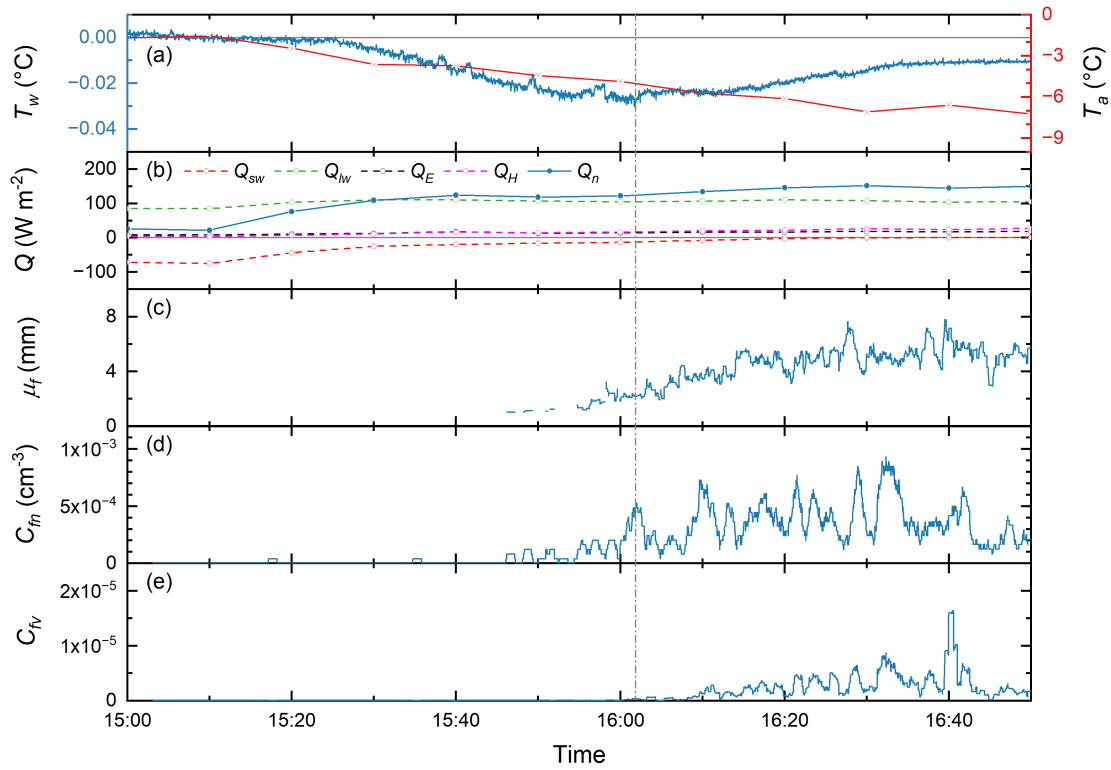


Figure 3.9: Time series of (a) water and air temperatures  $T_w$  and  $T_a$ , (b) heat flux  $Q$ , (c) floc mean size  $\mu_f$ , (d) floc number concentration  $C_{fn}$  and (e) floc volumetric concentration  $C_{fv}$  for deployment NSR-L4 on December 12, 2021. The vertical dashed grey line indicates the time when the peak supercooling temperature is achieved.

During KR-F1,  $T_w$  fluctuating continuously around  $-0.008 \text{ }^\circ\text{C}$ , except for one anomalous spike that occurred at 17:03 (Figure 3.10a), which was caused by ice contacting

the sensor when the polarizers were being rinsed. Additionally, periodic upward spikes with a period of 1 minute and magnitude of  $\sim 0.001$  °C were visible on the plot. While the cause of these spikes remains uncertain, it is worth noting that their magnitude falls within the range of accuracy of the sensor. The air temperature was relatively stable with  $T_a$  varying between -10 to -12 °C. In Figure 3.10b,  $Q_n$  rose during the deployment from  $-2$   $W/m^2$  to  $261$   $W/m^2$  largely due to the decrease in the magnitude of  $Q_{sw}$ . Note that the heat flux components here were computed on a 1-hour time interval. In Figure 3.10c-e, there are gaps in the data during these time periods 15:33 - 15:38, 16:17 - 16:23, 16:58 - 17:04, and 17:34 - 17:39, that are visible as short time series segments with zero slope. These were created when the images collected during the time periods when the polarizers were being rinsed were removed from the dataset. In Figure 3.10c,  $\mu_f$  fluctuated around  $\sim 4$  mm before significantly increasing at 17:40, eventually reaching 5.9 mm by the end of the deployment. Similar trends are evident in Figure 3.10d-e for  $C_{fn}$  and  $C_{fv}$ , respectively. At 17:41  $C_{fn}$  started to increase significantly and reached a peak value of  $4.5 \times 10^{-2}$   $cm^{-3}$  at 17:53 while  $C_{fv}$  started to increase significantly at 17:50 and eventually peaked at a value of  $2.8 \times 10^{-3}$ . A hydropeaking wave arrived at the Fortress site at 17:25 increasing the depth by 19 % by the end of the deployment and causing rapid increases in floc size and concentration.

During deployment PR-F2,  $T_w$  was initially at  $-0.006$  °C but then increased above zero at 10:21, and eventually reached  $0.033$  °C at the end of the deployment (Figure 3.11a).  $T_a$  followed a similar trend to  $T_w$  rising from  $-7.6$  to  $-4.1$  °C. The net heat loss  $Q_n$  steadily decreased from  $165$   $W/m^2$  to  $12$   $W/m^2$  (Figure 3.11b) due to an increase in the magnitude of  $Q_{sw}$ . In Figure 3.11c  $\mu_f$  fluctuated between 1 mm and 10 mm during the deployment with an average of 4 mm. In Figure 3.11d-e the time series of number and volume concentrations did not exhibit significant trends.  $C_{fn}$  ranged from  $4.1 \times 10^{-5}$   $cm^{-3}$  to  $2.4 \times 10^{-3}$   $cm^{-3}$  with an average of  $5.6 \times 10^{-4}$   $cm^{-3}$  while  $C_{fv}$  was negligible most of the time with occasional spikes up to  $4.2 \times 10^{-4}$ . One spike that occurred at 10:39 caused both  $C_{fn}$  and  $C_{fv}$  to reach their peak values. Visual exami-

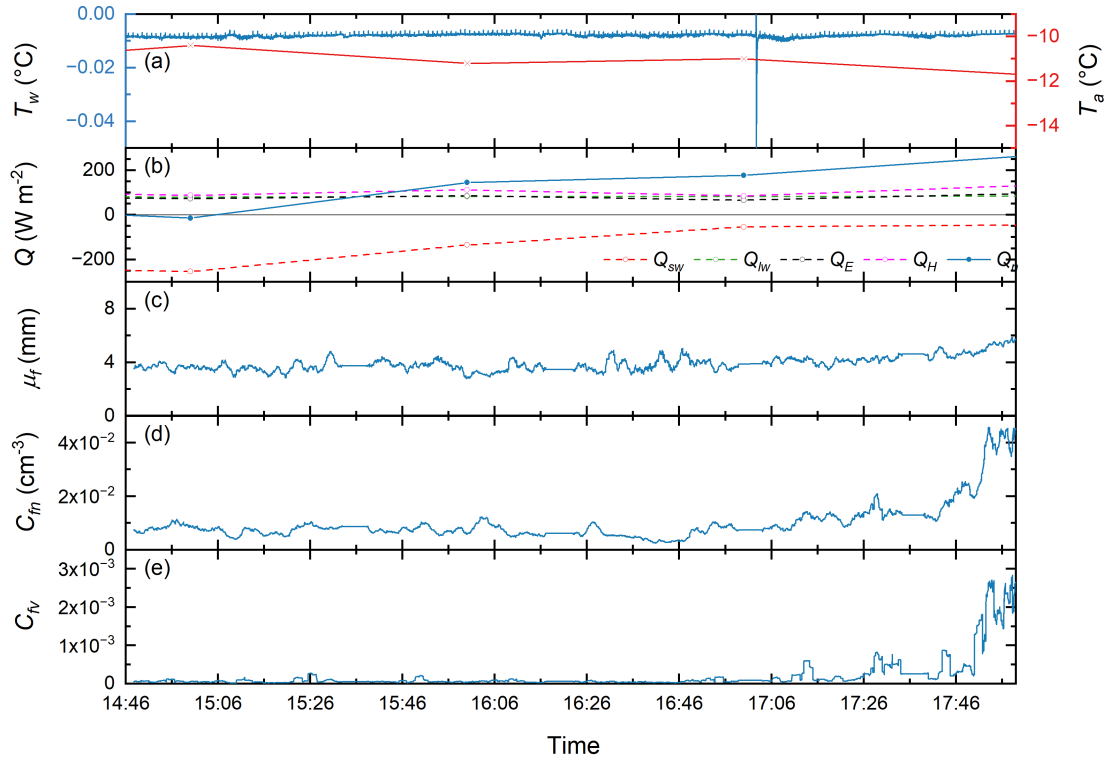


Figure 3.10: Time series of (a) water and air temperatures  $T_w$  and  $T_a$ , (b) heat flux  $Q$ , (c) floc mean size  $\mu_f$ , (d) floc number concentration  $C_{fn}$  and (e) floc volumetric concentration  $C_{fv}$  for deployment KR-F1 on January 30, 2023.

nation of the images shows that at this time the number of flocs increased significantly for three consecutive images and this was possibly caused by a large floc colliding with the camera frame and fracturing.

### 3.6 Discussion

Images of typical frazil flocs shown in Figure 3.7 illustrate the complexity of their morphology, which encompasses various ice crystal shapes, including disc-shaped, needle-shaped, and irregular particles. Disc-shaped ice particles were observed in flocs from all three rivers but were most pronounced in the NSR where flocs were almost all formed by disc-shaped particles of different sizes (Figure 3.7a-b). The growth of frazil ice in supercooled water is limited by the diffusive removal of the latent heat of solidification from the ice-water interface and by the slow attachment kinetics in the perpendicular

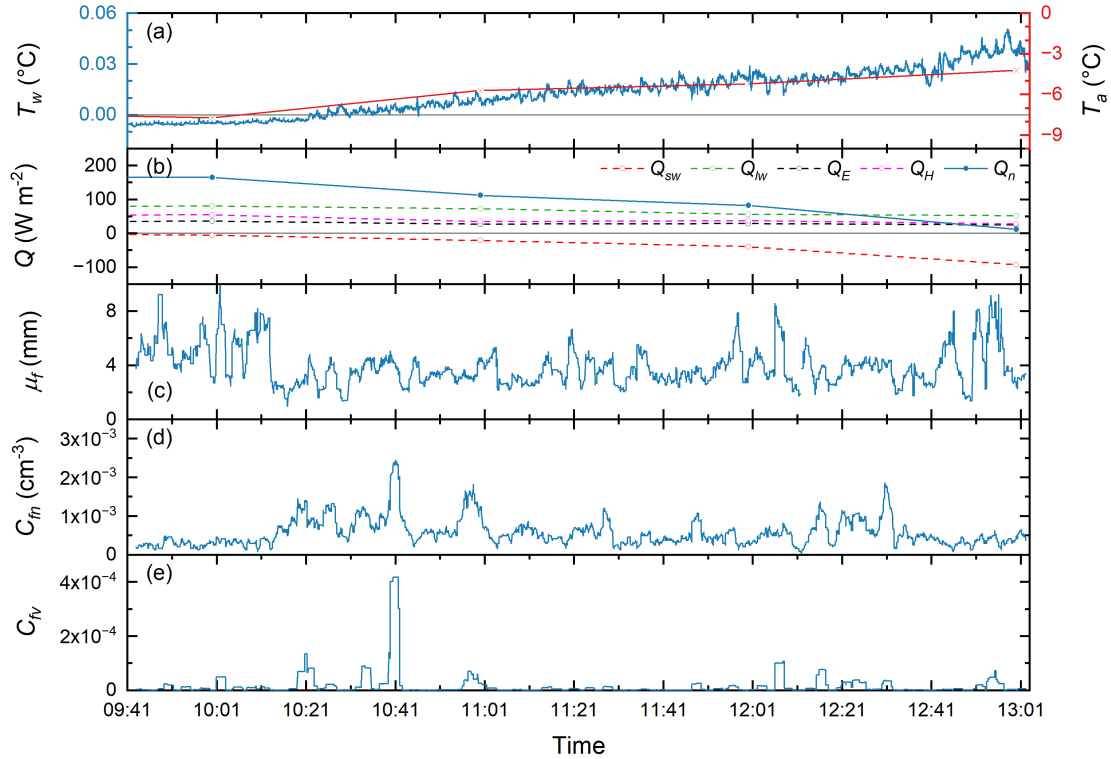


Figure 3.11: Time series of (a) water and air temperatures  $T_w$  and  $T_a$ , (b) heat flux  $Q$ , (c) floc mean size  $\mu_f$ , (d) floc number concentration  $C_{fn}$  and (e) floc volumetric concentration  $C_{fv}$  for deployment PR-F2 on December 13, 2022.

direction, which leads to the formation of disc-shaped particles (Mullins and Sekerka 1964; Rees Jones and Wells 2015). Flocs containing needle-shaped crystals as shown in Figure 3.7c were observed during deployment PR-F1 which had a very low mean air temperature of  $-20.64$  °C. These types of crystals have been found to form primarily at the surface of supercooled water (Hallett 1960; Clark and Doering 2002). The cold air temperature during deployment PR-F1 may have promoted the growth of these needle-shaped particles at the water surface before they were entrained in the water column and subsequently attached to flocs. Irregular particles were observed in flocs from both the KR and PR, most pronouncedly in deployment KR-E1 as shown in Figure 3.7d. Irregularly shaped particles are formed by unstable disk growth which is known to be caused by the formation of temperature gradients in the water surrounding the particles (Kallungal and Barduhn 1977). This suggests that during the KR and

PR deployments, frazil ice particles probably spent some time in relatively quiescent water where the turbulence intensity was so low that temperature gradients could form in the water surrounding the particles. Another possibility is that the particles were temporarily transported to the river surface exposing them to cold air, which may also lead to unstable disk growth. In addition, broken fragments of skim ice or border ice that were entrained into the water column are another possible source of irregular particles in flocs. Clark and Doering (2009) observed in the laboratory that flocs could become denser over time when the turbulence intensity was higher. During deployment KR-E1, although the locally measured depth-averaged velocity near the FrazilCam was relatively low at  $0.22\text{ m/s}$ , the water velocity  $\sim 70\text{ m}$  upstream of the deployment site was visually observed to be very turbulent due to the presence of four groins and a narrow channel width. Therefore, this may have contributed to the denser flocs that were observed during this deployment.

The data presented in Table 3.4 and Figure 3.8 are the first quantitative measurements of frazil floc sizes and concentrations in rivers. The mean floc size averaged over all deployments was  $3.80\text{ mm}$ , which was close to the mean values observed for most of the individual deployments except for deployments NSR-L3, NSR-L6, and KR-E1 which had mean floc sizes of  $1.87$ ,  $1.19$ , and  $5.64\text{ mm}$ , respectively. As noted in Section 3.5.1, flocs observed during deployments NSR-L3 and NSR-L6 were comprised of much smaller disc-shaped individual particles (Figure 3.7b) than the rest of the deployments (Figure 3.7a). Deployment NSR-L3 took place during a principal supercooling event in which the observed small frazil ice particles were likely newly formed and still growing, which could be the reason why the flocs were smaller and comprised of significantly smaller particles. In addition, deployment NSR-L3 took place as the crest of a hydropeaking wave was passing the site that resulted in a mean water depth of  $1.24\text{ m}$  which is  $37\%$  to  $55\%$  larger than the depths during the other NSR deployments (Table 3.3). The significantly higher water depth reduced the fractional height where the images were collected, which could also result in smaller floc sizes. This would be

consistent with measurements by Reimnitz et al. (1993) that showed that larger flocs have higher rise velocities. Deployment NSR-L6 occurred during the 2022 freeze-up season, which was the shortest freeze-up in  $\sim 10$  years lasting only three days. Significantly smaller flocs were observed during this deployment (see Figure 3.7b) and this may be because smaller relatively young flocs were generated during this rapid freeze-up process. The largest mean floc size, maximum floc size and largest concentration (see Table 3.4) were observed during deployment KR-E1 (Figure 3.7d). As discussed previously the particles that formed flocs during KR-E1 included irregularly shaped particles and this could have resulted in larger flocs compared to flocs formed entirely by disc-shaped particles.

The mean floc size and standard deviation ranged from 1.19 to 5.64 mm, and 0.88 to 5.03 mm, respectively as shown in Table 3.4. The 95<sup>th</sup> percentile of floc size ranged from 2.47 to 14.28 mm, and the largest flocs found was 99.69 mm in size. Schneck et al. (2019) conducted laboratory experiments in a frazil ice tank with an average turbulent dissipation rate of  $0.034 \text{ m}^2/\text{s}^3$  which falls within the range of the values estimated in the three rivers in this study ( $0.005 - 0.207 \text{ m}^2/\text{s}^3$ ). They found that in freshwater the size distribution of flocs followed a lognormal distribution and the mean size, 95<sup>th</sup> percentile of floc size, and maximum size were 2.57 mm, 6.91 mm, and 95.1 mm, respectively. The mean and 95<sup>th</sup> percentile sizes fall within the range of the values observed in this study. However, the overall mean floc size observed in the field was 3.80 mm, which is 48 % larger than the mean measured in the laboratory. The maximum floc sizes observed in the laboratory and field are comparable. It is worth noting that the largest floc size of 99.69 mm was just slightly smaller than the FOV dimensions and considerably larger than the 3.6 cm gap, indicating that the floc size measurements may have been physically limited by the FOV and the gap between the polarizers. Therefore, further increases in both the FOV and the gap between the polarizers may be needed in future studies to allow even larger flocs to be imaged and measured.

The size distributions obtained from different rivers are all a reasonable visual fit to

a lognormal distribution as shown in Figure 3.8, which is consistent with the laboratory measurements (Schneck et al. 2019). However, when the Chi-square test for goodness-of-fit was applied none of the size distributions were quantitatively confirmed to fit a lognormal distribution at the 5 % significance level. This could be primarily due to the use of the cut-off size to eliminate sediment particles which produced a sharp cut-off in the distributions. In addition, the small number of samples in some deployments resulted in noisy size distributions making it unlikely that they would be a good quantitative fit to a smooth lognormal distribution. Nonetheless, the good qualitative comparison of the floc size distributions measured in the field with theoretical lognormal distributions in Figure 3.8 does suggest that if the sample size was larger and sediment particles could be filtered out that floc size distributions in rivers would also closely follow a lognormal distribution.

The average floc number concentration  $\overline{C_{fn}}$  ranged from  $1.80 \times 10^{-4}$  to  $1.15 \times 10^{-1} \text{ cm}^{-3}$  (Table 3.4), Schneck et al. (2019) measured a peak floc number concentration of  $2.5 \times 10^{-1} \text{ cm}^{-3}$  in freshwater laboratory experiments, which is similar in magnitude to the upper limit of values measured in the field. The average floc volumetric concentration  $\overline{C_{fv}}$  ranged from  $2.05 \times 10^{-7}$  to  $4.56 \times 10^{-3}$  (Table 3.4). Previous studies reported suspended ice volumetric concentrations ranged from  $2 \times 10^{-6}$  to  $6 \times 10^{-3}$  (Tsang 1984; Marko and Jasek 2010; Richard 2011). These measurements were made using comparative resistance probes and acoustic devices which in theory detect all of the ice suspended in the water. The upper range of previous concentration measurements is comparable to that reported in this study. However, the lower range is one order of magnitude larger than this study, which may be due to the fact that the previous studies reported the total volume of frazil flocs and particles.

The time series of frazil floc properties in Figure 3.9 indicate that during the principal supercooling phase, floc number and mean size started to increase significantly just prior to peak supercooling and reached a maximum near the end of principal supercooling, the floc volumetric concentration only started to increase significantly after

peak supercooling occurred. Deployment NSR-L3 that captured almost the entire principal supercooling phase also showed a similar trend (see Figure A.3 in Appendix A). The increasing trend of floc mean size and number concentration generally agrees with previous laboratory measurements (Schneck et al. 2019; Pei et al. 2023). However, laboratory measured mean floc size and number concentration stopped increasing significantly shortly after peak supercooling, while in the field they stopped increasing later, near the end of the principal supercooling period. For example, Schneck et al. (2019) observed that the mean floc size and number concentration in freshwater stopped increasing significantly at dimensionless times of  $t/t_c = 1.13$  and  $1.27$ , respectively compared to  $t/t_c = 2.00$  and  $1.81$  for NSR-L4 ( $t_c$  is the time interval between the start of supercooling and peak supercooling and  $t$  is the time). The peak floc number concentration measured during the three Principal deployments in this study ranged from  $9.3 \times 10^{-4} \text{ cm}^{-3}$  to  $3.1 \times 10^{-3} \text{ cm}^{-3}$ , which was more than two orders of magnitude lower than the  $2.5 \times 10^{-1} \text{ cm}^{-3}$  measured in the laboratory tank by Schneck et al. (2019). These significantly lower floc concentrations suggest that particle concentrations in the field were also much lower compared to laboratory measurements. At lower suspended frazil concentrations the collision frequency of frazil particles would be reduced, increasing the time for flocs to gain mass via collision-induced particle-floc aggregation, which might explain the longer time period that mean floc size and number concentration was observed to increase in the field.

Figure 3.10 shows that during KR-F1 the mean floc size was approximately constant prior to the arrival of the hydropeaking wave during the residual supercooling phase. Similarly, there were no trends observed in floc size in five other Residual deployments, NSR-L2, NSR-L5, KR-E1, PR-F1 (see Figure A.2, Figure A.4, Figure A.7, and Figure A.6 in Appendix A) and PR-F2 (Figure 3.11). McFarlane et al. (2019b) found that in rivers the mean particle size remained approximately constant during the residual supercooling phase if the environmental conditions were relatively stable. Therefore, it follows that flocs observed during the residual supercooling phase would also have

a stable mean size unless hydraulic and/or meteorological conditions changed significantly. The mean floc size is the most stable during deployment KR-E1 (Figure A.7 in Appendix A) with a fluctuation range of only 1.5 mm, which could be in part due to the significantly larger sample size of 187,288. The only two Residual deployments that did not have a stable mean floc size were NSR-L6 and KR-F2 (Figure A.5 and Figure A.8 in Appendix A), and in both cases, the size decreased and this coincided with minor increases in  $T_w$  ( $\sim 0.005$  °C). These results indicate that during the residual phase the mean floc size does not typically vary significantly even at the end of the supercooling event when  $T_w$  rises above zero, as was the case in PR-F1 and PR-F2. During the two PR deployments the floc properties did not change significantly during the 1.3- and 2.5-hour time periods between when supercooling ended, and the measurements stopped. This is likely because the zero degree isotherm had moved upstream of the deployment site but the frazil being generated upstream of it was still advecting past the FrazilCam (*i.e.* the zero degree isotherm was not so far upstream that the advecting frazil had time to melt.)

As shown in Figure 3.10, during KR-F1 the residual supercooling water temperature remained mostly approximately constant at a temperature of approximately -0.01 °C. An approximately constant residual supercooling temperature was also observed in NSR-L2, KR-E1 and NSR-L5 (see Figure A.2, Figure A.7, and Figure A.4 in Appendix A). This means that during the residual supercooling phase ice was still growing and releasing latent heat that balanced the heat loss from the water surface in order to maintain the approximately constant water temperature. In this study, although the mean floc size did not vary significantly during most of the measured residual supercooling deployments, fluctuations and trends in the floc number and volume concentration time series were observed. This indicates that there may have been frazil ice particles still forming and growing, releasing latent heat to help balance the surface heat loss. In addition, during the residual phase anchor ice, border ice, and surface ice pans were likely growing as well and releasing latent heat, helping to maintain the stable residual

supercooling temperature.

The time series of water temperature  $T_w$  and net heat flux  $Q_n$  provided an opportunity to theoretically estimate the total ice growth in the water column, which could be compared to the measured floc volumetric concentration  $C_{fv}$  to estimate the fraction of ice sampled by the FrazilCam. Assuming there were no significant water temperature gradients in any direction (*i.e.* the river had a uniform temperature) and that the water depth was constant, the thermal balance of the water-ice mixture is given by:

$$\rho C_p \frac{dT_w}{dt} = -\frac{Q_n}{\bar{d}} + \rho_i L_i \frac{dC_i}{dt} \quad (3.15)$$

where  $\rho$  is the water density,  $C_p$  is the specific heat of water,  $\rho_i$  is the ice density,  $L_i$  is the latent heat of fusion of ice, and  $C_i$  is the total ice concentration due to thermal growth (Souillé et al. 2023). Equation (3.15) was then used to estimate,  $C_i$  for deployment NSR-L4, which captured the entire principal supercooling period. The result showed that the FrazilCam was only sampling at most 2 % of the total ice that was forming in the water. It should be noted that  $Q_n$  used in the calculation does not account for the effect of surface ice due to a lack of accurate surface ice data. In addition, mean water depth  $\bar{d}$  was used while in reality water depth varied spatially and temporally. These approximations create considerable uncertainty in the calculations of the total heat loss from the surface, and the volume of the water being cooled. Given all the simplifying assumptions that were made the uncertainty in the calculated  $C_i$  is potentially quite large, but is likely not greater than a factor of two or three. Therefore, despite this potential large uncertainty, the calculations suggest that the FrazilCam was only sampling less than  $\sim 5$  % of the total ice being formed in the river. Similar calculations were also performed using data collected in a laboratory frazil ice tank experiment using the laboratory version of the FrazilCam. In the laboratory environment the water depth is a constant, the tank has been shown to be well mixed and the surface heat loss can be quantified from the water cooling rate with reasonable accuracy. These results showed that  $C_i$  calculated using Equation (3.15) was comparable to the volumetric concentration of suspended ice calculated from the FrazilCam images prior to when flocs began

rising to the surface. This demonstrates that the FrazilCam does provide accurate measurements of the suspended ice concentrations. However, the only time the FrazilCam would be sampling a significant fraction of the total ice being formed in a river would be when suspended frazil is the only ice that is actively growing.

The effect of surface heat flux on floc properties was investigated. A positive mean net heat flux  $\overline{Q_n}$  was observed for all deployments indicating a net heat loss from the surface. The magnitude of  $\overline{Q_n}$  ranged from 95.4 to 318.8  $W/m^2$  as shown in Table 3.4. The dominant positive heat flux was  $Q_{lw}$  and  $Q_H$  for six and five deployments, respectively, while the dominant negative heat flux in all deployments was  $Q_{sw}$  which is consistent with previous studies (McFarlane and Clark 2021; Boyd et al. 2023). Efforts were made to correlate the mean net heat flux  $\overline{Q_n}$  with the measured floc properties listed in Table 3.4 (*i.e.* columns 5-11). No significant correlations were found when using data from all deployments or when only the data from the six NSR deployments that have 10-min heat flux data were used. It is worth noting that the heat flux analysis in this study did not account for varying surface ice concentrations and neglected several heat fluxes (*e.g.* sediment-water). Clearly, more comprehensive and frequent measurements of heat fluxes and surface ice properties are needed in future studies to more fully understand the impact of varying heat fluxes on frazil floc properties.

To investigate the effect of hydraulic conditions on the mean floc size  $\mu_f$ , the local Reynolds number  $Re$  is plotted versus  $\overline{\mu_f}$  in Figure 3.12 along with the following linear regression equation:

$$\overline{\mu_f} = 6.82 - 3.05 \times 10^{-5} Re \quad (3.16)$$

As  $Re$  increases from  $\sim 40,000$  to  $\sim 160,000$ ,  $\overline{\mu_f}$  decreases from approximately 5.5 mm to 2 mm and the coefficient of determination ( $R^2$ ) is 0.69, indicating that the two are moderately correlated. Clark and Doering (2009) found that higher turbulence intensity inhibited the formation of large flocs. This finding is consistent with the correlation presented in Figure 3.12 if it is assumed that turbulence intensity increased with  $Re$  in the three study rivers. However, this is not necessarily the case. An alternate ex-

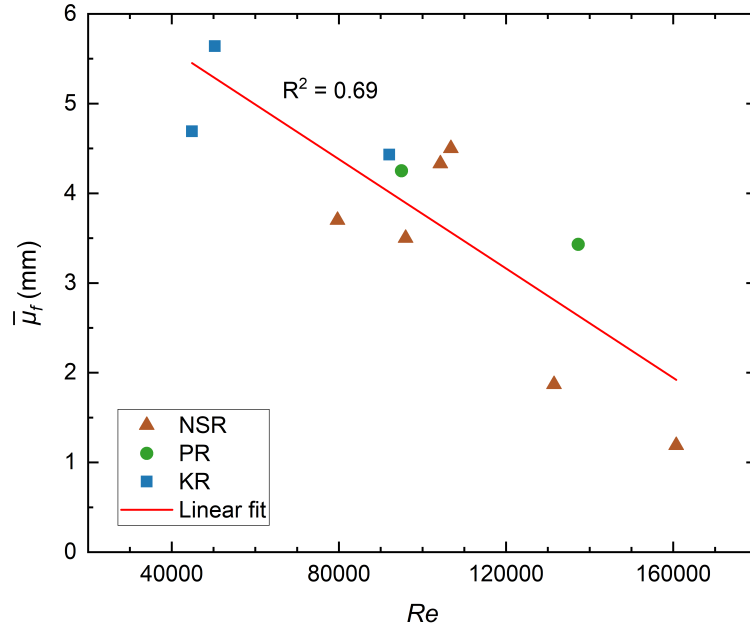


Figure 3.12: Relationship between local Reynolds number  $Re$  and mean floc size  $\bar{\mu}_f$  in mm.

planation for the observed correlation is that as  $Re$  increased flocs experienced higher shear strain rates (*i.e.* larger velocity gradients) and more violent floc-floc collisions which would tend to rupture larger flocs and reduce their mean size.

The effect of water depth on the floc volumetric concentration was investigated by correlating the average volumetric concentration with the fractional height  $d_m/\bar{d}$  where  $d_m = 0.198\text{ m}$  is the height above the bed at the centre of FrazilCam FOV and  $\bar{d}$  is the mean water depth. Figure 3.13 presents a scatter plot of the fractional height  $d_m/\bar{d}$  versus the average floc volumetric concentration  $\bar{C}_{fv}$ . Results show that there is a strong nonlinear correlation given by the following power law equation:

$$\bar{C}_{fv} = 4.80 \left( \frac{d_m}{\bar{d}} \right)^{9.69} \quad (3.17)$$

where the  $R^2$  value equals 0.99. Ye (2002) and Morse and Richard (2009) reported measurements of vertical frazil concentration profiles and found that the Rouse equation (Rouse 1937), previously used to characterize suspended sediment concentration

profiles, could be used to describe the frazil ice concentration profile. Equation (3.17) is similar in format to the Rouse equation, indicating that the vertical concentration of both frazil particles and flocs may be accurately described by power law equations.

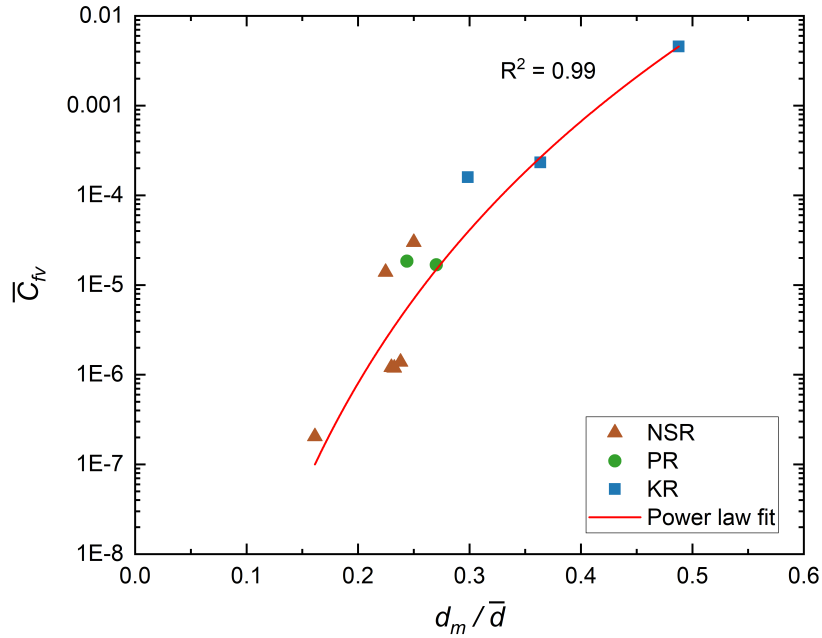


Figure 3.13: Relationship between the fractional height  $d_m / \bar{d}$  and the average floc volumetric concentration  $\bar{C}_{fv}$ .

### 3.7 Conclusions

A submersible high-resolution camera system was deployed during supercooling in three rivers from 2021 to 2023. Images from the eleven deployments were analyzed to investigate frazil floc properties and their evolution. Images showed that frazil flocs observed in the North Saskatchewan River were predominately formed by disc-shaped particles, while flocs in the Peace River and Kananaskis River were comprised of various ice crystal shapes, including disc-shaped, needle-shaped, and irregular particles. A lognormal distribution is a reasonable description of floc size distributions in rivers. The mean floc size ranged from 1.19 to 5.64 mm and the overall mean floc size was

3.80 mm. The mean floc size in rivers was found to 48 % larger than was previously observed in the laboratory by Schneck et al. (2019) while the maximum floc size was comparable in the laboratory and field. The average floc number concentration ranged from  $1.80 \times 10^{-4}$  to  $1.15 \times 10^{-1} \text{ cm}^{-3}$  and previous laboratory measurements fall within the range of the values observed in this study. The estimated average floc volumetric concentration ranged from  $2.05 \times 10^{-7}$  to  $4.56 \times 10^{-3}$ , with the upper bound being comparable to previous total ice volume concentration measurements while the lower bound is an order of magnitude smaller.

Time series analysis indicated that during the principal supercooling phase, floc number concentration and mean size increased significantly just before peak supercooling and reached a maximum near the end of principal supercooling. This increasing trend was also observed in previous laboratory measurements (Pei et al. 2023; Schneck et al. 2019) but the duration of the increasing trend was longer in the field. During the residual supercooling phase, the mean floc size did not typically vary significantly even 2.5 hours after the water temperature rises above zero degrees. The effect of the air-water heat flux on floc properties was investigated by conducting a linear regression analysis. However, no significant correlations were found, and this may be due to the limited dataset or the complexity of the field environment where heat fluxes can vary temporally and spatially. Future field measurements of floc properties, especially made during the principal supercooling phase and made continuously along multiple sites along a study reach, are needed to more fully understand the factors that govern their size and concentration.

Analysis of the influence of local hydraulic conditions on frazil floc properties showed that as the local Reynolds number increases, the mean floc size decreases linearly. The resulting equation can be used to estimate mean floc sizes in rivers using estimates of the mean velocity and depth. It was also shown that the averaged floc volumetric concentration can be related to the fractional height above the bed through a power law equation. This relationship may be useful for describing the vertical concentration

profiles of frazil flocs.

The detailed measurements of frazil floc properties and their evolution in rivers presented in this study could be used in several ways to enhance numerical modelling of river ice processes in order to improve predictions of river freeze-up. At the present time the frazil rise velocity is treated as a calibration parameter in comprehensive river ice process models (*e.g.* Shen 2010; Blackburn and She 2019). However, it could now be directly estimated by first using Equation (3.16) to predict the mean floc size using the local Reynolds number and then the rise velocity could be predicted using Reimnitz et al. (1993) measurements. In addition, the reported lognormal size distributions of flocs, as well as time series evolution of mean floc size and concentrations, measured in rivers for the first time, could provide opportunities to incorporate floc dynamics into numerical models with the goal of improving how realistically they simulate frazil ice evolution and surface ice progression.

In the future, it would be of interest to deploy the FrazilCam in lakes and oceans, where the flow regime and salinity may be considerably different, to investigate frazil particle and floc properties in these different environments. The FrazilCam system in principle can be deployed in any sufficiently transparent waters, however, the system would need to be modified to automate the polarizer rinsing process. This would be challenging but might be possible using a mechanical wiper which would allow deployments on the bottom of deeper water bodies. In addition, the system could be attached to an unmanned or autonomous underwater vehicle to allow observations to be made at various depths in the water column in lakes and oceans.

## Chapter 4

# Laboratory Study of Supercooling and Frazil Evolution Under Varied Heat Flux Scenarios

### 4.1 Introduction

Individual frazil ice particles are formed when turbulent water is supercooled below its freezing point and seed ice crystals are introduced into the water column. These tiny frazil ice particles, predominantly disk-shaped with sizes ranging from 0.022 to 6 mm (McFarlane et al. 2017), have been observed to form and grow in various natural bodies of water including rivers (Osterkamp and Gosink 1983), turbulent surface layers of lakes (Svensson and Omstedt 1998), and oceans (Martin 1981; Frazer et al. 2020). As they are transported by the turbulent flow, they may collide with each other due to spatially varying flow velocities and differential rise velocities (Mercier 1985). Collision may cause particles to freeze together into larger aggregates called frazil flocs in a process called flocculation (Clark and Doering 2009). In northern rivers, flocs typically increase in size until they become buoyant enough to rise to the water surface and contribute to the formation of a solid ice cover (Clark and Doering 2009). They may also be carried by the turbulent flow to the river bed forming anchor ice (Kempe et al. 1993). Frazil ice particles and flocs can adhere to underwater structures causing blockages to water intakes (Barrette 2021) and large accumulations of frazil ice both at the surface and on the riverbed may cause flooding and property damage

(Beltaos 2013). Therefore, it is important to better understand frazil ice particle and floc properties as well as their evolution with time during supercooling.

The supercooling temperature of water is a function of the latent heat released by the growing ice crystals and the heat loss from the water (Daly 2008). Previous laboratory studies have investigated supercooling characteristics by exposing turbulent water to a constant sub-zero air temperature. Under these conditions, an approximately constant heat loss from the water to the air is generated and this produces the so-called “classic” supercooling curve or water temperature time series (Carstens 1966; Ye et al. 2004; Clark and Doering 2006). During a classic supercooling event, the water temperature initially decreases at a constant cooling rate and frazil ice crystals begin to form shortly after the start of supercooling. The production and growth of the crystals release latent heat into the water which decreases the water cooling rate. A minimum water temperature referred to as the peak supercooling temperature is reached when the released latent heat balances the heat loss (Tsang and Hanley 1985). As the crystals grow and new crystals are generated, the latent heat overpowers the heat loss from the water. The water temperature then starts to increase until an approximately constant sub-zero temperature is reached due to the establishment of an equilibrium between the heat generated from frazil formation and heat loss from the water (Tsang and Hanley 1985). The period when the water temperature varies transiently is often referred to as the principal supercooling phase and the period when the water temperature maintains a stable residual temperature is called the residual supercooling phase (Michel 1972).

There have been several laboratory studies that measured the evolution of frazil ice particle properties during a classic supercooling event (Ye et al. 2004; McFarlane et al. 2015; Clark and Doering 2006; Schneck et al. 2019) and a few simultaneously measured frazil floc properties (Pei et al. 2023; Schneck et al. 2019). Frazil ice particles in suspension were observed to start forming a few minutes after the start of supercooling, then increase in number rapidly and the particle number concentration reached a maximum value shortly after peak supercooling (McFarlane et al. 2015). The intro-

duction and rapid multiplication of frazil ice particles are most commonly considered a result of secondary nucleation, which refers to the nucleation of new crystals due to the presence of a stable parent crystal (Evans et al. 1974). After that the particle number concentration continuously decreased to a negligible value due to flocculation and flocs rising to the surface (McFarlane et al. 2015). Floc number concentration time series was found to follow very similar trends as particle number concentration time series except that flocs tended to start forming slightly later than particles and decreased to negligible values earlier (Pei et al. 2023). Several previous supercooling studies investigated how different combinations of air temperature and turbulence intensity affected supercooling temperatures and frazil ice properties. It was found that lower air temperatures resulted in higher cooling rates, greater peak supercooling magnitudes (Carstens 1966), and larger maximum particle and floc number concentrations (Pei, She, et al. 2024). Lower turbulence intensities resulted in lower cooling rates (McFarlane et al. 2015) and smaller maximum particle and floc number concentrations (Pei, She, et al. 2024).

In rivers, the supercooling process may not always progress under a constant upward heat flux as it does in laboratory settings due to variations in meteorological conditions such as air temperature, solar radiation, and wind speed. Kalke et al. (2019) conducted field measurements of supercooling in the North Saskatchewan River and classified the shape of the supercooling curve into three types: classic, erratic, and parabolic. The results suggested that only approximately one-third of the observed supercooling events followed the classic supercooling curve shape likely produced by a constant heat flux. The rest were either erratic or parabolic in shape likely due to a temporally varying air-water heat flux. McFarlane and Clark (2021) investigated the heat budget during six supercooling events measured in the Dauphin River. They reported that the net heat flux during these supercooling events varied from  $-189$  to  $13.8 \text{ W/m}^2$  and the most significant negative heat flux during supercooling events was the net longwave radiation. Richard et al. (2015) recorded four supercooling events during freeze-up in the St. Lawrence River that occurred when the net heat flux dropped below  $-200 \text{ W/m}^2$

with the most extreme one reaching below  $-500 \text{ W/m}^2$ . Boyd et al. (2023) analyzed the surface energy budget during 190 supercooling events measured in two Alberta rivers and found the diurnal cycling of the net heat flux due to shortwave radiation was the most significant factor in determining the start and end of supercooling events. They also observed fluctuations in the net heat flux at the Peace River during one residual supercooling phase that ranged between  $-354$  to  $256 \text{ W/m}^2$  that did not produce any noticeable change in the water temperature.

There have only been a few studies that have measured the temporal evolution of frazil ice particles and flocs in rivers. It was found that in most cases mean frazil particle size remained approximately constant during the residual supercooling phase, but in some cases changing environmental conditions during the residual supercooling phase changed mean particle size (McFarlane et al. 2019b; Richard et al. 2011). No definitive conclusions were reached regarding the evolution of frazil ice properties during the principal supercooling phase due to limited data (McFarlane et al. 2019b). Pei, Yang, et al. (2024) measured floc sizes and concentrations during eleven supercooling events in three Alberta rivers. It was found that during the principal supercooling phase, floc number concentration and mean size increased significantly just before peak supercooling and reached maxima near the end of principal supercooling. During the residual supercooling phase, the mean floc size did not typically vary significantly even 2.5 hours after the water temperature had risen above zero degrees.

The only study that performed laboratory supercooling experiments during which the heat flux was varied was reported in Carstens (1966). He performed cold room experiments using a recirculating flume and measured the supercooling curve when the heat flux was increased during the residual supercooling phase by changing the wind speed from 0 to 3  $\text{m/s}$ . He observed that a secondary peak supercooling was generated with a magnitude significantly smaller than the first peak, but no frazil ice particle or floc properties were reported. At present, the relationship between the varying heat flux and the evolution of particle and floc properties remains largely unknown. This highlights

the need to investigate supercooling, frazil ice, and floc evolution under varying heat flux conditions in a controlled laboratory setting to better understand the fundamentals of the effect of heat flux variations that were commonly observed in the field to the evolution of frazil ice particles and flocs.

In this study, a series of laboratory experiments were performed to investigate the characteristics of supercooling, as well as the evolution of frazil ice particles and flocs, when the water heat loss was increased or decreased at different times during a supercooling event. Images of frazil ice particles and flocs passing between two cross-polarizing filters were captured using a high-resolution camera system. Precision temperature loggers were used to monitor water and air temperatures. The sizes and concentrations of frazil particles and flocs measured during supercooling events are presented. The effect of varying the heat flux at different times of supercooling on the supercooling temperature time series and on the properties of frazil ice particles and floc are discussed.

## 4.2 Methodology

### 4.2.1 Experimental Setup

The laboratory experiments were performed in the University of Alberta's Cold Room Facility in a frazil ice tank. The configuration of the experimental setup is shown in Figure 4.1. The air temperature in the cold room can be varied between +20 °C to -20 °C with  $\pm 2$  °C fluctuations. The tank has a base dimension of 0.8 by 1.2 m and was filled with filtered tap water to a depth of 1.3 m. Four synchronized propellers were mounted on the bottom of the tank and powered by a NEMA 34 DC variable speed electric motor to produce turbulent flow in the tank. The propellers were set to a constant speed of 325 rpm for all experiments using a laser tachometer. McFarlane et al. (2015) conducted ADV measurements in the same tank setup. They estimated the tank averaged turbulent kinetic energy dissipation rates  $\varepsilon$  was  $335.6 \text{ cm}^2/\text{s}^3$  at a propeller speed of 325 rpm. The side walls and bottom of the tank were insulated with

51 mm thick Owens Corning FOAMULAR C-200 XPS rigid foam insulation boards to minimize heat flux through the sides and bottom of the tank and to ensure that the heat flux across the air-water interface was dominant.

Two openings were cut in the insulation on the back and front of the tank to allow for backlighting and imaging of frazil particles and flocs. A Genaray SpectroLED Essential 360 Daylight LED light was used to provide backlighting and a 1.5 mm thick translucent plastic sheet was used to diffuse the light. Two 16 cm  $\times$  16 cm square Cavision glass linear polarizing filters, mounted 90° separated by a 3.1 cm gap, were installed inside the tank against the front glass so that frazil particles and flocs passing through the gap were visible in the images. The centre of the polarizers was located 29 cm below the water surface. A 36-megapixel Nikon D800 DSLR camera with a Micro-Nikkor 60 mm f/2.8D lens was mounted outside of the tank, focused on the polarizers to capture images of frazil particles and flocs as they were advected between the polarizers. The camera was programmed to capture images at 1 Hz with an ISO of 6400, a shutter speed of 1/2000 s, and a f-stop of f/25. The average image pixel size was 21.6  $\mu\text{m}$  and the field-of-view (FOV) was 159 mm  $\times$  106 mm. A space heater was placed beside the camera to blow warm air onto the glass window to prevent frost formation on the glass in the FOV. A Sea-Bird SBE 39plus temperature recorder (accuracy  $\pm 0.002$  °C) was mounted at the same depth as the polarizer centroid and programmed to sample water temperatures at 1 Hz. An RBR Solo T temperature logger (accuracy  $\pm 0.002$  °C) was mounted 15 cm above the water surface and sampled air temperatures at 1 Hz.

#### **4.2.2 Experimental Conditions and Procedures**

Table 4.1 presents a summary of experimental conditions. Two groups of experiments, named G1 and G2, were performed. Each group included five series of experiments with one series of baseline experiment conducted under a constant initial air temperature  $T_a$  and four other series of experiments in which the initial  $T_a$  was varied to a target  $T_a$  at different times during supercooling. Note the initial and target  $T_a$  refer to the set

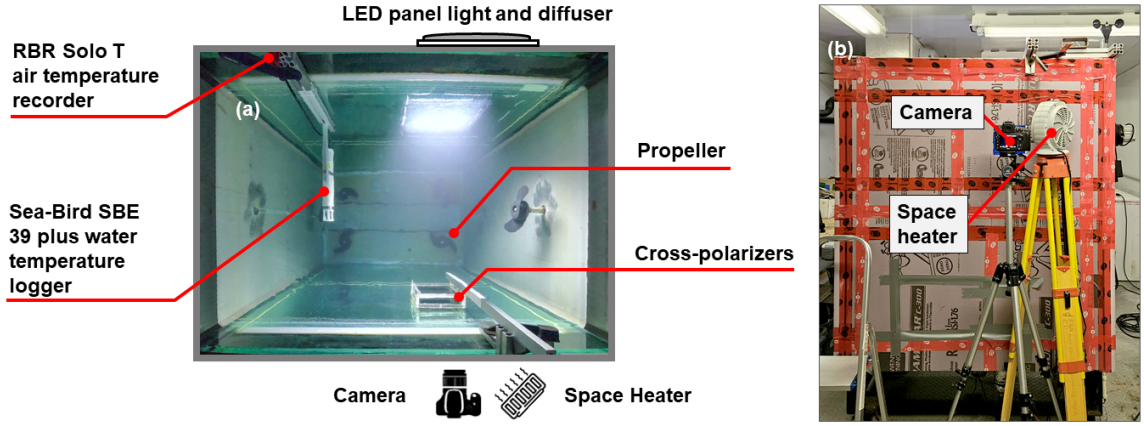


Figure 4.1: (a) Rectified plan view image of the frazil tank and (b) front view of the frazil tank showing the locations of instruments and equipment.

point temperatures of the cold room. Each of the 10 series of experiments (S1 - S10) included three repeated runs to reduce the uncertainty of the results.

Table 4.1: Summary of experimental conditions. Note that bolded series title denotes baseline series,  $t_{c1}$  (31 minutes) and  $t_{c6}$  (14 minutes) are the average cooling duration for baseline series S1 and S6, respectively.

| Exp. Group | Exp. Series | Initial $T_a$ (°C) | Target $T_a$ (°C) | $T_a$ Change Time | Exp. Group | Exp. Series | Initial $T_a$ (°C) | Target $T_a$ (°C) | $T_a$ Change Time |
|------------|-------------|--------------------|-------------------|-------------------|------------|-------------|--------------------|-------------------|-------------------|
|            | <b>S1</b>   | -5                 | N/A               | N/A               |            | <b>S6</b>   | -15                | N/A               | N/A               |
|            | S2          | -5                 | -15               | $0.5t_{c1}$       |            | S7          | -15                | -5                | $0.5t_{c6}$       |
| G1         | S3          | -5                 | -15               | $t_{c1}$          | G2         | S8          | -15                | -5                | $t_{c6}$          |
|            | S4          | -5                 | -15               | $1.5t_{c1}$       |            | S9          | -15                | -5                | $1.5t_{c6}$       |
|            | S5          | -5                 | -15               | $2t_{c1}$         |            | S10         | -15                | -5                | $2t_{c6}$         |

As shown in Table 4.1, in group G1, series S1 was the baseline series performed at a steady initial  $T_a$  of -5 °C. In S2 - S5,  $T_a$  was initially set to -5 °C and then decreased to -15 °C at four different times during supercooling to generate four increased heat flux scenarios. Conversely, in group G2, the baseline series S6 was conducted at a steady  $T_a$  of -15 °C. In series S7 - S10, the initial  $T_a$  of -15 °C was changed to -5 °C at four different

times to generate decreased heat flux scenarios. Note that in this study the term heat flux was used to describe an upward heat flux (heat loss) from water to air. The two air temperatures, -5 and -15 °C, were chosen because preliminary experiments showed that these two temperatures balanced the need to increase/decrease the cold room air temperature relatively quickly while at the same time producing a significant change in air-water heat flux.

The times when the cold room air temperature was changed were based on the average cooling duration for the baseline series S1 and S6, which were defined as  $t_{c1}$  and  $t_{c6}$ , respectively. The cooling duration was defined as the time between the start of supercooling (*i.e.* the first instance when the water temperature remained below zero for ten consecutive seconds) and the time when peak supercooling defined as  $T_p$  occurred. The average cooling durations  $t_{c1}$  and  $t_{c6}$ , were calculated to be 31 minutes and 14 minutes respectively, by averaging the cooling durations measured in the three repeated runs of each baseline series. The four  $T_a$  heat flux change times were set to 0.5, 1.0, 1.5 and 2.0 times the cooling durations  $t_{c1}$  and  $t_{c6}$ , respectively for groups G1 and G2 (Table 4.1). These times were spaced evenly with a dimensionless increment of 0.5 to assess the effect of varying heat flux during both the principal and residual supercooling phases on the supercooling curve and on the evolution of frazil particles and flocs.

At the start of each experiment, the space heater was turned on and the cold room was programmed to the initial  $T_a$  (Table 4.1). Filtered tap water was added to the tank if the water depth had dropped below 1.3 m prior due to evaporation. The air and water temperature loggers were programmed to start collecting data. Fifteen minutes before supercooling started, the polarizers were mounted in the tank and the camera was installed and focused on the polarizers. Scale images of a ruler placed at the front, middle and back of the polarizer gap were taken to determine the average pixel size. Ten background images were also captured prior to ice formation. One minute before supercooling started, the camera was programmed to begin taking images. The super-

cooling start time was recorded.

After supercooling started, the cold room temperature was reprogrammed to the target  $T_a$  of  $-15\text{ }^\circ\text{C}$  at the change times listed in Table 4.1 for S2 - S5 in G1 to increase the heat flux. For S7 - S10 in G2, preliminary experiments found that reprogramming the cold room temperature to  $-5\text{ }^\circ\text{C}$  resulted in a  $\sim 80$ -minute response time to reach the target temperature which was too long for this study considering  $t_{c6}$  was only 14 minutes. The cold room is an enclosed space designed to maintain a set cold air temperature and it was not designed to generate rapid temperature increases. To reduce the response time when the air temperature was increased, the following enhanced ventilation procedure was developed by trial-and-error and then implemented. At the exact  $T_a$  change times in S7 - S10, the cold room temperature was reprogrammed to the target  $T_a$  of  $-5\text{ }^\circ\text{C}$  and one minute after that the cold room door was fully opened for 8 minutes. A Commercial Electric 24 inch High Velocity Drum Fan was placed on the floor of the cold room 54 cm inside the door blowing cold air out of the cold room at an average wind speed of  $4\text{ m/s}$ , measured using a HoldPeak HP-866B digital anemometer. After 8 minutes the fan was removed, and the cold room door was closed. This procedure forced cold air out of the lower half of the door opening and due to mass conservation warm air from the room outside was drawn in through the upper half of the opening. Each experiment was run for a total duration of four times the baseline average cooling duration, which was 124 mins for group G1 and 56 minutes for G2. Note that during each G1 experiment, the memory card and battery of the camera needed to be manually replaced once which introduces a  $\sim 90$  second gap in the sampled image sequence.

### 4.2.3 Experiment Repeatability

For every experiment series, three repeated runs were performed, resulting in a total of 30 experimental runs. Figure 4.2 presents a total of 18 superimposed air and water temperature time series from six series of experiments in the two groups. Time series from other series were similar to the ones presented in Figure 4.2. Figure 4.2a-b show

the time series of  $T_a$  during the G1 and G2 experiments, respectively. In Figure 4.2a-b the time series of  $T_a$  for baseline series S1 and S6 show that the cold room maintained a stable air temperature with minor fluctuations ranging from -3.8 to -4.8 °C and -13.5 to -15.1 °C, respectively. This demonstrates that the cold room air temperature was well controlled with fluctuations less than 1.6 °C. The time series of  $T_a$  in Figure 4.2a-b of the three repeated runs for S2, S4, S7, and S9 in which  $T_a$  was increased or decreased at different times all aligned quite well within each series, demonstrating that the cold room air temperatures were being varied in a controlled and repeatable manner. The water temperature time series in Figure 4.2c-d show that the supercooling curves aligned quite well during the first half of the supercooling phase. However, in some series, they started to deviate slightly from each other after reaching peak supercooling  $T_p$ . This was most pronounced during S4 (Figure 4.2c) when the values of  $T_w$  varied by as much as  $\sim 0.005$  °C within the repeated runs. Despite the small variations observed, the trend of the supercooling curve within each series remained consistent throughout each experiment, indicating that the water temperature time series were sufficiently repeatable. Note that there are small spikes up to  $\sim 0.01$  °C in magnitude evident in the supercooling curves plotted in Figure 4.2c-d that were caused by ice momentarily contacting the thermistor tip of the Seabird logger. This makes the time series appear a little noisy but this did not significantly impact the results or conclusions of this study.

Table 4.2 presents a summary of statistics from the  $T_a$  and  $T_w$  time series for each experiment series. The statistics include the series averaged water cooling rate  $R_c$  and the peak supercooling temperature  $T_p$ . The cooling rate  $R_c$  is defined as the slope of the  $T_w$  time series from 10 minutes before supercooling started to the start of supercooling. In addition, the root mean square differences  $\text{RMSD}_a$  and  $\text{RMSD}_w$  of paired  $T_a$  and  $T_w$  time series (*i.e.* three pairs for each series) were calculated and averaged within each experiment series.  $\text{RMSD}_a$  and  $\text{RMSD}_w$  values ranged from 0.15 to 0.71 °C and from 0.001 to 0.0021 °C, respectively. The series-averaged cooling rate  $R_c$  was similar within each group, varying between -0.0019 and -0.0020 °C/min for G1 experiments, and be-

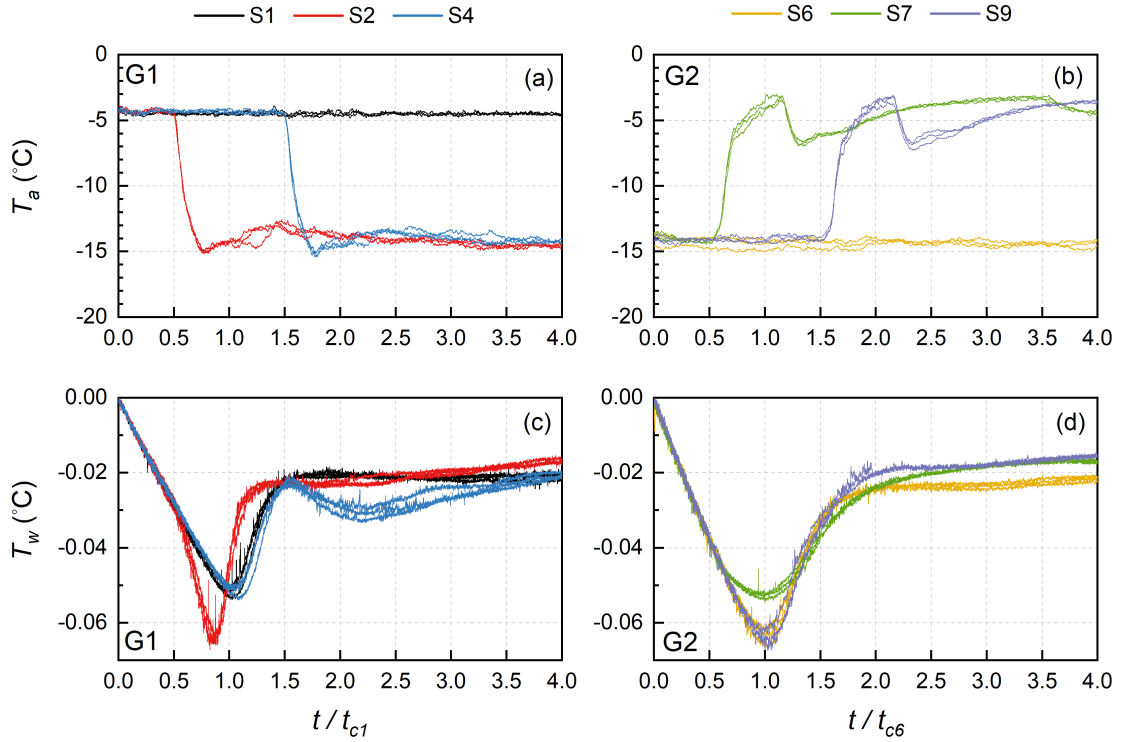


Figure 4.2: Time series of (a-b) air temperature  $T_a$  and (c-d) corresponding water temperature  $T_w$  time series from six series of experiments. Time  $t$  is normalized using the average cooling duration used for the G1 and G2 experiments  $t_{c1}$  and  $t_{c6}$ , respectively. Note each color represents one series of experiments with three repeated runs plotted and zero time is the start of supercooling.

tween  $-0.0056$  and  $-0.0057$   $^{\circ}\text{C}/\text{min}$  for G2 experiments. The series-averaged  $T_p$  ranged from  $-0.052$  to  $-0.066$   $^{\circ}\text{C}$ . The coefficient of variation (COV), defined as the standard deviation divided by the mean, was calculated for  $R_c$  and  $T_p$ , and they varied from 0.5 % to 5.5 % and 0.5 % to 4.6 %, respectively. Overall, this analysis demonstrated that the time series were repeatable within acceptable limits.

#### 4.2.4 Data Processing and Analysis

As noted in Section 4.2.1, the tank bottom and side walls are well insulated. In addition, Schneck et al. (2019) measured water temperature at different locations throughout the same tank under the same propeller speed, and concluded that the temperature was approximately uniform and the tank was well mixed. Therefore, by reasonably

Table 4.2: Summary of experimental statistics including the average root mean square difference for air and water temperature time series  $\text{RMSD}_a$  and  $\text{RMSD}_w$ , respectively, as well as the series averaged water cooling rate  $R_c$  and the peak supercooling temperature  $T_p$ .

| Exp. Group | Exp. Series | $\text{RMSD}_a$ (°C) | $\text{RMSD}_w$ (°C) | $R_c$ (°C/min) | $T_p$ (°C) |
|------------|-------------|----------------------|----------------------|----------------|------------|
| G1         | S1          | 0.1522               | 0.0014               | -0.0020        | -0.052     |
|            | S2          | 0.3120               | 0.0016               | -0.0019        | -0.066     |
|            | S3          | 0.7110               | 0.0016               | -0.0019        | -0.053     |
|            | S4          | 0.3040               | 0.0021               | -0.0019        | -0.053     |
|            | S5          | 0.3669               | 0.0016               | -0.0019        | -0.052     |
| G2         | S6          | 0.4147               | 0.0015               | -0.0057        | -0.065     |
|            | S7          | 0.2677               | 0.0010               | -0.0057        | -0.054     |
|            | S8          | 0.3971               | 0.0016               | -0.0056        | -0.065     |
|            | S9          | 0.2954               | 0.0017               | -0.0057        | -0.066     |
|            | S10         | 0.2514               | 0.0011               | -0.0056        | -0.065     |

assuming the tank water is well mixed and all the heat exchange between the water and the surrounding environment occurred across the air-water interface, prior to any significant ice formation, the net air-water heat flux  $Q$  in  $W/m^2$  is given by:

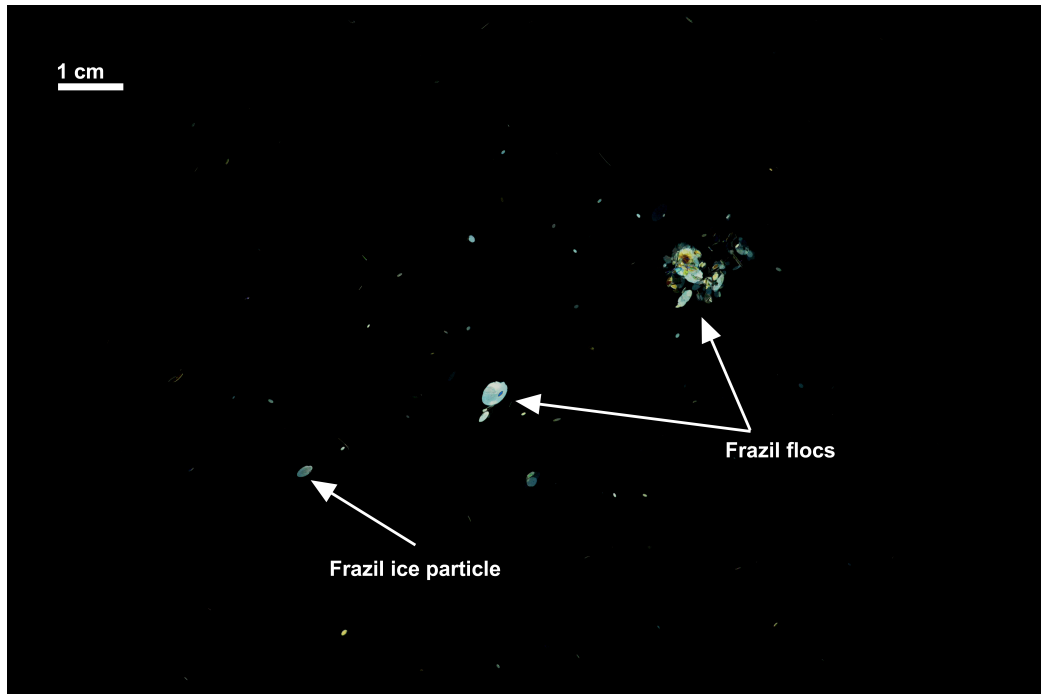
$$Q = \rho D C_p \frac{dT_w}{dt} \quad (4.1)$$

where  $\rho$  is the water density,  $D = 1.3$  m is the water depth,  $C_p$  is the specific heat of water and  $dT_w/dt$  is the water cooling rate. As shown in Table 4.2, the average cooling rate for all the G1 experiments that started with a constant air temperature of  $-5$  °C was  $-0.0019$  °C/min, and for all the G2 experiments that started with a constant air temperature of  $-15$  °C it was  $-0.0057$  °C/min. Therefore, the net air-water heat flux  $Q$  under steady  $-5$  °C and  $-15$  °C air temperatures equate to  $-173$   $W/m^2$  and  $-519$   $W/m^2$ , respectively. This indicates that the heat flux varied by approximately threefold when the air temperature was varied between  $-5$  °C and  $-15$  °C. However, in S4, S5, S9, and

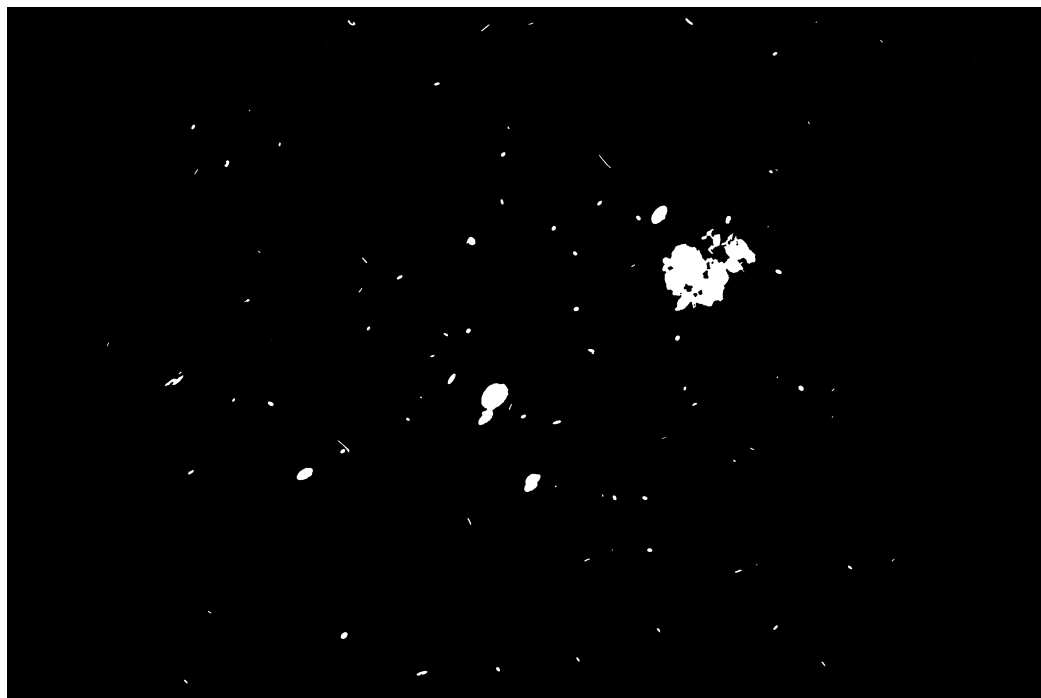
S10 the  $T_a$  change occurred after significant floc rises, and the presence of surface slush reduced the threefold heat flux increase/decrease applied in other series. In preliminary experiments, surface slush was manually removed periodically to maintain an ice-free water surface. However, it was found that this action caused resuspension of the frazil particles and flocs for up to 30 mins significantly affecting the time series of particle and floc properties. Therefore, it was not used in formal experiments. Instead, tank surface images at the time when the air temperature was varied in S4, S5, S9, and S10 were recorded using a GoPro HERO8 camera. The images were rectified using GIMP software and the surface slush was manually annotated to compute the percentage of surface slush coverage. The estimated surface slush coverage ranged from 31 - 37 % in S4, S5, S9, and S10, indicating in these cases the desired heat flux variation was being reduced at most 37 % and as a result, the heat flux was varied by a factor of two instead of three.

Images captured during each experiment were analyzed to identify frazil particles and flocs and to compute their properties. Figure 4.3a presents an example raw image captured during a laboratory experiment showing different shapes of frazil particles and flocs. Disk-shaped frazil particles appear in the image as shapes ranging from a line to circular with most being elliptical. Flocs are formed by the aggregation of frazil particles, resulting in different shapes depending on the number, shape, and size of attached particles. First, the average of the 10 background images was subtracted from each raw image to remove background noise. Then each image was iteratively thresholded following McFarlane et al. (2014) to obtain the corresponding binary image with particles and flocs or ice objects shown in white. Particles or flocs that intersected the image boundaries were eliminated. An example of a processed binary image is shown in Figure 4.3b.

The properties of each ice object including area  $a$  and perimeter  $P$  were computed from the binary images. An ellipse was fitted to each ice object and the corresponding ellipse major and minor axis lengths, aspect ratio (the ratio of the major axis length



(a)



(b)

Figure 4.3: An example of (a) an annotated raw image captured during a laboratory experiment, and (b) the corresponding processed binary image.

to the minor axis length), area, and perimeter were also computed. The size  $S$  of both frazil particles and flocs was defined as the major axis length of its fitted ellipse following previous studies (McFarlane et al. 2015; Clark and Doering 2009). An ellipse with a major axis of less than five pixels was deemed to be too pixelated for subsequent analysis and therefore ice objects with an  $S$  smaller than this were eliminated. Based on the computed geometrical properties, each ice object was classified as either a frazil ice particle or a frazil floc using criteria presented in Section 3.4.1. The criteria used were tested on a dataset comprised of 109 flocs and 459 frazil particles that were visually identified and the accuracy for particles and flocs was 97.0 % and 92.7 %, respectively (Section 3.4.1).

After classification, the mean particle size  $\mu_p$ , mean floc size  $\mu_f$ , particle number concentration  $N_p$ , floc number concentration  $N_f$ , and total ice volume concentration  $C_i$  were computed for each image, and a moving average over a period of 35 images was applied to the resulting time series to smooth the data. The measuring volume is the image FOV times the distance between the two polarizers and the number concentration is defined as the number of particles/flocs divided by the measuring volume. The total ice volume concentration is defined as the combined volume of particles and flocs divided by the measuring volume. Assuming a constant particle diameter-to-thickness ratio of 37 based on the mean particle diameter-to-thickness ratio measurements made by McFarlane et al. (2014), the particle ice volume  $V_p$  is given by:

$$V_p = \pi a^2 \times \frac{2a}{37} \quad (4.2)$$

where  $a$  is the semi-major axis length of the fitted ellipse of a given particle or floc. The ice volume of a floc, defined as  $V_f$ , is given by:

$$V_f = \frac{4}{3} \pi abc \times (1 - \eta) \quad (4.3)$$

where  $b$  is the semi-minor axis length of the fitted ellipse of a given particle or floc, the third semi-axis length  $c$  was assumed to be the average of  $a$  and  $b$  but not greater than

the spacing between the two polarizers (Schneck et al. 2019), and  $\eta$  is the floc porosity assumed to be 0.8 (Schneck et al. 2019).

The measured time series of water and air temperature  $T_w$  and  $T_a$  can be used to theoretically compute the time series of total ice growth in the water column, which could be compared to the estimated total ice volume concentration  $C_i$  to evaluate the fraction of ice sampled by the camera images. Assuming the tank was well mixed and  $C_i \ll 1$ , the thermal balance of the water-ice mixture is given by:

$$\rho C_p \frac{dT_w}{dt} = \frac{Q}{D} + \rho_i L_i \frac{dC_i}{dt} \quad (4.4)$$

where  $\rho_i = 920 \text{ kg/m}^3$  is the ice density,  $L_i = 3.33 \times 10^5 \text{ J/kg}$  is the latent heat of fusion. The time series of air-water heat flux  $Q$  can no longer be estimated using Equation (4.1) since frazil ice was forming and air temperature may change during the experiments. However,  $Q$  can be estimated by a linear relationship (Hicks 2016), which is given by:

$$Q = h_{wa}(T_w - T_a) \quad (4.5)$$

where  $h_{wa}$  is the linear heat transfer coefficient between water and air in  $W/(m^2 \text{ } ^\circ\text{C})$ .  $h_{wa} = -37.5 \text{ W}/(m^2 \text{ } ^\circ\text{C})$  is obtained by calibration using the air and water temperatures as well as the known  $Q$  calculated using Equation (4.1) from S1 and S6 experiments prior to significant ice formation. Using Equation (4.4) and Equation (4.5),  $C_i$  was calculated from the measured  $T_w$  and  $T_a$  data every second and an initial ice concentration  $C_0$  of  $3.5 \times 10^{-5}$  was added to the results to avoid negative  $C_i$  values. It should be noted that this method did not consider frazil rising, therefore the estimation is only appropriate for comparison to our suspended frazil ice measurements before  $N_p$  decreases significantly.

An example of a  $N_p$  time series from S2 experiments normalized by its maximum value ( $N_{pm}$ ) is plotted in Figure 4.4. Four specific times are labelled on the plot:  $t_{p10}$  and  $t_{p90a}$  are the times when  $N_p$  first reached 10 % and 90 % of  $N_{pm}$ , respectively, and  $t_{p90b}$  and  $t_{p30}$  are the times when  $N_p$  dropped below 90 % and 30 % of  $N_{pm}$ , respectively.

Clark and Doering (2006) found that during the time interval between  $t_{p10}$  and  $t_{p90a}$ ,  $N_p$  increased with an approximately linear slope. Similarly, between  $t_{p90b}$  and  $t_{p30}$ ,  $N_p$  decreased with an approximately linear slope. These approximately linear slopes are illustrated by dashed lines in Figure 4.4 and similar approximately linear slopes were observed in the  $N_f$  time series as well. Therefore, these two time intervals were used to estimate the production and decay rates of frazil particles and flocs. For each experiment run, the frazil particle production rate  $n_{pp}$  and decay rate  $n_{pd}$  expressed as the number of particles per cubic meter per second are given by:

$$n_{pp} = \frac{0.8N_{pm}}{t_{p90a} - t_{p10}} \quad (4.6)$$

$$n_{pd} = \frac{0.6N_{pm}}{t_{p30} - t_{p90b}} \quad (4.7)$$

Similarly, the floc production rate  $n_{fp}$  and decay rate  $n_{fd}$  are given by:

$$n_{fp} = \frac{0.8N_{fm}}{t_{f90a} - t_{f10}} \quad (4.8)$$

$$n_{fd} = \frac{0.6N_{fm}}{t_{f30} - t_{f90b}} \quad (4.9)$$

where  $N_{fm}$  is the peak value of  $N_f$ ,  $t_{f10}$  and  $t_{f90a}$  are the times when  $N_f$  first reached 10 % and 90 % of  $N_{fm}$ , respectively, in seconds, while  $t_{f90b}$  and  $t_{f30}$  are the times when  $N_f$  dropped below 90 % and 30 % of  $N_{fm}$ , respectively. The production and decay rates of particles and flocs were calculated for each run and averaged over the three runs within each experiment series and were presented as a series average with a standard error.

Furthermore, the mean particle and floc number concentration, defined as  $\bar{N}_p$  and  $\bar{N}_f$ , were computed by dividing the area under the  $N_p$  or  $N_f$  time series from each run by the duration.  $\bar{N}_p$  and  $\bar{N}_f$  were calculated for each run and presented as a series average with a standard error. After all image data within each experiment series were processed, the particle and floc size distributions were generated using all particles/flocs detected from all three repeated runs in a series, and the series mean and standard deviation of particle and floc sizes were computed.

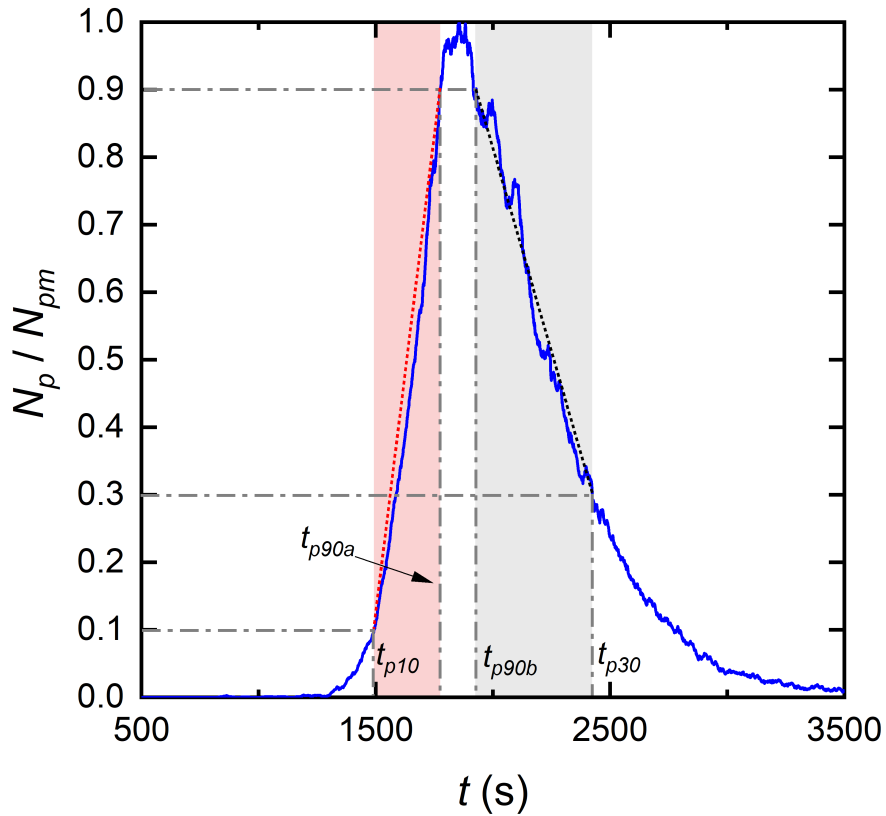


Figure 4.4: Typical time series of normalized particle number concentration  $N_p/N_{pm}$ . Note the data used for plotting is from a S2 experiment, the shaded areas represent the interval used to calculate the production (red) and decay (grey) rates.

## 4.3 Results

### 4.3.1 Time Series

Figure 4.5 presents a complete set of synchronized time series of air and water temperature, particle and floc number concentrations and mean sizes, and total ice volume concentration for all three repeated runs in S4 to demonstrate the repeatability and variations in the time series. It can be seen from Figure 4.5 that in all subplots, the time series from the three repeated runs have similar trends, confirming the repeatability of the experiments. In Figure 4.5c-g, notable variations caused by the random ice processes can be observed. In Figure 4.5c,  $N_{pm}$  are shifted slightly in both time and magnitude from each other, which could be due to the variations in the secondary nu-

cleation and flocculation processes. In Figure 4.5c-f, a significant deviation in the Run 1 time series between 3,400 s and 3,800 s can be observed. This was caused by re-entrainment of flocculated surface slush ice, leading to the appearance of particles and flocs in the images. Figure 4.5g shows that the time series of  $C_i$  are quite spiky. This is because  $C_i$  is very sensitive to the appearance of large flocs in the images. Similar time series plots of repeated runs from the rest of the series had similar characteristics to Figure 4.5 indicating that the three repeated runs in all series were sufficiently repeatable. Therefore, ensemble-averaged time series of air and water temperature, as well as particle and floc mean sizes and concentrations were generated by averaging the time series of the three repeated runs in each series. This averaging reduced the random errors in the time series data and improved the subsequent analysis and interpretation of the results.

Figure 4.6 presents the ensemble-averaged time series of air and water temperatures, particle and floc number concentrations, and mean sizes plotted versus the nondimensionalized time ( $t/t_{c1}$ ) for G1. Figure 4.6a shows that during S1,  $T_a$  remained steady with a mean value of  $-4.49$  °C. During S2 - S5,  $T_a$  initially aligned well with S1, then as expected started decreasing at  $t/t_{c1} = 0.5, 1.0, 1.5,$  and  $2.0,$  respectively, reached a minimum of approximately  $-15$  °C at  $\sim 0.27 t_{c1}$  after the change and then fluctuated between  $-13.24$  and  $-14.68$  °C.

Figure 4.6b shows that S1 has a "classic" supercooling curve with a  $T_p$  value of  $-0.052$  °C. During S2 the slope of the supercooling curve increased immediately after  $T_a$  was decreased at  $t/t_{c1} = 0.5,$  which resulted in a shorter cooling duration of  $0.87 t_{c1}$  and a significantly lower  $T_p$  of  $-0.064$  °C. A linear fit of the S2  $T_w$  time series before and after the  $T_a$  change gives a slope of  $-0.0019$  °C/min and  $-0.0038$  °C/min, respectively. This indicates that the water cooling rate increased by a factor of two in response to the three-fold increase in heat flux. During S3  $T_a$  was lowered at  $t/t_{c1} = 1$  (Figure 4.6a). The supercooling curve was very similar to S1 with a slightly longer cooling duration of  $1.09 t_{c1}$  and similar  $T_p$  value (Figure 4.6b). During S4 and S5 the supercooling curve

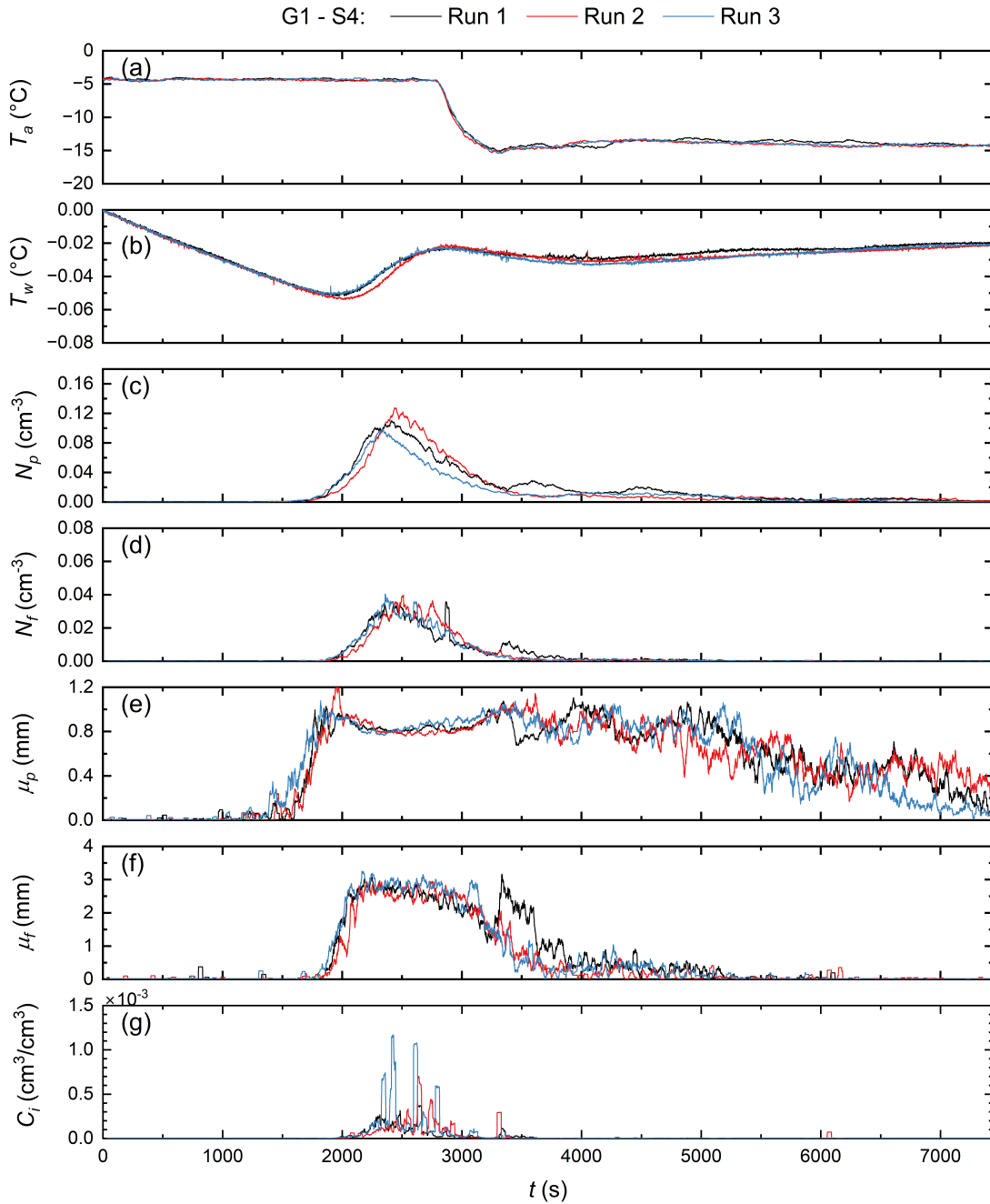


Figure 4.5: Time series of (a) air temperature  $T_a$ , (b) water temperature  $T_w$ , (c) particle number concentration  $N_p$ , (d) floc number concentration  $N_f$ , (e) particle mean size  $\mu_p$ , (f) floc mean size  $\mu_f$ , and (g) total ice concentration  $C_i$  for all S4 experiments in G1.

initially maintained a classic shape with similar  $T_p$  values and slightly longer cooling

durations of 1.05 and 1.08  $t_{c1}$ , respectively compared to S1 (Figure 4.6b). Shortly after  $T_a$  was decreased in S4 and S5, the water began to cool again at a rate of -0.0004 and -0.0003 °C/min, respectively, and reached a secondary local minimum of -0.031 and -0.033 °C, respectively (Figure 4.6b). These secondary local minimums, defined as  $T_{p2}$ , were both achieved at approximately 0.7  $t_{c1}$  after the decrease in  $T_a$ .

Figure 4.6c shows that in all series,  $N_p$  initially increased significantly prior to  $T_p$  and reached its maximum value  $N_{pm}$  at 0.14 - 0.24  $t_{c1}$  after  $T_p$ , and then decreased to a negligible value ( $< 0.001 \text{ cm}^{-3}$ ).  $N_{pm}$  in S2 and S3 were 0.15 and 0.14  $\text{cm}^{-3}$ , respectively, significantly higher than the  $\sim 0.1 \text{ cm}^{-3}$  in the rest of the series. In S4 and S5 where the heat flux change induced a second supercooling period (Figure 4.6b),  $N_p$  in S4 remained at a near-constant value of 0.01  $\text{cm}^{-3}$  before decreasing again at  $t/t_{c1} = \sim 2.5$ , while in S5  $N_p$  first decreased then started to rise again, reaching a secondary peak at  $t/t_{c1} = 2.88$  with a value of 0.02  $\text{cm}^{-3}$  before decreasing again. Figure 4.6d shows that the trend of  $N_f$  time series followed that of  $N_p$  closely and the time when  $N_f$  reached maximum is similar to the time  $N_p$  reached maximum.  $N_{fm}$  in S2 and S3 were 0.05 and 0.04  $\text{cm}^{-3}$ , respectively, significantly higher than the 0.03  $\text{cm}^{-3}$  in the rest of the series. During the second supercooling period in S4 and S5,  $N_f$  only reached 0.001 and 0.003  $\text{cm}^{-3}$ , respectively, an order of magnitude smaller compared to  $N_p$  in Figure 4.6c.

Figure 4.6e indicates that in all five time series  $\mu_p$  increased rapidly prior to when  $T_p$  was achieved, reaching a local maximum of  $\sim 1 \text{ mm}$ , and then plateauing for  $\sim 0.7 t_{c1}$ . During this plateaued period,  $\mu_p$  slowly decreased then increased again and reached a second local maximum of 0.85 mm in S2 and  $\sim 1 \text{ mm}$  in the rest of the series. After the second local maximum  $\mu_p$  had a decreasing trend in S1, S2 and S3, while in S4  $\mu_p$  stabilized and fluctuated around  $\sim 1 \text{ mm}$  and in S5  $\mu_p$  rebounded (*i.e.* first decreased then increased) to  $\sim 1 \text{ mm}$  again in response to the heat flux increase. In Figure 4.6f, time series of  $\mu_f$  shows that in all five series  $\mu_f$  increased rapidly shortly after a significant increase in  $\mu_p$  shown in Figure 4.6e and reached a maximum of  $\sim 3 \text{ mm}$ . After that  $\mu_f$  first decreased slowly then more rapidly to a negligible value in S1 - S3. While in S4

$\mu_f$  maintained at  $\sim 0.6$  mm before decreasing to a negligible value, and in S5  $\mu_f$  first decreased below 0.15 mm then started to increase and peaked again at 1.01 mm. The response of  $\mu_f$  during the second supercooling period was significantly weaker than  $\mu_p$  due to the significantly smaller number of flocs being generated during the same period as indicated in Figure 4.6d.

Figure 4.7 presents the ensemble-averaged time series of G2 experiments air and water temperature, particle and floc number concentrations, and mean sizes plotted versus the nondimensionalized time ( $t/t_{c6}$ ). It can be seen from Figure 4.7a that during S6  $T_a$  maintained a steady value averaging  $-14.35$  °C. During S7 - S10,  $T_a$  started to increase at  $t/t_{c6} = 0.5, 1.0, 1.5,$  and  $2.0$ , respectively, reaching the targeted  $-5$  °C  $\sim 0.3 t_{c6}$  after the change occurred which is comparable to the response time in the G1 experiments. After  $T_a$  reached  $-5$  °C it continued to rise to  $-3.3$  °C before decreasing to  $-6.8$  °C, eventually increased again to  $\sim -4$  °C in all four series. The average  $T_a$  values after it reached  $-5$  °C until the experiment ended were  $-4.34, -4.36, -4.72,$  and  $-5.03$  °C, respectively for S7 - S10, demonstrating the repeatability of these experiments.

Figure 4.7b shows that in S6 the supercooling curve has a  $T_p$  of  $-0.065$  °C and a residual temperature of  $-0.022$  °C. The only impact of increasing  $T_a$  at  $t/t_{c6} = 1, 1.5$  and  $2$  during S8 - S10, compared to the baseline case S6, was to slightly elevate  $T_w$  after  $T_a$  was increased and this resulted in a higher residual temperature of  $-0.016$  °C. However, during S7 the cooling rate was reduced immediately when  $T_a$  was increased at  $t/t_{c6} = 0.5$ , resulting in a significantly higher  $T_p$  of  $-0.053$  °C compared to S6 and the residual temperature was also slightly elevated to  $-0.016$  °C.

Figure 4.7c-d show that compared to S6, increasing  $T_a$  at  $t/t_{c6} = 1, 1.5$  and  $2$  during S8 - S10 did not significantly change the trends or magnitudes of the  $N_p$  and  $N_f$  time series. However, increasing  $T_a$  at  $t/t_{c6} = 0.5$  during S7 resulted in  $N_{pm}$  and  $N_{fm}$  values of  $0.11 \text{ cm}^{-3}$  and  $0.03 \text{ cm}^{-3}$ , a 21 % and 40 % reduction, respectively compared to S6. The times it took to reach the two maximums ( $N_{pm}$  and  $N_{fm}$ ) were also slightly longer compared to S6. Figure 4.7e shows that all  $\mu_p$  time series aligned quite well. This

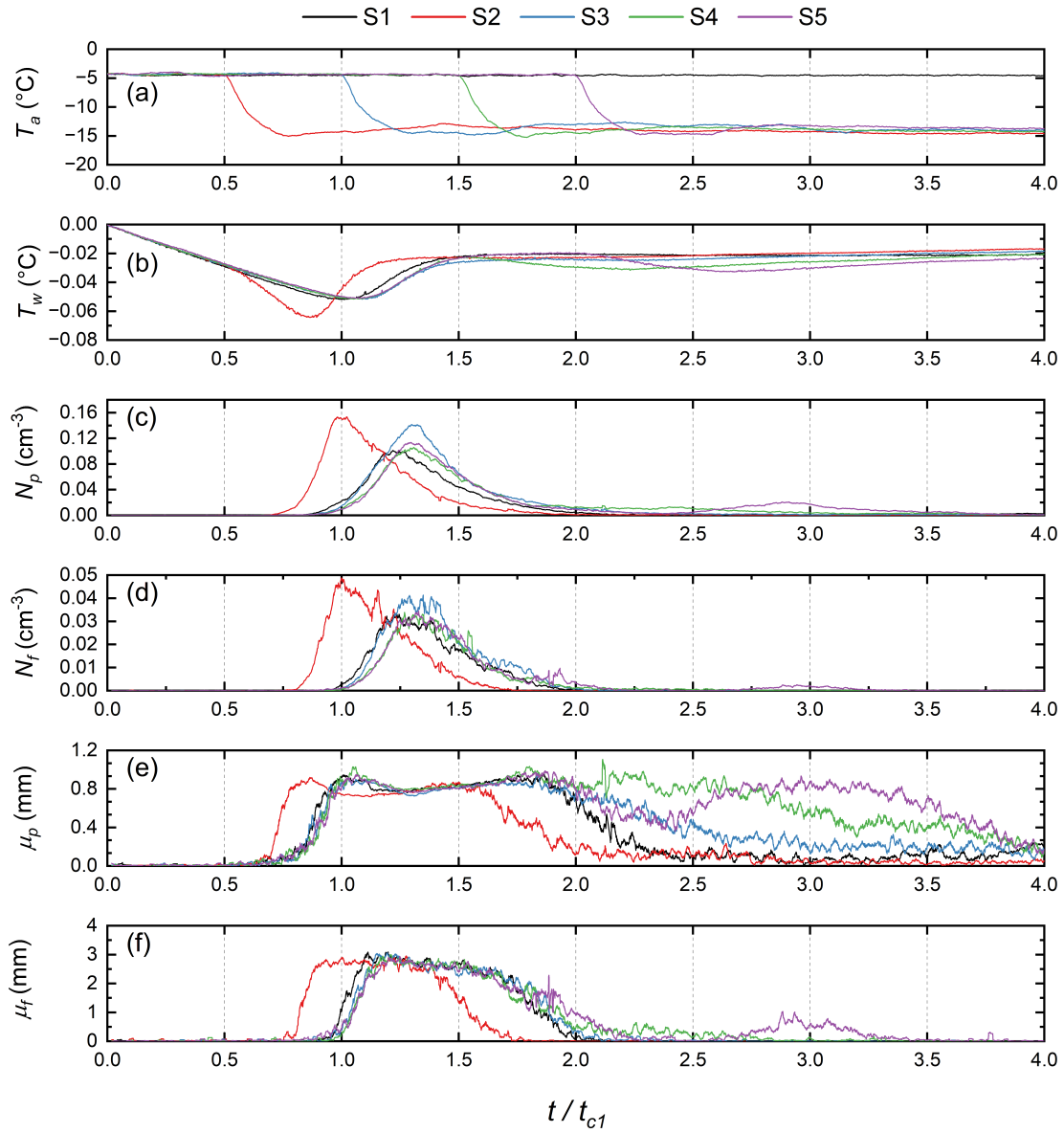


Figure 4.6: Ensemble-averaged time series of (a) air temperature  $T_a$ , (b) water temperature  $T_w$ , (c) particle number concentration  $N_p$ , (d) floc number concentration  $N_f$ , (e) particle mean size  $\mu_p$ , and (f) floc mean size  $\mu_f$  for all G1 experiments. Note the time  $t$  is nondimensionalized by  $t_{c1}$ , the averaged cooling duration obtained from the baseline experiment series S1.

was also the case for the  $\mu_f$  time series shown in Figure 4.7f except that during S7  $\mu_f$  increased slightly slower at the beginning and reached a maximum  $\sim 0.3 t_{c6}$  later than other series. Overall, results show that increasing  $T_a$  at  $t/t_{c6} = 0.5$  (S7) was

the only case that significantly impacted particle and floc number concentrations, by prolonging the time it took to achieve  $N_{pm}$  and  $N_{fm}$  and significantly reducing their values. Increasing  $T_a$  at different times did not significantly affect the evolution of particle and floc mean sizes.

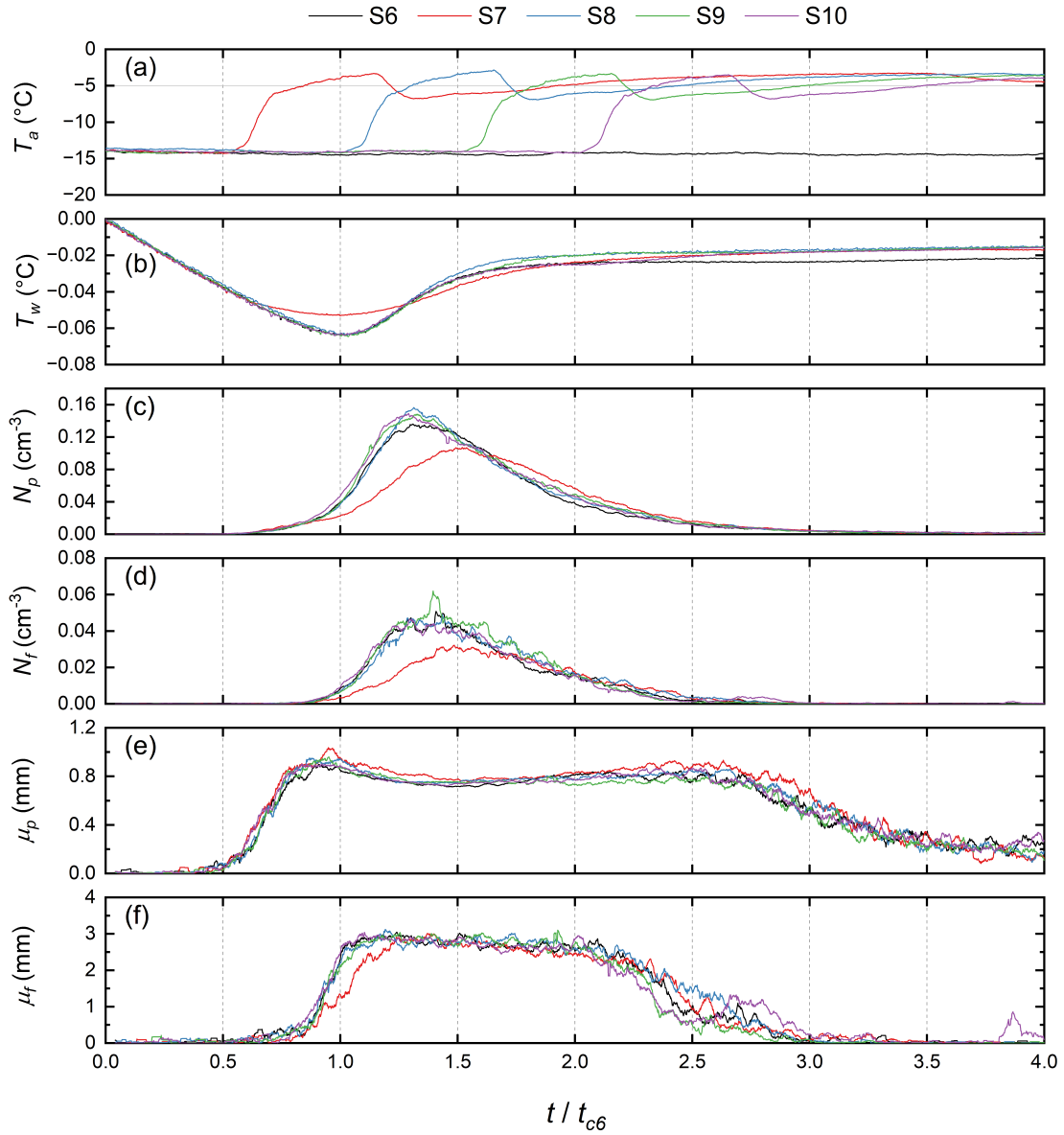


Figure 4.7: Ensemble-averaged time series of (a) air temperature  $T_a$ , (b) water temperature  $T_w$ , (c) particle number concentration  $N_p$ , (d) floc number concentration  $N_f$ , (e) particle mean size  $\mu_p$ , and (f) floc mean size  $\mu_f$  for all G2 experiments. Note the time  $t$  is nondimensionalized by  $t_{c6}$ , the averaged cooling duration obtained from the baseline experiment series S6.

Figure 4.8 shows time series of the ensemble-averaged measured and calculated (Equation (4.4) - Equation (4.5)) total volume ice concentration  $C_i$  versus nondimensionalized time for S1, S2, S6, and S7. The shaded area corresponds to the period when  $N_p$  the particle number concentration was decreasing, which can be seen in Figure 4.6c and Figure 4.7c. In Figure 4.8a-b the  $C_i$  time series for series S1 and S2 are plotted. Note that the time series for S3 - S5 are not presented since they were very similar to S1. In Figure 4.8a, the measured  $C_i$  increased significantly at  $t/t_{c1} = 1$ , and reached a maximum at  $0.45 \times 10^{-3}$  at  $t/t_{c1} = 1.2$  before decreasing to a negligible value due to the buoyancy driven vertical transport of suspended frazil ice to the water surface. Figure 4.8b shows that during S2 the measured  $C_i$  started to increase at  $t/t_{c1} = 0.8$  and reached a maximum at  $1 \times 10^{-3}$  at  $t/t_{c1} = 1$ , the maximum value is 2.2 times larger than in S1. Figure 4.8c-d presents the results for series S6 and S7, and plots of S8 - S10 were omitted due to their similarities with S6. In both S6 and S7, the measured  $C_i$  started to increase at  $t/t_{c6} = 1$  and reached a maximum at approximately  $t/t_{c6} = 1.3$ . In S6  $C_i$  reached a maximum at  $0.66 \times 10^{-3}$  while in S7 it reached the maximum at a significantly smaller value of  $0.35 \times 10^{-3}$ . It is worth noting that in all cases, the measured maximum  $C_i$  was reached at approximately 1.1 - 1.3 times their experiment cooling duration.

It is clear in Figure 4.8 that in all four series, the calculated  $C_i$  started rising earlier than the measured  $C_i$ . In Figure 4.8a-b the calculated  $C_i$  started to rise  $\sim 0.3 t_{c1}$  earlier and in Figure 4.8c-d it was  $\sim 0.9 t_{c6}$ . This is possibly because the measured data did not include the surface skim ice growth nor ice crystals smaller than the minimum size detectable by the camera system ( $108 \mu\text{m}$ ). The trend of calculated  $C_i$  generally followed measured values well after the measured  $C_i$  increased significantly. The percentage difference between the measured maximum  $C_i$  and its corresponding calculated value ranged from -5 % to 23 %. After that  $N_p$  started to decrease as indicated by the shaded area and measured  $C_i$  decreased accordingly while the calculated  $C_i$  was still increasing since the calculation did not account for the rising of flocs. Overall, the alignment

between the calculated and measured  $C_i$  time series prior to the rising of flocs demonstrates that the camera system used in this study did sample a significant fraction of the total ice being formed in the tank and provided accurate  $C_i$  measurements.

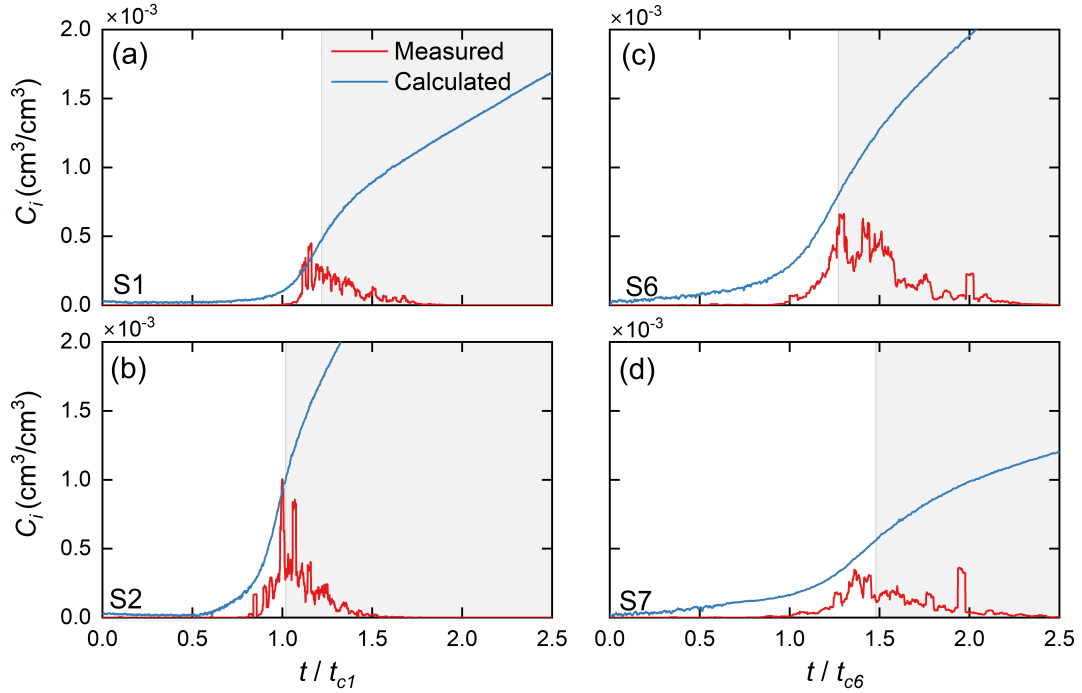


Figure 4.8: Ensemble-averaged time series of measured and theoretically calculated total ice concentration  $C_i$  for (a) S1, (b) S2, (c) S6, and (d) S7 experiments plotted with nondimensionalized time. The shaded area corresponds to the period after  $N_p$  started to decrease.

### 4.3.2 Production and Decay Rates

In Figure 4.9, bar plots of series-averaged production and decay rates of particles and flocs are presented. The error bar represents the standard error, and the number above the error bar indicates the significant p-value ( $< 0.05$ ) from a two-sample t-test comparing the means between the baseline series (S1 or S6) and other series. Note that heat flux change that occurred before or at  $t/t_{c1}$  ( $t/t_{c6}$ ) = 1 (*i.e.* S2, S3, S7, S8) could potentially impact both particle and floc production and decay rates since the change occurred prior to or during the period used for production rate calculation.  $T_a$  change that occurred at  $t/t_{c1}$  ( $t/t_{c6}$ ) = 1.5 (*i.e.* S4 and S9) may only affect particle and floc

decay rates since the change occurred after the period used for production rate calculation.  $T_a$  change occurred at  $t/t_{c1}$  ( $t/t_{c6}$ ) = 2 (*i.e.* S5 and S10) have negligible impact on both the particle and floc production and decay rates.

As can be seen in Figure 4.9a,  $n_{pp}$  values for S1, S3, S4 and S5 were similar ranging from 199 to 237 particles/( $m^3s$ ). The value for S2 was significantly larger at 453 particles/( $m^3s$ ) which was 2.3 times higher and the only statistically different value compared to S1. Particle decay rates  $n_{pd}$  ranged from 116 to 202 particles/( $m^3s$ ) and no statistically significant differences were found comparing S1 to the other series. Figure 4.9b shows that floc production and decay rates were 2 - 3 times smaller than the corresponding particle production and decay rates shown in Figure 4.9a. The effect of heat flux changes on the floc production rates  $n_{fp}$  was similar to the effect on particle production rates  $n_{pp}$ . For S2  $n_{fp}$  was 159 flocs/( $m^3s$ ) which was 1.9 times higher and statistically different compared to S1 while the values for the other series ranged from 79 to 96 flocs/( $m^3s$ ) and these were not statistically different from S1. The floc decay rates  $n_{fd}$  ranged from 54 to 67 flocs/( $m^3s$ ) and no significant differences were found.

Figure 4.9c-d show that decreasing the heat flux at  $t/t_{c6} = 0.5$  (S7) significantly reduced both  $n_{pp}$  and  $n_{fp}$  which is opposite to what was observed for G1 when the heat flux was increased. Particle ( $n_{pp}$ ) and floc ( $n_{fp}$ ) production rates were 172 particles/( $m^3s$ ) and 75 flocs/( $m^3s$ ), respectively for S7 and for the other series, they ranged from 343 to 403 particles/( $m^3s$ ) and 151 to 162 flocs/( $m^3s$ ), respectively. The production rates measured during S7 were comparable to those measured under a  $T_a$  of -5 °C in G1 (*i.e.* S1, S3, S4, and S5). However, the production rates measured during the rest of the G2 series were very similar to those measured in S2 when  $T_a$  was decreased from -5 to -15 °C at  $t/t_{c1} = 0.5$ . The decay rates plotted in Figure 4.9c-d show that  $n_{pd}$  and  $n_{fd}$  were 132 particles/( $m^3s$ ) and 43 flocs/( $m^3s$ ) for S7 and for the other series in G2 they ranged from 180 to 223 particles/( $m^3s$ ) and 69 to 120 flocs/( $m^3s$ ), respectively. Although no statistically significant differences were found comparing S6 to the other series, the decay rates measured in S7 were considerably smaller than the

rest of the series indicating that increasing  $T_a$  at  $t/t_{c6} = 0.5$  may also reduce the particle and floc decay rates.

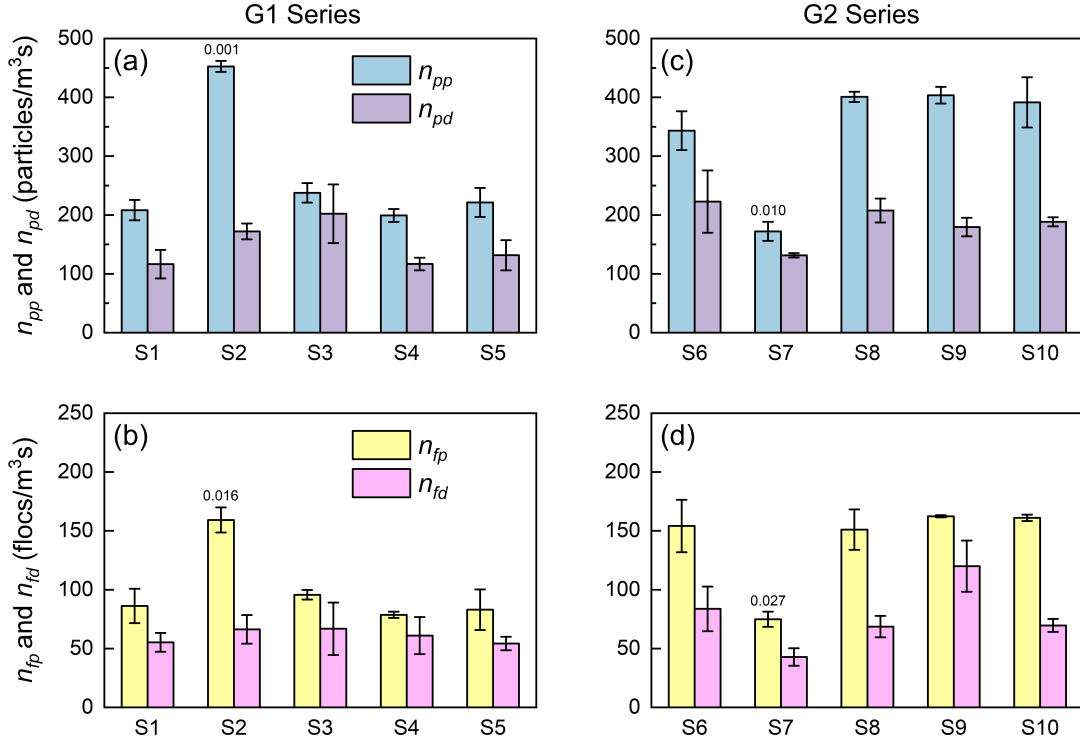


Figure 4.9: Bar plots of (a) particle production rate  $n_{pp}$  and particle decay rate  $n_{pd}$ , and (b) floc production rate  $n_{fp}$  and floc decay rate  $n_{fd}$  during G1 experiments, and (c-d) are for the G2 experiments. The error bar represents the standard error, and the number above the error bar indicates the significant p-value ( $< 0.05$ ) from a two-sample t-test comparing the means between the baseline series (S1 or S6) and the plotted experiment series.

### 4.3.3 Mean Number Concentrations

Figure 4.10 shows bar plots of  $\bar{N}_p$  and  $\bar{N}_f$  for both the G1 and G2 groups. As shown in Figure 4.10a,  $\bar{N}_p$  was  $0.012 \text{ cm}^{-3}$  in S1 and it ranged between  $0.015$  and  $0.016 \text{ cm}^{-3}$ , in S2 - S5 which was 25 - 33 % larger than S1. This increase was statistically significant for S2, S3, and S5 but was not for S4 due to its larger standard error.  $\bar{N}_f$  for all series in G1 ranged between  $0.0035$  and  $0.0044 \text{ cm}^{-3}$  and the values in S2 - S5 were not statistically significantly different from S1. Figure 4.10b shows that for the G2 series  $\bar{N}_p$  ranged

from 0.026 to 0.031  $\text{cm}^{-3}$  with no statistical difference between S6 and S7 - S10 values. However,  $\bar{N}_p$  in S7 was 10 % smaller than S6.  $\bar{N}_f$  ranged from 0.007 to 0.01  $\text{cm}^{-3}$  and the value of 0.007  $\text{cm}^{-3}$  in S7 was statistically different from S6 and was 22 % smaller than S6. The values of  $\bar{N}_p$  and  $\bar{N}_f$  in G2 (Figure 4.10b) were on average approximately twice as large as those in G1 (Figure 4.10a). As indicated in Section 4.2.4,  $\bar{N}_p$  or  $\bar{N}_f$  were calculated by dividing the area under the curve of  $N_p$  or  $N_f$  time series by the experiment duration, and G1 experiments have 2.2 times longer duration than G2. Therefore, the approximately twice larger values of  $\bar{N}_p$  and  $\bar{N}_f$  indicate that the area under the curve of the  $N_p$  or  $N_f$  time series of G1 and G2 experiments are similar. This suggests that the tank used in this study may only produce a certain amount of frazil particles due to its limited water volume.

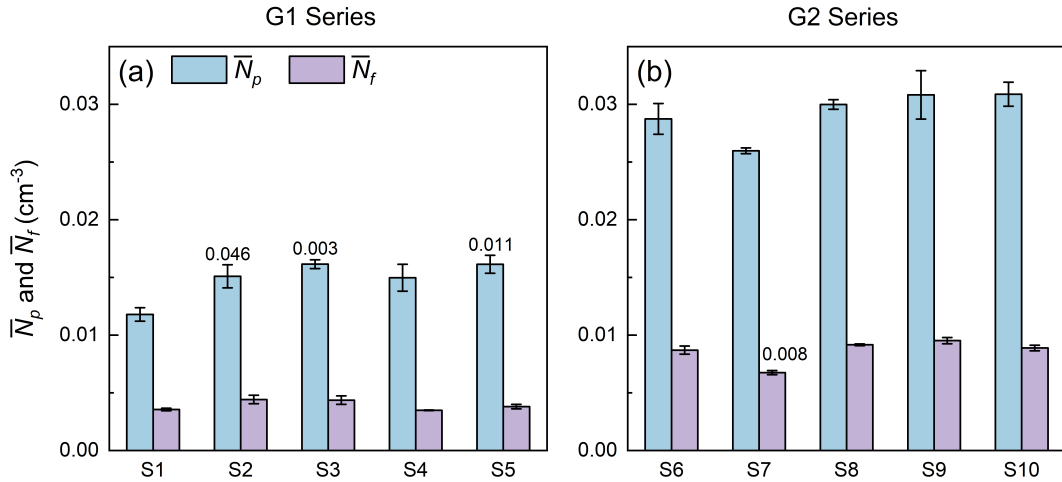


Figure 4.10: Bar plots of  $\bar{N}_p$  and  $\bar{N}_f$ , the mean particle and floc number concentration, respectively, for the entire experiment duration of (a) G1 and (b) G2 experiments. The error bar represents the standard error, and the number above the error bar indicates the significant p-value ( $< 0.05$ ) from a two-sample t-test comparing the means of the baseline series (S1 or S6) and the indicated experiment series.

### 4.3.4 Size Distributions and Properties

In Figure 4.11a-b the frequency size distributions of frazil particles and flocs, respectively for the S2 series are plotted along with theoretical lognormal distributions. Note that data over the entire duration of each experimental run were included when calculating these distributions. Although only distributions from the S2 series are presented, plots from other series were very similar. It is apparent that both particle and floc size distributions are slightly bimodal and deviate from a theoretical lognormal distribution. In Figure 4.11a, the particle size distribution has a small secondary peak centred at an  $S_p$  value of  $\sim 2$  mm. In Figure 4.11b, the floc size distribution has two approximately equal peaks and the location of the dip between the two peaks is also at  $\sim 2$  mm. This suggests that some flocs with sizes of  $\sim 2$  mm are likely being misclassified as particles. Overall, a theoretical lognormal distribution was found to be a reasonable fit for both the particle and floc size distributions.

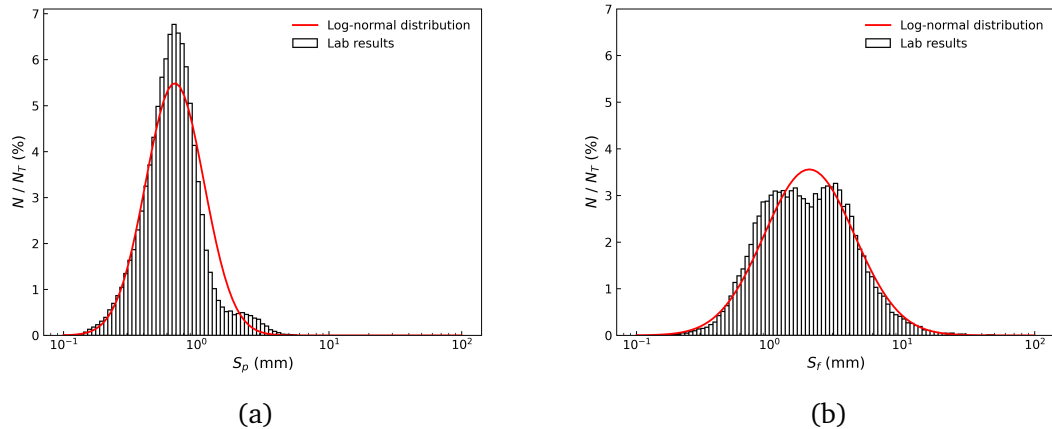


Figure 4.11: Frequency distributions of (a) particle size  $S_p$  and (b) floc size  $S_f$  in S2. The red line is a fitted log-normal distribution,  $N$  is the number of particles/flocs in each bin and  $N_T$  is the total number of particles/flocs.

Figure 4.12 shows the empirical cumulative frequency distributions of particle and floc sizes obtained from each series in G1. In Figure 4.12a the occurrence probability of S4 is the lowest compared to other series at a given  $S_p$ , and in Figure 4.12b S1 has the lowest occurrence probability at a given  $S_f$ . This indicates that the particles observed

in S4 and the flocs observed in S1 are distributed towards larger size bins compared to other plotted series. However, all particle or floc cumulative size distributions aligned closely with each other regardless of the heat flux change. Distributions from S6 - S10 in group G2, although not presented, also aligned closely with each other. This suggests that changes in the heat flux scenarios did not result in significant changes in the shape of the particle or floc size distributions.

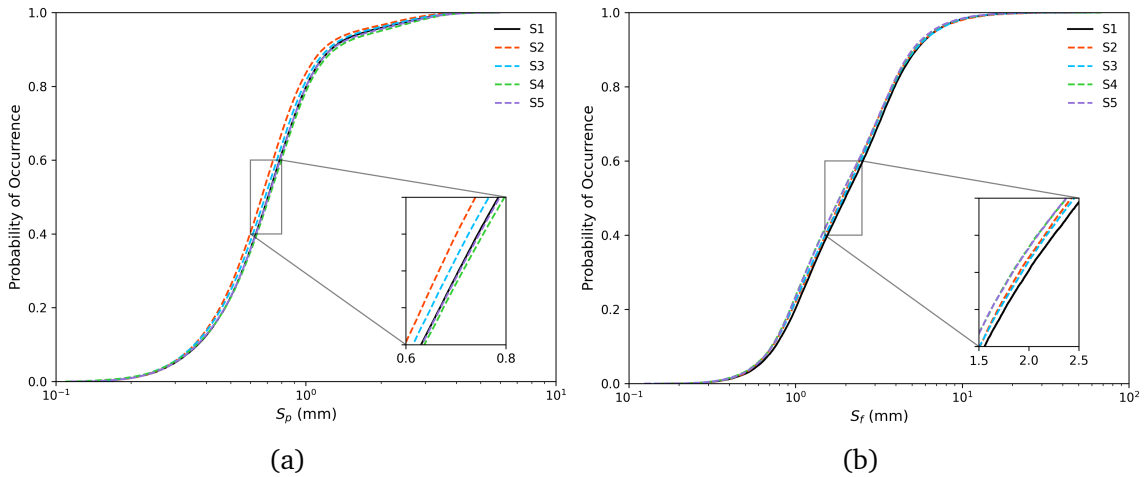


Figure 4.12: Empirical cumulative frequency distributions of (a) particle size  $S_p$  and (b) floc size  $S_f$  for series S1 - S5 in group G1. The y-axis limits for all inserts are from 0.4 to 0.6.

Table 4.3 summarizes the particle and floc mean sizes  $\mu_p$  and  $\mu_f$ , and corresponding standard deviations  $\sigma_p$  and  $\sigma_f$  calculated from the entire dataset from each series (*i.e.* data that included the entire duration from three repeated runs). The data in Table 4.3 show that in seven out of eight varied heat flux series  $\mu_p$  was statistically significantly different compared to the baseline experiments. However, only in S2 and S7 when the heat flux was varied at  $0.5 t_{c1}(t_{c6})$  resulted in changes larger than 5 % in  $\mu_p$ . In S2  $\mu_p$  was 0.77 mm which was 6 % smaller than in S1 but was similar to in S6. Note that S6 was conducted under S2's target air temperature of  $-15$  °C. Conversely, in S7  $\mu_p$  was 0.82 mm which was 8 % larger than in S6 but was similar to in S1. For the flocs in the G1 group, the mean floc size  $\mu_f$  was 2.71 mm in S1 and was decreased by 2 % to 5 % as the heat flux increased later and later from S2 to S5 and these changes were statistically

significant.  $\sigma_f$  decreased from 2.7 to 2.41 mm as well. In the G2 group,  $\mu_f$  in both S7 and S10 were statistically significantly different than S6 but S7 had the most distinct difference decreasing by 5 %. In the eight series with varied heat flux, seven resulted in a decreased  $\mu_f$  compared to their baseline experiments, and only one (S9) resulted in a slightly increased  $\mu_f$  compared to its baseline experiments (S6). This may indicate that the mean floc size generally reduces when the surface heat flux is varied. Overall  $\mu_p$  and  $\sigma_p$  ranged from 0.76 to 0.84 mm and 0.46 to 0.58 mm, respectively, and  $\mu_f$  and  $\sigma_f$  ranged from 2.57 to 2.78 mm and 2.41 to 2.95 mm, respectively. Varying heat flux resulted in a maximum of 8 % and 5 % change in  $\mu_p$  and  $\mu_f$ , respectively compared to the baseline series, indicating that the heat flux variations do not significantly change mean particle or floc sizes.

Table 4.3: Ensemble particle and floc mean sizes  $\mu_p$  and  $\mu_f$ , and corresponding standard deviations  $\sigma_p$  and  $\sigma_f$  in each series. The bolded number indicates the significantly different values (p-value < 0.05) comparing the means of the baseline series (S1 or S6) and the indicated experiment series using a two-sample t-test.

| Group | $\mu_p \pm \sigma_p$ (mm) | $\mu_f \pm \sigma_f$ (mm) | Group | $\mu_p \pm \sigma_p$ (mm) | $\mu_f \pm \sigma_f$ (mm) |
|-------|---------------------------|---------------------------|-------|---------------------------|---------------------------|
| G1    |                           |                           | G2    |                           |                           |
| S1    | 0.82 ± 0.54               | 2.71 ± 2.54               | S6    | 0.76 ± 0.46               | 2.77 ± 2.73               |
| S2    | <b>0.77</b> ± 0.49        | <b>2.67</b> ± 2.70        | S7    | <b>0.82</b> ± 0.53        | <b>2.63</b> ± 2.42        |
| S3    | <b>0.80</b> ± 0.53        | <b>2.65</b> ± 2.56        | S8    | <b>0.78</b> ± 0.50        | 2.76 ± 2.86               |
| S4    | <b>0.84</b> ± 0.58        | <b>2.59</b> ± 2.52        | S9    | 0.77 ± 0.48               | 2.78 ± 2.95               |
| S5    | <b>0.82</b> ± 0.56        | <b>2.57</b> ± 2.41        | S10   | <b>0.77</b> ± 0.48        | <b>2.73</b> ± 2.66        |

## 4.4 Discussion

### 4.4.1 Supercooling Under Varied Heat Flux Scenarios

During the varied heat flux experiments, changing  $T_a$  between -5 °C and -15 °C equates to a net heat flux variation between -173  $W/m^2$  and -519  $W/m^2$ , respectively, as discussed in Section 4.2.4. Several studies have reported heat flux analysis during super-

cooling events in rivers. Richard et al. (2015) recorded four supercooling events during the 2005 - 2006 freeze-up season in the St. Lawrence River that occurred when the net heat flux dropped below  $-200 \text{ W/m}^2$  with the most extreme one dropping below  $-500 \text{ W/m}^2$ . McFarlane and Clark (2021) recorded six supercooling events in the Dauphin River in Manitoba which occurred when the net heat flux varied between  $-189$  and  $13.8 \text{ W/m}^2$ . Boyd et al. (2023) observed diurnal fluctuations in the net heat flux during one prolonged supercooling event at the Peace River that ranged between  $-354$  to  $256 \text{ W/m}^2$ . The net heat flux variation in this study was close to the range of observations from Richard et al. (2015), but the lower value of  $-519 \text{ W/m}^2$  was considerably below the most extreme events reported by McFarlane and Clark (2021) and Boyd et al. (2023). This suggests that the heat fluxes generated in this laboratory study were simulating more extreme field conditions.

Figure 4.6b shows that increasing heat flux at different times resulted in different supercooling responses compared to the baseline experiments S1. A threefold heat flux increase at  $t/t_{c1} = 0.5$  (S2) led to an immediate and significant increase in the cooling rate and a significantly higher  $T_p$  magnitude. This is likely because at the time of the temperature change there was no significant ice formation (see Figure 4.6c-d) releasing latent heat to compensate for the increased heat flux, as a result, the heat flux change is directly reflected in the increased cooling rate of water. Changes of heat flux after when peak supercooling or  $T_p$  was achieved, at  $t/t_{c1} = 1.5$  and  $2$  during S4 and S5, resulted in a second milder supercooling curve, with a smaller secondary cooling rate and smaller magnitude peak supercooling compared to the first supercooling curve. Carstens (1966) observed a similar secondary supercooling peak in cold room experiments conducted using a recirculating flume, when the heat flux was increased at twice the cooling duration time by changing the wind speed from  $0$  to  $3 \text{ m/s}$ . Carstens (1966) reported that the smaller peak supercooling magnitude compared to the first was probably due to significant surface ice coverage when the heat flux was increased. As mentioned in Section 4.2.4, the surface slush insulated approximately one-third of

the water surface. In addition, the growth of surface slush would also have been releasing latent heat into the water. The effect of both reduced the cooling rates resulting in milder second supercooling events during S4 and S5. In S3 when the heat flux increased at the time of peak supercooling (*i.e.*  $t/t_{c1} = 1$ ), the supercooling curve and the magnitude of  $T_p$  surprisingly did not change significantly compared to S1 although the timing of  $T_p$  was slightly later than S1. However, both maximum particle and floc number concentrations were significantly higher than S1 (Figure 4.6c-d). At the time when  $T_p$  was achieved, the latent heat released by ice just reached balance with the surface heat loss. After the heat flux increased, the increased frazil particles and floc number concentrations further balanced the elevated heat loss, thus maintaining an unchanged supercooling curve.

Figure 4.7b shows that a threefold heat flux decrease at  $t/t_{c6} = 0.5$  (S7) reduced the cooling rate and significantly decreased  $T_p$  magnitude compared to the baseline series S6. Decreasing heat flux at  $t/t_{c6} = 1, 1.5$  and  $2$  only slightly elevated  $T_w$  afterwards and resulted in a 27 % higher residual supercooling temperature compared to S6, but it did not change the "classic" shape of the supercooling curve. This was expected since after significant ice was formed, the decreased heat flux does not create new demand for particle formation and growth, therefore, the latent heat released by ice only increased the water temperature until a rebalance between the reduced surface heat loss and latent heat was achieved. As a result, the residual supercooling temperature was raised slightly.

Kalke et al. (2019) classified field measurements of supercooling in the North Saskatchewan River into three types and concluded that about one-third of the observed events followed the classic supercooling curve shape which was probably produced under approximately constant upward air-water heat flux. However, in this study, classic supercooling curves were observed when the heat flux increased at  $t/t_{c1} = 1$  (S3) in G1 experiments, and decreased at or after  $t/t_{c6} = 1$  (S8 - S10) in G2 experiments. These observations demonstrated that approximately constant heat flux is not necessarily re-

quired to achieve a classic-shaped supercooling curve.

#### 4.4.2 Particle and Floc Number Concentrations

The ensemble-averaged time series of particle and floc number concentrations  $N_p$  and  $N_f$  in G1 experiments (Figure 4.6c-d) showed that, increasing heat flux threefold at  $t/t_{c1} = 0.5$  and 1 increased the maximum number concentration of particles and flocs by 40 - 50 % and 33 - 67 %, respectively. Increasing heat flux threefold at  $t/t_{c1} = 1.5$  and 2 resulted in secondary maximums in particle and floc number concentrations that were 5 - 30 times smaller than the first. Overall, the heat flux increase led to increases in the mean particle number concentration  $\bar{N}_p$  by 25 to 33 % but did not significantly increase the mean floc number concentration  $\bar{N}_f$  as shown in Figure 4.10a. The increase in particle number concentration when the heat flux increased is logical since more latent heat release by ice generation is required to balance the increased heat flux regardless of the timing of the heat flux increase, the increased  $N_p$  provides an increased likelihood for particles to flocculate, thereby increasing  $N_f$  as well. Another interesting observation is that increasing heat flux threefold at  $t/t_{c1} = 1$  led to increases in both maximum number concentration of particles and flocs but did not increase the  $T_p$  magnitude (Figure 4.6b). This may suggest that the seeding particles were sufficient in the cold room environment to trigger the nucleation and growth of frazil particles in response to the increased heat flux. Instead, if the seeding particles were limited preventing more frazil particles from forming to compensate for the surface heat loss, the water temperature may continue to decrease resulting in a much higher  $T_p$  magnitude.

The ensemble-averaged time series of particle and floc number concentrations  $N_p$  and  $N_f$  in G2 experiments (Figure 4.7c-d) showed that only by decreasing heat flux threefold at  $t/t_{c6} = 0.5$  (S7) did it significantly decrease the maximum particle and floc number concentration by 21 and 40 %, respectively, which also decreased  $\bar{N}_p$  and  $\bar{N}_f$  by 10 and 22 %, respectively as shown in Figure 4.10b. During S7, the heat flux decreased prior to significant ice formation when the water was still cooling. Therefore,

the decrease in heat flux directly decreased the demand for frazil particle production, thus reducing particle and floc number concentrations and increasing water temperature. Results from S8 - S10 show that decreasing heat flux at or after  $T_p$  was achieved did not significantly reduce particle and floc number concentrations. In these series, the heat flux decrease occurred when or after latent heat released by frazil growth already balanced the initial heat flux condition. This indicates that a significant amount of ice, including small particles not visible to the camera, had already formed at the time of the heat flux decrease. These particles likely continued growing with inertia and producing new particles by secondary nucleation even after the heat flux was reduced. Therefore, the particle and floc number concentrations shown in Figure 4.7c-d did not decrease but remained similar to S6.

Series-averaged particle and floc production and decay rates shown in Figure 4.9 indicate that increasing or decreasing heat flux at a dimensionless time of 0.5 approximately increases or decreases the particle and floc production rates by a factor of two and that these changes are statistically significant. This indicates that the production of particles and flocs quickly adapts when the heat flux is varied prior to the start of significant ice formation. But particle and floc production rates did not change significantly when the heat flux was varied at  $T_p$ . As discussed earlier at that time significant number of ice particles might had already formed and would grow and multiply with inertia. Therefore, the production rates did not change significantly.

It is worth noting that Clark and Doering (2009) measured particle production rate in a laboratory counter-rotating flume and the values ranged from 82 to 1119 particles/( $m^3s$ ). In this study, the particle production rate ranged from 172 to 453 particles/( $m^3s$ ), which falls within the range observed by Clark and Doering (2009). Clark and Doering (2009) also noted that the particle production rate increases with increasing turbulence intensity and larger magnitudes of peak supercooling. Although in this study the turbulence intensity was kept constant, larger magnitudes of peak supercooling did correspond to higher particle production rates.

### 4.4.3 Particle and Floc Sizes

Time series plots in Figure 4.6e-f show that significant changes in the trends and magnitudes of the  $\mu_p$  and  $\mu_f$  time series were observed in S4 and S5. In S4 increasing heat flux at  $t/t_{c1} = 1.5$  prolonged the plateau period duration of  $\mu_p$  fluctuating around 1 mm and led to a secondary maximum in  $\mu_f$  of  $\sim 0.6$  mm, while in S5 increasing heat flux at  $t/t_{c1} = 2$  caused a rebound in the time series of  $\mu_p$  and  $\mu_f$  with both peaking at  $\sim 1$  mm before they decreased again. These changes were accompanied by slight increases in the particle and floc number concentrations as seen in Figure 4.6c-d, indicating that a small number of particles were forming and growing again in response to the increased heat flux during the residual supercooling phase. Time series plots in Figure 4.7e-f show that decreasing heat flux did not result in significant changes in the trends or magnitudes of  $\mu_p$  and  $\mu_f$  regardless of the time of change. This is logical since decreasing heat flux does not create new demands for particles to form and grow, therefore does not affect the size evolution of the existing particles and flocs.

Previous field measurements reported mean particle size measurements ranged from 0.32 to 1.32 mm (Marko and Jasek 2010; Richard et al. 2011; McFarlane et al. 2019b) and mean floc size ranged from 1.19 to 5.64 mm (Pei, Yang, et al. 2024). Table 4.3 shows that the mean particle and floc sizes ranged from 0.76 to 0.84 mm and 2.57 to 2.78 mm, respectively, which falls within the range of those observed in field environments. However, the range of mean sizes observed in this study is considerably smaller than the range observed in the field. This could be because this study only examined varied heat flux scenarios, whereas in the field the availability of seeding particles and varying hydraulic conditions might also affect the evolution of particle and floc.

## 4.5 Conclusions

A total of 30 experiments were performed to generate and image frazil ice particles and flocs under constant air-water heat flux, as well as when the heat flux was increased or decreased approximately threefold at different times during supercooling events.

The sizes and concentrations of frazil particles and flocs were measured. The effect of varying heat flux at different times of supercooling events on the characteristics of the supercooling curve, as well as the frazil particle and floc properties, were investigated. Results show that increasing heat flux at different times during supercooling raised the mean particle number concentration  $\bar{N}_p$  by 25 - 33 % but did not significantly affect the mean floc number concentration  $\bar{N}_f$ . Decreasing heat flux significantly reduced mean particle and floc number concentrations ( $\bar{N}_p$  and  $\bar{N}_f$ ) by 10 and 22 %, respectively, but only when the change occurred prior to peak supercooling. Overall, changes in heat flux only had a minor effect on the mean particle and floc sizes and did not alter their lognormal size distributions.

It is evident that increasing heat flux prior to peak supercooling (*i.e.* at  $0.5 t_{c1}$  or  $t_{c6}$ ), when no significant ice formation is detected, results in an immediate increase in the cooling rate, raising the magnitude of peak supercooling, and significantly increasing the particle and floc production rates as well as maximum number concentrations to a level similar to constant heat flux experiments performed under the target heat flux condition. Conversely, decreasing heat flux prior to peak supercooling reduces the cooling rate and the peak supercooling magnitude, and significantly decreases production rates and maximum number concentrations aligning them with post-change constant heat flux experiments. This suggests that the formation and evolution of frazil particles and flocs quickly adjust to the new heat flux conditions if the heat flux increases or decreases prior to any significant ice formation. Increasing heat flux after peak supercooling (*i.e.* at  $1.5$  and  $2t_{c1}$ ) initiated a second supercooling period with five times smaller cooling rates and 1.6 times smaller peak supercooling than the first supercooling period. During this second supercooling period, particle and floc number concentrations reached a second maximum before decreasing although they were significantly smaller than the first. This indicates that particles and flocs could start forming again during the residual phase in response to the increased heat flux.

The most interesting observation is that increasing heat flux at peak supercooling

(i.e. at  $1 t_{c1}$ ) does not significantly change the shape of the supercooling curve or the peak supercooling magnitude despite significant increases in particle and floc number concentrations. This is important for two reasons: first, it demonstrates that the classic supercooling curve does not always indicate constant heat flux conditions; second, particle and floc production does not necessarily cause dramatic changes in the supercooling curve. The fact that the peak supercooling magnitude did not increase while particle and floc production increased significantly suggests that the laboratory experiments may have been conducted under sufficient seeding particles. It also implies that a lack of seeding particles might drive the peak supercooling to greater magnitudes rather than keeping it unchanged, resulting in different particle and floc evolution processes.

This study demonstrates that varying heat flux during different stages of supercooling leads to significantly different responses in particle and floc evolution. This highlights the need to simultaneously monitor water temperature and heat fluxes in natural environments where heat flux is rarely a constant. It is also worth noting that this study only examined threefold heat flux variation and the surface ice coverage in some cases further reduced the magnitude of variation. The availability of seeding particles was also not controlled and the hydraulic condition was kept the same. Therefore, future studies should reduce the effect of surface ice coverage, and explore varying seeding availability and hydraulic conditions together with heat flux to gain a more comprehensive understanding.

# Chapter 5

## Laboratory Study of the Correlation Between Frazil Ice Particle and Floc Properties

### 5.1 Introduction

Frazil ice particles form in turbulent water that is supercooled below its freezing point by heat loss to the atmosphere. Suspended frazil ice particles may collide and adhere to each other in the turbulent flow, forming clusters of particles known as frazil flocs and this process is referred to as flocculation (Clark and Doering 2009). The collision between existing ice, as well as fluid shear, may also cause breakage of ice particles/flocs. As frazil flocs grow in size, their buoyancy may overcome the turbulence of the flow and then they will rise to the surface forming frazil ice pans (Hicks 2016). Typically, the accumulation of surface ice pans results in the formation of a solid ice cover which insulates the water and halts the supercooling as well as the frazil ice generation. The evolution of frazil floc properties and subsequent floc rise has a profound influence on surface ice generation and ice cover formation. However, it is still relatively poorly understood.

A number of laboratory studies have investigated the size and concentration evolution of frazil ice particles during supercooling (Ye 2002; Clark and Doering 2006; McFarlane et al. 2015; Schneck et al. 2019). It was found that the number concentration of suspended particles first increased slowly and then more rapidly, reaching a maximum

just after peak supercooling (*i.e.* the minimum water temperature) occurred. After peaking the particle concentration decreased. The mean particle diameter increased before reaching a maximum around the time peak supercooling occurred, began to decrease and level off to an approximately constant size once the number of particles began to decrease. Schneck et al. (2019) also reported simultaneous measurements of floc properties together with particle properties. It was found that in freshwater, the floc number concentration and mean size started to increase significantly just prior to peak supercooling, and reached a maximum shortly afterwards. After that floc number concentration decreased slowly while the mean floc size continually increased very slowly. The evolution of particle and floc sizes and concentrations are clearly correlated as flocs are formed by the flocculation of particles. However, no detailed quantitative study on the correlation between particle and floc properties during different stages of supercooling has been reported. Therefore, it is of interest to look into the correlation between the properties of particles and flocs during supercooling in order to further our understanding of the physics behind frazil flocculation and improve frazil ice dynamics models that simulate the frazil flocculation process (Hammar and Shen 1995; Rees Jones and Wells 2018).

In this study, a series of laboratory cold room experiments were performed in a frazil ice tank to investigate the correlation between frazil ice particles and floc number concentrations and sizes under different air temperatures and turbulent dissipation rates. Time series images of suspended frazil ice particles and flocs were obtained using a high-resolution camera system. Images were analyzed to compute frazil ice particles and floc number concentrations and sizes. Precision temperature recorders were used to measure water and air temperatures. Time series of frazil ice particle and floc sizes and concentrations are presented, and their correlation during different stages of supercooling was analyzed. Effects of different turbulent dissipation rates and air temperatures on the correlation between frazil ice and floc properties are discussed.

## 5.2 Experimental Setup and Methods

The laboratory experiments were conducted inside the University of Alberta's Cold Room Facility in a frazil ice tank. The tank has a base dimension of 0.8 m by 1.2 m and was filled with filtered tap water to a depth of 1.3 m. As shown in Figure 5.1, Four synchronized propellers were mounted on the bottom of the tank and powered by a NEMA 34 DC variable speed electric motor to generate turbulent flow in the tank. The side walls and bottom of the tank were insulated with Owens Corning FOAMULAR C-200 XPS rigid foam insulation board with a thickness of 51 mm so that the majority of heat exchange occurred across the air-water interface.

Two openings were cut from the insulation. The back opening was used for mounting a Genaray SpectroLED Essential 360 Daylight LED light against the back glass to provide backlighting. The light was diffused by a translucent plastic sheeting with a thickness of 1.5 mm. The front opening was located directly opposite to the light and was used as a viewing window for the camera. Two 16 cm  $\times$  16 cm square Cavision glass linear polarizing filters, mounted 90° separated by a 3.1 cm gap, were installed inside the tank firmly against the front tank glass so that the ice particles and flocs passing through the gap were visible in the front opening. A 36-megapixel Nikon D800 DSLR camera with a Micro-Nikkor 60 mm f/2.8D lens was mounted outside of the tank, focused on the polarizers to capture images of frazil particles and flocs as they were advected between the polarizers. The camera was programmed to capture images at 1 Hz with an ISO of 6400, a shutter speed of 1/2000 s, and a f-stop of f/25. The configuration resulted in an average image pixel size of 21.6  $\mu\text{m}$  per pixel and a 159 mm  $\times$  106 mm field of view. A space heater was mounted beside the camera to blow warm air onto the glass window to prevent frost formation. In addition, the water temperature was logged in real-time at 1 Hz using a Sea-Bird SBE 39plus temperature recorder (accuracy  $\pm$  0.002 °C) mounted at the same water depth as the polarizer centroid. An RBR Solo T temperature recorder (accuracy  $\pm$  0.002 °C) was mounted on the top of the tank 15 cm above the water surface to measure the air temperature every second.

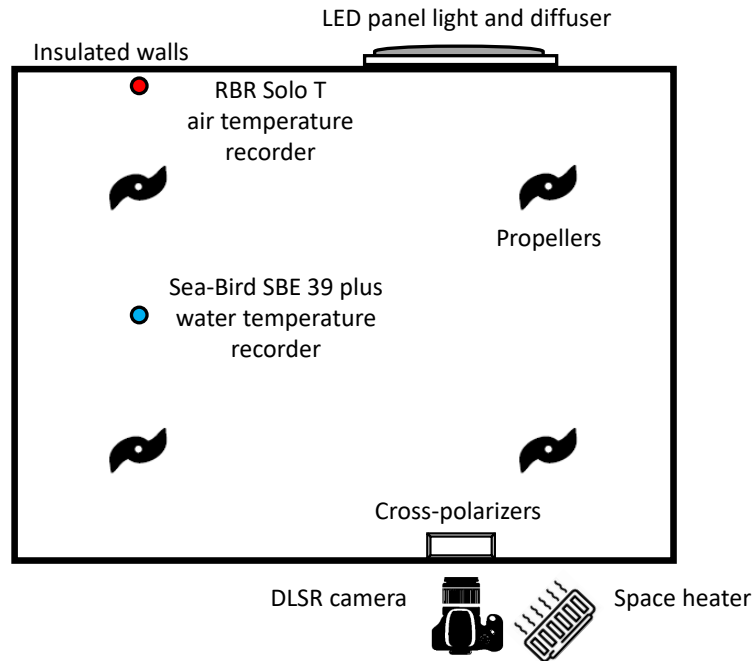


Figure 5.1: Plan view of the frazil tank showing the locations of instrumentation and equipment.

At the start of each experiment, the space heater was turned on, the cold room was programmed to maintain a target steady air temperature, and the bottom propellers were set to a desired constant speed using a laser tachometer. The air and water temperature recorders were programmed to start collecting data. Fifteen minutes before supercooling started, the polarizers were mounted in the tank and the camera was positioned and focused on the polarizers. Scale images of a ruler placed at the front, middle, and back of the polarizer gap were taken to determine the average pixel resolution. Ten background images prior to ice formation were captured. One minute before supercooling started, the camera was programmed to begin taking images. The supercooling start time as well as the time when peak supercooling temperature (*i.e.* minimum water temperature, defined as  $T_p$ ) was achieved were recorded, and the period between was defined as the cooling period  $t_c$ . Each experiment was run for at least a total duration of  $3.5 t_c$  to allow most suspended frazil ice particles and flocs to rise to the surface, after that the equipment was retrieved from the cold room and the air

temperature in the cold room was raised above zero degrees to thaw the ice.

Three groups of experiments were performed to examine the effect of turbulence and air temperature on the correlation between particle and floc properties. Group #1 (G1) and #2 (G2) were performed with a cold room air temperature of  $-5\text{ }^{\circ}\text{C}$  and propeller speeds of 325 rpm and 225 rpm, respectively. Group #3 experiments (G3) were performed using a propeller speed of 325 rpm and a cold room air temperature of  $-15\text{ }^{\circ}\text{C}$ . McFarlane et al. (2015) conducted ADV measurements in ice-free water in the same tank and estimated the tank averaged turbulent kinetic energy dissipation rates  $\varepsilon$  to be 85.5 and  $335.6\text{ cm}^2/\text{s}^3$  at propeller speeds of 225 and 325 rpm, respectively. Therefore, changing the propeller speed from 225 rpm to 325 rpm resulted in a  $\sim 4$  fold increase in  $\varepsilon$ .

### 5.3 Experiment Repeatability

For each experimental group, three repeat experiments were conducted to reduce the uncertainty of the results. Figure 5.2 shows the superimposed air and water temperature time series from the three repeated G1 experiments. Note each color represents one repeat experiment and the time series were aligned by the start time of supercooling (*i.e.* water temperature first drops to below  $0\text{ }^{\circ}\text{C}$ ). Figure 5.2a shows that the air temperature fluctuated between  $-3.8$  to  $-4.8\text{ }^{\circ}\text{C}$  with a mean of  $-4.49\text{ }^{\circ}\text{C}$ , indicating that the cold room was controlled within a  $1\text{ }^{\circ}\text{C}$  range of fluctuation. Figure 5.2b shows that the supercooling curves aligned quite well despite local spikes up to  $\sim 0.01\text{ }^{\circ}\text{C}$  in magnitude which were caused by ice momentarily contacting the thermistor tip of the Seabird logger.

Table 5.1 presents a summary of propeller speed and statistics from the repeatability analysis for each experimental group including the mean ( $\mu$ ) and the coefficient of variation (COV) for the mean air temperature  $T_{a\mu}$ , water cooling rate  $R_c$ , cooling period  $t_c$ , and the peak supercooling temperature  $T_p$ . The cooling rate  $R_c$  is defined as the slope of the water temperature time series from 10 mins prior to the start of supercooling

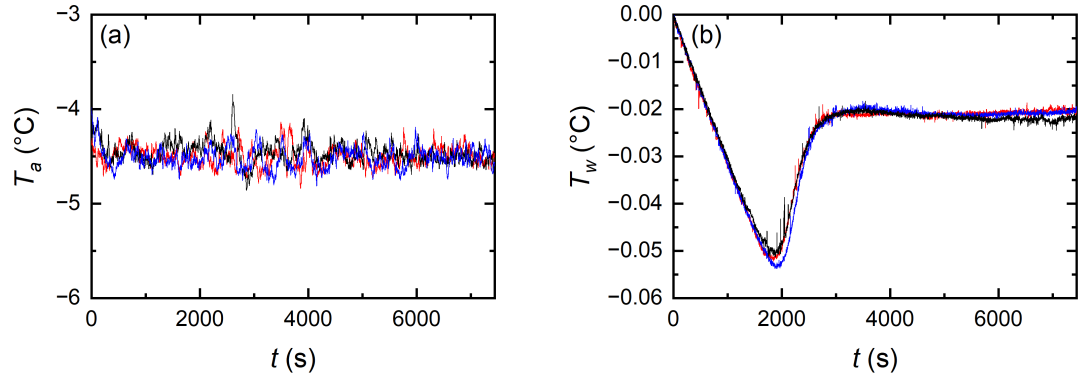


Figure 5.2: Superimposed (a) air temperature  $T_a$  and (b) water temperature  $T_w$  time series from Group #1 experiments. Note each color represents one repeat experiment.

to the start of supercooling, an illustration is provided in Figure 5.3 showing  $R_c$ ,  $t_c$ , and  $T_p$  labelled in a typical supercooling curve. As shown in Table 5.1, the measured mean air temperature  $T_{a\mu}$  was  $-4.49$  °C,  $-4.56$  °C and  $-14.35$  °C for G1, G2 and G3, respectively. The cooling rate  $R_c$ , cooling period  $t_c$ , and peak supercooling temperature  $T_p$  ranged from  $-0.002$  to  $-0.0057$  °C/min, 13.91 to 35.69 minutes, and  $-0.052$  to  $-0.071$  °C, respectively. Overall, the COV varied from 0.6 % to 4.9 %, demonstrating that the air and water temperatures were well-controlled and the time series were repeatable within acceptable limits.

Table 5.1: Summary of propeller speed and statistics including the mean ( $\mu$ ) and the coefficient of variation (COV) for the actual mean air temperature  $T_{a\mu}$ , water cooling rate  $R_c$ , cooling period  $t_c$ , and the peak supercooling temperature  $T_p$  for each experimental group.

| Exp. | Propeller speed (rpm) | $T_{a\mu}$ |         | $R_c$          |         | $t_c$       |         | $T_p$      |         |
|------|-----------------------|------------|---------|----------------|---------|-------------|---------|------------|---------|
|      |                       | $\mu$ (°C) | COV (%) | $\mu$ (°C/min) | COV (%) | $\mu$ (min) | COV (%) | $\mu$ (°C) | COV (%) |
| G1   | 325                   | -4.49      | 0.6     | -0.0020        | 1.4     | 31.27       | 0.2     | -0.052     | 2.4     |
| G2   | 225                   | -4.56      | 0.6     | -0.0023        | 4.9     | 35.69       | 3.2     | -0.071     | 2.1     |
| G3   | 325                   | -14.35     | 0.9     | -0.0057        | 0.7     | 13.91       | 3.1     | -0.065     | 4.0     |

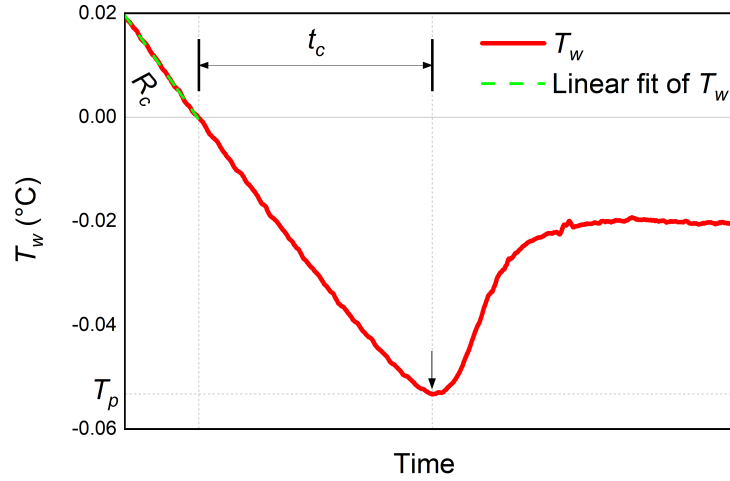


Figure 5.3: Schematics of water temperature time series during a supercooling event showing the cooling rate  $R_c$ , the cooling period  $t_c$ , and peak supercooling temperature  $T_p$ .

## 5.4 Data Processing

Sequences of images captured during each experiment were analyzed to compute the properties of frazil ice particles and flocs. First, the average of the background images was subtracted from each raw image to remove background noise. Each image was then processed using an iterative thresholding algorithm developed by McFarlane et al. (2014) to obtain the corresponding binary image containing the location and extent of each ice object (*i.e.* frazil ice particles and flocs) that did not intersect the image boundaries. The properties of each ice object such as area  $a$  and perimeter  $P$  were computed from the binary images. Each ice object was also fitted to an ellipse and the corresponding ellipse area  $a_e$ , perimeter  $P_e$ , as well as the major and minor axis lengths were computed. The size  $S$  of both frazil particles and flocs was defined as the major axis length of its fitted ellipse following previous studies (McFarlane et al. 2015; Clark and Doering 2009). Particles with a size smaller than  $108 \mu\text{m}$  (five times of pixel resolution) were eliminated because they were too pixelated. Next, each ice object was classified as either a frazil ice particle or floc based on their geometrical properties

following the criteria described in Section 3.4.1.

After classification, the mean particle size  $\mu_p$ , mean floc size  $\mu_f$ , particle number concentration  $N_p$ , and floc number concentration  $N_f$  were computed for each image. This time series data was smoothed by taking an average every 35 seconds and placing the average value at the end of each time window. The ensemble-averaged time series of water temperature as well as particle and floc number concentrations and mean sizes for each group were then computed. The number concentration is defined as the number of particles/flocs per unit volume. The measuring volume used for the number concentration calculation was the image field-of-view times the distance between the two polarizers. Several key times were defined to help characterize their evolution: the time when peak supercooling temperature was achieved ( $t_p$ ), the time when  $N_p$  first reached a threshold value of  $0.001 \text{ cm}^{-3}$  ( $t_s$ ), the time when  $N_p$  reached its maximum ( $t_N$ ), and the time when  $N_p$  first dropped below a threshold of  $0.001 \text{ cm}^{-3}$  ( $t_e$ ). The mean particle size  $\mu_p$  time series show that  $\mu_p$  first increased significantly, reaching a first local maximum, then decreased slightly before increasing again reaching a second local maximum, and afterwards it decreased continuously. Therefore, two additional times  $t_{\mu 1}$  and  $t_{\mu 2}$  were defined as the times when  $\mu_p$  reached the first and second local maximum, respectively.

## 5.5 Results and Discussion

### 5.5.1 Time Series

Ensemble-averaged time series plots of water temperature  $T_w$ , number concentration of particle ( $N_p$ ) and floc ( $N_f$ ), as well as particle ( $\mu_p$ ) and floc ( $\mu_f$ ) mean size for experiments G1, G2 and G3 are presented in Figure 5.4, Figure 5.5 and Figure 5.6, respectively. Key times are labelled in the plots as reference lines, and the period between  $t_s$  and  $t_e$  is shaded in yellow. For G1, supercooling reached a  $T_p$  of  $-0.052 \text{ }^\circ\text{C}$  at  $t_p$  of 1,882 s (Figure 5.4a), and then reached a residual temperature of  $-0.021 \text{ }^\circ\text{C}$  at 3,000 s. Figure 5.4b shows that both  $N_p$  and  $N_f$  increased above the threshold before  $t_p$ , reach-

ing a maximum of 0.10 and 0.03 cm<sup>-3</sup>, respectively at the same time ( $t_N$ ), and then decreased below 0.001 cm<sup>-3</sup> during the residual supercooling phase. It is worth noting that  $N_p$  increased above the threshold 245 s earlier than  $N_f$  and decreased below it 483 s later. The earlier increase was likely because a certain concentration of particles is required to form flocs and the later time that  $N_p$  fell below the threshold because flocs rise to the surface quicker than particles. In Figure 5.4c,  $\mu_p$  increased rapidly immediately after  $t_s$ , peaked locally at 0.90 mm at  $t_{\mu 1}$ , and then reached equilibrium from  $t_{\mu 1}$  to  $t_{\mu 2}$ . During this time  $\mu_p$  slowly decreased to 0.76 mm and increased again to a second local maximum of 0.96 mm at  $t_{\mu 2}$ . After that  $\mu_p$  continually decreased.  $\mu_f$  started to increase significantly slightly later than  $\mu_p$ , peaked at 3.02 mm 210 s before  $t_N$ , decreased slowly to 2.18 mm 945 s after  $t_N$  and then more rapidly till it reached negligible values. Both  $\mu_f$  and  $\mu_p$  were increasing before  $t_{\mu 1}$  and decreasing after  $t_{\mu 2}$ . However, from  $t_{\mu 1}$  to  $t_{\mu 2}$ ,  $\mu_f$  was mostly increasing as  $\mu_p$  decreased slightly, then decreased when  $\mu_p$  started to increase again as shown in Figure 5.4c.

In Figure 5.5a, supercooling reached a lower  $T_p$  value (-0.070 °C) at a longer duration of 2,070 s than in G1 experiments that have higher propeller speed (Table 5.1). Figure 5.5b shows that the overall trend of  $N_p$  and  $N_f$  were similar to G1. However, the peak value of  $N_p$  and  $N_f$  was 0.08 and 0.02 cm<sup>-3</sup>, respectively, which was 20 % and 33 % lower than in G1, respectively. The trend of  $\mu_p$  and  $\mu_f$  shown in Figure 5.5c were also similar to those in G1. The two local peaks of  $\mu_p$  reached 0.92 mm at  $t_{\mu 1}$  and 0.93 mm at  $t_{\mu 2}$ , respectively, both resembling those in G1.  $\mu_f$  peaked at 2.80 mm at 2,589 s, which was slightly lower than in G1.

Figure 5.6a shows that for G3 experiment with three times colder air temperature than G1, a lower  $T_p$  value of -0.064 °C and a shorter  $t_p$  value of 860 s was achieved compared to G1. Figure 5.6b-c shows for G3 experiments the particle and floc number concentrations and mean sizes have similar trends compared to the other two groups.  $N_p$  and  $N_f$  peaked at 0.13 and 0.05 cm<sup>-3</sup> (Figure 5.6b), respectively, both were the largest in the three experimental groups.  $\mu_p$  reached the first local peak with a value of 0.89

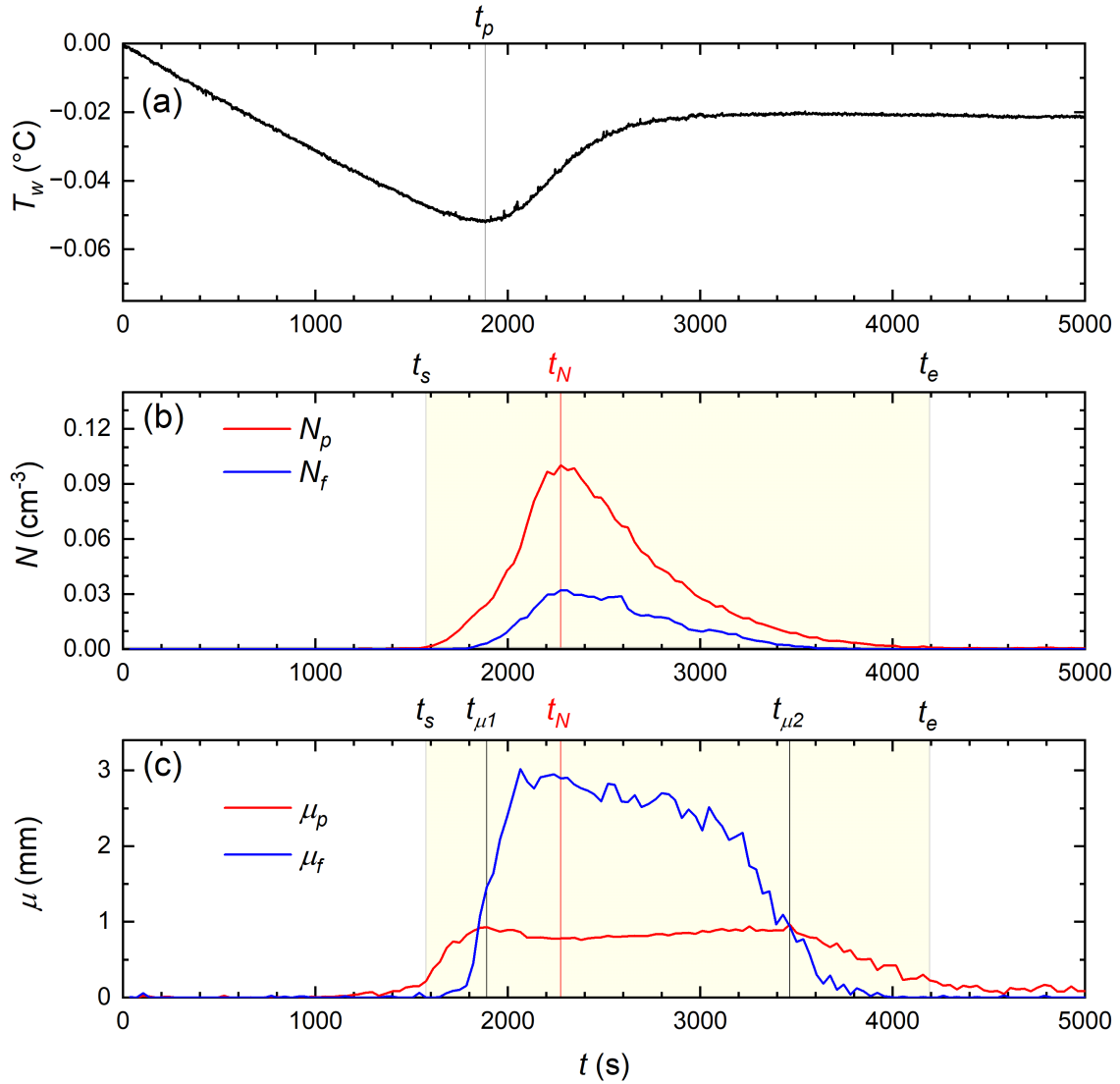


Figure 5.4: Ensemble-averaged time series of (a) water temperature  $T_w$ , (b) number concentration  $N$  of particle and floc, and (c) mean size  $\mu$  of particle and floc for G1 experiments. The time period between  $t_s$  and  $t_e$  is shaded in yellow.

mm, decreased slowly to 0.72 mm before reaching the second local peak at 0.83 mm, while  $\mu_f$  reached a peak value of 2.97 mm before decreasing to a negligible value.

It is evident from Figure 5.4 to Figure 5.6 that the overall trend of particle and floc number concentrations, as well as mean sizes, remained very similar as the turbulent dissipation rate and air temperature were varied. The trend of the  $N_f$  time series followed that of  $N_p$  closely, except that  $N_f$  started to increase later and fell to a negligible

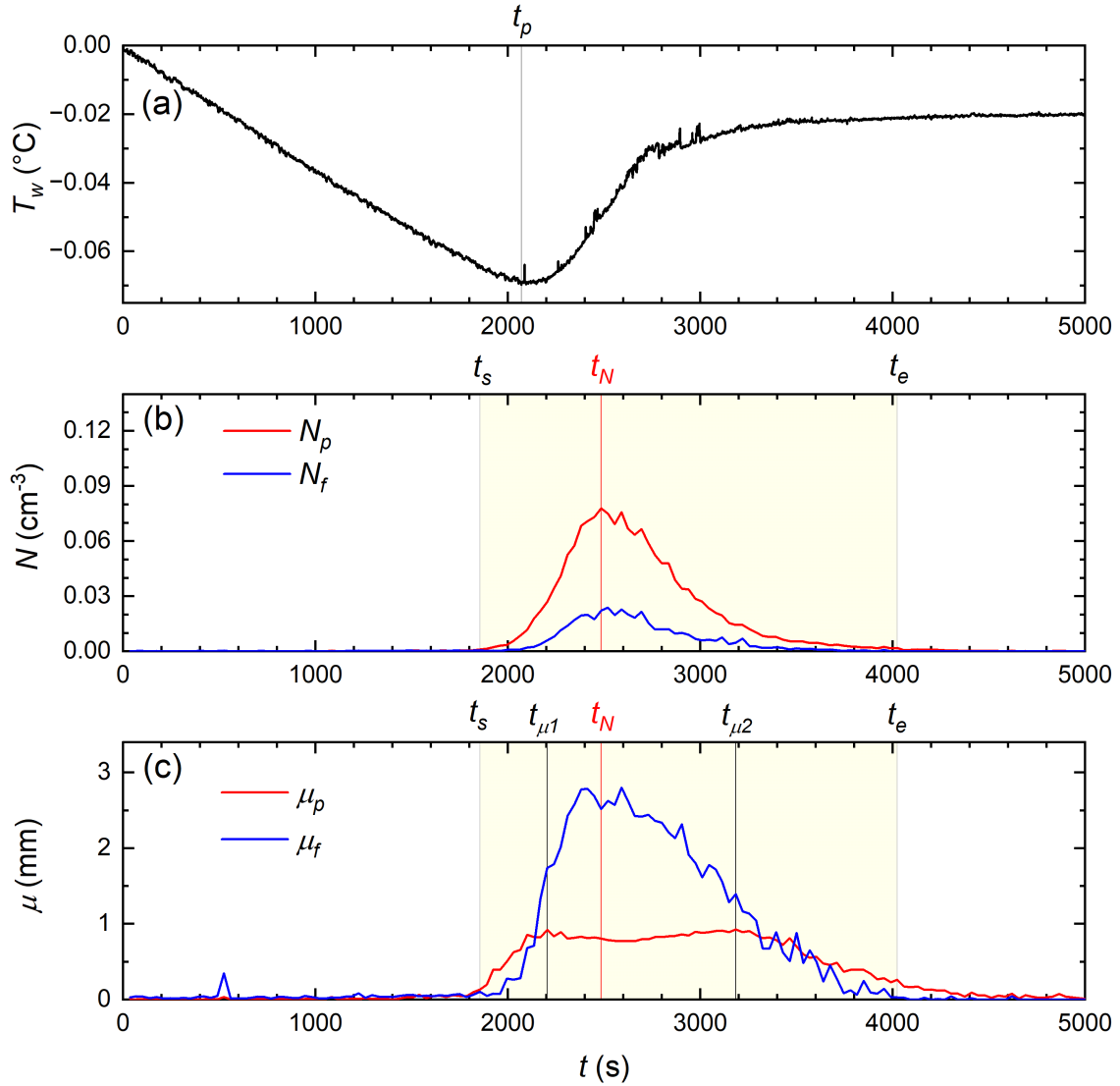


Figure 5.5: Ensemble-averaged time series of (a) water temperature  $T_w$ , (b) number concentration  $N$  of particle and floc, and (c) mean size  $\mu$  of particle and floc for G2 experiments. The time period between  $t_s$  and  $t_e$  is shaded in yellow.

level prior to  $N_p$ . As for mean sizes, both  $\mu_p$  and  $\mu_f$  increased between  $t_s$  and  $t_{\mu1}$  and decreased after  $t_{\mu2}$ . Between  $t_{\mu1}$  and  $t_{\mu2}$ , the trends in  $\mu_p$  and  $\mu_f$  were generally inversely correlated. Comparing the G1 and G2 time series it can be seen that decreasing the turbulent dissipation rate resulted in a longer cooling period and lower peak supercooling temperature, which agrees with previous numerical and experimental results (Hammar and Shen 1995; McFarlane et al. 2015). The lower turbulent dissipation rate

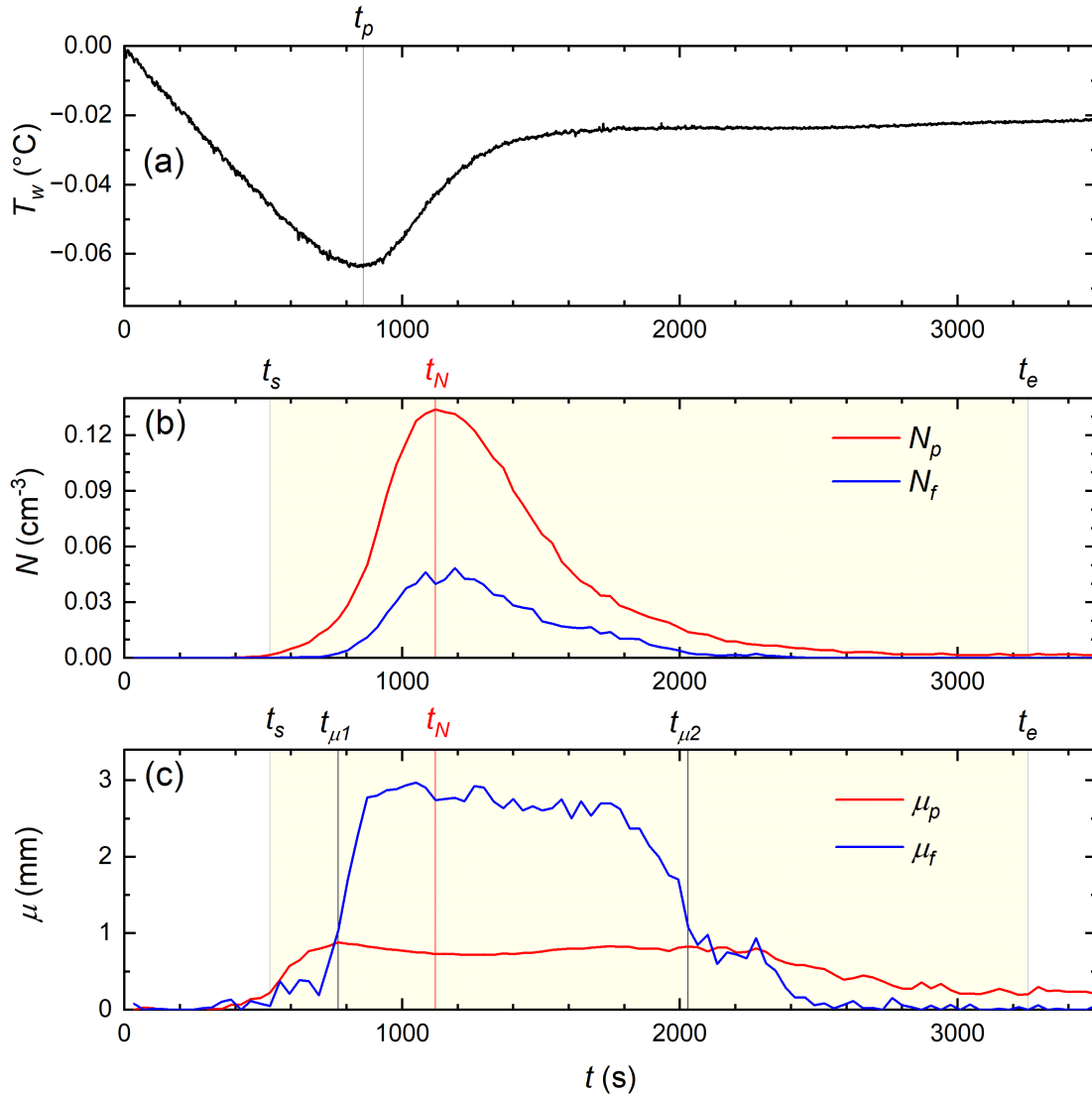


Figure 5.6: Ensemble-averaged time series of (a) water temperature  $T_w$ , (b) number concentration  $N$  of particle and floc, and (c) mean size  $\mu$  of particle and floc for G3 experiments. The time period between  $t_s$  and  $t_e$  is shaded in yellow.

also decreased the peak particle and floc number concentrations by 20 - 30 %, respectively. A lower dissipation rate leads to lower turbulence intensity, making particles less likely to collide likely reducing the secondary nucleation rate. Therefore, fewer particles would be produced resulting in a slower heat balance between water heat loss and latent heat of fusion. Comparing the G1 and G3 time series it is evident that lower air temperature resulted in a short cooling period, lower peak supercooling temperature,

and larger peak particle and floc number concentrations.

### 5.5.2 Correlation Between Particle and Floc Number Concentrations

The ensemble-averaged time series of particle and floc number concentrations were broken into two time periods to investigate their correlations. The *increasing period* was defined as the time from  $t_s$  to  $t_N$  when  $N_p$  was increasing, and the *decreasing period* was defined as the time from  $t_N$  to  $t_e$  when  $N_p$  was decreasing. In Figure 5.7a-b,  $N_p$  and the corresponding  $N_f$  values from each time step (35 seconds) during the two periods were plotted against each other. A linear regression was fitted to each relationship and plotted in Figure 5.7a-b as well. In all cases  $N_f$  increased linearly as  $N_p$  increased with an  $R^2$  value greater than 0.97. The strong linear relationships indicate that in both the *increasing* and *decreasing periods*,  $N_f$  was proportional to  $N_p$  regardless of variations in air temperature or turbulent dissipation rate. The linear fitted slope for G1 and G3 experiments during the *increasing period* was both 0.33 (Figure 5.7a) and during the *decreasing period* they also had similar but slightly larger slope values of 0.35 and 0.34 (Figure 5.7b), respectively. The slope of the regression equations for G2 experiments was 0.29 during both the *increasing* and *decreasing period*, which was significantly different at the 95% confidence level compared to the other two groups with values 12% and 15~17% smaller during the *increasing* and *decreasing period*, respectively. This is possibly because the decreased turbulent dissipation rate in G2 lowered the collision frequency of suspended particles, reducing the proportion of flocs. The intercepts of the *increasing period* regression equations were -0.003 and -0.0032 for G1 and G3, respectively, which is significantly larger compared to the G2 value of 0.0009. This indicates that when the turbulent dissipation rate was higher,  $N_p$  was significantly higher when flocs first started to form (*i.e.*  $N_f$  started to increase significantly), hence the time between when particles and flocs started to form was longer. Figure 5.8 shows the comparison between the observed  $N_f$  time series and the time series calculated based on the obtained linear relationships. The calculated values aligned well with the

observed values, confirming the goodness-of-fit of the obtained linear relationships.

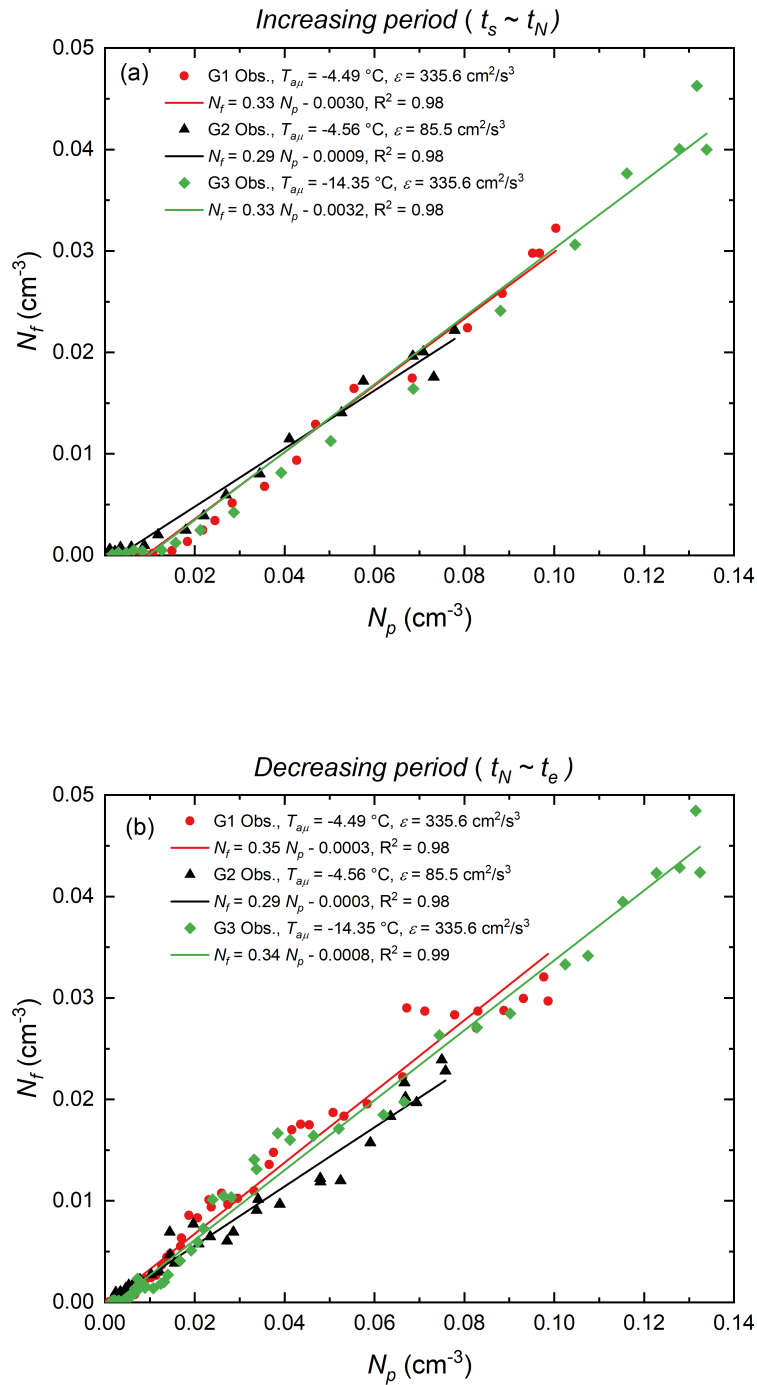


Figure 5.7: Correlation between particle number concentration  $N_p$  and floc number concentration  $N_f$  during (a) the *increasing period* from  $t_s$  to  $t_N$  and (b) the *decreasing period* from  $t_N$  to  $t_e$ .

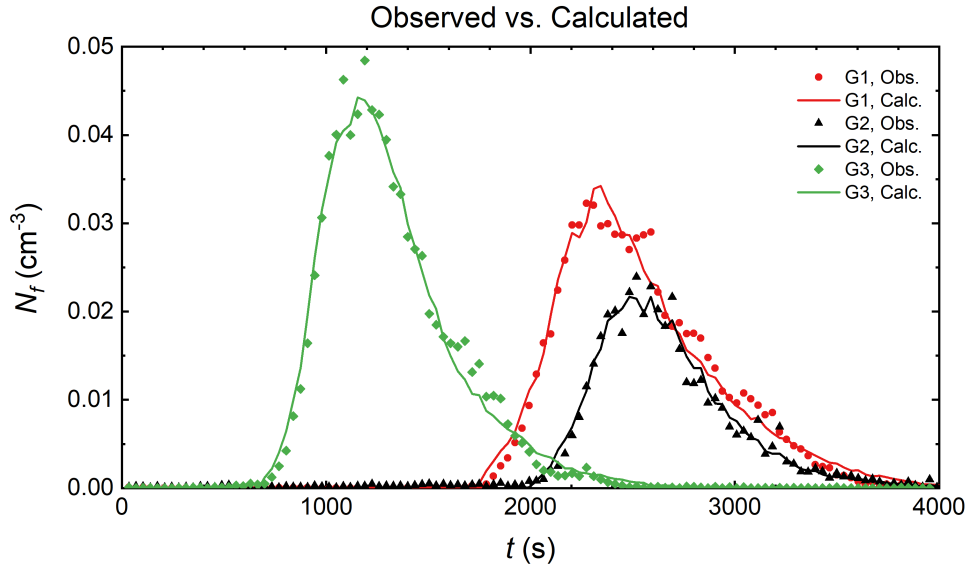


Figure 5.8: A comparison between observed and calculated floc number concentration time series for the three groups of experiments.

### 5.5.3 Correlation Between Particle and Floc Mean Sizes

The ensemble-averaged time series of particle and floc mean sizes were broken into three time periods to explore their correlations. The first period was from  $t_s$  to  $t_{\mu_1}$  when both  $\mu_p$  and  $\mu_f$  was increasing. The second period was from  $t_{\mu_1}$  to  $t_{\mu_2}$  when  $\mu_p$  reached equilibrium (*i.e.*  $\mu_p$  was approximately constant varying between 0.7 and 1.0 mm) and  $\mu_p$  and  $\mu_f$  were approximately inversely correlated. The third period was from  $t_{\mu_2}$  to  $t_e$  when both  $\mu_p$  and  $\mu_f$  was decreasing.

In Figure 5.9 plots of  $\mu_p$  versus  $\mu_f$  at each time step during the three time periods are presented. As shown in Figure 5.9a, during the first period, the fitted nonlinear regression curves show that  $\mu_f$  generally increased exponentially as  $\mu_p$  increased, the correlation was strong for experiments G1 and G2 with  $R^2$  values of 0.99 and 0.86, respectively and weaker in G3 with an  $R^2$  value of 0.57. During this initial period, particles and flocs had just started to form and it is reasonable to assume that flocculation was likely limited by the relatively small number of particles, that flocs were all formed by aggregation of particles and breakup of flocs was rare. Also, during this

period the mean particle size increased rapidly and larger and larger particles were incorporated into the newly formed flocs. This possibly leads to the exponential increase in the mean size of flocs. During the equilibrium period (Figure 5.9b), linear regression analysis shows that  $\mu_f$  generally decreased as  $\mu_p$  increased, confirming the inverse correlation observed from Figure 5.4 to Figure 5.6. The linear regressions have  $R^2$  ranging from 0.24 to 0.72 indicating weak to moderate correlation. This period is particularly interesting since  $\mu_p$  was approximately constant while at the same time both  $N_p$  and  $N_f$  were varying continually and reached their maximum values. This indicates that during this period the rate of flocculation (*i.e.* the rate at which particles are incorporated into flocs) was likely varying significantly, yet the average size of particles did not vary significantly. As shown in the time series  $\mu_p$  first decreased slightly as  $\mu_f$  continuously increasing, then started to increase again as  $\mu_f$  started to decrease. The gradual decrease in  $\mu_p$  after  $t_{\mu 1}$  was probably due to the preferential flocculation of larger particles since their higher cross-sectional area results in higher collision volumes. The subsequent gradual increase in  $\mu_p$  that occurred as  $\mu_f$  already decreased may be due to the fact that at this time larger flocs were breaking up, causing  $\mu_f$  to decrease and  $\mu_p$  to increase. Figure 5.9c shows during the third period  $\mu_f$  decreased exponentially as  $\mu_p$  decreased and all correlations had an  $R^2$  above 0.8. This is not surprising since flocs were removed significantly faster than small particles by rising to the surface.

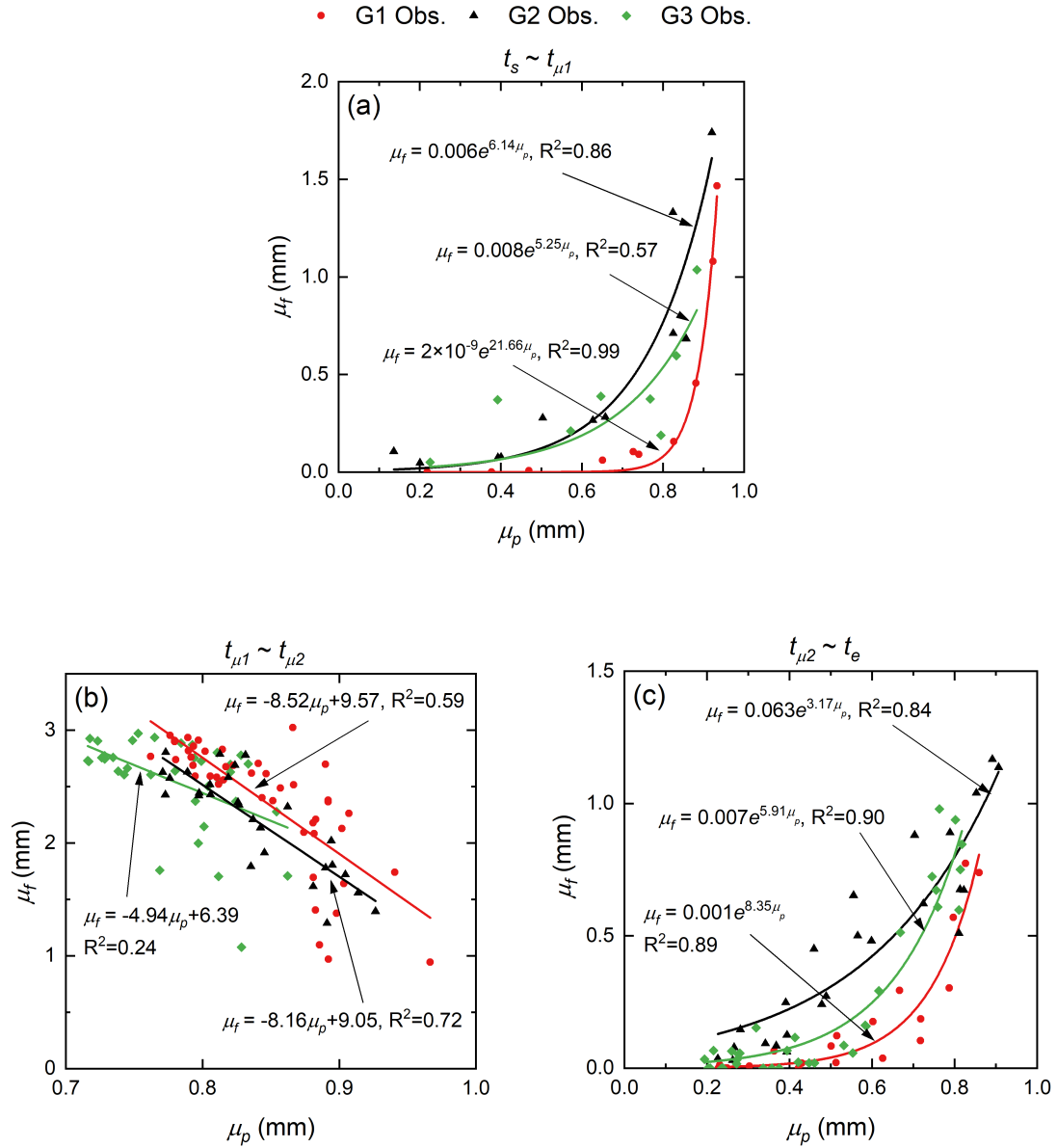


Figure 5.9: Correlation between particle mean size  $\mu_p$  and floc mean size  $\mu_f$  during (a) the period from  $t_s$  to  $t_{\mu 1}$ , (b) the period from  $t_{\mu 1}$  to  $t_{\mu 2}$ , and (c) the period from  $t_{\mu 2}$  to  $t_e$  for the three groups of experiments.

## 5.6 Conclusions

A series of experiments were performed to produce and image frazil particles and flocs under different turbulent dissipation rates and air temperatures during supercooling. The time evolution of the frazil particle and floc number concentration and mean size were obtained and their correlations during different time periods were investigated. Results show a strong linear relationship between particle and floc number concentrations with the ratio  $N_f/N_p$  ranging from 0.29 - 0.35 in both the *increasing* and *decreasing periods*. This ratio did not change significantly with changing air temperatures but was reduced by 12 - 17 % at a lower turbulent dissipation rate. Three time periods were identified to establish the relationship between particle and floc mean sizes. It was found that there was a moderate to strong nonlinear correlation between mean particle size and mean floc size described by an exponential relationship when particle mean sizes increased or decreased significantly. When particle mean size reaches an approximate equilibrium, a weak to moderate linear correlation was found between mean particle and floc size and the negative slope suggests they are inversely correlated. These relationships provide new insights into the evolution of flocs and the flocculation process during supercooling, the robust linear relationship between particle and floc number concentrations may be useful for estimating the time evolution of floc number concentration in frazil dynamics models (e.g. Rees Jones and Wells 2018). Further numerical modelling that accounts for the dynamics and population balance of both frazil particles and flocs may help increase our understanding of the physics behind those relationships.

# Chapter 6

## Conclusions

### 6.1 Summary and Conclusions

As beautiful as it looks, the river freeze-up process that begins with frazil formation and ends with solid ice coverage may pose significant challenges to structures in rivers and generate serious flooding particularly if ice jams occur (Ettema and Zabilansky 2004; Barrette 2021). Therefore, understanding river freeze-up is of great interest to cold region communities because such knowledge helps them effectively monitor river ice conditions. It would also allow engineers to better predict hazards related to river ice formation and ice cover progression. A number of studies have focused on observations of frazil ice particles during the freeze-up process (Daly and Colbeck 1986; Ye 2002; Clark and Doering 2006; McFarlane et al. 2015; McFarlane et al. 2019b). However, the mechanics of flocculation and the processes by which they rise to the water surface forming frazil ice pans are still largely unknown which is in part due to the limited data available on frazil flocs and surface ice pans. In this thesis, a series of field and laboratory measurements were made to investigate the frazil flocs and surface ice properties. These measurements led to the completion of four studies described in detail in Chapters 2 to 5, each briefly revisited and key results summarized below.

Chapter 2 investigated the possibility of utilizing low-resolution public cameras that were not set up for river ice research for long-term monitoring of surface ice conditions. A deep learning based hybrid image processing algorithm consisting of image

classification, rectification, segmentation, and ice pan properties extraction was developed to process images from a distant and oblique-viewed public camera mounted on a building rooftop near the North Saskatchewan River. The accuracy of the algorithm was assessed by comparing ice concentration results from processed images and manually annotated ground truth images, and by comparing concentrations from the public camera to results from bridge camera images with a much higher resolution. A mean absolute difference of surface ice concentration between 2 - 3 % was achieved. The algorithm was used to process images collected during five freeze-up seasons under changing environmental conditions. It was found that for all five seasons, the ice pan size distribution follows a lognormal distribution and no significant annual variations in the size and shape of ice pans were observed. The diameter of ice pans ranged from 0.55 to 15.03 m with a mean of 1.82 m. The pans were generally elliptically shaped with an average aspect ratio of 1.71. Time series of water temperature and ice pan properties show that supercooling events and the appearance of ice pans coincided, and daily mean ice pan diameter varied from 1 to 3 m. These results demonstrated that this method provides valuable information on both long- and short-term temporal variations in river ice conditions and ice pan properties, which opens opportunities for river ice researchers to identify and utilize river ice images for long-term surface ice monitoring from suitable existing public cameras.

Chapter 3 presented detailed measurements of frazil ice flocs in rivers and investigated the key hydraulic and meteorological factors that govern the properties and evolution of frazil flocs. Time series images of frazil ice particles and flocs were captured during eleven field deployments in three Alberta rivers using a submersible high-resolution camera system. Images were processed to accurately identify flocs and to calculate their sizes and concentrations. It was found that a lognormal distribution was a good fit for the floc size distribution. The mean floc size ranged from 1.19 to 5.64 mm and the overall mean floc size was 3.80 mm. The mean floc size decreased linearly as the local Reynolds number increased. The average floc number concentration ranged

from  $1.80 \times 10^{-4}$  to  $1.15 \times 10^{-1} \text{ cm}^{-3}$ . The average floc volumetric concentration ranged from  $2.05 \times 10^{-7}$  to  $4.56 \times 10^{-3}$  and was found to correlate strongly with the fractional height above the river bed described by a power law relationship. No significant correlations were found between the air-water heat flux and floc properties. During the principal supercooling phase, floc number concentration and mean size were found to increase significantly just prior to peak supercooling and reached a maximum near the end of principal supercooling. During the residual supercooling phase, the mean floc size did not typically vary significantly. The correlation between mean floc size and the local Reynolds number can be used to estimate mean floc sizes given mean flow velocity and depth. The reported lognormal size distributions of flocs, time series of mean floc size and concentration evolutions, as well as the two correlations obtained, provide opportunities to incorporate floc dynamics into numerical models to more realistically simulate frazil ice evolution and surface ice formation.

In Chapter 4 results from a laboratory study investigating how the supercooling curve as well as the properties of frazil ice particles and flocs vary under different air-water heat flux scenarios were reported. A total of 30 cold room laboratory experiments were performed in a frazil ice tank where the cold room air temperature was increased or decreased threefold at different times during supercooling events. Images of frazil particles and flocs were captured and processed to obtain time series of their sizes and concentrations. Results indicate that increasing the heat flux at different times raised the mean particle number concentration  $\bar{N}_p$  by 25 - 33 % but did not significantly affect the mean floc number concentration  $\bar{N}_f$ . However, decreasing the heat flux only significantly reduced  $\bar{N}_p$  and  $\bar{N}_f$  by 10 and 22 %, respectively when the change occurred prior to peak supercooling. Time series analysis showed that increasing or decreasing heat flux prior to peak supercooling led to an immediate increase or decrease in the cooling rate and peak supercooling magnitude. This caused the particle and floc production rates and maximum number concentrations to change to levels that were similar to those observed during constant heat flux experiments. Increasing the heat

flux after peak supercooling resulted in a second milder supercooling period and smaller secondary maximum particle and floc number concentrations compared to the first supercooling period. Increasing the heat flux at peak supercooling did not significantly change the shape of the supercooling curve despite significant increases in particle and floc number concentrations. These results demonstrated that heat flux variations at different times during a supercooling event led to significantly different responses in the supercooling curve and particle and floc time series.

Chapter 5 explored the correlation between frazil particle and floc properties under different air temperatures and turbulent dissipation rates to further our understanding of the frazil flocculation process. Frazil ice particles and flocs were produced and measured in a frazil ice tank inside a cold room under air temperatures of  $-5\text{ }^{\circ}\text{C}$  and  $-15\text{ }^{\circ}\text{C}$ , respectively and turbulent dissipation rates of  $85.5$  and  $335.6\text{ cm}^2/\text{s}^3$ , respectively. A strong linear relationship between particle and floc number concentrations was found with a floc-to-particle number concentration ratio ranging from  $0.29 - 0.35$ . The ratio was reduced by  $12 - 17\%$  at the lower turbulent dissipation rate. A moderate to strong nonlinear correlation was found between mean particle size and mean floc size described by an exponential relationship when particle mean sizes increased or decreased significantly. At times when particle mean size reached an approximate equilibrium, a weak to moderate linear correlation was found between mean particle and floc size and the negative slope indicated that they are inversely correlated. The fact that the floc-to-particle number concentration ratio was only significantly affected by turbulent dissipation rate demonstrated the importance of the role of turbulence in the flocculation process. These observations provide novel insights into the flocculation process and the linear relationship between particle and floc number concentration may be used to estimate the temporal variations in floc number concentration in frazil dynamics models that currently only model individual frazil ice particles.

In summary, this study offers novel insights into the properties and evolution of frazil flocs and surface ice under changing environmental conditions, which advanced our

understanding of river freeze-up processes and is a significant step toward linking underwater frazil formation with surface ice generation. Some of the findings in this study may help engineers estimate frazil ice conditions without directly measuring frazil particle and floc properties. For example, mean floc sizes could be estimated using the local Reynolds number which only requires measurements of the depth-averaged flow velocity and flow depth. In addition, laboratory observations showed that increases in the air-water heat flux that occur earlier during a supercooling event led to higher particle number concentrations. This observation could be useful for predicting increased frazil ice generation and increased risk of water intake blockage by simply monitoring water temperature and meteorological parameters.

The detailed measurements of particle, floc, and surface ice properties could be used to enhance numerical modeling of river ice processes and thus improve predictions of the river freeze-up. For example, accurate estimates of long-term surface ice concentrations can provide calibration and validation data, as well as boundary condition inputs for comprehensive river ice process models such as River1D (Blackburn and She 2019) and CRISSP1D (Shen 2010). Ice pan properties and size distributions could be used to generate realistic discrete surface ice parcels to improve predictions of ice bridging locations and modelling of freeze-up jams. The relationship between mean floc size and local Reynolds numbers that was developed can be used in conjunction with the relationship between floc size and rise velocity reported by Reimnitz et al. (1993) to estimate frazil rise velocity, a key parameter in river ice processes models. In addition, comprehensive river ice processes models (Blackburn and She 2019; Shen 2010), as well as frazil ice dynamics models (Daly 1984; Souillé et al. 2020), assume frazil ice in the water column consists solely of disc-shaped particles and neglect frazil flocs due to limited data. The reported simultaneous time series measurements of particle and floc mean sizes and concentrations, as well as the correlations between particle and floc mean sizes and number concentrations, provide observational data for researchers to incorporate floc dynamics into numerical models to improve how realistically they

simulate the frazil flocculation process.

## 6.2 Recommendations for Future Research

Chapter 2 and Chapter 3 of this study demonstrated that the sizes and concentrations of both surface ice pans and underwater frazil ice flocs can be accurately quantified in rivers. This is the foundation for future field studies that simultaneously measure the time series of both underwater frazil production and surface ice conditions, ideally in longer river reaches over longer period of time. These comprehensive field measurements may help us better understand the relationship between frazil ice production and surface ice generation. For example, how long after the start of significant underwater frazil production do flocs rise to the surface and solidify into crusty frazil ice pans, and how do different geo-morphological, hydrological and meteorological conditions in different reaches affect this process. The current FrazilCam would need to be deployed with a power supply cable and a data logger for a longer deployment duration, and it would need to be modified to automate the polarizer rinsing process, for example using a mechanical wiper to periodically wipe the ice off of the polarizers. As for surface ice monitoring, appropriately located low-budget game cameras may be deployed along the river reaches downstream of the FrazilCam and the glare of the sun may be reduced using a polarizing filter on the camera lens.

In Chapter 3, time series images containing both frazil ice particles and flocs were obtained in three Alberta rivers. However, only floc data was presented and analyzed because to minimize the effect of suspended sediments a high cut-off size was introduced which eliminated most of the small individual frazil ice particles. McFarlane et al. (2019a) developed a site-specific SVM to distinguish between ice particles and sediments, which requires ice-free sediment images at each site for SVM training. Future field work could be carried out with the goal of collecting ice-free sediment images at the four deployment sites listed in Chapter 3, and to train SVMs to get rid of the effect of sediments on the frazil ice particle data. With the effect of sediments eliminated,

particle and floc sizes and concentrations could be evaluated simultaneously, and their correlations could be investigated to see if the laboratory findings presented in Chapter 5 are valid in the field. Since Chapter 3 only reported three deployments during the principal supercooling phase, more efforts could also be made to collect particle and floc images during principal supercooling to better understand particle and floc evolution in rivers.

Another important future study that would improve our understanding of the frazil flocculation process would be to measure the rise velocity of frazil flocs. Floc rise velocity determines the time scale for frazil flocs to rise to the surface forming surface pans. Incorporating accurate estimates of rise velocities into current river ice models should lead to more accurate simulations of surface ice formation and progression. The only floc rise velocity measurements available in the literature were made by Reimnitz et al. (1993) using a stirred vertical tube or tank filled with seawater. They reported floc rise velocities ranged from 1 to 5 *cm/s* for floc sizes up to 5 cm, and noted that the floc rise velocities were functions of their size. However, rapidly rising large flocs were observed generating small-scale turbulence which caused their rise velocity to deviate from the obtained linear function. Chapter 3 demonstrated that flocs found in different hydraulic conditions were comprised of different shapes of ice crystals, including disc-shaped, needle-shaped, and irregular particles. Therefore, it is of interest to investigate the effect of different floc sizes as well as the predominate crystal shape in a floc on the floc rise velocity.

# Bibliography

- ACIS. 2021. *Current and Historical Alberta Weather Station Data Viewer*. <http://agriculture.alberta.ca/acis/weather-data-viewer.jsp>.
- Andres, D. 1982. "Nucleation and Frazil Production during the Supercooling Period." In *Proceedings of the 2nd Workshop on Hydraulics of Ice-Covered Rivers*, 148–175. Edmonton, Canada: CGU-HS Committee on River Ice Processes and the Environment (CRIPE).
- Ansari, S., C. D. Rennie, O. Seidou, J. Malenchak, and S. G. Zare. 2017. "Automated Monitoring of River Ice Processes Using Shore-Based Imagery." *Cold Regions Science and Technology* 142 (October): 1–16. ISSN: 0165-232X. <https://doi.org/10.1016/j.coldregions.2017.06.011>.
- Ansari, S., C. Rennie, S. Clark, and O. Seidou. 2021. "IceMaskNet: River Ice Detection and Characterization Using Deep Learning Algorithms Applied to Aerial Photography." *Cold Regions Science and Technology* (June): 103324. ISSN: 0165232X. <https://doi.org/10.1016/j.coldregions.2021.103324>.
- Ansari, S., C. D. Rennie, S. P. Clark, and O. Seidou. 2019. "Application of a Fast Super-pixel Segmentation Algorithm in River Ice Classification." In *Proceedings of the 20th Workshop on the Hydraulics of Ice Covered Rivers*, 9. Ottawa, Canada.
- Ashton, G. D. 1978. "River Ice." *Annual Review of Fluid Mechanics* 10, no. 1 (January): 369–392. ISSN: 0066-4189, 1545-4479. <https://doi.org/10.1146/annurev.fl.10.010178.002101>.
- Ashton, G. D. 2013. "Chapter 2 – Thermal Processes." In *River Ice Formation*, 19–76. Committee on River Ice Processes and the Environment.
- Barrette, P.D. 2021. "Understanding Frazil Ice: The Contribution of Laboratory Studies." *Cold Regions Science and Technology* 189 (September): 103334. ISSN: 0165232X. <https://doi.org/10.1016/j.coldregions.2021.103334>.
- Beltaos, S. 2013. *River Ice Formation*. Committee on river ice processes and the environment, Canadian geophysical union hydrology section. ISBN: 978-0-9920022-0-6.
- Blackburn, J., and Y. She. 2019. "A Comprehensive Public-Domain River Ice Process Model and Its Application to a Complex Natural River." *Cold Regions Science and Technology* 163 (July): 44–58. ISSN: 0165232X. <https://doi.org/10.1016/j.coldregions.2019.04.010>.

- Bourgault, D. 2008. "Shore-Based Photogrammetry of River Ice." *Canadian Journal of Civil Engineering* 35, no. 1 (January): 80–86. ISSN: 0315-1468, 1208-6029. <https://doi.org/10.1139/L07-087>.
- Boyd, S., T. Ghobrial, and M. Loewen. 2023. "Analysis of the Surface Energy Budget during Supercooling in Rivers." *Cold Regions Science and Technology*, 103693. ISSN: 0165232X. <https://doi.org/10.1016/j.coldregions.2022.103693>.
- Boyd, S., T. Ghobrial, M. Loewen, M. Jasek, and J. Evans. 2022. "A Study of Supercooling in Rivers." *Cold Regions Science and Technology* 194 (February): 103455. ISSN: 0165232X. <https://doi.org/10.1016/j.coldregions.2021.103455>.
- Carstens, T. 1966. "Experiments with Supercooling and Ice Formation in Flowing Water." *Geophysica Norvegica* 26:1–18.
- Chassiot, L., P. Lajeunesse, and J.-F. Bernier. 2020. "Riverbank Erosion in Cold Environments: Review and Outlook." *Earth-Science Reviews* 207 (August): 103231. ISSN: 0012-8252. <https://doi.org/10.1016/j.earscirev.2020.103231>.
- Chollet, F. 2015. *Keras: Deep Learning for Humans*. <https://keras.io/>.
- Clark, S. P., and J. C. Doering. 2009. "Frazil Flocculation and Secondary Nucleation in a Counter-Rotating Flume." *Cold Regions Science and Technology, An Overview of River Ice Problems: CRIPE 07*, 55 (2): 221–229. ISSN: 0165-232X. <https://doi.org/10.1016/j.coldregions.2008.04.002>.
- Clark, S., and J. Doering. 2006. "Laboratory Experiments on Frazil-Size Characteristics in a Counterrotating Flume." *Journal of Hydraulic Engineering* 132, no. 1 (January): 94–101. ISSN: 0733-9429, 1943-7900. [https://doi.org/10.1061/\(ASCE\)0733-9429\(2006\)132:1\(94\)](https://doi.org/10.1061/(ASCE)0733-9429(2006)132:1(94)).
- Clark, S., and J. Doering. 2008. "Experimental Investigation of the Effects of Turbulence Intensity on Frazil Ice Characteristics." *Canadian Journal of Civil Engineering* 35, no. 1 (January): 67–79. ISSN: 0315-1468, 1208-6029. <https://doi.org/10.1139/L07-086>.
- Clark, S. P., and J. C. Doering. 2002. "Laboratory Observations of Frazil Ice." In *Ice in the Environment: Proceedings of the 16th IAHR International Symposium on Ice*. Dunedin, New Zealand: International Association of Hydraulic Engineering and Research.
- Daly, S. F. 2008. "Evolution of Frazil Ice." In *19th IAHR International Symposium on Ice*. Vancouver, British Columbia, Canada.
- Daly, S. F., K. Carey, and L. Gatto. 1986. "Mapping River Ice Conditions Using Videographic Techniques." In *Proceedings of the 4th Workshop on the Hydraulics of Ice Covered Rivers*. Montreal, Quebec, June.
- Daly, S. F. 1984. *Frazil Ice Dynamics*. Technical report CRREL Monograph 84-1. Hanover, New Hampshire: U.S. Army Cold Regions Research and Engineering Laboratory, April.

- Daly, S. F., and S. C. Colbeck. 1986. "Frazil Ice Measurements in Crrel's Flume Facility." In *Proceedings of the 8th IAHR International Symposium on Ice (Iowa 1986)*, 427–438. Iowa City, Iowa, USA: International Association of Hydraulic Engineering and Research.
- Emond, J., B. Morse, M. Richard, E. Stander, and A. A. Viau. 2011. "Surface Ice Observations on the St. Lawrence River Using Infrared Thermography." *River Research and Applications* 27 (9): 1090–1105. ISSN: 1535-1467. <https://doi.org/10.1002/rra.1445>.
- Eschweiler, D., T. V. Spina, R. C. Choudhury, E. Meyerowitz, A. Cunha, and J. Stegmaier. 2019. "CNN-Based Preprocessing to Optimize Watershed-Based Cell Segmentation in 3D Confocal Microscopy Images." In *2019 IEEE 16th International Symposium on Biomedical Imaging (ISBI 2019)*, 223–227. April. <https://doi.org/10.1109/ISBI.2019.8759242>.
- Ettema, R., and L. Zabilansky. 2004. "Ice Influences on Channel Stability: Insights from Missouri's Fort Peck Reach." *Journal of Hydraulic Engineering* 130, no. 4 (April): 279–292. ISSN: 0733-9429, 1943-7900. [https://doi.org/10.1061/\(ASCE\)0733-9429\(2004\)130:4\(279\)](https://doi.org/10.1061/(ASCE)0733-9429(2004)130:4(279)).
- Evans, T. W., G. Margolis, and A. F. Sarofim. 1974. "Mechanisms of Secondary Nucleation in Agitated Crystallizers." *AIChE Journal* 20 (5): 950–958. ISSN: 1547-5905. <https://doi.org/10.1002/aic.690200516>.
- Frazer, E. K., P. J. Langhorne, G. H. Leonard, N. J. Robinson, and D. Schumayer. 2020. "Observations of the Size Distribution of Frazil Ice in an Ice Shelf Water Plume." *Geophysical Research Letters* 47 (21): e2020GL090498. ISSN: 1944-8007. <https://doi.org/10.1029/2020GL090498>.
- Ghobrial, T., A. Pierre, S. Boyd, and M. Loewen. 2023. "Ice Accumulation at a Water Intake: A Case Study on the Mille-Iles River, Québec." *Canadian Journal of Civil Engineering* (July): cjce-2023–0076. ISSN: 0315-1468, 1208-6029. <https://doi.org/10.1139/cjce-2023-0076>.
- Ghobrial, T. R., and M. R. Loewen. 2021. "Continuous in Situ Measurements of Anchor Ice Formation, Growth, and Release." *The Cryosphere* 15, no. 1 (January): 49–67. ISSN: 1994-0416. <https://doi.org/10.5194/tc-15-49-2021>.
- Ghobrial, T. R., M. R. Loewen, and F. E. Hicks. 2013. "Continuous Monitoring of River Surface Ice during Freeze-up Using Upward Looking Sonar." *Cold Regions Science and Technology* 86 (February): 69–85. ISSN: 0165-232X. <https://doi.org/10.1016/j.coldregions.2012.10.009>.
- Government of Alberta. 2023. *Alberta Environment and Parks - Alberta River Basins Flood Alerting, Advisories, Reporting and Water Management - Lower Kananaskis Lake*. <https://rivers.alberta.ca/>. Interactive GIS.

- Hallett, J. 1960. "Crystal Growth and the Formation of Spikes in the Surface of Supercooled Water." *Journal of Glaciology* 3 (28): 698–704. ISSN: 0022-1430, 1727-5652. <https://doi.org/10.3189/S0022143000017998>.
- Hammar, L., and H. T. Shen. 1995. "Frazil Evolution in Channels." *Journal of Hydraulic Research* 33, no. 3 (May): 291–306. ISSN: 0022-1686, 1814-2079. <https://doi.org/10.1080/00221689509498572>.
- Hicks, F. E. 2016. *An Introduction to River Ice Engineering for Civil Engineers and Geoscientists*. CreateSpace Independent Publishing Platform. ISBN: 1-4927-8863-5 978-1-4927-8863-8.
- Hicks, F. E. 1997. *An Analysis of Historical Freeze-up Data on the North Saskatchewan River Below the Bighorn Dam*. Technical report. Calgary, Canada: TransAlta Utilities Corporation.
- Howley, R. 2021. "A Modelling Study of Complex River Ice Processes in an Urban Reach of the North Saskatchewan River." M.Sc. Thesis, University of Alberta.
- Ibrahim, Y., B. Nagy, and C. Benedek. 2019. "CNN-Based Watershed Marker Extraction for Brick Segmentation in Masonry Walls." In *International Conference on Image Analysis and Recognition*, 11662:332–344. Cham: Springer International Publishing. ISBN: 978-3-030-27201-2 978-3-030-27202-9. [https://doi.org/10.1007/978-3-030-27202-9\\_30](https://doi.org/10.1007/978-3-030-27202-9_30).
- Jasek, M. 2016. "Investigations of Anchor Ice Formation and Release Waves." In *Proceedings of the 23rd IAHR International Symposium on Ice*, 11. Ann Arbor, Michigan USA: International Association of Hydro-Environment Engineering and Research, May.
- Jasek, M., and A. Pryse-Phillips. 2015. "Influence of the Proposed Site C Hydroelectric Project on the Ice Regime of the Peace River." *Canadian Journal of Civil Engineering* 42, no. 9 (September): 645–655. ISSN: 0315-1468. <https://doi.org/10.1139/cjce-2014-0425>.
- Kalke, H., and M. Loewen. 2018. "Support Vector Machine Learning Applied to Digital Images of River Ice Conditions." *Cold Regions Science and Technology* 155 (November): 225–236. ISSN: 0165-232X. <https://doi.org/10.1016/j.coldregions.2018.08.014>.
- Kalke, H., V. McFarlane, T. Ghobrial, and M. Loewen. 2019. "Field Measurements of Supercooling in the North Saskatchewan River." In *20th Workshop on the Hydraulics of Ice Covered Rivers*. Ottawa, Ontario, Canada: CGU-HS Committee on River Ice Processes and the Environment (CRIPE), May.
- Kallungal, J. P., and A. J. Barduhn. 1977. "Growth Rate of an Ice Crystal in Subcooled Pure Water." *AIChE Journal* 23 (3): 294–303. ISSN: 1547-5905. <https://doi.org/10.1002/aic.690230312>.

- Kellerhals, R., C. Neill, and D. Bray. 1972. *Hydraulic and Geomorphic Characteristics of Rivers in Alberta*. River Engineering and Surface Hydrology Report, 72-1. Edmonton : Alberta Cooperative Research Program in Highway and River Engineering 1972.
- Kempema, E. W., E. Reimnitz, J. R. Clayton, and J. R. Payne. 1993. "Interactions of Frazil and Anchor Ice with Sedimentary Particles in a Flume." *Cold Regions Science and Technology* 21, no. 2 (January): 137–149. ISSN: 0165-232X. [https://doi.org/10.1016/0165-232X\(93\)90003-Q](https://doi.org/10.1016/0165-232X(93)90003-Q).
- Kempema, E. W., and R. Ettema. 2011. "Anchor Ice Rafting: Observations from the Laramie River." *River Research and Applications* 27 (9): 1126–1135. ISSN: 1535-1467. <https://doi.org/10.1002/rra.1450>.
- Kempema, E. W., E. Reimnitz, and P. W. Barnes. 2001. "Anchor-Ice Formation and Ice Rafting in Southwestern Lake Michigan, U.S.A." *Journal of Sedimentary Research* 71, no. 3 (May): 346–354. ISSN: 1527-1404. <https://doi.org/10.1306/2DC40948-0E47-11D7-8643000102C1865D>.
- Konzelmann, T., R. S. W. van de Wal, W. Greuell, R. Bintanja, E. A. C. Henneken, and A. Abe-Ouchi. 1994. "Parameterization of Global and Longwave Incoming Radiation for the Greenland Ice Sheet." *Global and Planetary Change, Greenland Ice Margin Experiment (GIMEx)*, 9, no. 1 (January): 143–164. ISSN: 0921-8181. [https://doi.org/10.1016/0921-8181\(94\)90013-2](https://doi.org/10.1016/0921-8181(94)90013-2).
- Lawrence, S., C. Giles, Ah Chung Tsoi, and A. Back. 1997. "Face Recognition: A Convolutional Neural-Network Approach." *IEEE Transactions on Neural Networks* 8, no. 1 (January): 98–113. ISSN: 1045-9227, 1941-0093. <https://doi.org/10.1109/72.554195>.
- Li, Q., W. Cai, X. Wang, Y. Zhou, D. D. Feng, and M. Chen. 2014. "Medical Image Classification with Convolutional Neural Network." In *2014 13th International Conference on Control Automation Robotics Vision (ICARCV)*, 844–848. December. <https://doi.org/10.1109/ICARCV.2014.7064414>.
- Lin, T.-Y., P. Goyal, R. Girshick, K. He, and P. Dollar. 2017. "Focal Loss for Dense Object Detection." In *Proceedings of the IEEE International Conference on Computer Vision (ICCV)*, 2980–2988. October.
- Maggiori, E., Y. Tarabalka, G. Charpiat, and P. Alliez. 2017. "Convolutional Neural Networks for Large-Scale Remote-Sensing Image Classification." *IEEE Transactions on Geoscience and Remote Sensing* 55, no. 2 (February): 645–657. ISSN: 0196-2892, 1558-0644. <https://doi.org/10.1109/TGRS.2016.2612821>.
- Marko, J. R., and M. Jasek. 2010. "Sonar Detection and Measurement of Ice in a Freezing River II: Observations and Results on Frazil Ice." *Cold Regions Science and Technology* 63, no. 3 (September): 135–153. ISSN: 0165-232X. <https://doi.org/10.1016/j.coldregions.2010.05.003>.

- Martin, S. 1981. "Frazil Ice in Rivers and Oceans." *Annual Review of Fluid Mechanics* 13, no. 1 (January): 379–397. ISSN: 0066-4189, 1545-4479. <https://doi.org/10.1146/annurev.fl.13.010181.002115>.
- Masad, E., D. Olcott, T. White, and L. Tashman. 2001. "Correlation of Fine Aggregate Imaging Shape Indices with Asphalt Mixture Performance." *Transportation Research Record: Journal of the Transportation Research Board* 1757, no. 1 (January): 148–156. ISSN: 0361-1981, 2169-4052. <https://doi.org/10.3141/1757-17>.
- McFarlane, V., and S. P. Clark. 2021. "A Detailed Energy Budget Analysis of River Supercooling and the Importance of Accurately Quantifying Net Radiation to Predict Ice Formation." *Hydrological Processes* 35 (3): e14056. ISSN: 1099-1085. <https://doi.org/10.1002/hyp.14056>.
- McFarlane, V., M. Loewen, and F. Hicks. 2014. "Laboratory Measurements of the Rise Velocity of Frazil Ice Particles." *Cold Regions Science and Technology* 106–107 (October): 120–130. ISSN: 0165-232X. <https://doi.org/10.1016/j.coldregions.2014.06.009>.
- McFarlane, V., M. Loewen, and F. Hicks. 2015. "Measurements of the Evolution of Frazil Ice Particle Size Distributions." *Cold Regions Science and Technology* 120 (December): 45–55. ISSN: 0165-232X. <https://doi.org/10.1016/j.coldregions.2015.09.001>.
- McFarlane, V., M. Loewen, and F. Hicks. 2017. "Measurements of the Size Distribution of Frazil Ice Particles in Three Alberta Rivers." *Cold Regions Science and Technology* 142 (October): 100–117. ISSN: 0165-232X. <https://doi.org/10.1016/j.coldregions.2017.08.001>.
- McFarlane, V., M. Loewen, and F. Hicks. 2019a. "Field Measurements of Suspended Frazil Ice. Part I: A Support Vector Machine Learning Algorithm to Identify Frazil Ice Particles." *Cold Regions Science and Technology* 165 (September): 102812. ISSN: 0165-232X. <https://doi.org/10.1016/j.coldregions.2019.102812>.
- McFarlane, V., M. Loewen, and F. Hicks. 2019b. "Field Measurements of Suspended Frazil Ice. Part II: Observations and Analyses of Frazil Ice Properties during the Principal and Residual Supercooling Phases." *Cold Regions Science and Technology* 165 (September): 102796. ISSN: 0165-232X. <https://doi.org/10.1016/j.coldregions.2019.102796>.
- Mercier, R. S. 1985. "The Reactive Transport of Suspended Particles: Mechanisms and Modeling." PhD diss., Massachusetts Institute of Technology.
- Michel, B. 1972. "Properties and Processes of River and Lake Ice." In *International Symposium on the Role of Snow and Ice in Hydrology; The Role of Snow and Ice in Hydrology: Proceedings of the Banff Symposia; 1973*. September.
- Morse, B., M. Hessami, and C. Bourel. 2003. "Characteristics of Ice in the St. Lawrence River." *Canadian Journal of Civil Engineering* 30, no. 4 (August): 766–774. ISSN: 0315-1468, 1208-6029. <https://doi.org/10.1139/103-030>.

- Morse, B., and M. Richard. 2009. "A Field Study of Suspended Frazil Ice Particles." *Cold Regions Science and Technology* 55, no. 1 (January): 86–102. ISSN: 0165232X. <https://doi.org/10.1016/j.coldregions.2008.03.004>.
- Mullins, W. W., and R. F. Sekerka. 1964. "Stability of a Planar Interface During Solidification of a Dilute Binary Alloy." *Journal of Applied Physics* 35, no. 2 (February): 444–451. ISSN: 0021-8979. <https://doi.org/10.1063/1.1713333>.
- Nafziger, J., F. Hicks, P. Thoms, V. McFarlane, R. Cunjak, and J. Banack. 2013. "Measuring Supercooling Prevalence on Small Regulated and Unregulated Streams in New Brunswick and Newfoundland, Canada." In *Proceedings of the 17th CGU HSE CRIPE Workshop on River Ice*, 21–24. Edmonton, Canada, July.
- Osterkamp, T. E., and J. P. Gosink. 1983. "Frazil Ice Formation and Ice Cover Development in Interior Alaska Streams." *Cold Regions Science and Technology* 8, no. 1 (August): 43–56. ISSN: 0165-232X. [https://doi.org/10.1016/0165-232X\(83\)90016-2](https://doi.org/10.1016/0165-232X(83)90016-2).
- Park, C., and R. Gerard. 1984. "Hydraulic Characteristics of Frazil Flocs—Some Preliminary Experiments." In *Proceedings of the 7th IAHR International Symposium on Ice*, 3:27–35. Hamburg, Germany: International Association of Hydraulic Engineering and Research.
- Pei, C., Y. She, and M. Loewen. 2023. "Laboratory Study of Frazil Ice Particle and Floc Evolution under Increased Heat Flux during Supercooling." In *Proceedings of the 22nd Workshop on the Hydraulics of Ice Covered Rivers*. Canmore, Canada: CGU-HS Committee on River Ice Processes and the Environment (CRIPE).
- Pei, C., Y. She, and M. Loewen. 2024. "Laboratory Study of the Correlation between Frazil Ice Particle and Floc Properties." In *Proceedings of the 27th IAHR International Symposium on Ice*. Gdańsk, Poland: International Association of Hydro-Environment Engineering and Research.
- Pei, C., J. Yang, Y. She, and M. Loewen. 2021. "Field Measurements of Supercooling and Anchor Ice Properties." In *Proceedings of the 21st Workshop on the Hydraulics of Ice Covered Rivers*. Saskatoon, Canada: CGU-HS Committee on River Ice Processes and the Environment (CRIPE), August.
- Pei, C., J. Yang, Y. She, and M. Loewen. 2022. "Field Measurements of Frazil Floc Properties." In *Proceedings of the 26th IAHR International Symposium on Ice*. Montréal, Canada: International Association of Hydro-Environment Engineering and Research.
- Pei, C., J. Yang, Y. She, and M. Loewen. 2024. "Measurements of Frazil Ice Flocs in Rivers." *The Cryosphere* 18, no. 9 (September): 4177–4196. ISSN: 1994-0424. <https://doi.org/10.5194/tc-18-4177-2024>.
- Pillai, R. 2018. *Image Classification by Keras and Tensorflow*.

- Raphael, J. M. 1962. "Prediction of Temperature in Rivers and Reservoirs." *Journal of the Power Division* 88:157–181. <https://doi.org/10.1061/jpweam.0000338>.
- Rees Jones, D. W., and A. J. Wells. 2015. "Solidification of a Disk-Shaped Crystal from a Weakly Supercooled Binary Melt." *Physical Review E* 92, no. 2 (August): 022406. ISSN: 1539-3755, 1550-2376. <https://doi.org/10.1103/PhysRevE.92.022406>.
- Rees Jones, D. W., and A. J. Wells. 2018. "Frazil-Ice Growth Rate and Dynamics in Mixed Layers and Sub-Ice-Shelf Plumes." *The Cryosphere* 12, no. 1 (January): 25–38. ISSN: 1994-0424. <https://doi.org/10.5194/tc-12-25-2018>.
- Reimnitz, E., J. R. Clayton, E. W. Kempema, J. R. Payne, and W. S. Weber. 1993. "Interaction of Rising Frazil with Suspended Particles: Tank Experiments with Applications to Nature." *Cold Regions Science and Technology* 21, no. 2 (January): 117–135. ISSN: 0165-232X. [https://doi.org/10.1016/0165-232X\(93\)90002-P](https://doi.org/10.1016/0165-232X(93)90002-P).
- Richard, M. 2011. "Field Investigation of Freshwater Frazil Ice Dynamics." PhD diss., UNIVERSITÉ LAVAL.
- Richard, M., and B. Morse. 2008. "Multiple Frazil Ice Blockages at a Water Intake in the St. Lawrence River." *Cold Regions Science and Technology* 53, no. 2 (July): 131–149. ISSN: 0165-232X. <https://doi.org/10.1016/j.coldregions.2007.10.003>.
- Richard, M., B. Morse, and S. F. Daly. 2015. "Modeling Frazil Ice Growth in the St. Lawrence River." *Canadian Journal of Civil Engineering* 42, no. 9 (September): 592–608. ISSN: 0315-1468, 1208-6029. <https://doi.org/10.1139/cjce-2014-0082>.
- Richard, M., B. Morse, S. F. Daly, and J. Emond. 2011. "Quantifying Suspended Frazil Ice Using Multi-Frequency Underwater Acoustic Devices." *River Research and Applications* 27 (9): 1106–1117. ISSN: 1535-1467. <https://doi.org/10.1002/rra.1446>.
- Roerdink, J. B. T. M., and A. Meijster. 2000. "The Watershed Transform: Definitions, Algorithms and Parallelization Strategies." *Fundamenta Informaticae* 41, nos. 1-2 (January): 187–228. ISSN: 0169-2968. <https://doi.org/10.3233/FI-2000-411207>.
- Ronneberger, O., P. Fischer, and T. Brox. 2015. "U-Net: Convolutional Networks for Biomedical Image Segmentation." In *Medical Image Computing and Computer-Assisted Intervention – MICCAI 2015*, edited by N. Navab, J. Hornegger, W. M. Wells, and A. F. Frangi, 234–241. Cham: Springer International Publishing. ISBN: 978-3-319-24574-4. [https://doi.org/10.1007/978-3-319-24574-4\\_28](https://doi.org/10.1007/978-3-319-24574-4_28).
- Al-Rousan, T., E. Masad, E. Tutumluer, and T. Pan. 2007. "Evaluation of Image Analysis Techniques for Quantifying Aggregate Shape Characteristics." *Construction and Building Materials* 21, no. 5 (May): 978–990. ISSN: 09500618. <https://doi.org/10.1016/j.conbuildmat.2006.03.005>.
- Rouse, H. 1937. "Modern Conceptions of the Mechanics of Fluid Turbulence." *Transactions of the American Society of Civil Engineers* 102, no. 1 (January): 463–505. ISSN: 0066-0604, 2690-4071. <https://doi.org/10.1061/TACEAT.0004872>.

- Ryan, P. J., D. R. F. Harleman, and K. D. Stolzenbach. 1974. "Surface Heat Loss from Cooling Ponds." *Water Resources Research* 10, no. 5 (October): 930–938. <https://doi.org/10.1029/WR010i005p00930>.
- Satterlund, D. R. 1979. "An Improved Equation for Estimating Long-Wave Radiation from the Atmosphere." *Water Resources Research* 15 (6): 1649–1650. ISSN: 1944-7973. <https://doi.org/10.1029/WR015i006p01649>.
- Schneck, C. 2018. "Laboratory Measurements of the Properties of Frazil Ice Particles and Floccs in Saline Water." M.Sc. Thesis, University of Alberta.
- Schneck, C. C., T. R. Ghobrial, and M. R. Loewen. 2019. "Laboratory Study of the Properties of Frazil Ice Particles and Floccs in Water of Different Salinities." *The Cryosphere* 13, no. 10 (October): 2751–2769. ISSN: 1994-0424. <https://doi.org/10.5194/tc-13-2751-2019>.
- Shen, H. T. 2005. *CRISSP1D/CRISSP2D Programmer's Manual*. Technical report. Potsdam, N.Y.: Department of Civil Engineering, Clarkson University.
- Shen, H. T. 2010. "Mathematical Modeling of River Ice Processes." *Cold Regions Science and Technology* 62, no. 1 (June): 3–13. ISSN: 0165232X. <https://doi.org/10.1016/j.coldregions.2010.02.007>.
- Simoës, J., and S. P. Clark. 2020. "Quantification of Border Ice Growth on the Assiniboine River." *Journal of Cold Regions Engineering* 34, no. 1 (March): 04019016. ISSN: 0887-381X, 1943-5495. [https://doi.org/10.1061/\(ASCE\)CR.1943-5495.0000200](https://doi.org/10.1061/(ASCE)CR.1943-5495.0000200).
- Singh, A., H. Kalke, M. Loewen, and N. Ray. 2019. *Alberta River Ice Segmentation Dataset*, June. <https://doi.org/10.21227/ebax-1h44>.
- Singh, A., H. Kalke, M. Loewen, and N. Ray. 2020. "River Ice Segmentation With Deep Learning." *IEEE Transactions on Geoscience and Remote Sensing* 58, no. 11 (November): 7570–7579. ISSN: 0196-2892, 1558-0644. <https://doi.org/10.1109/TGRS.2020.2981082>.
- Sola, D., and K. A. Scott. 2022. "Efficient Shallow Network for River Ice Segmentation." *Remote Sensing* 14, no. 10 (January): 2378. ISSN: 2072-4292. <https://doi.org/10.3390/rs14102378>.
- Souillé, F., C. Goeury, and R.-S. Mouradi. 2023. "Uncertainty Analysis of Single- and Multiple-Size-Class Frazil Ice Models." *The Cryosphere* 17, no. 4 (April): 1645–1674. ISSN: 1994-0416. <https://doi.org/10.5194/tc-17-1645-2023>.
- Souillé, F., F. Taccone, and C. E. Mertahi. 2020. "A Multi-class Frazil Ice Model for Shallow Water Flows." In *2020 TELEMAC User Conference*, 9.
- Svensson, U., and A. Omstedt. 1998. "Numerical Simulations of Frazil Ice Dynamics in the Upper Layers of the Ocean." *Cold Regions Science and Technology* 28, no. 1 (August): 29–44. ISSN: 0165-232X. [https://doi.org/10.1016/S0165-232X\(98\)00011-1](https://doi.org/10.1016/S0165-232X(98)00011-1).

- Toyota, T., S. Takatsuji, and M. Nakayama. 2006. “Characteristics of Sea Ice Floe Size Distribution in the Seasonal Ice Zone.” *Geophysical Research Letters* 33 (2). ISSN: 1944-8007. <https://doi.org/10.1029/2005GL024556>.
- Tsang, G. 1982. *Frazil and Anchor Ice: A Monograph*. Technical report. Ottawa, Canada: National Research Council of Canada.
- Tsang, G. 1984. “Concentration of Frazil in Flowing Water as Measured in Laboratory and in the Field.” In *Proceedings of the 7th IAHR International Symposium on Ice (Hamburg 1984)*, 99–111. Hamburg, Germany: International Association of Hydraulic Engineering and Research.
- Tsang, G., and T. O. Hanley. 1985. “Frazil Formation in Water of Different Salinities and Supercoolings.” *Journal of Glaciology* 31 (108): 74–85. ISSN: 0022-1430, 1727-5652. <https://doi.org/10.3189/S0022143000006298>.
- University of Alberta. 2021. *EAS Weather Station | Earth and Atmospheric Sciences*. <https://www.ualberta.ca/earth-sciences/facilities/weather.html>.
- University of Calgary. 2023. *Environmental Data | Research | Biogeoscience Institute | Biogeoscience Institute | Research at UCalgary | University of Calgary*. <https://research.ucalgary.ca/biogeoscience-institute/research/environmental-data>.
- Vandermause, R., M. Harvey, L. Zevenbergen, and R. Ettema. 2021. “River-Ice Effects on Bank Erosion along the Middle Segment of the Susitna River, Alaska.” *Cold Regions Science and Technology* 185 (May): 103239. ISSN: 0165232X. <https://doi.org/10.1016/j.coldregions.2021.103239>.
- Vuyovich, C. M., S. F. Daly, J. J. Gagnon, P. Weyrick, and M. Zaitsoff. 2009. “Monitoring River Ice Conditions Using Web-Based Cameras.” *Journal of Cold Regions Engineering* 23, no. 1 (March): 1–17. ISSN: 0887-381X, 1943-5495. [https://doi.org/10.1061/\(ASCE\)0887-381X\(2009\)23:1\(1\)](https://doi.org/10.1061/(ASCE)0887-381X(2009)23:1(1)).
- Water Survey of Canada. 2023. *Sediment Data Search - Water Level and Flow - Environment Canada*. [https://wateroffice.ec.gc.ca/search/sediment\\_e.html](https://wateroffice.ec.gc.ca/search/sediment_e.html).
- Xing, F., Y. Xie, and L. Yang. 2016. “An Automatic Learning-Based Framework for Robust Nucleus Segmentation.” *IEEE Transactions on Medical Imaging* 35, no. 2 (February): 550–566. ISSN: 0278-0062, 1558-254X. <https://doi.org/10.1109/TMI.2015.2481436>.
- Yang, J., Y. She, and M. Loewen. 2023. “Assessing Heat Flux Formulas Used in the Full Energy Budget Model for Rivers during Freeze-Up.” In *Proceedings of the 22nd Workshop on the Hydraulics of Ice Covered Rivers*. Canmore, Canada: CGU-HS Committee on River Ice Processes and the Environment (CRIPE).
- Ye, S. Q., J. Doering, and H. T. Shen. 2004. “A Laboratory Study of Frazil Evolution in a Counter-Rotating Flume.” *Canadian Journal of Civil Engineering* 31, no. 6 (December): 899–914. ISSN: 0315-1468, 1208-6029. <https://doi.org/10.1139/104-056>.

- Ye, S. 2002. "A Physical and Mathematical Study of the Supercooling Process and Frazil Evolution." PhD diss., University of Manitoba.
- Yen, J.-C., F.-J. Chang, and S. Chang. 1995. "A New Criterion for Automatic Multilevel Thresholding." *IEEE Transactions on Image Processing* 4, no. 3 (March): 370–378. ISSN: 1941-0042. <https://doi.org/10.1109/83.366472>.
- Zhai, B., L. Liu, H. T. Shen, and S. Ji. 2022. "A Numerical Model for River Ice Dynamics Based on Discrete Element Method." *Journal of Hydraulic Research* 0, no. 0 (February): 1–14. ISSN: 0022-1686. <https://doi.org/10.1080/00221686.2021.2004254>.
- Zhang, X., J. Jin, Z. Lan, C. Li, M. Fan, Y. Wang, X. Yu, and Y. Zhang. 2020. "ICENET: A Semantic Segmentation Deep Network for River Ice by Fusing Positional and Channel-Wise Attentive Features." *Remote Sensing* 12, no. 2 (January): 221. ISSN: 2072-4292. <https://doi.org/10.3390/rs12020221>.
- Zhang, X., Y. Zhou, J. Jin, Y. Wang, M. Fan, N. Wang, and Y. Zhang. 2021. "ICENETv2: A Fine-Grained River Ice Semantic Segmentation Network Based on UAV Images." *Remote Sensing* 13, no. 4 (January): 633. ISSN: 2072-4292. <https://doi.org/10.3390/rs13040633>.

# Appendix A: Time Series Plots for the Remaining Eight Field FrazilCam Deployments

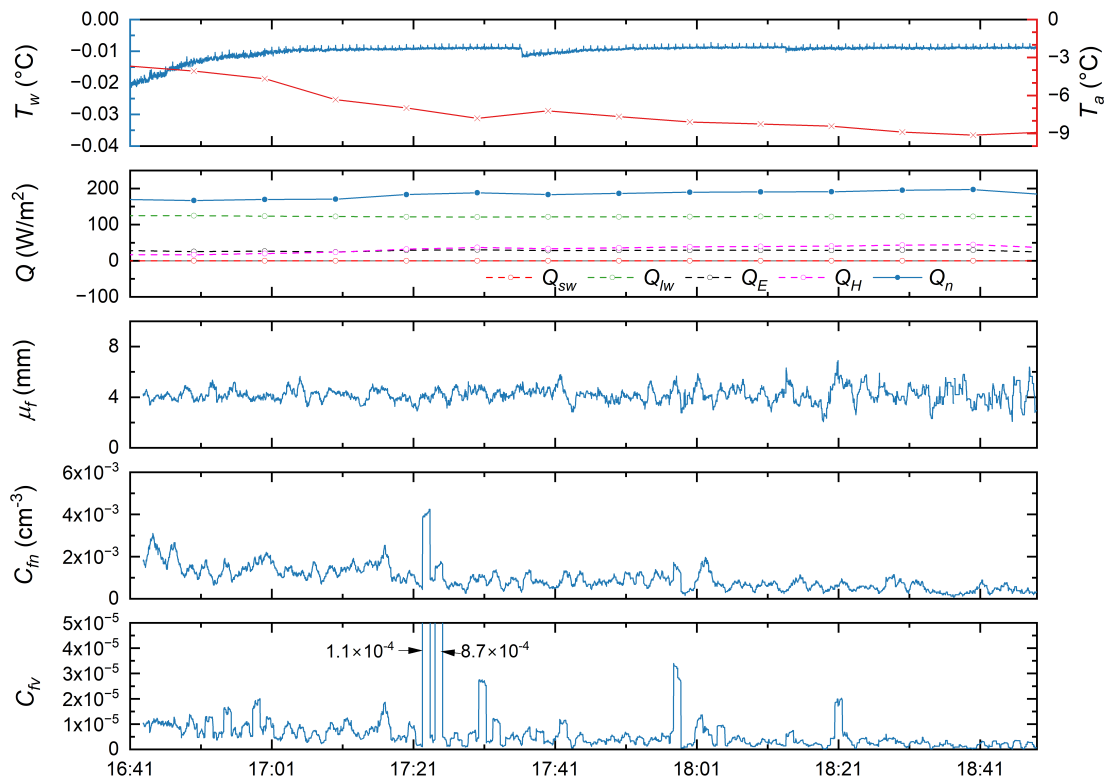


Figure A.1: Time series of (a) water and air temperatures  $T_w$  and  $T_a$ , (b) heat flux  $Q$ , (c) floc mean size  $\mu_f$ , (d) floc number concentration  $C_{fn}$  and (e) floc volumetric concentration  $C_{fv}$  for deployment NSR-L1 on December 3, 2021.

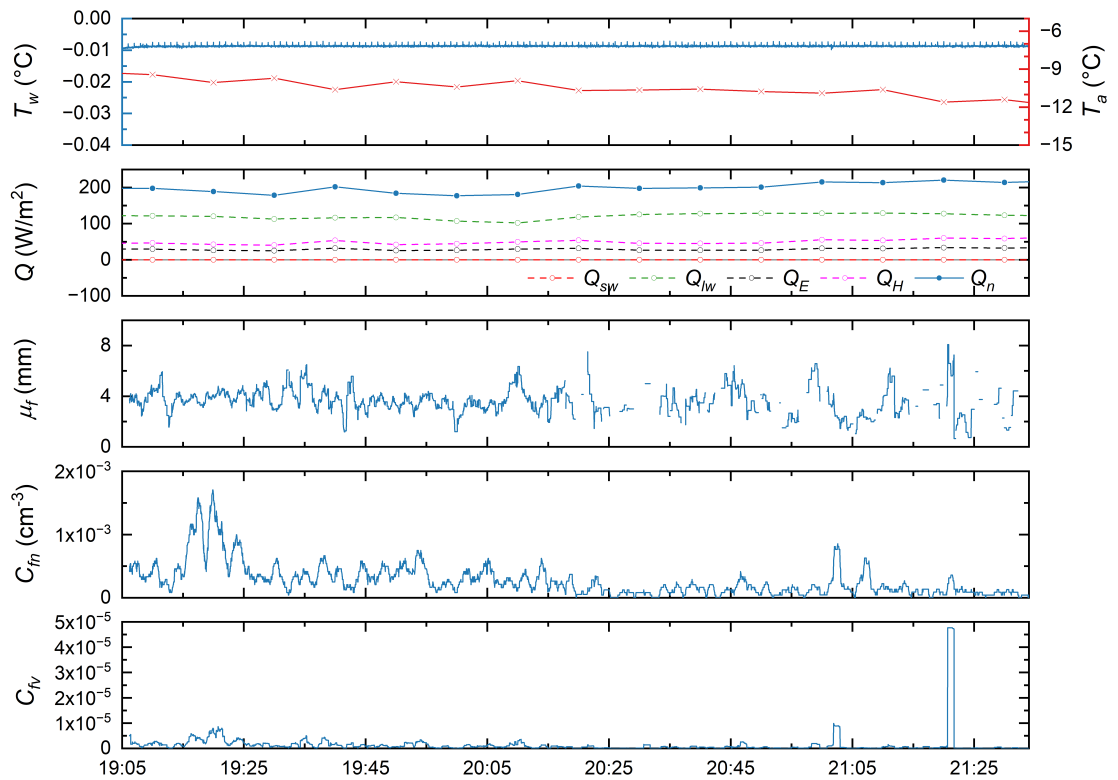


Figure A.2: Time series of (a) water and air temperatures  $T_w$  and  $T_a$ , (b) heat flux  $Q$ , (c) floc mean size  $\mu_f$ , (d) floc number concentration  $C_{fn}$  and (e) floc volumetric concentration  $C_{fv}$  for deployment NSR-L2 on December 3, 2021.

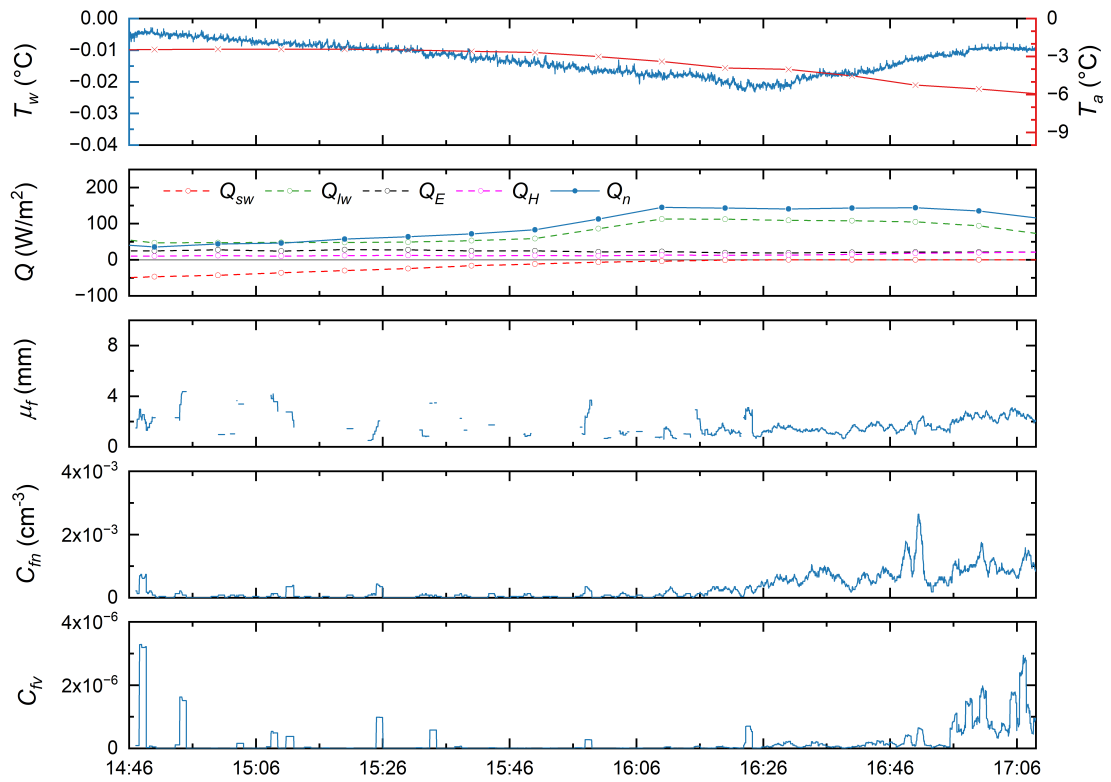


Figure A.3: Time series of (a) water and air temperatures  $T_w$  and  $T_a$ , (b) heat flux  $Q$ , (c) floc mean size  $\mu_f$ , (d) floc number concentration  $C_{fn}$  and (e) floc volumetric concentration  $C_{fv}$  for deployment NSR-L3 on December 9, 2021.

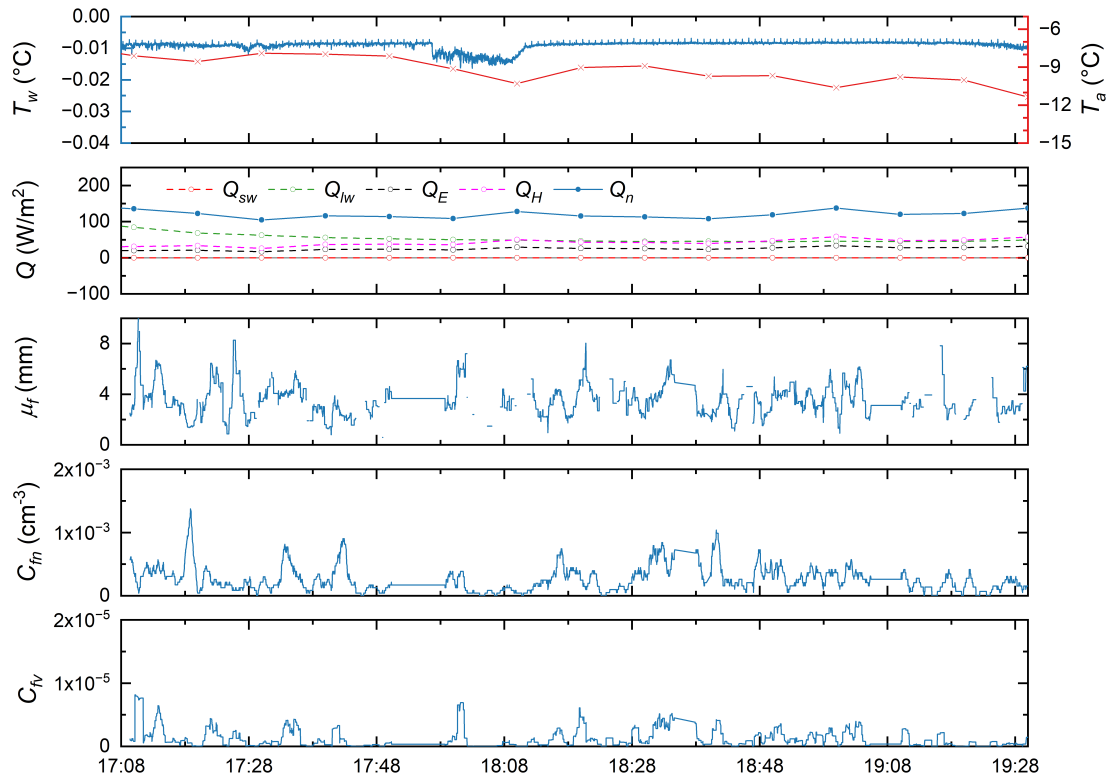


Figure A.4: Time series of (a) water and air temperatures  $T_w$  and  $T_a$ , (b) heat flux  $Q$ , (c) floc mean size  $\mu_f$ , (d) floc number concentration  $C_{fn}$  and (e) floc volumetric concentration  $C_{fv}$  for deployment NSR-L5 on December 12, 2021.

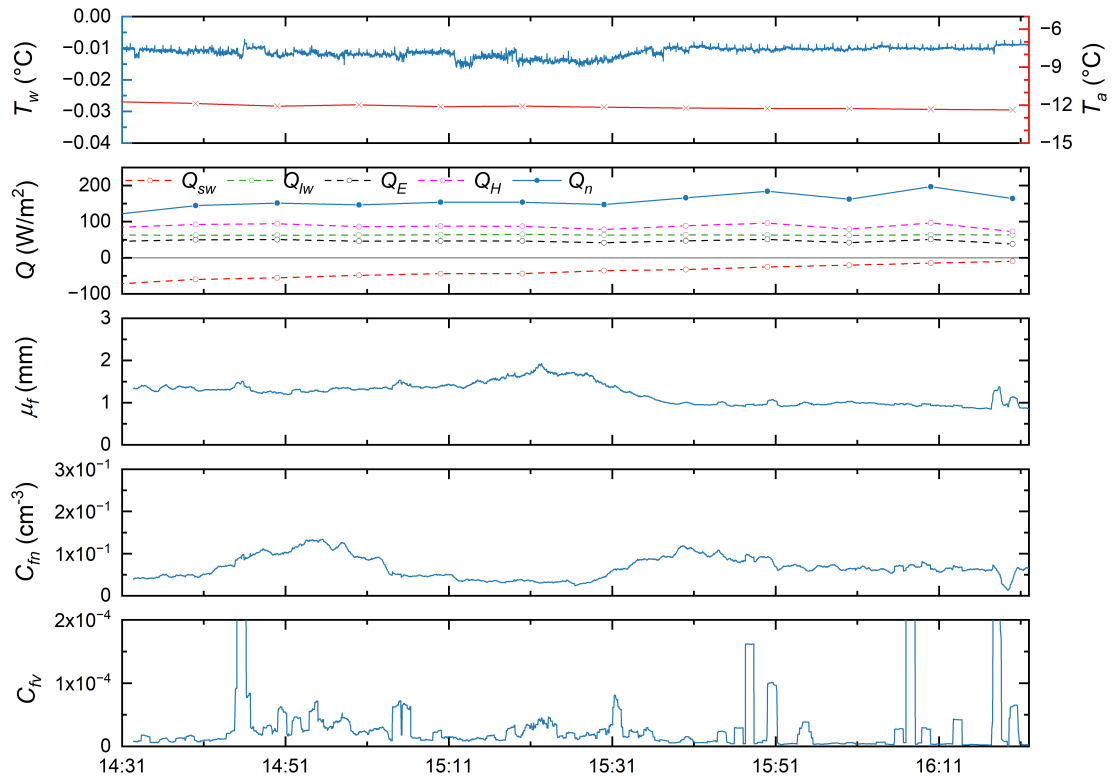


Figure A.5: Time series of (a) water and air temperatures  $T_w$  and  $T_a$ , (b) heat flux  $Q$ , (c) floc mean size  $\mu_f$ , (d) floc number concentration  $C_{fn}$  and (e) floc volumetric concentration  $C_{fv}$  for deployment NSR-L6 on November 7, 2022.

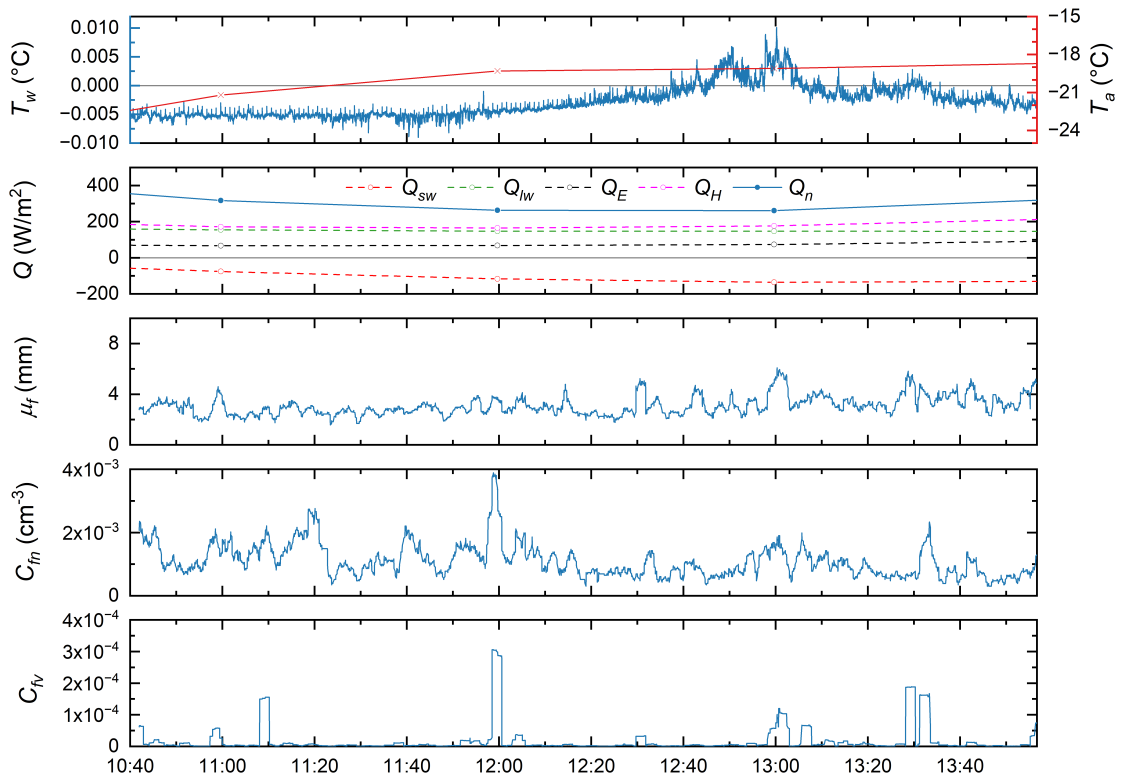


Figure A.6: Time series of (a) water and air temperatures  $T_w$  and  $T_a$ , (b) heat flux  $Q$ , (c) floc mean size  $\mu_f$ , (d) floc number concentration  $C_{fn}$  and (e) floc volumetric concentration  $C_{fv}$  for deployment PR-F1 on December 12, 2022.

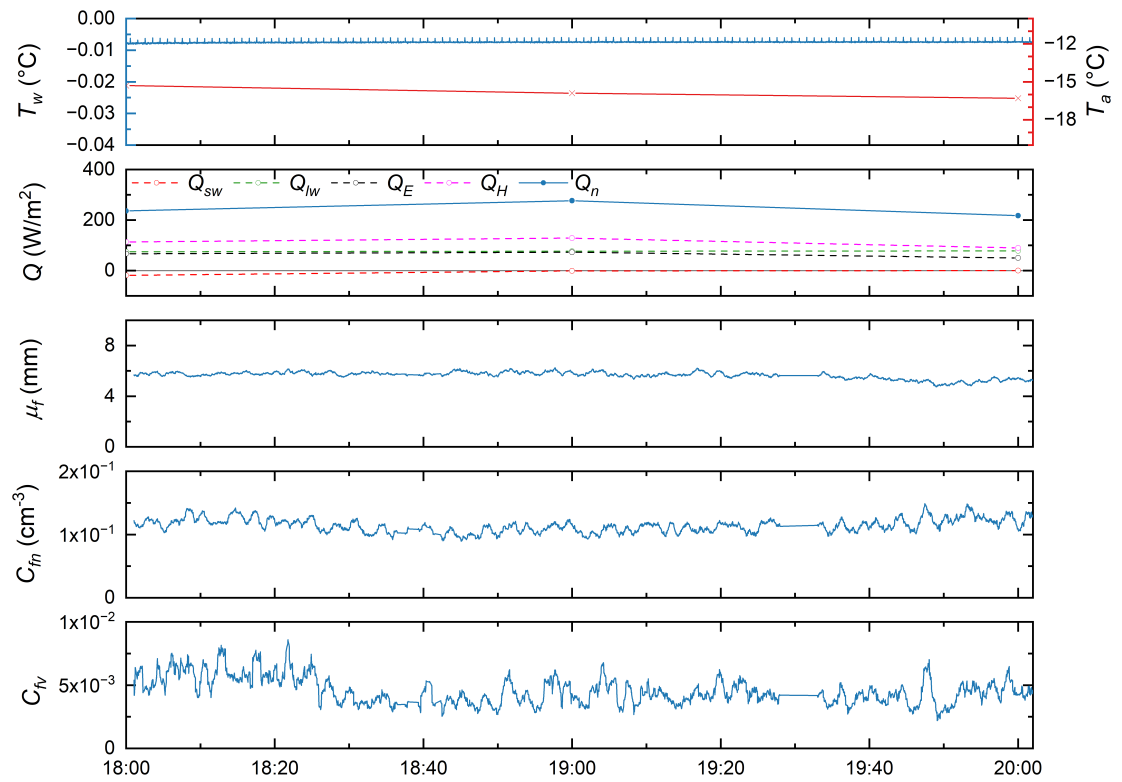


Figure A.7: Time series of (a) water and air temperatures  $T_w$  and  $T_a$ , (b) heat flux  $Q$ , (c) floc mean size  $\mu_f$ , (d) floc number concentration  $C_{fn}$  and (e) floc volumetric concentration  $C_{fv}$  for deployment KR-E1 on January 29, 2023.

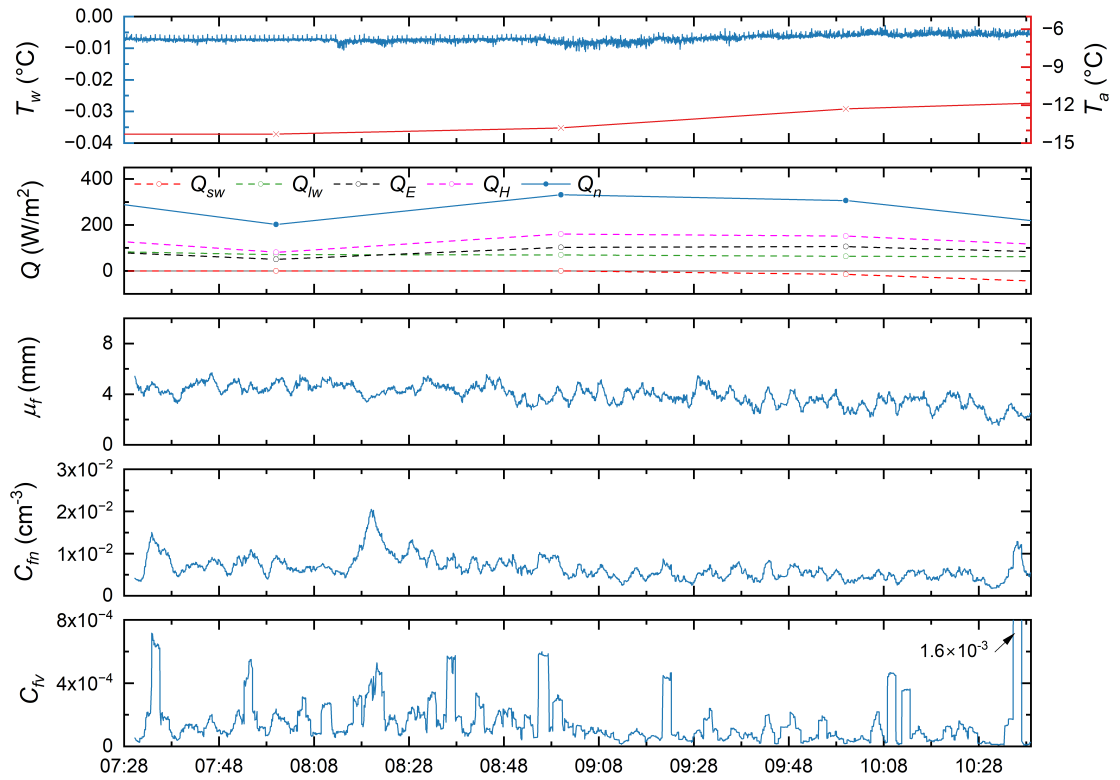


Figure A.8: Time series of (a) water and air temperatures  $T_w$  and  $T_a$ , (b) heat flux  $Q$ , (c) floc mean size  $\mu_f$ , (d) floc number concentration  $C_{fn}$  and (e) floc volumetric concentration  $C_{fv}$  for deployment KR-F2 on January 31, 2023.